Roughness and Adhesion Effects on Pre-Sliding Friction: Modelling and Experiments M. Bazr Afshan

Roughness and Adhesion Effects on Pre-Sliding Friction: Modelling and Experiments

Mohammad Bazr Afshan Fadafan

materials innovation institute

ISBN: 978-90-365-4785-7
DOI : 10.3990/1.9789036547857

Roughness and Adhesion Effects on Pre-Sliding Friction: Modelling and Experiments

Mohammad Bazr Afshan Fadafan

Faculty of Engineering Technology,

Laboratory of Surface Technology and Tribology,

University of Twente

This dissertation has been approved by
Supervisor: Dr.ir. M.B. de Rooij
Co-supervisor: Prof.dr.ir D.J. Schipper

ROUGHNESS AND ADHESION EFFECTS ON PRE-SLIDING FRICTION: MODELLING AND EXPERIMENTS

DISSERTATION

to obtain
the degree of doctor at the University of Twente,
on the authority of the rector magnificus,
Prof.dr. T.T.M. Palstra,
on account of the decision of the Doctorate Board,
to be publicly defended
on Friday 21st of June 2019 at 12:45

By:

Mohammad Bazr Afshan Fadafan

Born on 19th of September 1987

in Kashmar, Iran

This research was carried out under project number S61.1.13492 in the framework of the Partnership Program of the Materials innovation institute M2i (www.m2i.nl) and the Netherlands Organization for Scientific Research NWO (www.nwo.nl).

Doctorate Board:

Prof. dr. G.P.M.R. Dewulf, University of Twente, Chairman/Secretary
Dr.ir. M.B. de Rooij, University of Twente, Supervisor
Prof. dr. ir. D.J. Schipper, University of Twente, Co-supervisor
Prof. Dr. A. de Boer, University of Twente
Prof. Dr. D. Brouwer, University of Twente
Prof. Dr. S. Franklin, University of Sheffield
Dr.ir. R.A.J. van Ostayen, Delft University of Technolgy

Bazr Afshan Fadafan, Mohammad
Roughness and Adhesion Effects on Pre-Sliding Friction: Modelling and Experiments
Ph.D. Thesis, University of Twente, Enschede, The Netherlands, June 2019

ISBN: 978-90-365-4785-7
DOI : 10.3990/1.9789036547857

to Shirin
and
my parents

Summary

Controlling friction and adhesion at a wafer-waferstage interface is in direct relation with high precision and stability of the positioning mechanisms of a lithography machine. Understanding these two phenomena is the first and key step in controlling them. This thesis aims at developing a BEM (Boundary Element Method) model for an adhesive frictional contact of a rough interface, representing the wafer-waferstage interface, along with experiments to verify the validity of the model. The developed model consists of two main blocks which are interacting with one another: adhesion and pre-sliding friction.

Adhesion is considered to be dominated by the van der Waals forces (in vacuum conditions) and the capillary force (in ambient conditions). In the first step, a previously developed algorithm for the non-adhesive normal contact of rough surfaces is extended to include the adhesion effect due to van der Waals forces. This BEM model is further extended, in the second step, to account for the capillary force due to a humid environment and thin water films adsorbed on the contacting surfaces. In the developed model, the effects of various parameters, such as work of adhesion, roughness properties, and relative humidity are investigated. To verify the accuracy of the model, a series of pull-off force measurements, both in vacuum and ambient conditions, is conducted using an Atomic Force Microscope (AFM) at the contact of a cantilever with an SiO_2 colloidal probe and a silicon wafer. The experimental results are then compared with the model predictions for the measured forces.

In the second block, a BEM model is developed for the pre-sliding behavior of a rough interface formed by two contacting surfaces. The adhesive terms are then embedded in this model. The influences of different parameters, such as work of adhesion and roughness parameters, on the friction hysteresis loops, pre-sliding displacement, and static friction force are studied. To validate the model, friction measurements are carried out in an in-house setup, named VAFT (Vacuum Adhesion-Friction Tester), for the contact of a polymeric ball against a silicon wafer under various normal loads.

The developed BEM model, as the output of this thesis, can be used as a tool to design textures on the waferstage in order to achieve a desirable level of friction and adhesion aiming at a higher level of precision, stability, and durability during the lithography process.

Samenvatting

Het beheersen van wrijving en adhesie op het wafer-waferstage interface staat in directe relatie met een hoge precisie en stabiliteit van de positioneringsmechanismen van een lithografiemachine. Het begrijpen van deze twee verschijnselen is de eerste stap in het beheersen ervan. Dit proefschrift is gericht op het ontwikkelen van een BEM (Boundary Element Method) -model voor het adhesieve wrijvingscontact in een ruwe interface, die de wafer-waferstage interface representeert.Ook zijn er experimenten uitgevoerd om het model te valideren. Het ontwikkelde model bestaan uit twee samenhangende onderdelen: een adhesie contact model en een pre-sliding model.

Adhesie wordt beschouwd te worden gedomineerd door van der Waals-krachten (in vacuüm) en de capillaire kracht (in de aanwezigheid van water). In de eerste stap is een eerder ontwikkeld algoritme voor het niet-adhesieve contact van ruwe oppervlakken uitgebreid met adhesie vanwege van der Waals-krachten. Dit BEM-model is verder uitgebreid, in de tweede stap naar een omgeving waarbij dunne waterfilms geadsorbeerd zijn op de contactoppervlakken. Met het ontwikkelde model zijn de effecten van verschillende parameters, zoals werk of adhesie, ruwheidseigenschappen en relatieve vochtigheid, onderzocht. De nauwkeurigheid van het model zijn middels een serie "pull-off" krachtmetingen, zowel onder vacuüm- als omgevingsomstandigheden, uitgevoerd met behulp van een Atomic Force Microscope (AFM) bij het contact van een cantilever met een SiO2 colloïdale probe en een siliconwafer. De experimentele resultaten worden vergeleken met de modelvoorspellingen voor deze gemeten krachten.

In het tweede blok wordt een BEM-model ontwikkeld voor het pre-sliding van de ruwe interface van de twee contactoppervlaken. De invloeden van verschillende parameters, zoals werk of adhesie en ruwheidsparameters, op de frictiehysterese-lussen, pre-sliding en de statische wrijvingskracht zijn geanalyseerd. Om het model te valideren, worden wrijvingsmetingen uitgevoerd op een in-house opstelling, genaamd VAFT (Vacuum Adhesion-Friction Tester), voor het contact van een siliconwafer onder verschillende normaal belastingen.

Het ontwikkelde BEM-model kan worden gebruikt als een hulpmiddel om texturen op de waferstage te ontwikkelen die bijdragen aan een hogere precisie en stabiliteit van het lithografie proces.

Acknowledgement

Now that I am at the end of an important stage of my life, I would like to thank all the people who directly or indirectly helped me with conducting my research smoothly.

First, I would like to express my greatest gratitude to my supervisors Matthijn and Dik for all the support and guidance in the past four years.

I would thank Mahdiar Valefi, Muhammad Adeel Yaqoob, Satish Achanta, Subodh Singh, Stef Janssens, Aydar Akchurin and Bart Stel from ASML for the useful discussions on the progress of this research study and also assisting me with the experiments.

I would also thank all my friends and colleagues at the Surface Technology and Tribology group of the University of Twente; Erik and Walter are sincerely thanked for the technical support in the laboratory; I am very grateful to Belinda and Debbie for their managerial support. Also my deep gratitude goes to my good friends: Milad, Dariush, Febin, Xavier, Tanmaya, Melkamo, Dennis, Shivam, Dimitry, Can, Faizan, Matthijs, Michel, Yuxin, Muhammad, Ida, Hilwa and Marina.

Special thanks to my family for their love and support.

Last but not least, I should give my sincerest gratitude to my wife, Shirin, who came with me to the Netherlands and supported me in these four years with her love, patience, and energy.

Contents

Part II

Publications

Paper A. Numerical method for the adhesive normal contact analysis based on a Dugdale approximation, M. Bazrafshan, M.B. de Rooij, M. Valefi, D.J. Schipper, Tribology International, 112, 117-128, 2017. DOI: 10.1016/j.triboint.2017.04.001

Paper B. Adhesive force model at a rough interface in the presence of thin water films: The role of relative humidity, M. Bazrafshan, M.B. de Rooij, D.J. Schipper, International Journal of Mechanical Sciences, 140, 471-485, 2018. DOI: 10.1016/j.ijmecsci.2018.03.024

Paper C. The Effect Surface Roughness on Adhesion: Experimental Evaluation of a BEM Model, M. Bazrafshan, M.B. de Rooij, E.G. de Vries, D.J. Schipper, submitted to Journal of Adhesion Science and Technology

Paper D. On the role of adhesion and roughness in stick-slip transition at the contact of two bodies: A numerical study, M. Bazrafshan, M.B. de Rooij, D.J. Schipper, Tribology International, 121, 381-388, 2018. DOI: 10.1016/j.triboint.2018.02.004

Paper E. The Effect of Adhesion and Roughness on Friction Hysteresis Loops, M. Bazrafshan, M.B. de Rooij, D.J. Schipper, International Journal of Mechanical Sciences, 155, 9-18, 2019. DOI: 10.1016/j.ijmecsci.2019.02.027

Paper F. Evaluation of Pre-Sliding Behavior at a Rough Interface: Modelling and Experiment, M. Bazrafshan, M.B. de Rooij, E.G. de Vries, D.J. Schipper, submitted to Tribology Letters

Other publications

1. Extending the Double-Hertz Model to Allow Modeling of an Adhesive Elliptical Contact, N.H.M. Zini, M.B. de Rooij, M. Bazr Afshan Fadafan, N. Ismail, D.J. Schipper, Tribology Letters 66 (1), 2018, 30.

2. Response to Dr Greenwood's Comments on "Extending the Double-Hertz Model to Allow Modeling of an Adhesive Elliptical Contact", N.H.M. Zini, M.B. de Rooij, M. Bazr Afshan Fadafan, N. Ismail, D.J. Schipper, Tribology Letters 66, 2018

3. Comparison of Lennard-Jones Interaction and Maugis-Dugdale models of Adhe-sion for the Adhesive Contact Analysis for a Bisinusoidal Interface, M. Bazrafshan, M.B. de Rooij, D.J. Schipper, 17th Nordic Symposium on Tribology - Nordtrib 2016, Aulanko, Finland.

4. On the role of adhesion and roughness in stick-slip transition at the contact of two bodies: A numerical study, M. Bazrafshan, M.B. de Rooij, D.J. Schipper, 6th European Conference on Tribology, EcoTrib 2017, Ljubljana, Slovenia.

5. Adhesive force model at a rough interface in the presence of thin water films: The role of relative humidity, M. Bazrafshan, M.B. de Rooij, D.J. Schipper, 1st International Workshop on Adhesion and Friction: Simulation, Experiments, and Applications, 2017, Berlin, Germany.

6. The Effect of Adhesion and Roughness on Friction Hysteresis Loops, M. Bazrafshan, M.B. de Rooij, D.J. Schipper, 3rd International Brazilian Conference on Tribology, TriboBR 2018, Florianopolis, Brazil.

Nomenclature

Roman symbols

A_0	Nominal contact area	m^2
$A_{adhesive}$	Adhesive area	m^2
A_c	Contact area	m^2
A_{slip}	Slip area	m^2
A_{stick}	Stick area	m^2
a	Contact radius	m
$C(q)$	Surface roughness power spectrum	m^4
d	Separation between two surfaces	m
E	Elastic modulus	Nm^{-2}, Pa
E_s	Effective elastic modulus	Nm^{-2}, Pa
e	Water film thickness	m
F_0	External normal force	N
F_0^+	Contact repulsive force	N
F_0^-	Adhesive force	N
F_f	Friction force	N
F^*	Amplitude of oscillating friction force	N
F_{adh}	Adhesive force	N
F_n	Normal force	N
F_{nr}	Normalized friction force	$-$
$F_{pull-off}$	Pull-off force	N
$g(r)$	Separation profile at the interface	m
H	Hurst exponent	$-$
$H(x,y)$	Heaviside function	$-$
$h(x,y)$	Roughness height	m
$h_w(x,y)$	Profile of the water film free surface	m
$K(m,n)$	Boussinesq kernel function in frequency domain	$N^{-1}m^{-2}$
$k(x,y)$	Boussinesq kernel function in spatial domain	mN^{-1}
k	Wavelength ratio	$-$
N	Total number of asperities	$-$
n	Expected number of contacts	$-$
P	Interfacial pressure	Nm^{-2}, Pa
$P(x,y)$	Pressure profile	Nm^{-2}, Pa
$P(\sigma,\xi)$	Stress distribution	$N^{-1}m^2$
p_0	Nominal pressure	Nm^{-2}
$\tilde{p}_{if}(q)$	Interfacial stress in frequency domain	N

q	Wavevector	$-$
q_0	Lower cut-off wavevector	$-$
$\|q\|$	Shear stress magnitude	$Nm^{-2},\ Pa$
$q_{x,y}$	Shear stress in x and y directions	$Nm^{-2},\ Pa$
R_c	Radius of curvature of a bi-sinusoidal surface	m
R_g	Universal gas constant	$Jmol^{-1}K^{-1}$
$\|s\|$	Relative displacement magnitude	m
$s_{x,y}$	Relative displacement in x and y directions	m
T	Temperature	K
t	Time	s
$u(x,y)$	Deformation profile	m
$\tilde{u}(q)$	Deformation profile in frequency domain	m^3
V	Molar volume of water	m^3mol^{-1}
x,y	Spatial coordinates	m
z	distance from reference plane	m
z_0	Equilibrium distance	m

Greek letters

α	Degree of waviness of a wavy profile	$-$
β	Asperity radius of curvature	m
$\Delta\gamma$	Total work of adhesion	Jm^{-2}
$\Delta s_{x,y}$	Rate of change in relative displacement	m
δ	Kronecker delta function	$-$
δ_0	Pre-sliding displacement (Mindlin)	m
δ_x	Tangential displacement	m
δ_z	Rigid displacement in normal direction	m
ζ	Magnification (Persson's theory)	$-$
λ	Roughness length scale	m
μ	Friction coefficient	$-$
μ_f	Friction coefficient	$-$
μ_k	Kinetic friction coefficient	$-$
μ_s	Static friction coefficient	$-$
μ_T	Tabor parameter	$-$
ν	Poisson's ratio	$-$
σ_0	Dugdale stress	Nm^{-2}
$\sigma_{adh}(r)$	Adhesive stress	nm^{-2}
σ_s	RMS of summits heights	m
σ_u	Unit pressure	Nm^{-2}
τ	Critical shear stress	Nm^{-2}
$\phi(z)$	Gaussian distribution of asperity heights	m^{-1}
Ω	Computation domain	$-$

Abbreviations

AFM	Atomic Force Microscope
BEM	Boundary Element Method
DMT	Derjaguin-Muller-Toporov
FEM	Finite Element Method
GFMD	Green's Function Molecular Dynamics
JKR	Johnson-Kendall-Roberts
MD	Molecular Dynamics
MD	Maugis-Dugdale
RH	Relative Humidity
DLC	Diamond-Like Carbon

Part I

Chapter 1

INTRODUCTION

1.1 Background

Adhesion (stickiness) and friction (the resistance to sliding motion between two contacting surfaces) are the two fundamental interfacial phenomena that can be found in thousands of daily situations. For instance, friction between a shoe and floor is required for walking (beneficial friction). Wear and energy loss due to the friction in bearings and gears is another example (undesirable friction). Examples of adhesion can be found in sealants, printing, cell biology, medicine, engineering, etc.

In nature, many living creatures can achieve a high level of controllability in the adhesion and friction of their biological attachment structures. Such surface structures are implemented for their movement. Spiders, lizards, and insects are good examples of creatures with this ability. Another example is a gecko with its elegant hierarchical fibrillar architecture on its toe-pad which enables it to climb and traverse walls and ceilings very fast, despite its relatively large body weight. Inspired by these biological systems, in the modern technology, it is also very desirable to control adhesion and friction at the mating surfaces, especially in nanotribology applications such as Micro/Nano Electro-Mechanical Systems (MEMS and NEMS) and micro-scale devices like hard disk drives. More specifically, following the recent advances in semiconductor technology, the roadmap to achieve a better accuracy in design and fabrication of smaller and smaller computer chips requires high precision and stability of the positioning mechanisms of the lithography machines.

Start-stop of a positioning mechanism and loading the wafer on the waferstage are two of the most prominent examples in semiconductor applications where adhesion and friction are considered the key factors of precision. However, a lack of deep understanding of these two phenomena impedes engineers to design a dedicated mechanism or surface texture to achieve a high level of precision and accuracy in manufacturing tiny computer chips. Thus, understanding friction and adhesion is of great importance in such

applications.

1.2 Surfaces in contact

Surfaces scale always have micro/nano scale roughness even if they look very smooth. In other words, the contact between two surfaces, in practice, consists of a number of micro-contacts between the high asperities on both contacting surfaces, as schematically shown in Figure 1.1. In this regard, Bowden made this analogy that "Putting two solids together is rather like turning Switzerland upside down and standing it on Austria – the area of intimate contact will be small" [1]. To study adhesion and friction, thus, it is necessary to first understand the contact of rough surfaces, since these two phenomena are strongly dependent on the interaction between the contacting asperities.

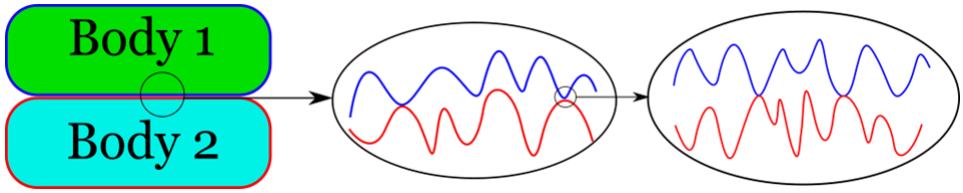

Figure 1.1: Schematic representation of the contact of two surfaces.

1.2.1 Adhesion

Adhesion is the tendency of two surfaces to stick to one another. The energy and force required to separate them are called work of adhesion and pull-off force, respectively. The strength of adhesion is related to the surface energies of the contacting surfaces and the medium through which the contact has formed. In practice, this strength is often very small, while it can be considerable for smooth and compliant surfaces. Two surfaces in contact usually adhere to each other; if not, it could be due to three reasons: a small real area of contact, contamination layers or particles on the surfaces, and residual elastic stresses which can break up the adhesion bonds. Adhesion typically consists of different components, each or a combination of which can contribute to the total adhesive force. A few of these forces are as follow:

- Van der Waals forces: Short-range and weak electrostatic forces between uncharged surfaces due to the interaction between transient or permanent dipole moments.
- Capillary force: meniscus force arising from the water bridges formed around the contact asperities or at the near-contacting asperities due to the adsorbed water films from the humid environment on the surfaces.

- Electrostatic force: Strong and long-range force acting between charged surfaces.

1.2.2 Friction

Friction is the resistance to motion as two surfaces are rubbed along each other. The earliest studies of friction date back to the 15th century where Leonardo da Vinci presented the rules governing the sliding of a rectangular block on a flat surface. Unfortunately, his studies had no scientific impact as his notes remained unpublished for hundreds of years. It was, later on, Amonton who introduced the friction rules which are now known as Amonton's laws of friction [2]:

- The friction force is proportional to the normal load
- The friction force is independent of the apparent contact area

A third law was later added by Coloumb which states that [3]:

- The friction force is independent of sliding velocity.

The first law can be mathematically expressed as:

$$F_f = \mu F_n \tag{1.1}$$

where F_f and F_n are the friction and normal force, respectively, and μ is the proportionality factor or namely the coefficient of friction. This expression also implies the second law of Amonton which states that the friction does not depend on the apparent contact area. The third law states that, once the motion starts, the friction force does not depend on the sliding velocity. In addition, Coulomb made a clear distinction that the static coefficient friction, μ_s, is larger than the kinetic one, μ_k. Adhesion was initially proposed to be the cause of friction. This hypothesis appeared to contradict the Amonton's second law. Bowden and Tabor cleared up this contradiction in the 1930s by introducing the concept of the real contact area made up of a number of small regions of contact, referred to as asperities, where atomic contacts take place [1]. This implies that only a small fraction of the apparent contact area really touches the counter surface.

1.3 Application

In a lithography process, the accuracy at which a layer is placed on top of the previous one is called overlay error. It is an important specification determining the smallest feature size that can be printed. Less overlay error means a better functionality of the computer chip. Therefore, reduction of this error is of special interest. One of the main contributors to the overlay error is the interaction between the wafer and waferstage. For a lithography process,

the wafer needs to be loaded at a high level of accuracy and reproducibility. This requires specific and stable friction/stiction properties between the wafer and the waferstage over long periods of time. On a waferstage, burls are present to reduce the contact between the wafer and waferstage (see Figure 1.2). As friction and adhesion are strongly dependent on the microgeometry (roughness) of the contacting surfaces, a dedicated texture on the burls should be designed to minimize adhesion and reach a stable level of friction at this interface. In one hand, it is proven that the roughness can reduce adhesion by orders of magnitude. On the other hand, a rougher surface is more susceptible to wear at a frictional contact. This emphasizes the significance of designing an appropriate surface texture. Prior to such a design, the relation between the surface microgeometry (roughness) and adhesion and friction phenomena needs to be comprehensively understood.

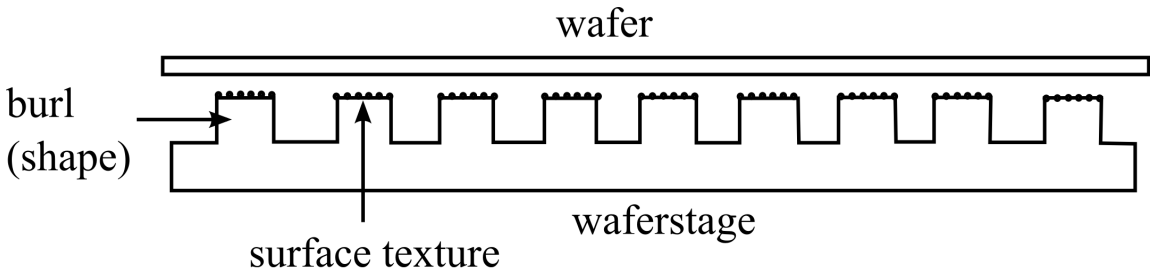

Figure 1.2: The contact between a wafer and waferstage.

1.4 Objectives of the project

The main aim of the project is to find out how friction and adhesion are related to the surface topography at the burl-wafer interface. More specifically, the transition from stick to slip (which occurs at the start-stop conditions) and how it is affected by adhesion are concerned. The objective is to develop a numerical model to study the stick-slip transition and pre-sliding displacement at a rough interface in the presence of adhesion. For this, a BEM (Boundary Element Method) model is developed and validated at different environmental conditions. This model is developed in different stages listed below:

- Developing a BEM model for the normal adhesive contact at a rough interface of two contacting surfaces, where the adhesion originates from van der Waals forces (representing a vacuum environment).
- Extending the model to include the capillarity effect at such an interface due to the adsorbed water films on the surfaces and the humidity of the ambient environment.
- Performing pull-off force measurements using an AFM (Atomic Force Microscope) at various environmental conditions and comparing the results with the model

prediction.

- Extending the model to include the effect of a shear force to study the transition from stick to slip.
- Investigating the effect of adhesion on the stick-slip transition.
- Performing friction experiments using an existing experimental setup to verify the accuracy of the frictional model.

  The outcoming knowledge can be used as a tool to design surface textures on a burl in order to achieve a controlled and desirable level of friction and adhesion.

1.5 Outline of the thesis

This thesis focuses on the influence of adhesion, coming from either van der Waals forces or capillary force, on the (partial) slip contact at a rough interface of two surfaces. The thesis consist of two main parts: Part I and Part II. Part I gives an overview of the problem, the literature, and the main outcomes of the thesis. Part II provides the published studies of the author and his co-authors within the framework of the thesis objectives. Part I includes four chapters. The current chapter describes the problem along with the aim and objectives. The second chapter summarizes the existing continuum contact models for rough surfaces. In its first section, various approaches for the normal contact of rough surfaces including analytical models of Greenwood-Williamson and Persson's theory, and numerical methods, such as finite element, boundary element and Green's function molecular dynamics are compared. In the second section, the literature on the transition from stick to slip at a tangential contact of two surfaces is provided. In the end, the boundary element method is chosen to be the most appropriate numerical scheme for the problem at hand. The third chapter summarizes the main outcomes of the papers, presented in Part II of the thesis. In the end, chapter four provides conclusions and recommendations for further research. Part II of the thesis includes the six publications coming from the findings of this research (papers A to F).

Chapter 2

CONTACT OF ROUGH SURFACES

2.1 Normal contact

When two rough surfaces are pressed against each other, they touch at a number of high peaks or asperities which deform elastically or plastically to form micro-contact areas. The sum of these areas is typically a small fraction of the apparent (nominal) area over which the two surfaces are brought into contact. This leads to high pressures at these micro-contacts to which the severity of wear and surface fatigue are related.
The real area of contact depends on the surface topography, material properties, and interfacial loading conditions. The proximity of the asperities leads to adhesive contacts due to interatomic interactions. When the two surfaces experience a relative movement, the adhesion of asperities along with other sources of surface interactions contribute to the friction force. Repeated surface interactions and the developed stresses at the interface result in the formation of wear particles and finally failure. Thus, modeling the contact between rough surfaces is crucial in friction and wear studies.

2.1.1 Greenwood-Williamson model

Dealing with the contact of rough surfaces is demanding and has been treated by different approaches in the past few decades. One of the first studies of the real area of contact was the elegant work of Greenwood and Williamson which applies to the contact of two flat elastic planes, one of which is smooth and the other is rough [4]. In the GW model, it is assumed that the rough surface is represented by asperities with identical radius of curvature, β, while their heights follow a Gaussian (or a known) distribution as:

$$\phi(z) = \frac{1}{\sigma_s} e^{-z^2/2\sigma_s^2} \tag{2.1}$$

with σ_s being the rms of summit heights. Considering the separation of d between the two surfaces, as shown in Figure 2.1, the probability of the contact for an asperity is:

$$P(z > d) = \int_d^\infty \phi(z)dz \tag{2.2}$$

Assuming that the total number of asperities, N, is large enough so that the expected number of contacts, n, is expressed as:

$$n = N \int_d^\infty \phi(z)dz \tag{2.3}$$

As the Hertzian theory applies to each asperity contact (refer to Appendix A for details), the total area of contact, A_c, and total contact force, F_0, can be obtained as:

$$A_c = \pi\beta N \int_d^\infty (z-d)\phi(z)dz$$

$$F_0 = \frac{3}{2}\sqrt{\beta}NE_s \int_d^\infty (z-d)^{3/2}\phi(z)dz \tag{2.4}$$

where $1/E_s = (1-\nu_1^2)/E_1 + (1-\nu_2^2)/E_2$ is the effective elastic modulus.

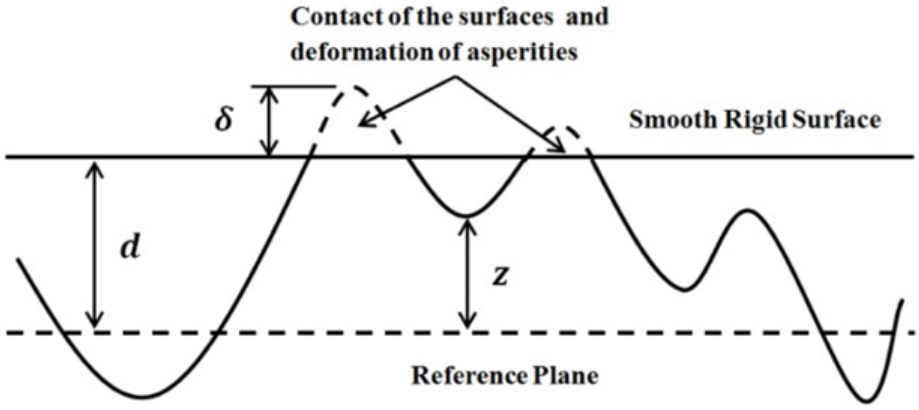

Figure 2.1: Contact of a rough elastic surface against a rigid smooth flat surface.

Multi-asperity contact theory was initiated by this original GW model and was later refined by Bush, Gibson, and Thomas (BGT) [5], McCool [6], Greenwood [7], Carbone and Bottiglione [8] and Carbone [9].
One of the main limitations of the original GW model is that it assumes that all

asperities deform independently. Although, this assumption makes the calculation of the total force very simple and straightforward, it ignores the fact that all asperities touch the same substrate. Each individual contacting asperity deforms the substrate and shifts down all other asperities and in this way, reduces the number of contacting asperities or in general, the real area of contact. Ciavarella et al. extended the GW model to incorporate the interaction between asperities by treating the contact pressures and resulting deformations as uniformly distributed on the apparent contact area [10]. This improvement results in a reduction of real contact area and total contact force for a given separation. Another improvement to the GW model by means of inclusion of the interaction between asperities was proposed by Chandeasekar et al. [11]. They developed a finite element model of a representative model of a rough surface where the interaction between asperities is governed by the Hertzian theory. To account for the interaction between asperities, Vakis implemented the statistical summation of asperity forces while the interaction between non-contacting asperities are also taken into account [12]. He also proposed a curve-fitted expression for the asperity interaction by the nominal contact force predicted by other models.

Adhesion modeling in GW

To deal with adhesion at a rough interface using the GW model, researchers couple a single asperity adhesive contact model such as JKR, DMT, MD, and or a numerical model (see Appendix A for details) with a statistical distribution of summit heights such as Gaussian or deterministically using a measured rough surface profile [13–20].
Accounting for the capillary force for a rough contact using the GW theory follows the same approach (see Appendix A for details). Authors have extended the single asperity meniscus models to the contact of rough surfaces and studied the effects of the roughness parameters and the relative humidity of the environment on the total adhesive force and friction coefficient [21–26]. The important phenomenon that is ignored in such models is the role of the water films available at the interface. These thin films, adsorbed from the humid environment, mediate the formation of the micro-meniscus islands and, depending on their thickness, can considerably alter the total adhesive force.

Limitations of GW models

In addition to neglecting the interaction between neighboring asperities, there are still limitations attributed to the multi-asperity contact models. Since the surface is described only in terms of the summit geometry, the geometry of the remaining of the surface is discarded. This information loss is problematic when the separation profile is needed for adhesive interaction, for instance. In addition, the independence of each individual asperity deformation from its neighboring ones is unrealistic. For loads, high enough compared to the elastic modulus or roughness size, contact regions might physically get close enough

to combine and form a larger domain. Whereas, there is no mechanism in such models to account for this. Furthermore, the distribution of the size and shape of asperities depends on the measurement parameters i.e. bandwidth sufficiency and multiscale nature of rough surfaces. In one hand, if the roughness profile is bandwidth limited, the sampling frequency must be high enough to completely resolve the profile. On the other hand, considering the broadband multi-scale character of the profile is a more subtle issue. All these limitations are even more severe for the contact of rough surfaces or compliant materials [27].

2.1.2 Persson's theory

Figure 2.2 depicts the contact between two rough surfaces at increasing magnification ζ. At the lowest magnification, $\zeta = 1$, it looks that there is a complete contact at the macro-asperities contact zones while increasing the magnification, the roughness at smaller and smaller length scales is detected revealing that the contact is taking place only at high asperities. As a matter of fact, the real area of contact would vanish if there would be no short distance cut-off [28]. In reality, yet, there must be such a short distance cut-off as the shortest scale possible is the atomic distance. It must be noted that increasing the magnification results in higher asperity pressures. In reality, this asperity pressure could become so high, at high magnifications, that the interface yields plastically before reaching the atomic scale. Therefore, the largest magnification should be determined by the interface yield stress [29].

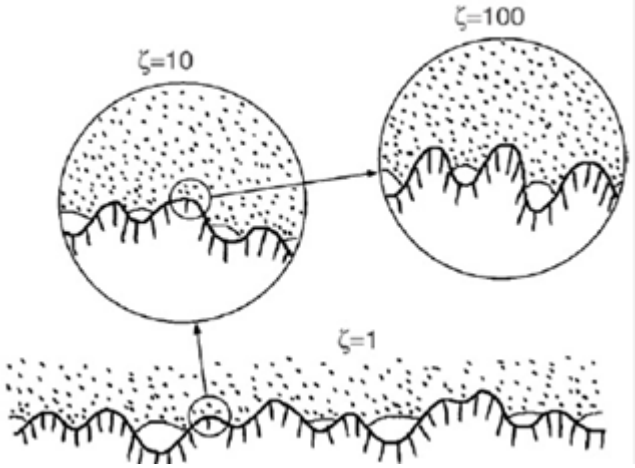

Figure 2.2: A rough interface at increasing magnifications (adapted from [28]).

The fundamental idea behind the Persson's theory of contact is to include all the roughness length scales [30]. Therefore, defining $A(\lambda)$ to be the contact area on the length scale λ (while assuming the surface to be smooth for all length scales shorter than λ), the relative fraction of the surface area is expressed as:

$$P(\zeta) = \frac{A(\lambda)}{A_0} \tag{2.5}$$

in which A_0 is the nominal contact area. In addition, $q_0 = 2\pi/\lambda_0$ and $q = q_0\zeta$ are defined as the wavevector at lowest magnification and at magnification ζ, respectively. $P(\sigma, \zeta)$, denoting as the stress distribution in the contact area at magnification ζ, satisfies the diffusion like equation:

$$\frac{\partial P}{\partial \zeta} = f(\zeta)\frac{\partial^2 P}{\partial \sigma^2} \tag{2.6}$$

in which:

$$f(\zeta) = \frac{\pi E_s^2}{4} q_L q^3 C(q) \tag{2.7}$$

where $C(q)$ is the surface roughness power spectrum at the wavevector q. For the elastic contact of a rectangular block against a flat substrate with the uniform stress σ_u (and neglecting the edge effects), $P(\sigma, 1) = \delta(\sigma - \sigma_u)$ is the initial condition. It is noted that $P(\sigma, \zeta)$ must vanish as $\sigma \to \infty$ which is considered one of the two boundary conditions. The other one is $P(0, \zeta)$, which says the stress distribution is zero for all magnifications in absence of an external normal pressure. Solving Eq.2.6 for $P(\sigma, \zeta)$ gives:

$$P(\sigma, \zeta) = \frac{1}{2\sqrt{\pi G}} \left(e^{-(\sigma-\sigma_u)^2/4G} - e^{-(\sigma+\sigma_u)^2/4G} \right) \tag{2.8}$$

$$P(\zeta) = \int_0^\infty P(\sigma, \zeta) d\sigma = erf(\sigma_u / 2\sqrt{G}) \tag{2.9}$$

where:

$$G(\zeta) = \frac{\pi}{4} E_s^2 \int_{q_L}^{\zeta q_0} q^3 C(q) dq \tag{2.10}$$

As an example for a self-affine fractal rough surface, the power spectrum of the profile, $C(q)$, is expressed as:

$$C(q) = \begin{cases} C_0 & q_L < q < q_0 \\ C_0 \left(\frac{q}{q_0} \right)^{-2(H+1)} & q > q_0 \end{cases} \tag{2.11}$$

where H is the Hurst exponent and q_0 is the lower cut-off (roll-off) wavevector. C_0 is also determined by the surface rms roughness, h_{rms}, as [31]:

$$h_{rms}^2 = \frac{\pi C_0}{\alpha H} q_0^2, \quad \alpha = \frac{1}{(1 + H - (q_L/q_0)^2 H)} \tag{2.12}$$

Consider a self-affine fractal surface of a $100\mu m \times 100\mu m$ square patch with roughness rms of $5nm$, the Hurst exponent of $H = 0.8$, and the roll-off wavevector, q_0, to be 10 times larger than q_L. Figure 2.3(a) illustrates the power spectrum of this surface. Figure 2.3(b) shows the stress distribution for two different magnifications. As previously stated, increasing the magnification, the stress distribution becomes wider, its peak becomes smaller and shifts to higher pressures [29]. This means higher local pressures and a higher possibility for smaller asperities to deform plastically. Applying a normal pressure of $\sigma_u = 0.001 E_s$, Figure 2.3(c) displays the decrease of the relative contact area with the magnification. As the roll-off wavevector is $\pi/q_s = 10^{-5} m^{-1}$, the highest magnification to reach the atomic distance of $2 \times 10^{-5} m$ is approximately $\zeta = 4.7$. This confirms that although the relative contact area vanishes for very high magnifications, the largest physically possible magnification (up to atomic scale distances) results in a noticeable relative area of contact. Figure 2.3(d) depicts the variation of the relative contact area vs. the nominal pressure for three different magnifications (assuming an elastic contact). It is observed that the contact area at lower magnifications reaches the full-contact conditions at a lower nominal pressure.

Limitations of Persson's theory

In principle, the Persson's theory needs only the height auto-correlation function (or power spectrum in frequency domain) of the contacting surfaces as well as their mechanical and surface properties to evaluate the contact area and pressure distribution. Though, it does not give the profile of the pressure or the contacting areas. In addition the validity regarding the assumption of a diffusive process is questioned for some reasons [32]. Another criticism to this theory has been raised in [33] showing that the pressure distribution and true contact area differ between surfaces with either a self-affine or experimentally measured rough profiles provided that everything else is identical.

2.1.3 Finite Element Models

Initial studies of the contact between rough surfaces by means of the finite element model (FEM) was conducted by Hyun et al. and Pei et al. [34, 35]. In these studies, the roughness is dealt with down to the discretization scale. In addition, they described the height profile by only one node per asperity which results in an overestimation of the contact area [36]. Although these methods can obtain a good approximation of the contact clusters distributions, they fail to give precise results for the local behavior of separate contact clusters. This disadvantage was corrected in later studies by introducing the shortest wavelength to be much longer than the surface discretization scale [37].

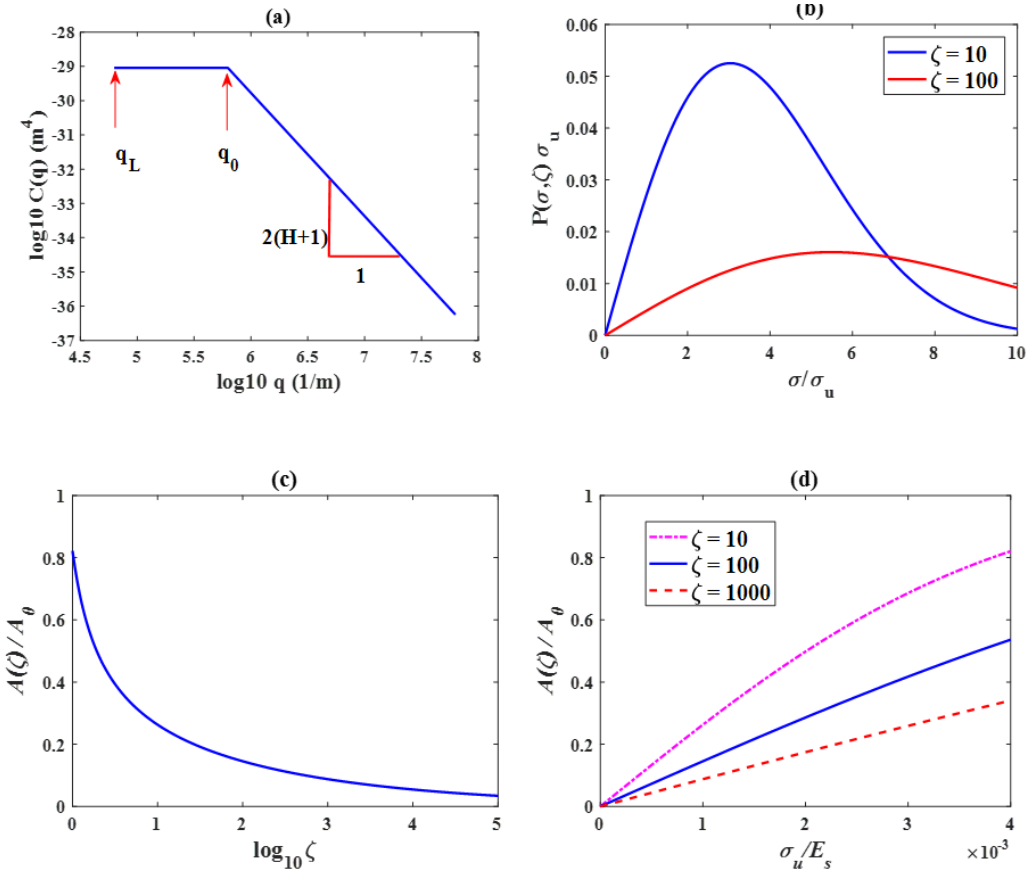

Figure 2.3: (a) Power spectrum of a self-affine rough surface (b) stress distribution for two different magnifications (c) contact area decay vs. magnification (d) evolution of contact area vs. nominal pressure for different magnifications.

Adhesion modeling in FEM

Modeling adhesion at the interface of two surfaces by means of FEM goes back to the study of Cho and Park [38]. They investigated the adhesive elastic contact of a ball against a half-space where the adhesion energy is governed by the Lennard-Jones potential. An extension to this study to include the adhesive interaction at very small scales was carried out by Sauer and Li [39];. Later on, Sauer and Wriggers performed a FEM simulation on the adhesive contact at nano-scale while considering the adhesion to be either a body force or a surface force [40]. They found the model treating with adhesion as a surface force more efficient but less accurate for a strong adhesion energy. The dynamic adhesive contact model through a FEM simulation with application to the adhesion of a gecko spatula was proposed by Sauer [41].

Limitations of FEM models

The main problem of FEM simulations in tribology is that, in essence, the entire physical domain must be discretized which makes it inefficient in comparison to other numerical methods considering only the boundary of the domain, namely the contact interface, such as the Boundary Element Method and Green Function's Molecular Dynamics. This is even more severe for the contact of rough surfaces where the interface itself already requires a very fine mesh and high amount of computation to solve the contact problem.

2.1.4 Green's Function Molecular Dynamics (GFMD)

GFMD is, in principle, a Boundary Value Problem which is solved using regular molecular dynamics. The main idea behind GFMD is to use the fluctuation-dissipation theorem to calculate the Green's function of homogeneous solids [42]. Using this method, it is possible to compute the dynamic response of a semi-infinite elastic solid to external boundary (surface) forces [43]. Concerning the damped dynamics (static case), in tribology, it has been used to simulate the contact mechanics of rough surfaces [33, 42–46]. One of the merits of GFMD is that it only needs the knowledge of the displacements at the surface of the solid. In other words, only does the surface of the contacting bodies need to be discretized and not the bulk. It is stated that GFMD can handle a very large number of elements which even exceeds the size of very accurate surface topography measurements. Convergence can be achieved within a few thousand time steps. However, it is inefficient when the relative contact area is less than 0.1% for which hundred thousand iterations might be required [47].
For an elastic contact at an interface, where a nominal pressure p_0 is applied, the problem is to solve Eq.2.13 for $\tilde{p}_{if}(q)$ [43].

$$\frac{E_s}{2} q\tilde{u}(q) + \tilde{p}_{if}(q) + \tilde{p}_{ext}(q) = 0 \tag{2.13}$$

where $\tilde{X}$ is the Fourier transform of X. Here, $\tilde{p}_{ext}(q) = p_0\delta_{0,q}$, where δ is the Kronecker delta function. In addition, $\tilde{u}(q)$ and $\tilde{p}_{if}(q)$ are the deformation and interfacial stress which are related to one another through:

$$\tilde{p}_{if}(q) = \begin{cases} -p_0, & q = 0 \\ -\frac{E_s}{2} q\tilde{u}(q), & q \neq 0 \end{cases} \tag{2.14}$$

It is noted that the case $q = 0$ represents a smooth contact where the interfacial stress is everywhere uniform and equal to the external nominal pressure.
GFMD attempts to solve Eq.2.13 for the interfacial stress where one can assume a hard-wall interaction at the interface meaning that the interacting bodies cannot penetrate into one another. In other words, as two atoms start to penetrate into each other, the

interaction energy immediately goes to infinity with respect to the penetration depth. As this assumption might not be straightforward, an exponentially repulsive potential can be implemented instead, where, in contrast to the hard-wall condition, the interaction energy exponential increases with the penetration depth as the two atoms penetrate [42, 48]. As it can be seen in Figure 2.4, Campana and Muser showed that, for a Hertzian contact, the hard-wall interaction can reproduce the sharp features of the analytical pressure profile. For the case of exponentially repulsive potential, however, the transition between contact and non-contact regions is faded out [42]. Yet, they believe that the real interactions between surfaces extend over a nonzero penetration and this exponentially repulsive potential might be physically more realistic than the hard-wall assumption.

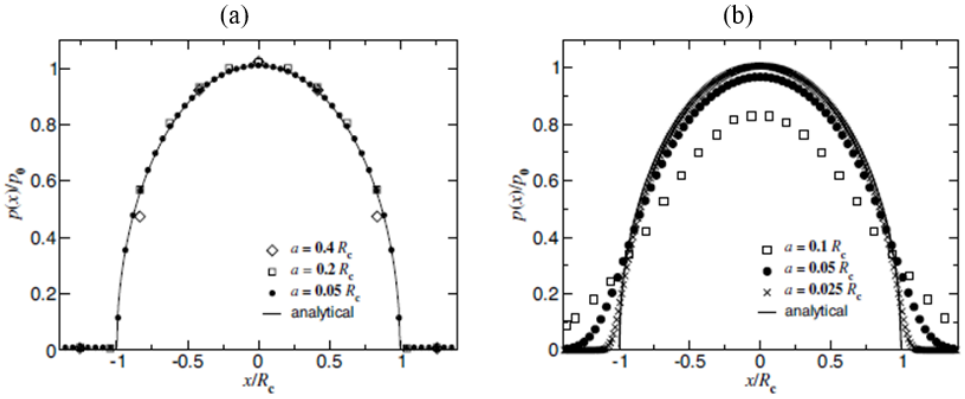

Figure 2.4: GFMD solution for the pressure distribution of a Hertzian contact for different values of the resolution, a (R_c is the contact area), assuming (a) a hard-wall interaction and (b) an exponentially repulsive potential adapted from [42].

Adhesion modeling in GFMD

In the case of an adhesive contact, the interfacial stress in Eq.2.13 has to change. Muser expressed this term in the Fourier domain as [45]:

$$\tilde{p}_{if}(q) = \frac{1}{A_0} \int d^2r \; exp(-iqr) \left\{ \sigma_c(r) + \sigma_{adh}(r) \right\} \tag{2.15}$$

in which, $\sigma_c(r)$ is the stress function required to satisfy the hard-wall interaction (or the exponentially repulsive potential) and $\sigma_{adh}(r)$ is the adhesive stress which is explicitly dependent on the separation at the interface, $g(r)$. This dependence can be expressed by different definitions as [49, 50]:

$$\sigma_{adh}(r) = -\frac{\Delta\gamma}{z_0} \times \begin{cases} \frac{g(r)}{z_0} \exp\left(-\frac{g(r)^2}{2z_0^2}\right), & \text{Gauss model} \\ \frac{2g(r)/z_0}{\left(1+\frac{g(r)^2}{z_0^2}\right)^2} & \text{van der Waals model} \\ \frac{16}{9\sqrt{3}} H\left(\frac{9\sqrt{3}}{16} z_0 - g(r)\right) & \text{Maugis-Dugdale model} \\ \frac{8}{3}\left[\left(\frac{z_0}{g(r)+z_0}\right)^9 - \left(\frac{z_0}{g(r)+z_0}\right)^3\right] & \text{Lennard-Jones model} \\ \exp\left(-\frac{g(r)}{z_0}\right) & \text{Exponential model} \end{cases} \tag{2.16}$$

where $H(x)$ denotes the Heaviside function. Figure 2.5 compares the mentioned adhesive models for their dependence on the separation. It must be noted the total work of adhesion for all models, i.e. the area under the shown curve, is the same and equal to $\Delta\gamma$. It is also observed that at zero separation, the Exponential and Maugis-Dugdale models have a finite adhesive stress while the other three models define a zero stress.

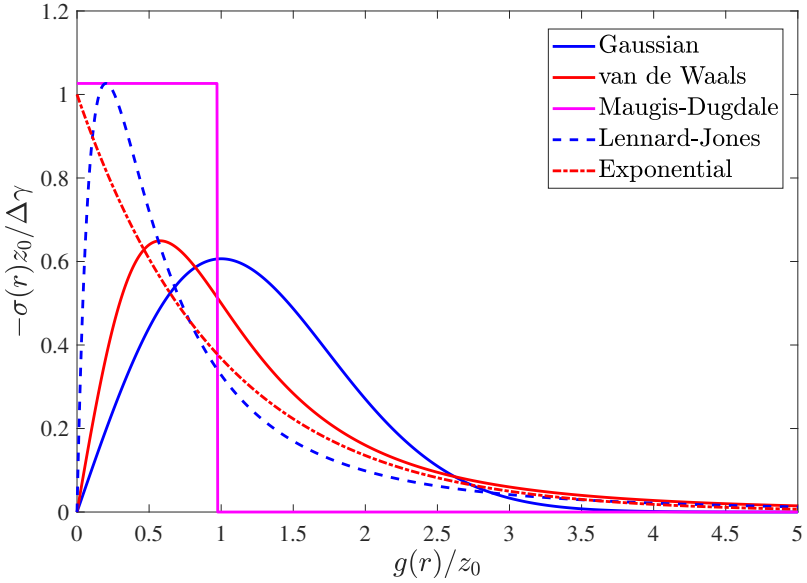

Figure 2.5: Separation dependence of adhesive stress models.

2.1.5 Boundary Element Method

The Boundary Element Method is, in general, a numerical method to solve linear partial differential equations by mapping them on the boundary of the domain. In the contact of rough surfaces, rather than discretizing the entire 3D domain, the contact interface is divided into small patches where the unknown functions are approximated in terms of

nodal values, and the integral equations are discretized and solved numerically. As all the approximations are transformed to the boundary, the BEM has better accuracy and efficiency (since the dimensionality reduces by one order) in contact of rough surfaces than other numerical methods such as the finite element method and molecular dynamics.
For the non-adhesive frictionless contact of two bodies, BEM, in principle, minimizes the total complementary potential energy for which, the variational form is expressed as [51]:

$$F(P) = h^* P + \frac{1}{2} P^T k P, \quad P \geq 0 \tag{2.17}$$

where $h^* = h - \delta_z$, with h and δ_z being the initial (undeformed) interfacial separation and the prescribed normal displacement, respectively. The composite deformation of the two surfaces, due to the interfacial pressure P, over the region Ω is given by:

$$u(x,y) = \int_\Omega k(x-\xi, y-\eta) P(\xi,\eta)\, d\eta d\xi \tag{2.18}$$

where x and y are the spatial coordinates and $k(x,y)$ is the Boussinesq kernel function and is expressed as [52]:

$$k(x,y) = \frac{1}{\pi E_s} \frac{1}{\sqrt{x^2+y^2}} \tag{2.19}$$

The final (deformed) interfacial separation, $g(x,y)$, is related to the deformation through:

$$g(x,y) = u(x,y) + h(x,y) - \delta_z \tag{2.20}$$

The non-adhesive contact problem necessitates the pressure to be positive at the contact regions, where there is no separation between the two surfaces (where $g(x,y) = 0$). On the other hand, at separated areas (where $g(x,y) > 0$), the pressure must be zero. Moreover, the pressure distribution must balance the applied normal load, F_0. In other words, the non-adhesive frictionless contact problem is summarized as:

$$P(x,y) > 0 \quad at \quad g(x,y) = 0, \tag{2.21a}$$

$$P(x,y) = 0 \quad at \quad g(x,y) > 0, \tag{2.21b}$$

$$\int_\Omega P(x,y) dx dy = F_0 \tag{2.21c}$$

In order to perform a numerical solution to this problem, Eqs. 2.18-2.21 need to be expressed in the discretized format. To discretize the calculation area, Ω, it is divided into N^2 rectangular surface elements with grid sizes of Δx and Δy. Therefore, one can assume a piecewise constant function within each surface element for the contact pressure distribution. The discrete form of the convolution integral of Eq.2.18 is then given by:

$$u_{ij} = \sum_{k=1}^{N} \sum_{l=1}^{N} K_{i-k,j-l} P_{kl}, \quad i,j = 1,2,...,N \tag{2.22}$$

where u_{ij} is the surface deformation at node (i,j), P_{kl} is the uniform pressure acting upon the element centered at node (k,l), and K_{ij} are the influence coefficients, expressed as (x_i and y_j are the spatial coordinates of node (i,j)):

$$K_{ij} = \int_{-\Delta x/2}^{\Delta x/2} \int_{-\Delta y/2}^{\Delta y/2} k(x_i - \xi, y_j - \eta)\, d\eta d\xi, \quad i,j = 1,2,...,N \tag{2.23}$$

The discretized contact problem is then expressed as:

$$P_{ij} > 0 \quad at \quad g_{ij} = 0, \tag{2.24a}$$

$$P_{ij} = 0 \quad at \quad g_{ij} > 0, \tag{2.24b}$$

$$\Delta x \Delta y \sum_{i=1}^{N} \sum_{j=1}^{N} P_{ij} = F_0 \tag{2.24c}$$

There are several numerical schemes to solve Eq.2.23 as it is mathematically a quadratic optimization problem. The first attempts to solve this problem were carried out through the simplex method by Conrey and Seireg [53] and then, Kalker and van Randen [54]. Gauss elimination is an alternative which is limited to small values of N due to its large computation time [55]. An iteration-based scheme is more efficient and originally developed by [56, 57], where they start with an initial contact area and indentation (prescribed displacement) and solve Eq.2.23 by means of a standard iteration scheme like the Gauss-Seidel method. Then, the contact area and indentation are modified to satisfy the inequalities of the problem. The process is repeated until the contact area and indentation remain fixed [51]. Polonsky and Keer proposed a 2D Multi-Level Multi-Summation (MLMS), originally developed by Brandt and Lubrecht [58], to calculate the deformation along with the Conjugate Gradient Method (CGM) to minimize to complementary energy. The principal idea behind the MLMS is to perform the summation of Eq.2.18 on a coarse grid and then, transfer the outputs to a fine grid based on a Lagrange polynomial interpolation [59]. An efficient and quite fast approach to calculate the deformation is to evaluate Eq.2.18 in the Fourier domain where the space domain convolution converts to the frequency domain multiplication for which the Fast Fourier Transform (FFT) can be implemented. The implementation of this approach along with a CGM iteration scheme was first conducted by Nobi and Kato [60], and modified later on by Liu et al. [61]. Ever since, as a fast and accurate numerical algorithm, it has been extensively exploited for various non-adhesive contact problems in order to determine the normal and tangential contact stresses and contact area [62–70].

Adhesion modeling in BEM

Until recently, most of the studies on an adhesive contact employing BEM was mostly focused on a single asperity contact [71–73], where the geometry of a spherical asperity is estimated by a parabola and the Lennard-Jones potential was used to describe the separation-dependence of the adhesive stress. Carbone et al. studied the adhesive contact of a soft semi-infinite solid and a randomly rough rigid surface with a self-affine fractal profile [74]. Recently, Medina and Dini proposed a BEM model based on a Multi-Level Multi-Integration scheme for the adhesive contact at an interface and studied the contact of a rigid rough sphere against a flat half-space, where the LJ potential was used to describe the adhesive stress outside the contact area [49]. They found out that the strength of adhesion depends on the roughness level in such a way that the roughness can either increase or decrease the adhesive force. Recently, a few authors have combined DC-FFT method with CGM to study the adhesive contact at a rough interface, where adhesion is described by the exponential model [75, 76], LJ potential [77], and a Dugdale approximation [78]. These methods showed very fast convergence and a high level of accuracy.

The studies of the capillary force for the contact of rough surfaces using BEM is pretty scarce. Rostami and Streator proposed a deterministic approach to study the liquid-mediated adhesion between rough surfaces [79]. Based on the liquid volume available at the interface, they defined a wetting radius and the non-contact areas inside the wetting radius would experience a constant capillary pressure. They, however, neglected the contribution of mobile liquid at the interface, which indeed contributes to the meniscus formation. As mentioned before, a significant contributor to the capillary force is the adsorbed water films from the humid environment onto the contacting surfaces. It was Tian and Bhushan who pioneered such a study [51]. They studied the effect of ultra-thin liquid films adsorbed on the rough surfaces on the formation of micro-menisci islands within the interface in the contact area and on friction. They found out the greater the thickness of the liquid film, the larger the contact area and static friction force. In their calculations, however, they did not incorporate the elastic deformations due to the adhesive stress. Moreover, they considered the film thickness to be uniform all over the rough surface. However, due to the capillary pressure and the liquid surface tension, the film is distributed in such a way to be thinner at the peaks and thicker in the valleys.

Since the local thickness of the film, especially at the peaks, influences the distance to which the micro-meniscus extends, it sounds crucial to take into account the true distribution of the film. Therefore, the leveling dynamics of a thin liquid film on a substrate gives the non-uniform and true distribution of the film on a rough substrate. This issue is highly important in painting and coating industries. It was Orchard who first found out the effect of interplay between the surface tension and viscosity, in one hand, reduces the free surface irregularities, and on the other hand, limit the flow due to the leveling dynamics [80]. Ahmed et al. and Seeler et al. numerically studied the effect

of rheology on the leveling of thin fluid films on solid substrates [81, 82]. Surface topography is also another factor which needs to be considered for the leveling dynamics [83–85]. A comprehensive numerical model for the leveling dynamics of thin paint film flow, including the effects of evaporation and complex rheology of the paint, was proposed by Figliuzzi et al. [86]. Considering the Newtonian behavior of water and neglecting the evaporation effect, this model can be used to find the true non-uniform distribution of a thin water film on a rough surface which helps to estimate the capillary force at a rough interface more accurately (the reader is referred to Appendix B for the details of this model).

2.2 Frictional contact and partial-slip

Despite the vast usage of friction since the early human, such as making fire using the heat generated by the friction between two wood pieces, the understanding of its nature is still of fundamental interest. There are, in general, two categories of friction: partial-slip friction and steady-state friction (gross-sliding or full-slip friction). The latter state is reached when the contacting bodies are macroscopically sliding (slipping) over one another.

In the partial slip regime, the bodies are macroscopically observed to be sticking and there is only local relative displacements taking place at the interface. This state is also called stick-slip as it is in practice the transition from a full-sticking contact to a full-slipping one. The beautiful sound of a violin is due to macroscopic stick-slip between the hair of the bow and the strings. It is also the cause of jerking of brakes, squeal and chatter in bearings, and inaccuracy in machining and positioning mechanisms. During the stick phase, the friction force builds to a critical value, called static friction. Once this critical force has been reached, full slip or macroscopic sliding at the interface starts and due to the energy release, the friction force decreases and remains constant with time and displacement.

2.2.1 Partial slip at an ideally smooth interface

The first study on the partial slip contact was conducted independently by Cattaneo [87], and Mindlin [88] for the contact of a smooth interface of a ball and a flat. Figure 2.6(a) shows the circular contact of an elastic ball against a rigid flat half-space due to a fixed normal load. Initially, in the absence of an external shear force, the entire contact area, as shown in Figure 2.6(b), experiences a full stick condition, where there is no relative displacement between the two bodies. Upon the application of a tangential force, a ring of slip, surrounding the central sticking area, forms and develops toward the center of contact along with further increase in the tangential force. As soon as this slipping ring covers the entire contact area (and the sticking area disappears at the center), gross sliding occurs. The force required to start gross-sliding is called the static friction force as, based on the Amonton's law of friction, is proportional to the normal load by means of a factor named

the static coefficient of friction, μ_s. The tangential displacement at the start of gross sliding is called the pre-sliding displacement (also known as preliminary displacement) and serves as an important specification in precision engineering.

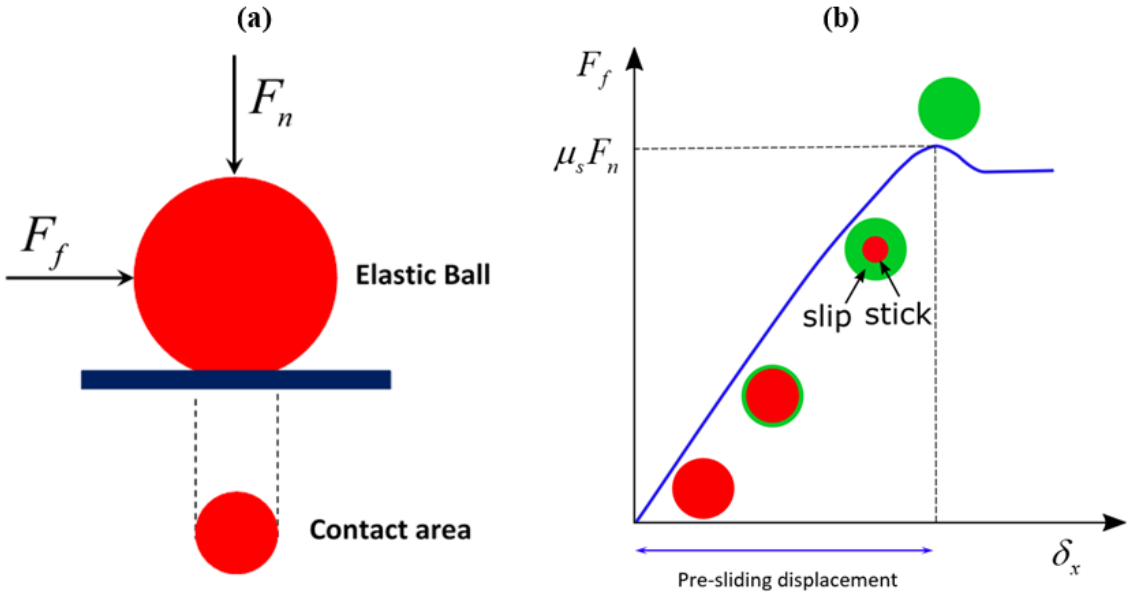

Figure 2.6: Transition from stick to slip, based on the Mindlin solution

For such an asperity contact, the tangential displacement is expressed by [52]:

$$\delta_x = \delta_0 \left\{ 1 - \left(1 - \frac{F_f}{\mu_s F_n} \right)^{2/3} \right\} \tag{2.25}$$

in which, the pre-sliding distance, δ_0, is given by:

$$\delta_0 = \frac{3\mu_s F_n}{4a} \frac{(2-\nu)(1+\nu)}{E} \tag{2.26}$$

here, E, ν are the elastic modulus and Poisson's ratio of the contacting materials and a is the contact radius.

Later on, Mindlin and Deresiewicz extended this solution to account for an oscillating tangential force, which leads to friction hysteresis behavior [89]. The amplitude of the oscillating friction force is insufficient to cause gross-sliding. Figure 2.7(a) depicts the friction loading steps, which is divided into three general paths of OA, ABC, and CDE. The tangential displacement, in these three paths, is given by:

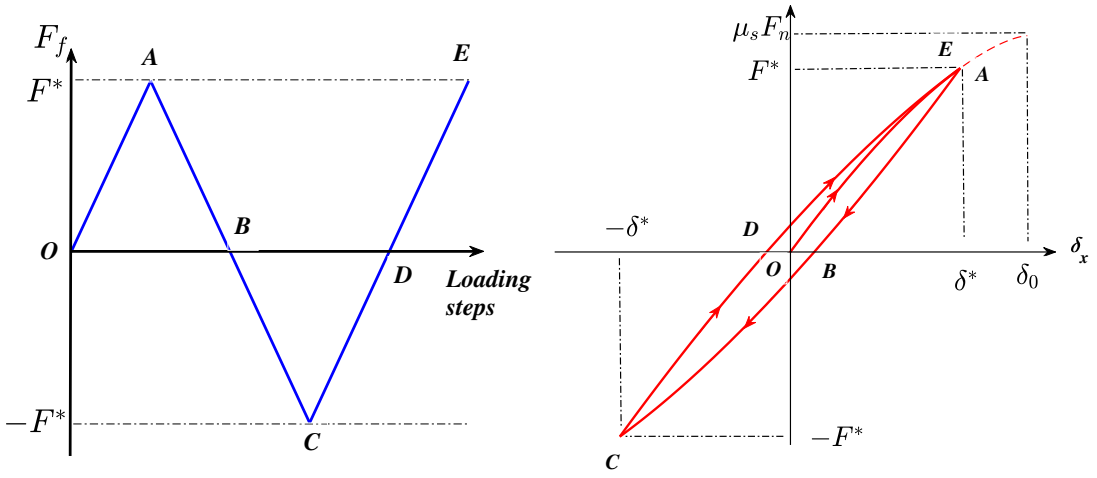

Figure 2.7: Hysteresis behavior of a single asperity contact based on the Mindlin solution

$$\delta_x^{OA} = \delta_0 \left\{ 1 - \left(1 - \frac{F_f}{\mu_s F_n} \right)^{2/3} \right\} \tag{2.27a}$$

$$\delta_x^{AC} = \delta_0 \left\{ 2 \left(1 - \frac{F^* - F_f}{2\mu_s F_n} \right)^{2/3} - \left(1 - \frac{F^*}{\mu_s F_n} \right)^{2/3} - 1 \right\} \tag{2.27b}$$

$$\delta_x^{CE} = -\delta_0 \left\{ 2 \left(1 - \frac{F^* + F_f}{2\mu_s F_n} \right)^{2/3} - \left(1 + \frac{F^*}{\mu_s F_n} \right)^{2/3} - 1 \right\} \tag{2.27c}$$

in which F^* is the amplitude of oscillating tangential force (see Figure 2.7). In the original Mindlin solution, it was assumed that the contacting materials are identical. This assumption simplifies the solution since the normal pressure and shear stress components become decoupled and cannot affect each other as they cannot induce any deformation in the other directions. The contact of dissimilar materials, nevertheless, does not follow this condition and the normal pressure and shear stress components are coupled. There has been no analytical solution for this complex problem and researchers have resorted to numerical solutions for it. Kogut and Etsion conducted a FEM simulation on the contact of a rigid flat pressed against an elastic perfectly plastic ball [90]. They used an approximate analytical solution to evaluate the static friction force. Rather than using the Amonton's law of friction, they treated the sliding friction as failure mechanism based on the plastic yield. Wang et al. proposed a FEM model to study the partial slip fretting contact of a ball against a flat, where the friction coefficient in the slip region is not fixed [91]. Yue and Abdel Wahab studied the effect of a variable

coefficient of friction on the gross-sliding and partial slip conditions of fretting wear [92]. They found out that considering a variable coefficient of friction is more crucial for the partial slip conditions and the FEM results are close to the experimental ones. Chen and Wang developed a 3D numerical model for the partial slip contact of elastically dissimilar materials [93]. They used a CGM-based algorithm to determine the contact area and stick region. Wang et al. followed the same strategy to study the partial slip on a 3D elastic layered half-space, which is suitable to study the effect of a coating on the contact problem [66]. An extension to this model to simulate the friction hysteresis behavior in the partial slip contact mode is provided in [94]. Rodriguez-Tembleque et al. proposed a BEM formulation to model wear under gross-sliding and partial slip conditions [95]. Gallego et al. also proposed a CGM-based model and implemented DC-FFT to calculate the convolution integrals to simulate the fretting modes I, II, and III [96]. They found a discrepancy between their numerical results and those of the Mindlin solution for the contact of dissimilar materials. In contrast to the Mindlin solution, the development of the slipping area is no longer symmetric. Furthermore, due to the dissimilarity of the elastic properties of the contacting bodies, normal pressure causes relative displacement at the interface and therefore, a slipping area in the absence of a shear stress.

2.2.2 Partial slip at a rough interface

Despite the recent advances of modeling the normal contact, the tangential contact of rough surfaces is not well-understood yet, due to the complexity of adhesion, stick to slip transition, lubrication, and wear. The initial studies were conducted by combining the Mindlin solution and Greenwood-Williamson statistical model to investigate the proportionality of the friction force and normal load at a rough interface [97]. Further similar research, known as multi-asperity contact models, were conducted to study the partial slip and gross-sliding friction [66, 94, 95, 98].

As one of the main limitations of multi-asperity models is that the interaction between asperities is not taken into account, other numerical approaches have been employed by researchers. Pohrt and Li [68], and Paggi et al. [99], proposed a CGM-based BEM model for the partial slip contact at a rough interface. They assumed a uni-directional shear stress proportional to the normal pressure in the slip zone. Yet, they did not take the coupling between the normal pressure and shear stress into account. Grzemba et al. proposed a characteristic length parameter defining the crossover from sticking to slipping for the contact of self-affine fractal surfaces [100]. Kasarekar et al. developed a numerical approach to study the fretting wear under partial slip conditions [101]. They found the roughness details at small length-scales a major factor in wear simulations. Chen and Wang extended their previously developed BEM model for the point contact of dissimilar materials to evaluate the static friction force and coefficient of friction at a rough interface of a ball and a flat [102]. Rather using the Amonton's law of friction, they set a constant shear strength all over the contact area, τ_m, as a local criterion for transition from stick to slip. Therefore,

dividing the contact area into stick and slip regions, one can distinguish between these two by the following definition:

$$A_{stick}: \ |q| = \sqrt{q_x^2 + q_y^2} < \tau_m, \ \ |s| = \sqrt{s_x^2 + s_y^2} = 0, \tag{2.28a}$$

$$A_{slip}: \ |q| = \sqrt{q_x^2 + q_y^2} = \tau_m, \ \ |s| = \sqrt{s_x^2 + s_y^2} > 0 \tag{2.28b}$$

where $|q|$ and s are shear stress and relative displacement at the interface, respectively. This criterion states that in the stick zone, there is no relative displacement between the two contacting bodies and the shear stress is smaller than the constant shear strength, whereas these two are greater than zero and equal to the shear strength at the slip region, respectively. Base on the Amonton's law of friction, Chen and Wang developed a BEM model for the partial slip contact at the interface of two contacting bodies of dissimilar materials [93]. There, the stick and slip regions are distinguished based on the following criterion:

$$A_{stick}: \ |q| = \sqrt{q_x^2 + q_y^2} < \mu_s p, \ \ |s| = \sqrt{s_x^2 + s_y^2} = 0, \tag{2.29a}$$

$$A_{slip}: \ |q| = \sqrt{q_x^2 + q_y^2} = \mu_s p, \ \ |s| = \sqrt{s_x^2 + s_y^2} > 0 \tag{2.29b}$$

which implies that the slipping crossover is not a fixed value all over the contact area but depends on the coefficient of friction and local pressure, similar to Amonton's law of friction. Due to the dissimilarity of the contacting materials, the pressure profile is affected by shear stress components, too, and therefore, the contact needs to be solved iteratively to find the pressure profile and the contact area.

Although there is rich literature on the influence of adhesion on the contact pressure and contact area, the studies on the effect of this phenomenon on friction and specially partial slip is quite scarce. Sari et al. studied the effect the plane-strain version of the Cattaneo-Mindlin problem in the presence of adhesion where the contact area is determined using the Maugis theory independent of the tangential forces [103]. The contact area is composed of a central stick zone surrounded by an annulus of slip in which the shear stress is assumed constant. Adams studied the adhesive pre-sliding contact of a smooth curved elastic body and a flat half-space [104]. He assumed the surface energy to be in a manner similar to the JKR theory for spherical contact. In the plane strain condition, the contact is in full stick until the tangential force reaches a critical value where there is a transition either directly to gross-sliding or to a partial slip state in which the central stick region is surrounded by two slip stripes.

2.3 Research gaps

As the main objective of this thesis is to study the adhesion and partial slip interaction between a silicon wafer and a burl, a comprehensive numerical model needs to be developed for the contact of (slightly) rough surfaces.

Given the topographies of the mating surfaces along with their mechanical and surface properties, the model must be able to calculate the contacting region(s) and the corresponding pressure. The limitations of GW models and Persson's theory make them inappropriate for the purposes of this thesis. In practice, the interface of a wafer and waferstage is only lightly loaded which restricts the contact to be a very small fraction of the apparent contact area. The use of GFMD is here controversial as it is not efficient for such low values of real area of contact.

The model must also be able to simultaneously deals with the adhesive components, namely the van der Waals and capillary forces, as these can strongly affect the contact area. The literature, however, is mostly focused on the normal contact in the presence of van der Waals forces, for which, there is still a big debate in the scientific community in terms of accuracy and efficiency of the proposed numerical models. On the other hand, the role of the capillary force in the normal contact problems of rough surfaces is, to a large extent, limited to the GW models. To the best of the author's knowledge, there is no proper numerical model dealing with the capillary force at a rough interface where the formation of micro-menisci islands is mediated by the adsorbed water films from the humid environment. Therefore, the strength of the capillary force is in direct relation with the local thickness of these films. Thus, a big gap, here, is the distribution of the water films over the contacting rough surfaces which is neither flat nor follows the topography of the rough surface, but, due to the capillary effect, is thinner at the summits and thicker in the valleys. The numerical model must also consider this effect.

The model must simulate the transition from stick to slip when the external tangential force is not large enough to cause full slip at the interface. Although there is a number of numerical studies for this transition for the contact of rough surfaces, the presence of adhesion is always neglected, while, as mentioned before, adhesion increases the contact area and consequently increases both the pre-sliding displacement and the static friction force. Therefore, the model must be capable of taking these effects into account.

This chapter summarized the frequently used models for the normal and tangential contact of rough surfaces in the absence and presence of adhesion. Among the proposed methods, BEM is a better approach to follow since very fine resolution surface measurements can be implemented to describe the topography of the contacting surfaces and at the same time doing all the computations in a reasonable amount of computational time and memory. It is also very powerful and efficient since all the approximations are transformed into the boundaries and the dimensionality reduces by one order.

Chapter 3

SUMMARY OF THE RESEARCH

3.1 Introduction

The aim of the thesis is to find the relation between adhesion and friction at the rough interface of a wafer and the wafer stage. Specifically, the effect of the adhesion force, originating from van der Waals and capillary forces (depending on the medium in which the contact is made), on the stick-slip transition or partial slip contact at such an interface. A lithography machine operates either in vacuum or ambient conditions. In vacuum, the van der Waals forces between the two contacting solids are responsible for the adhesion force. In ambient, however, both van der Waals and capillary forces contribute to the total adhesion force, while the effect of the latter one is more prominent. The vapor in the humid environment condenses and adsorbs on the surfaces to fill in the holes and gaps at the contact interface. There are three adhesive components to be considered: the solid-solid van der Waals interaction, the solid-water van der Waals interaction, and the capillary force origination from the tensile stress inside the micro-menisci islands formed around the contacting and at the near-contacting asperities. Given the normal loads and surface topographies of the surfaces in contact (here the silicon wafer and a burl) along with their mechanical and adhesive properties, a numerical model is needed to solve for the pressure distribution at the interface. The numerical procedure for the calculation of the normal contact pressure in presence of adhesion is depicted in the flowchart of Figure 3.1. In the first step, mechanical properties, surface topographies, adhesion details (work of adhesion and relative humidity), and the normal load are input to the algorithm. In step 2, an initial guess is made for the normal pressure. Using this pressure profile, the deformation at the interface in step 3 and then in step 4, the separation or gap is calculated. Adhesive components, which are directly or indirectly dependent on the local gap at the interface, are also set at this step. Step 5 checks for convergence in the pressure profile

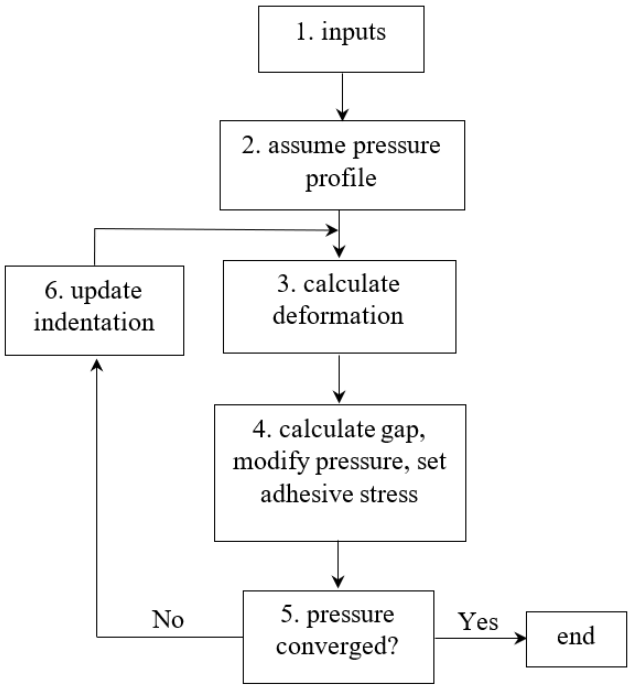

Figure 3.1: Calculation of the normal pressure in presence of adhesion

and if it is not met, the indentation (normal rigid body displacement) is updated in step 6 and then another iteration is started over from step 2 using the new pressure profile. The iteration loop should be repeated until the pressure profile reaches convergence. The mathematical description of these steps are provided in papers A and B of Part II of the thesis.

The total effect of adhesion, no matter where it originates from, is to increase both the contact area and the contact repulsive force which, in any case, leads to a higher friction force and pre-sliding displacement. Given the adhesive normal pressure, the partial-slip problem is solved based on the flowchart shown in Figure 3.2. The static coefficient of friction and the tangential loads along with the parameters required for the normal pressure calculation are input in step 1. Step 2 solves the adhesive normal pressure as explained previously. In step 3, the shear stress components are calculated using the assumed rigid body displacements caused by the external tangential loads. Shear forces are estimated in step 5 and compared with the external ones in step 5. If they are not within an acceptable level of tolerance, the rigid body displacements are updated in step 6 and another loop of iteration is repeated. As soon as the shear forces converge, the normal pressure is checked for convergence in step 7 and if it is not converged, the geometry is updated by considering

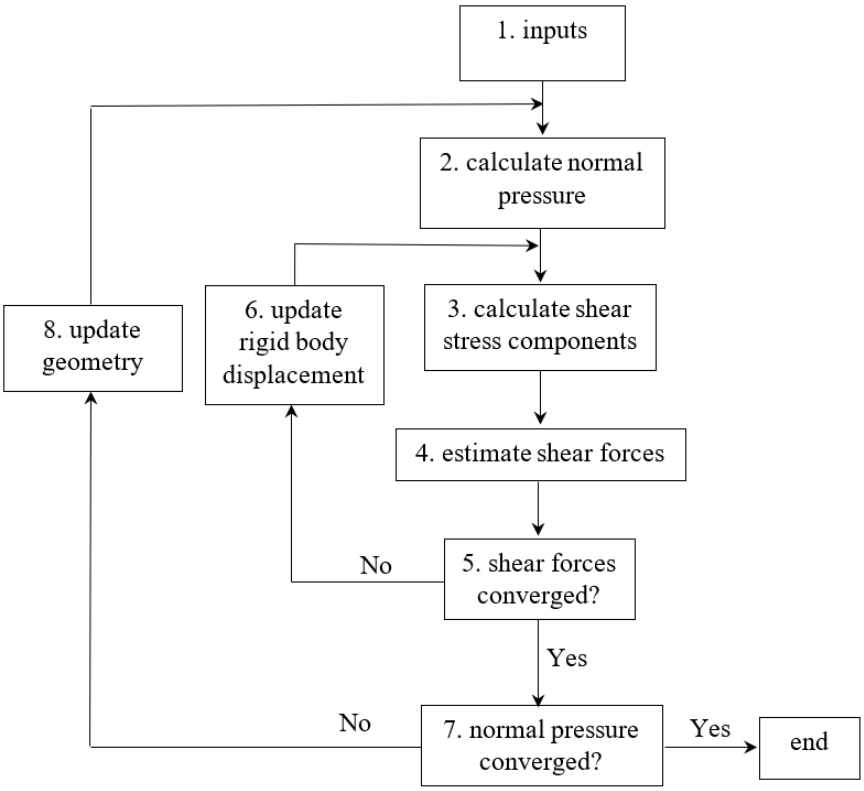

Figure 3.2: Flowchart of the partial-slip contact problem.

the deformation in the contact geometry due to the shear stress components and then the outer level of iteration is repeated until these components make no noticeable change in the normal pressure and geometry. Papers D and E of Part II of thesis explain the mathematical details of these steps.

It should be noted at this stage that it is crucial to consider the contribution of the interfacial phenomena in the stick-slip transition. Hence, the entire study is divided into two major sections. The first is to simulate adhesion at a rough interface and the second is to simulate the transition from a stick to full slip state and how it is affected by adhesion.

3.2 Normal contact and adhesion

When two rough surface are brought into contact, high asperities touch the counter surface and deform either elastically or plastically to form micro-contacts. In the absence of adhesion, the formation of these contact patches depends on the topographies of the contacting surfaces, their mechanical properties, and the loading conditions i.e. the

normal force. Formation of adhesive bonds directly (for the van der Waals forces) or indirectly (for the capillary force) depends on the proximity of the surfaces in contact. The areas right around the micro-contact patches where the two surfaces are slightly separated, have the potential to experience such bonds, depending on the surface energies of the bodies in contact and the medium through which the contact has formed. To analyze the adhesion and its effect on the contact area and pressure, thus, it is very important to initially locate the micro-contacts with corresponding pressure distribution. The pressure profile, in the absence of adhesion, must fulfill the complementarity conditions based on which the pressure must be zero at separated regions and non-zero at contacting areas. Provided that the mechanical properties, the normal force, and the surface topographies are all known, a BEM numerical scheme implements the Conjugate Gradient Method (CGM) (as an optimization algorithm to solve the contact problem with these conditions), is implemented to calculate the resulting pressure and separation profiles.

3.2.1 Adhesion due to van der Waals forces

To include the effect of adhesion, the CGM was first extended to treat this phenomenon, originating solely from van der Waals forces at this state, as a constant negative stress in locations with a separation smaller than a specific value. This is called a Dugdale approximation of the Lennard-Jones potential, which expresses the separation dependence of the adhesion between two parallel planes, as explained in Appendix A. The algorithm is described, in detail, in Paper A of Part II of the thesis. The model is verified by comparison to the well-known model of Maugis-Dugdale for an adhesive contact of an elastic ball against a half-space (Figure 3.3), and for a ball against a wavy substrate (Figure 3.4).

The model is also used to analyze the pull-off force of a bi-sinusoidal interface, as a monomodal representation of a rough interface, and fit a master curve on the results to give an expression for the pull-off force as a function of geometrical properties and work of adhesion at the interface. The pull-off force is found to be:

$$F_{pull-off} = 10.39 R_c \Delta\gamma k^{0.041} \tag{3.1}$$

where k is the wavelength ratio. The pull-off force, similar to JKR and DMT models (as expressed in Appendix A), is independent of the elastic modulus and linearly proportional to the work of adhesion and radius of curvature, R_c, at the contact point.

Finally, to check the capability of the developed model to simulate the adhesive contact of rough surfaces, it is used to investigate the contact of a smooth ball and a rough half-space with a wide range of roughness values starting from a molecular level up to a few nanometers (Figure 3.5). Although it is known that roughness decreases adhesion, a slight level of roughness can cause local regions within the contact area to experience very small separations and therefore adhesive stress which in the end results in an increase in the

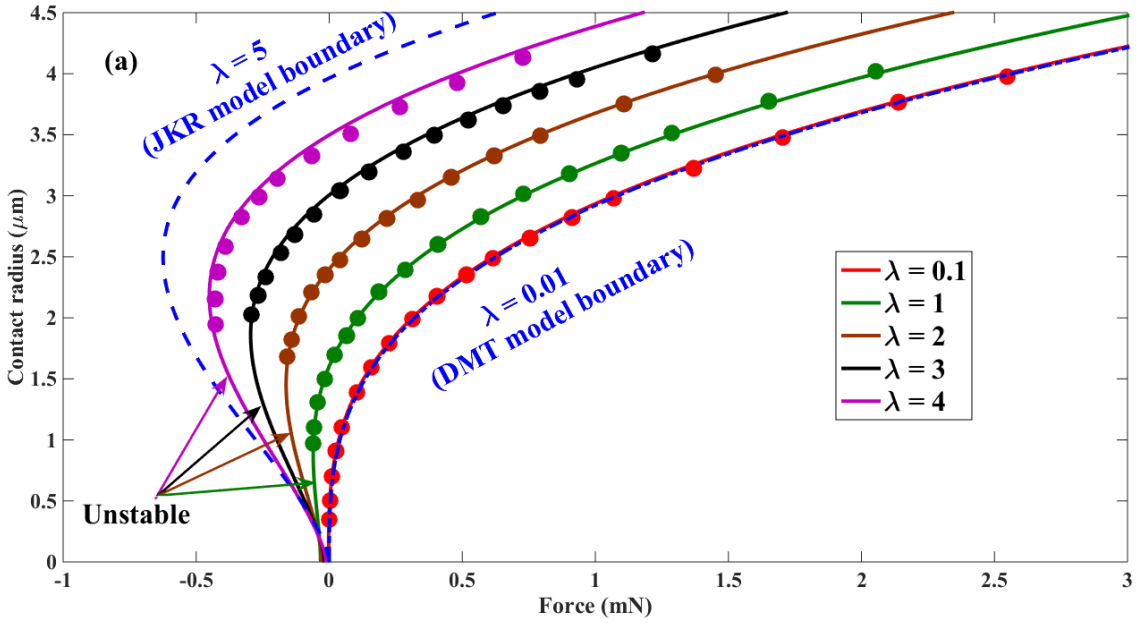

Figure 3.3: Variation of contact radius with normal force, for different values of the adhesive parameter, $\lambda = 1.16\mu_T$. Solid lines and dots are respectively due to the MD model and numerical expressions for pressure (ball-on-flat contact with $E = 73GPa,\ \nu = 0.17,\ R = 2.5mm$).

adhesion force. A further increase in roughness level, separate the majority of the micro-contact zones by greater distances, where they experience no adhesive forces. Only local areas surrounding the asperities with a positive pressure experience a high adhesive force. This trend can be realized through the normalized adhesive force curve in Figure 3.6 for two values of the Tabor parameter.

3.2.2 Adhesion due to van der Waals and capillary forces

The previously developed model for the adhesive contact between two surfaces of arbitrary geometry was then extended to take into account the effect of a humid environment and the resulting capillary force. In ambient conditions, water vapor condenses and adsorbs on the surfaces and fill in the gaps and holes of a contact interface. The volume of adsorbed water depends on the available vapor in the environment which is typically a function of the relative humidity. Usually a very thin water film (around a few nanometers) is adsorbed on a surface. This film is neither uniform (following the topography of the surface) nor flat (to immerse all the high asperities of a surface), but in the form shown in Figure 3.7, due to the capillary pressure and the water surface tension. Here, the water film surface

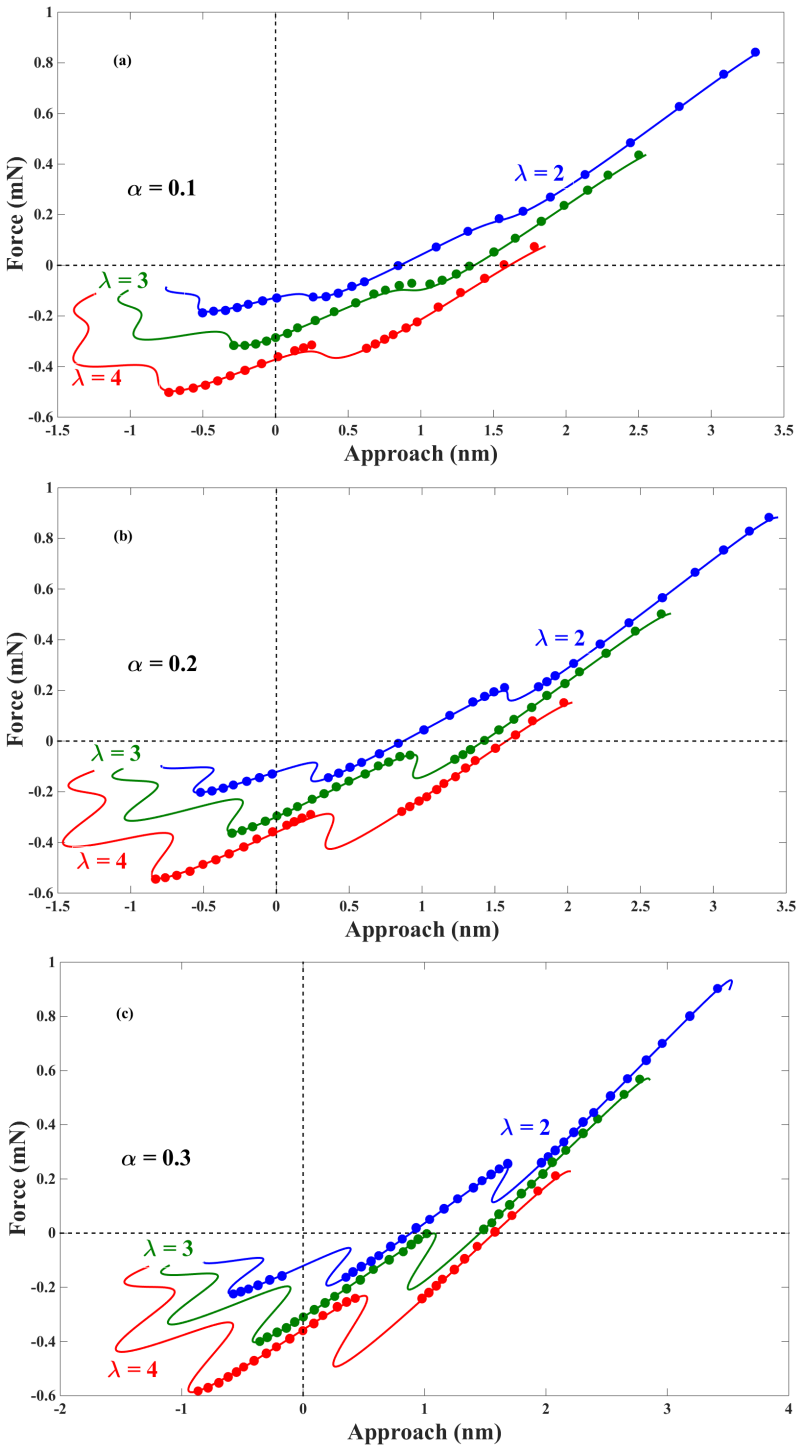

Figure 3.4: Variation of normal force with approach for different values of λ in the contact of a sphere over a wavy surface, (a) $\alpha = 0.1$, (b) $\alpha = 0.2$, (c) $\alpha = 0.3$. Solid lines and dots are respectively due to the analytical MD model and (current) numerical expressions for pressure (ball-on-wavy flat contact with $E = 73GPa$, $\nu = 0.17$, $R = 2.5mm$ and α being the degree of profile waviness (refer to Paper A of Part II)).

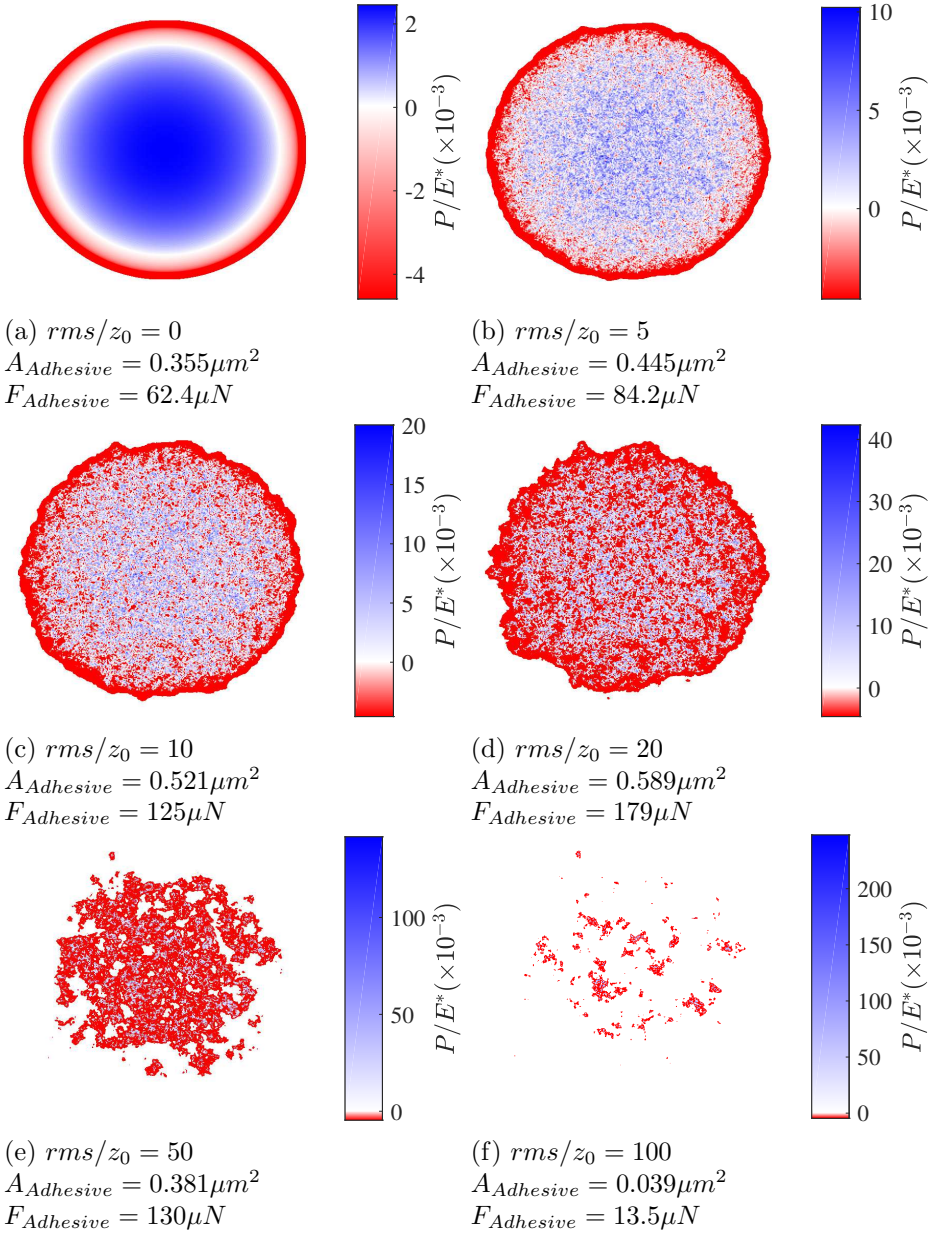

(a) $rms/z_0 = 0$
$A_{Adhesive} = 0.355\mu m^2$
$F_{Adhesive} = 62.4\mu N$

(b) $rms/z_0 = 5$
$A_{Adhesive} = 0.445\mu m^2$
$F_{Adhesive} = 84.2\mu N$

(c) $rms/z_0 = 10$
$A_{Adhesive} = 0.521\mu m^2$
$F_{Adhesive} = 125\mu N$

(d) $rms/z_0 = 20$
$A_{Adhesive} = 0.589\mu m^2$
$F_{Adhesive} = 179\mu N$

(e) $rms/z_0 = 50$
$A_{Adhesive} = 0.381\mu m^2$
$F_{Adhesive} = 130\mu N$

(f) $rms/z_0 = 100$
$A_{Adhesive} = 0.039\mu m^2$
$F_{Adhesive} = 13.5\mu N$

Figure 3.5: Contact pressure for a smooth and rough ball of different roughness rms on a smooth flat at the same normal load for $\mu_T = 2$ (ball-on-flat contact with $E = 73GPa,\ \nu = 0.17,\ R = 2.5mm$ and $F_0 = 10\mu N$).

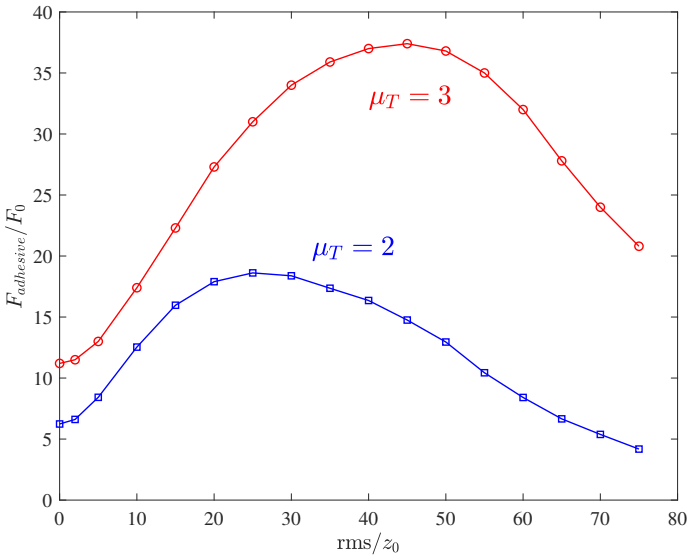

Figure 3.6: The effect of roughness rms on the normalized adhesive force for two different values of μ_T

height, roughness profile, and the local thickness of the film at time t are denoted by h_w, h_s, and e, respectively. Thus, finding the distribution of a water film on a rough surface is the first step to simulate micro-menisci formations at a rough interface (see Appendix B for the details of the numerical algorithm for this problem).

The second step is to locate the areas where these micro-menisci islands are formed and developed, depending the capillary rise level (see Appendix A for more details on the capillary force at a single-asperity contact in the presence of thin water films). Theses islands form around the contacting asperities and at the near-contacting ones (where the separation is smaller than the summation of the local water film thickness on the two surfaces) and develop to an extent depending on the capillary rise (which is a function of relative humidity), see Figure 3.8. All such areas experience a constant capillary pressure which is controlled by the relative humidity. In addition to the capillary force, the solid-solid and water-solid van der Waals interactions contribute to the total adhesive force, whose effect is less dominant in ambient and humid environments. As the humidity level of the environment rises, more water is adsorbed on the surfaces, which gives rise to larger micro-menisci islands and therefore, a larger capillary force. At very high humidity levels, however, due to the drop in the capillary pressure and lack of room for further development of the micro-menisci islands, the total capillary force drops quickly. See, for example, Figure 3.9 which shows this behavior vs. relative humidity. More details and examples are provided in Paper B of Part II of the thesis.

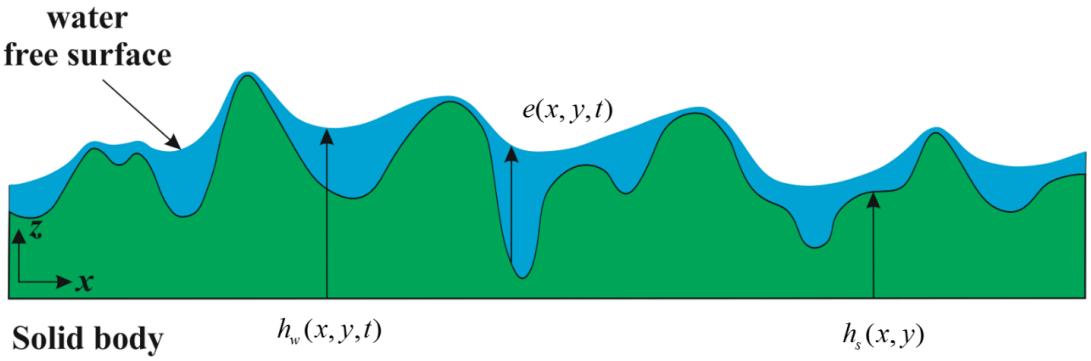

Figure 3.7: Leveling of a water film over a rough surface.

3.2.3 Experimental validation of the normal contact model

This stage focuses on experimental evaluation of the normal adhesive contact block of the developed BEM model. The measurement and numerical prediction pull-off force, as an indicative of the adhesion strength between two bodies under specific environmental conditions, is a suitable approach to compare the model with experiments. For this purpose, Atomic Force Microscopy (AFM) is here used to measure the pull-off force between an AFM cantilever with a $5\mu m$ SiO_2 colloidal probe and a substrate both in vacuum and in ambient conditions, where different types of adhesive components (van der Waals and capillary forces) can contribute to the total adhesive force. Two substrates are implemented for this purpose: a silicon wafer and a $300nm$ thick SiO_2 film deposited on a silicon wafer. The measurements are performed at three states. State 1 refers to the initial pull-off force measurements in ambient conditions, where the temperature and relative humidity are 22°C and 35%, respectively. State 2 is a vacuum condition (HV) with 10^{-5}mbar of pressure which is left overnight, before performing the pull-off force measurements, to remove the organic contaminants from the substrate. Finally, state 3 starts 10 minutes after we vent the vacuum chamber and open it, where the samples are exposed to the ambient conditions again. For each state and substrate, the pull-off force is carried out on 256 spots. The topography of the substrates and their power spectral density (PSD) are shown in Figure 3.10, where the PSD suggests that the SiO_2 is rougher than Si.

Figure 3.11 also illustrates the topography of the probe before and after the entire measurements, implying that it has changed (smoothened) during the measurements. The spread (the mean value with error bars) of measured and predicted pull-off forces at the mentioned three states are plotted in Figure 3.12(a) and (b) for the Si and SiO_2 substrates, respectively. The simulations have also performed five topographies (only one of which is shown here).

The steep rise in the measured pull-off force from the ambient conditions of state 1 to the vacuum conditions of state 2 is attributed to two phenomena: one is the removal of

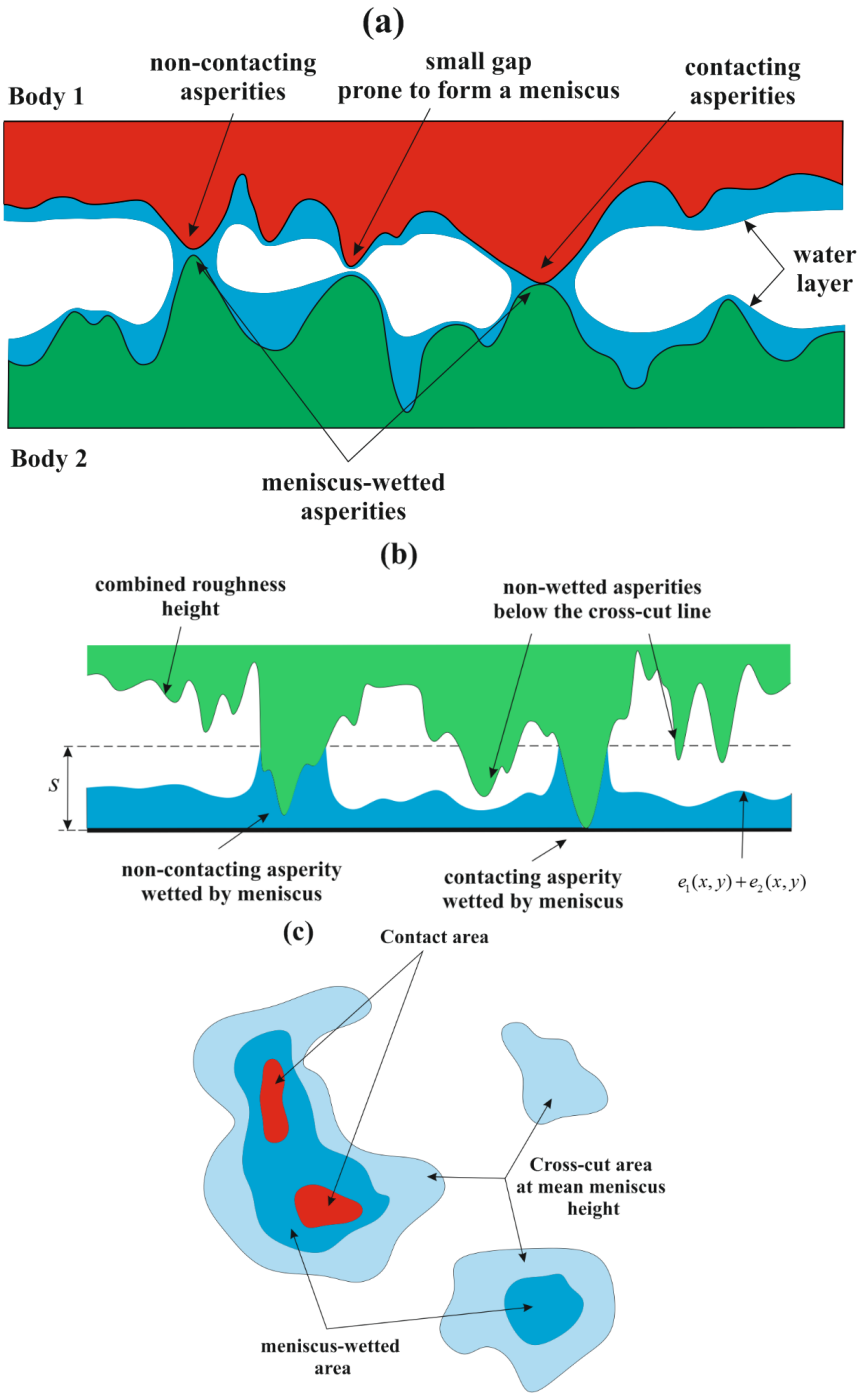

Figure 3.8: (a) Meniscus formation at the contact of two rough surfaces in the presence of adsorbed water films (b) strategy to find meniscus-wetted asperities (c) a schematic diagram of contact area, meniscus-wetted area, and cross-cut area at mean meniscus height.

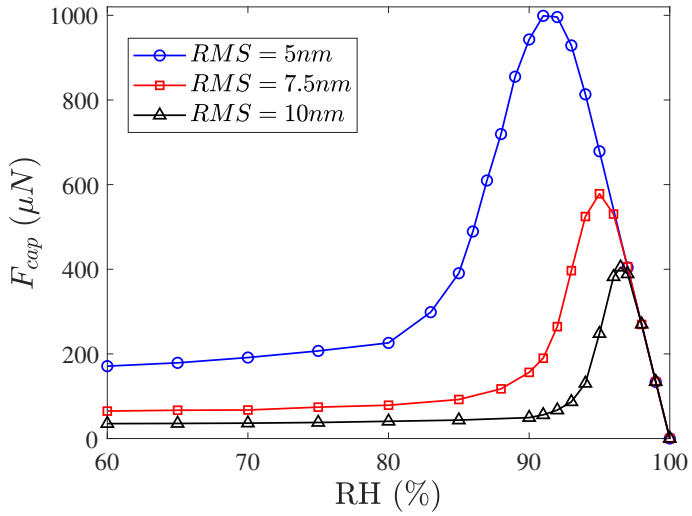

Figure 3.9: Comparison of the capillary force for a rough interface with different RMS values (rough flat-on-flat contact with $E = 64GPa$, $\nu = 0.17$ and $F_0 = 500\mu N$).

the existing hydrocarbon contamination film from the substrates in vacuum and the other one is the change in the topography of the probe since a large number of measurements have been performed on it. Figure 3.13 shows a typical measured force-distance curve for the SiO_2 substrate. The curvy snap-in shape in the approach part of state 1 suggests that the probe is first touching a soft material. Since this behavior is not observed in state 3, where there is water monolayers adsorbed on the substrate, it is suggested that this soft material is a hydrocarbon contamination film (and perhaps a mix of water molecules and contamination) which is removed in vacuum. This contamination film reduces the surface energy of the contacting materials, leading to a lower pull-off force than expectation.

The measured surface topographies before the tests are implemented to predict the pull-off force in the ambient conditions of state 1. Although there seems to be good agreement between simulations and experiments for both Si and SiO_2 substrates, the agreement is merely a coincidence since the impact of the contamination layer on the measurements of this state is not considered in the simulations.

The probe roughness measured after the experiments is used to predict the pull-off force for states 2 and 3. The predicted pull-off force for state 2 is lower than the measurements due to neglecting the effect of existing water monolayers in vacuum on the predicted pull-off force for this state. This can be confirmed by the slight increase in the measured pull-off force from state 2 to 3, where a larger increase, as also suggested by the simulations, is expected.

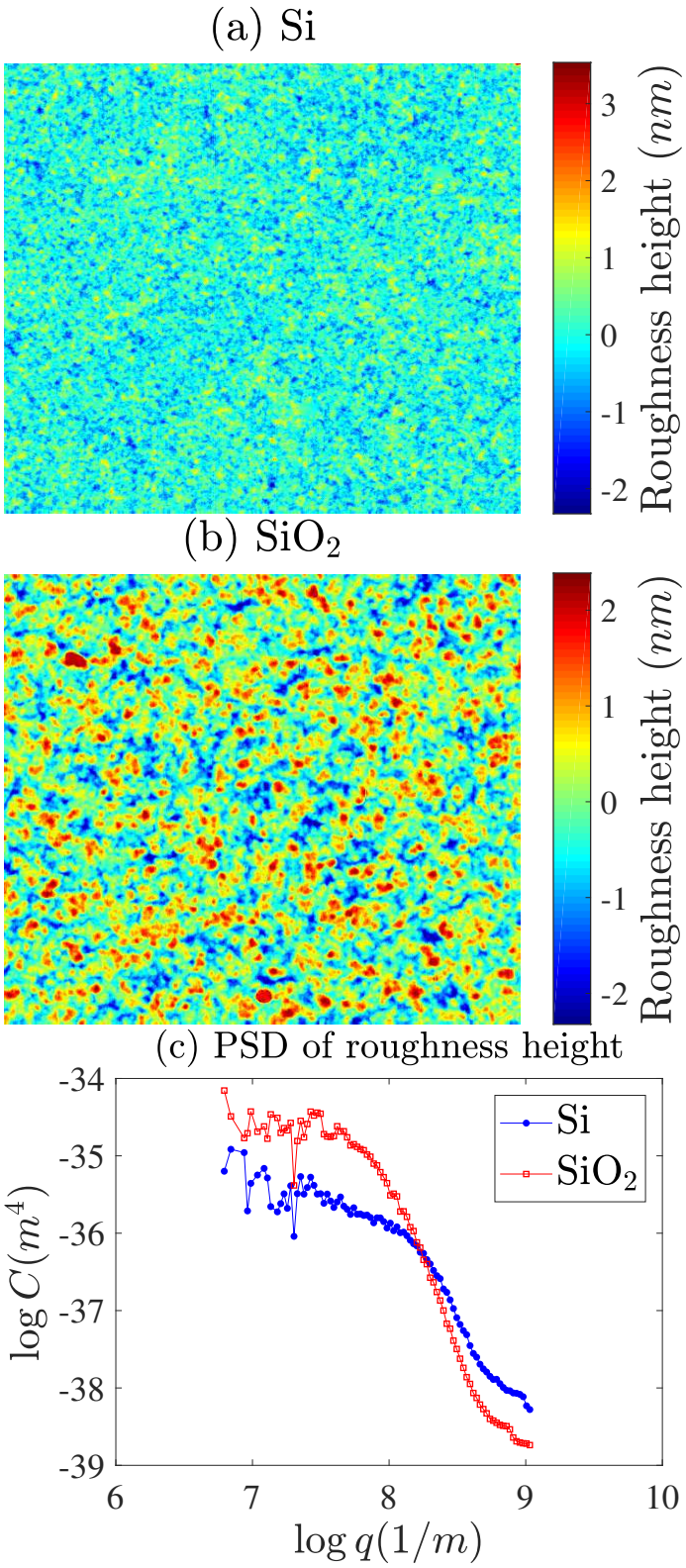

Figure 3.10: Roughness height of (a) Si and (b) SiO_2 substrates on a $2\mu m \times 2\mu m$ area (512×512 pixels) and (c) their PSD

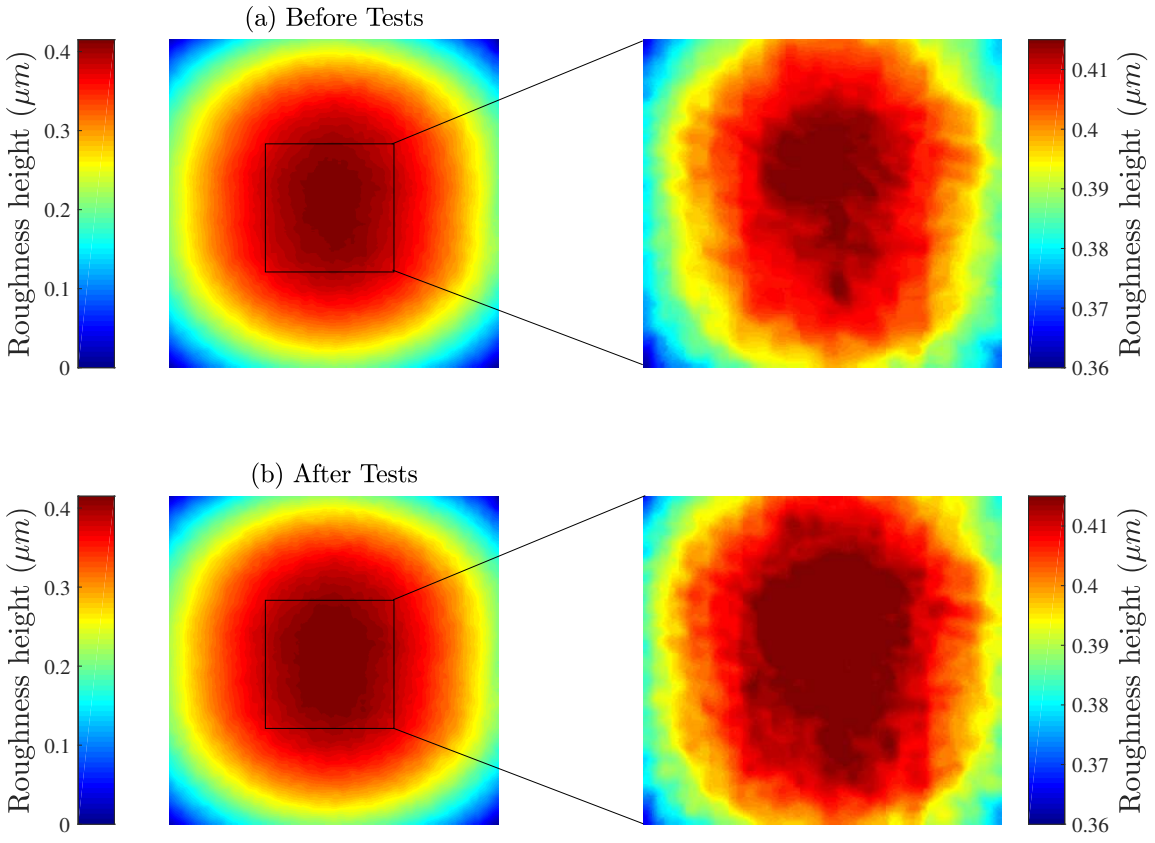

Figure 3.11: The zoomed-in view of the colloidal probe topography (a) before and (b) after the tests on $2\mu m \times 2\mu m$ (left) and $0.8\mu m \times 0.8\mu m$ (right) areas

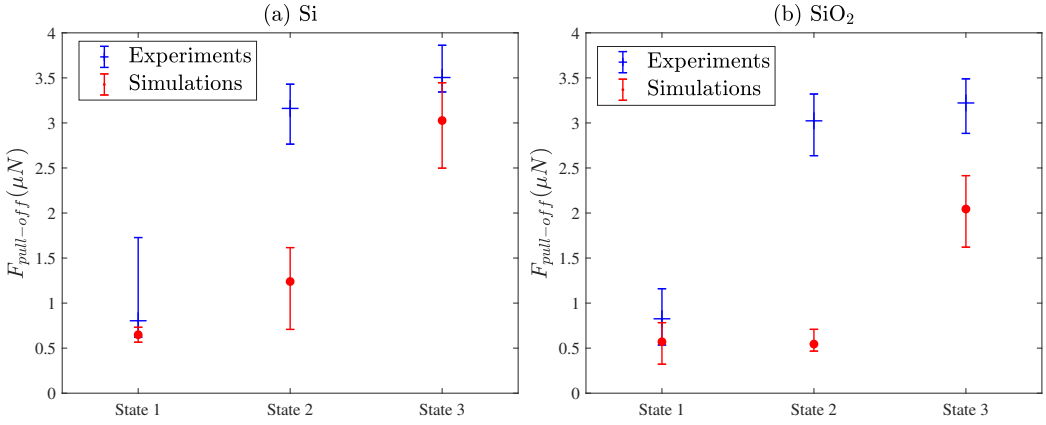

Figure 3.12: Comparison of measured (blue) and predicted (red) pull-off forces for (a) Si and (b) SiO_2 substrates

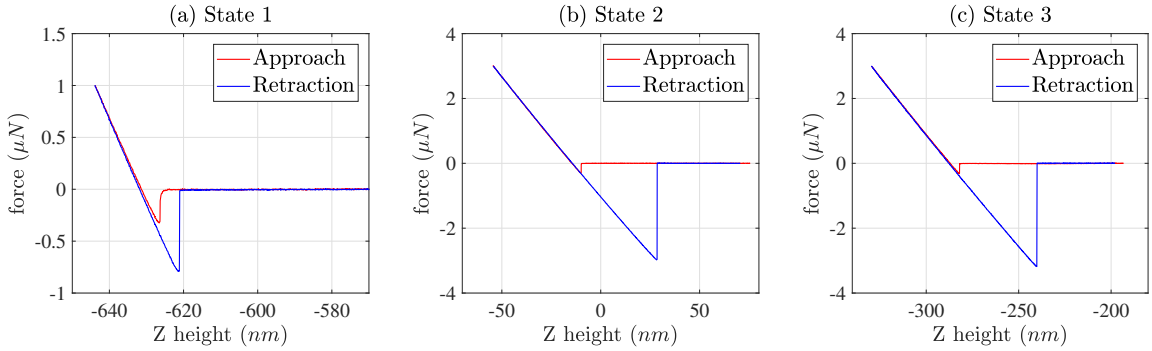

Figure 3.13: Typical measured force-distance curve for the SiO_2 substrate at three states

3.3 Pre-sliding behavior and the role of adhesion

Now that the impact of the adhesive components on the contact pressure and contact area are clarified, one has to explore to what extent it can alter the pre-sliding behavior. The fact that the friction force is proportional to the real area of contact is an indicator of the significant role of adhesion in the pre-sliding behavior. Adhesion increases both the real contact area and contact repulsive force which both result in a higher static friction force and pre-sliding displacement. Similar to the normal contact case, first the model for a non-adhesive contact must be developed.

3.3.1 Partial slip

When two surfaces in contact are tangentially loaded by a force smaller than the static friction force (static friction force is the tangential force required to make two surfaces in contact starts to slide over one another), surface stresses and strains are not uniformly distributed over the interface. Thus, the entire contact area is divided into two regimes of tangential contact namely stick and slip. In the stick region, the surfaces are sticking to each other so that there is no relative displacement. In the slip region, there is a non-zero relative displacement. In total, only a part of the contact is slipping, though, there is no macroscopic relative displacement. That is why this state is called partial slip. As the tangential force increases, the slip region develops (and simultaneously the stick region shrinks) to cover the entire contact area as soon as the tangential force reaches the static friction force. It is frequently assumed that in the slip region, through an analogy to the Amonton's law of friction, the shear stress is proportional to the contact pressure and the proportionality factor is the static coefficient of friction. However, the shear stress in the stick region is unknown and it must be in a form to meet the sticking conditions and balance the tangential load in combination with the shear stress in the slip region. It was mentioned, in the previous chapter, that for the contact of a ball on a flat, the Mindlin solution only applies to the contact of identical materials, while the problem needs to be

Table 3.1: Comparison between different Tabor parameters in terms of the corresponding positive and adhesive forces and normalized tangential forces.

μ_T	$F_0^-(\mu N)$	$F_0^+(\mu N)$	$F_{nr} = F_x/\mu_f F_0$	$F_x/\mu_f F_0^+$
0	0	10.000	0.97	0.9700
0.5	-6.088	16.088	1.56	0.9697
1	-16.018	26.018	2.52	0.9685
2	-42.114	52.114	5.04	0.9690

solved numerically when the materials are dissimilar. In this case, the normal pressure and shear stress components are coupled, meaning that each of the three stress components can induce deformations in all three directions. Therefore, the calculation of the normal pressure must include the geometry change due to the deformations in the normal direction caused by shear stress components and vice versa, which is achieved via an iterative scheme.

The Conjugate Gradient Method is again used here to meet the conditions imposed by the partial slip contact. The first impression that the results make is that even in the absence of an external shear stress, a part of the contact is slipping due to the difference in the elastic properties of the contacting surfaces since the in-plane deformations are coupled with not only the shear stress but also the normal pressure. Second, the development of the slip region over the contact area is asymmetric, in contrast to Mindlin solution which predicts a symmetric development of the annular slip region toward the center of contact. This behavior is shown in Figure 3.14 for various values of the normalized friction force, $F_{nr} = F_x/\mu_f F_0$, with F_x and F_0 being the tangential and normal loads.

The effect of adhesion on the pre-sliding behavior can be included by means of changing the normal pressure with an adhesive contact pressure, as described previously. An assumption, here, is that there is no shear stress in the adhesive region. The details of the algorithm are described in Paper D of Part II of the thesis.

Figure 3.15 shows the variation of stick area to contact area ratio and rigid body displacement vs. normalized friction force for increase values of the Tabor parameter for a smooth ball on flat contact under a fixed value of the external normal force. The graph confirms that adhesion increases both static friction force (normalized friction force) and pre-sliding displacement. In addition, the normalized friction force, as an indicator of the start of the gross-sliding, is controlled by the contact repulsive force, F_0^+ and not the external normal force (see Table 3.1). As the external normal load, which is the summation of the adhesive force, F_0^-, and the contact repulsive force, is fixed, an increase in adhesion increases the adhesive force and therefore the contact repulsive force too.

This finding is even more significant for the contact of rough surfaces where the adhesive force is, to a large extent, dependent on the roughness details. The numerical

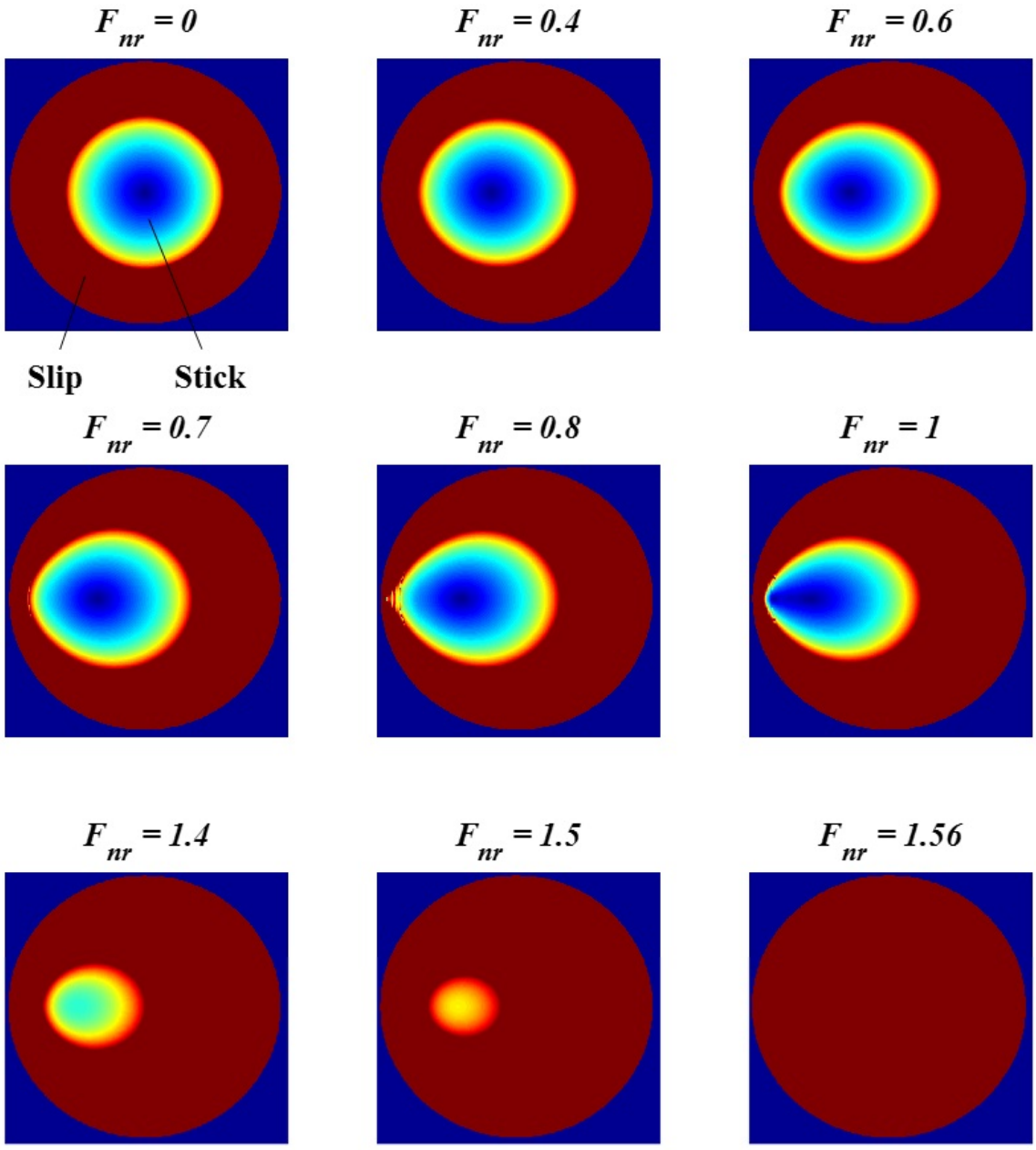

Figure 3.14: Development of the slip region over the contact area vs. normalized friction force (ball-on-flat contact with $E = 130GPa$, $\nu = 0.3$, $R = 10\mu m$, $F_0 = 10\mu N$, $\mu_f = 0.2$ and $\mu_T = 0.5$).

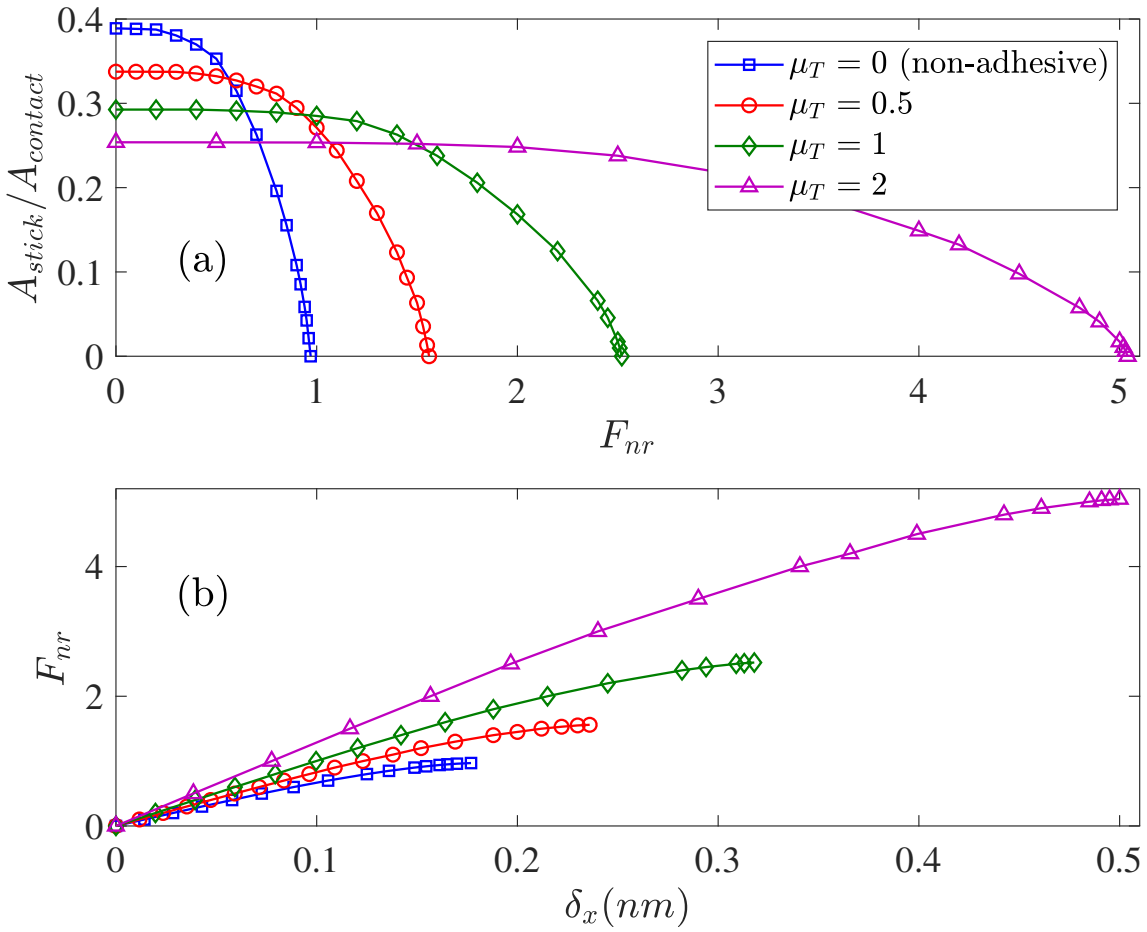

Figure 3.15: (a) Variation of the stick area to contact area as a function of the normalized tangential force (b) Normalized tangential force vs. rigid body displacement in x direction

simulations for the contact of a ball on a rough flat with different levels of roughness rms under a fixed external normal force suggest that, for a non-adhesive contact, roughness can increase the pre-sliding displacement, while the static friction force is entirely independent of the roughness. For the adhesive contact, however, the combined effect of adhesion and roughness is not cumulative but symbiotic (see Figures 3.16 and 3.17).

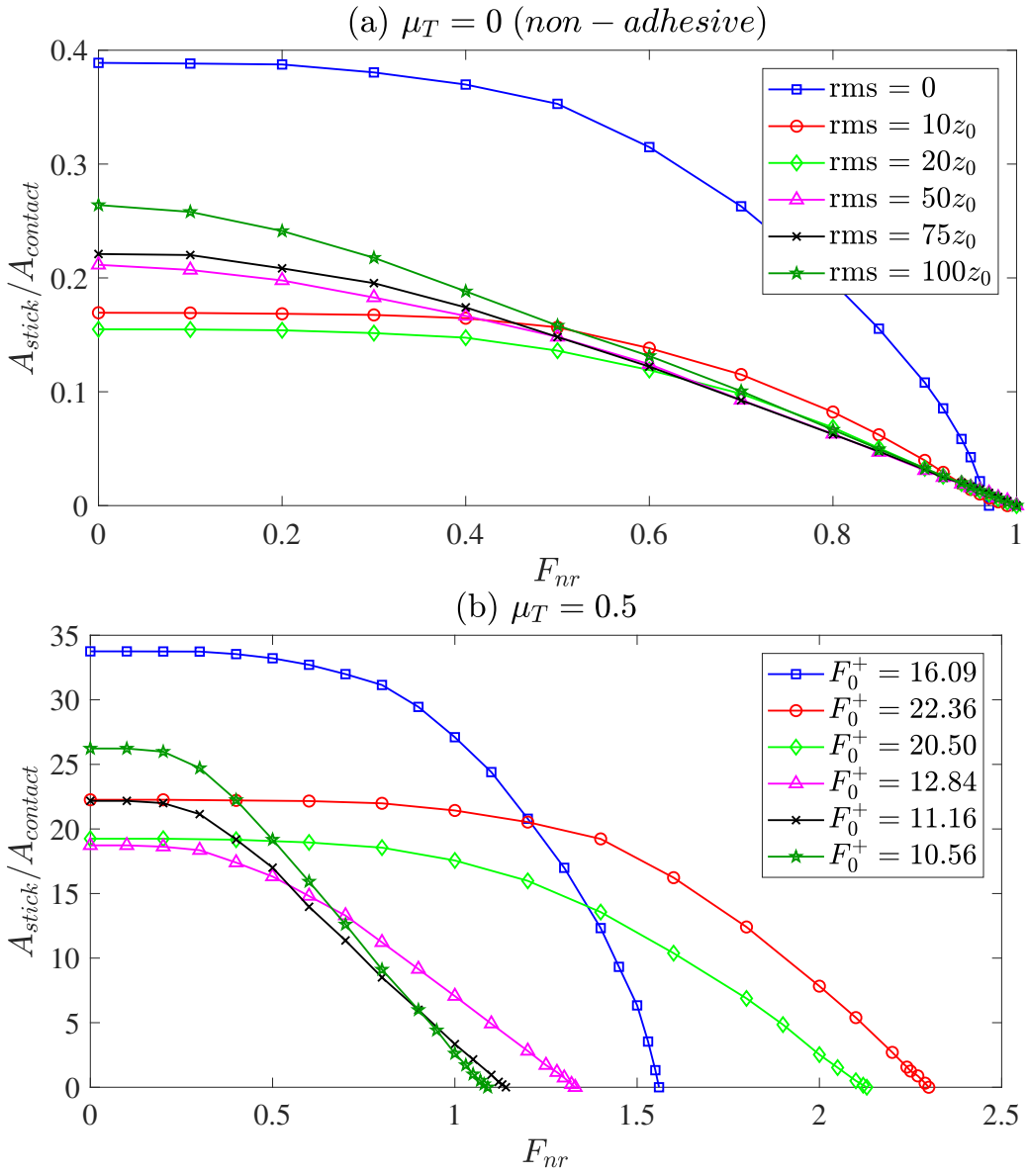
(a) $\mu_T = 0$ $(non - adhesive)$
$A_{stick}/A_{contact}$
F_{nr}
rms $= 0$
rms $= 10z_0$
rms $= 20z_0$
rms $= 50z_0$
rms $= 75z_0$
rms $= 100z_0$
(b) $\mu_T = 0.5$
$A_{stick}/A_{contact}$
F_{nr}
$F_0^+ = 16.09$
$F_0^+ = 22.36$
$F_0^+ = 20.50$
$F_0^+ = 12.84$
$F_0^+ = 11.16$
$F_0^+ = 10.56$

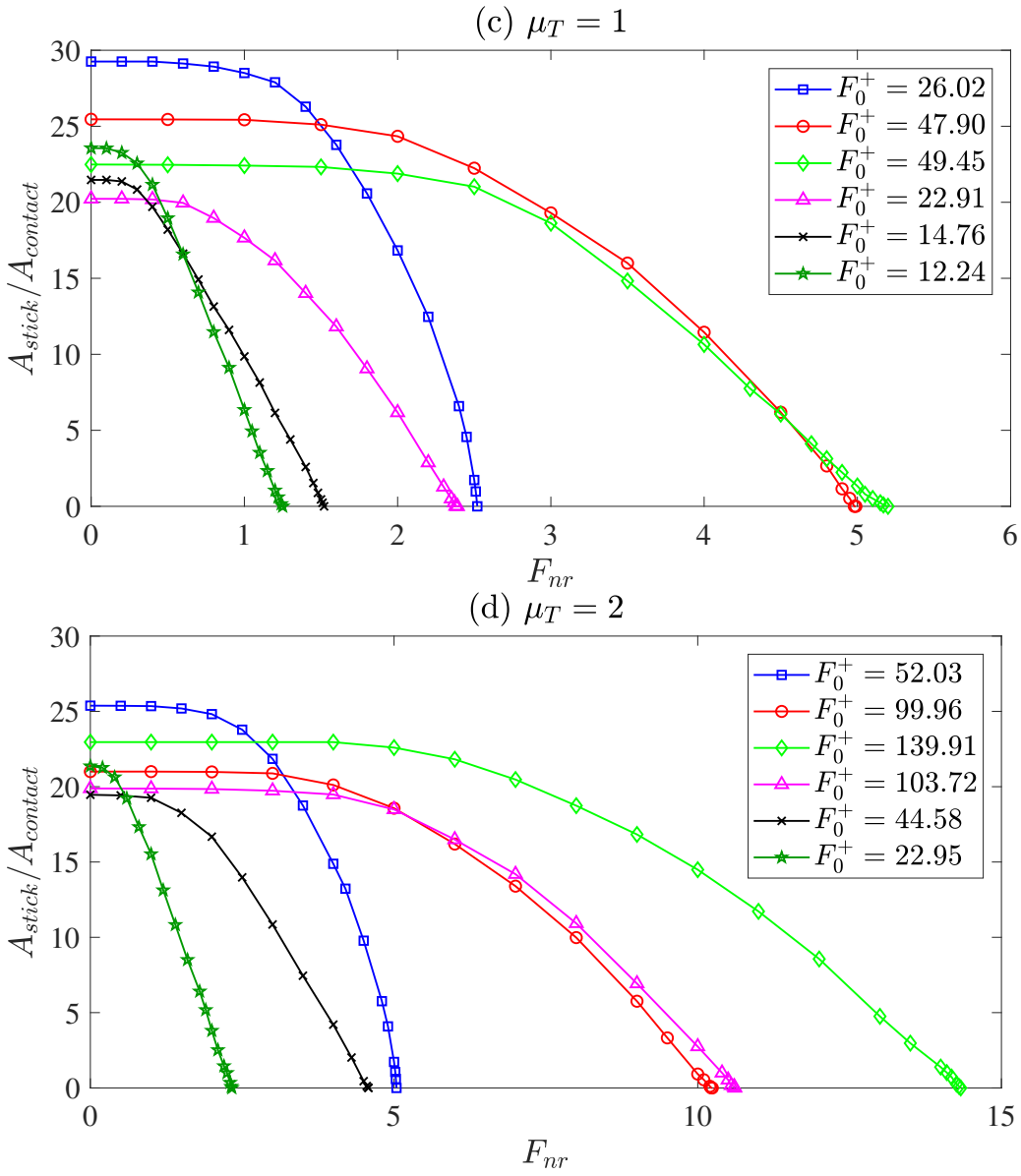

Figure 3.16: The variation of $A_{stick}/A_{contact}$ versus normalized tangential force, F_{nr}, for a non-adhesive case and three different values of the Tabor parameter, μ_T, and different rms values; subplots (b), (c), and (d) have the same legends as subplot (a) for rms values

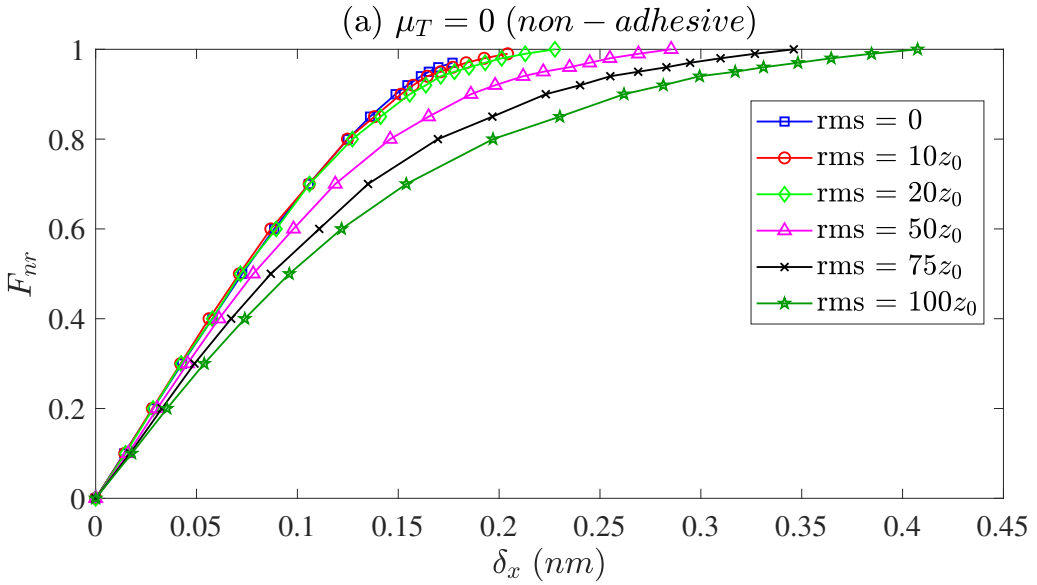
(a) $\mu_T = 0$ $(non - adhesive)$
F_{nr}
δ_x (nm)
rms = 0
rms = $10z_0$
rms = $20z_0$
rms = $50z_0$
rms = $75z_0$
rms = $100z_0$

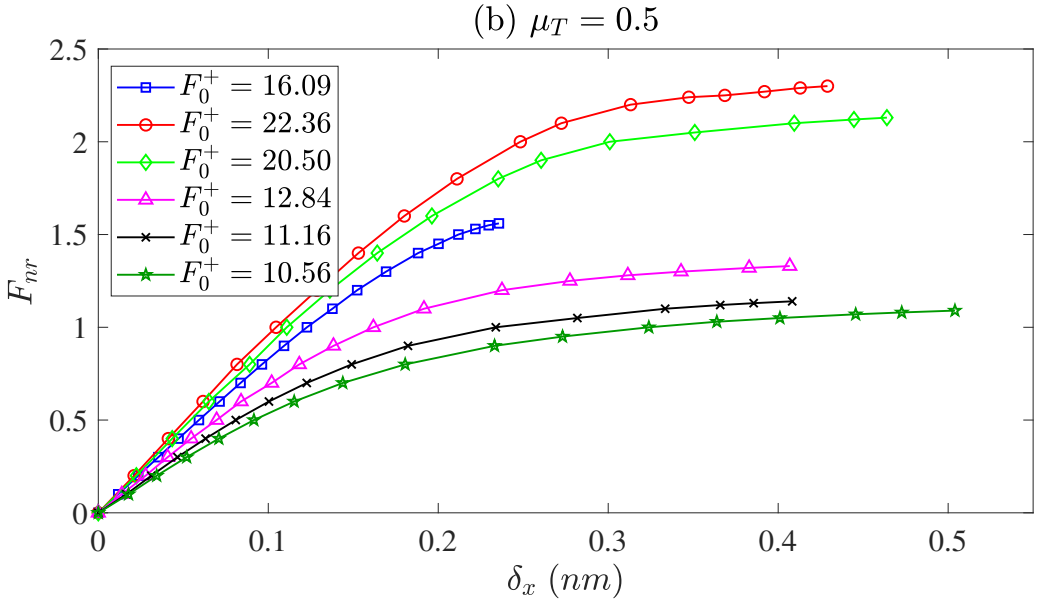
(b) $\mu_T = 0.5$
F_{nr}
δ_x (nm)
$F_0^+ = 16.09$
$F_0^+ = 22.36$
$F_0^+ = 20.50$
$F_0^+ = 12.84$
$F_0^+ = 11.16$
$F_0^+ = 10.56$

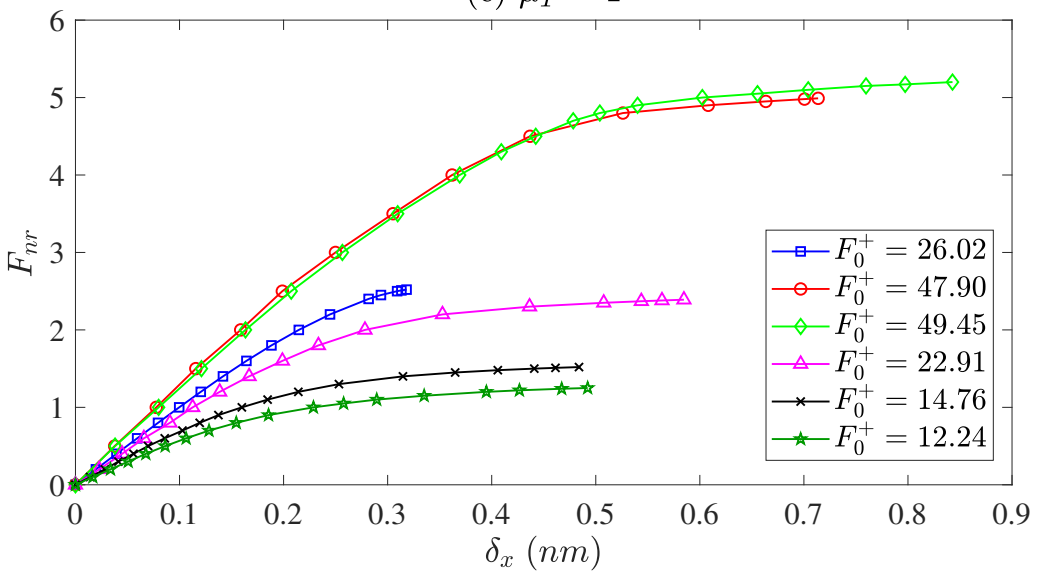
(c) $\mu_T = 1$
F_{nr}
δ_x (nm)
$F_0^+ = 26.02$
$F_0^+ = 47.90$
$F_0^+ = 49.45$
$F_0^+ = 22.91$
$F_0^+ = 14.76$
$F_0^+ = 12.24$

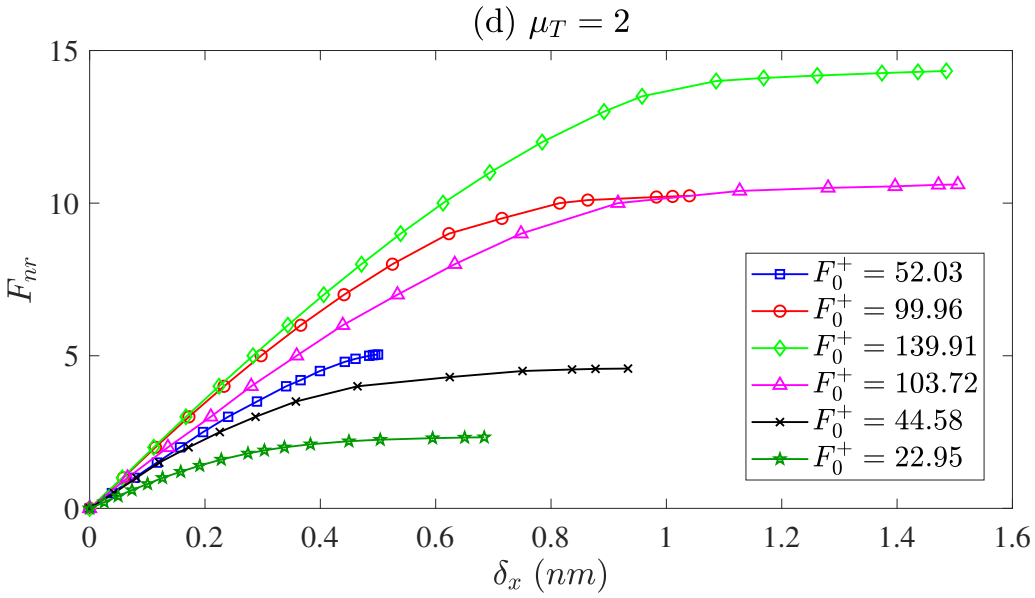

Figure 3.17: The variation of δ_x versus normalized tangential force, F_{nr}, for a non-adhesive case and three different values of the Tabor parameter, μ_T, and different rms values; subplots (b), (c), and (d) have the same legends as subplot (a) for rms values

3.3.2 Friction hysteresis and its history dependence

In the previous pre-sliding model, the tangential force is applied in one single step. In reality, however, the friction force is applied in an incremental manner. As a consequence, this single-step loading cannot simulate the hysteresis behavior of friction since it does not include the history-dependence of the friction force. To modify the model to achieve this objective, the definition of stick and slip regions needs to be changed. Here, rather than considering merely the relative displacement at the interface, the rate of change in the relative displacement is set as the criterion to distinguish between stick and slip regions. For an incremental tangential force, the rate of relative displacement in zero and non-zero (yet small compared to the contact radius) for stick and slip regions, respectively. It is noted that the shear stress is still proportional to the normal pressure in the slip zone. The details of the model are explained in Paper E of Part II of the thesis.

To study the hysteresis behavior of friction, the tangential force oscillates between two entities. The amplitude of the tangential force is smaller than the static friction force in order for the contact to remain in the partial slip contact. Since it was previously shown that it is the contact repulsive force which controls the start of gross-sliding and, not the external normal force, the amplitude of the friction force is chosen to be $\mu_f F_0^+$ and the loading path is shown in Figure 3.18, while the normal load is fixed.

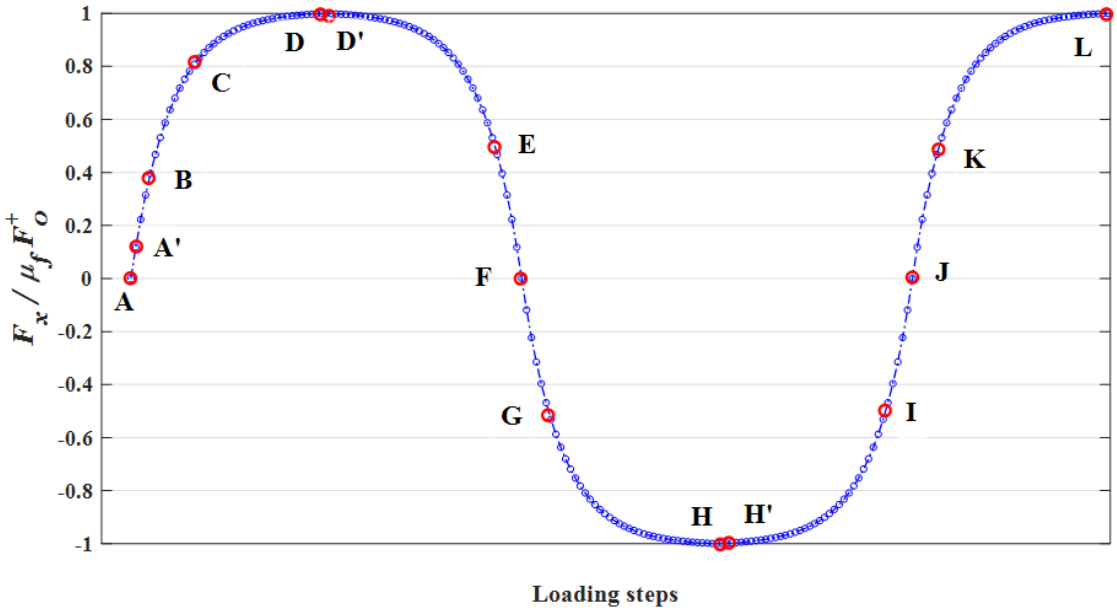

Figure 3.18: Tangential loading path.

The first point that this hysteresis behavior differs from the previous model is the transition from stick to slip, as shown in Figure 3.19. When a pure normal force is applied on such a configuration (point A), an annulus of slip surrounds a circular sticking area. As soon as an infinitesimal friction force is applied (corresponds to point A' which is placed right after point A in the loading path), the shape of the stick zone changes (Figure 3.19A'). Further increase in the friction force makes the sticking area shrink and disappear at the turning point D, which corresponds to a full slip state. At this point, the friction force direction is reversed and the whole contact area experiences a full-stick state which shrinks towards the center similar to the Mindlin solution (however non-symmetrically) as shown for points D' to H. At the turning point H, the friction force direction is again reversed, and the same behavior is repeated up to the next turning point.

In the presence of adhesion, the previously mentioned statements about static friction force and pre-sliding displacement still hold.

3.3.3 Experimental evaluation of the pre-sliding behavior

At this stage, the pre-sliding block of the model is evaluated experimentally. As performing measurement to see the effect of adhesion was not possible with the available equipment, it was decided to use an in-house built setup for friction measurements in order to study the pre-sliding behavior. Specifications of the setup necessitates to have a soft and rough interface to obtain sufficiently large pre-sliding displacements. Therefore,

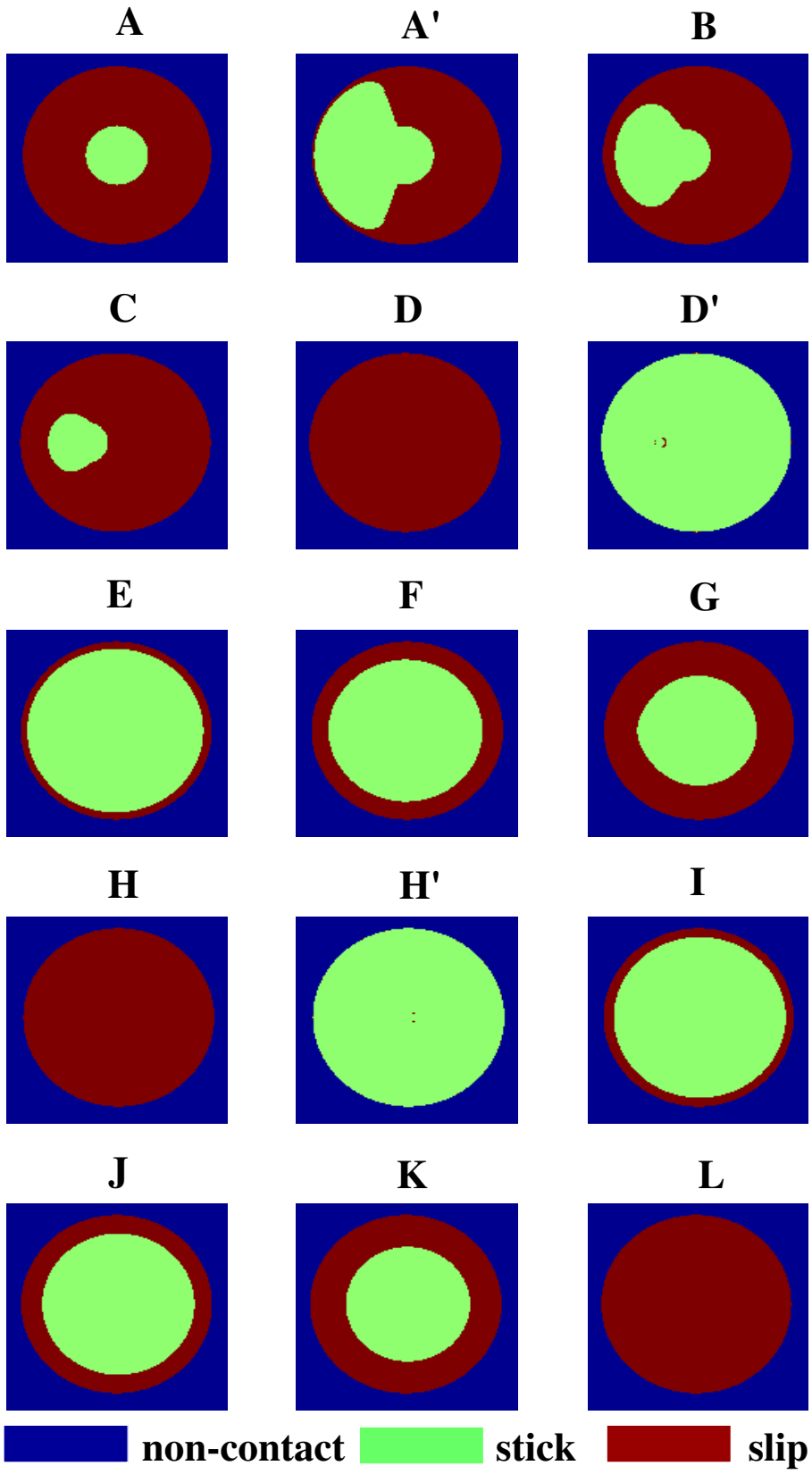

Figure 3.19: Transition from stick to slip for the contact of dissimilar materials, numerical solution (ball-on-flat contact with $E = 70GPa$, $\nu = 0.3$, $R = 50\mu m$, $F_0 = 10\mu N$, $\mu_f = 0.2$ and $\mu_T = 0$)

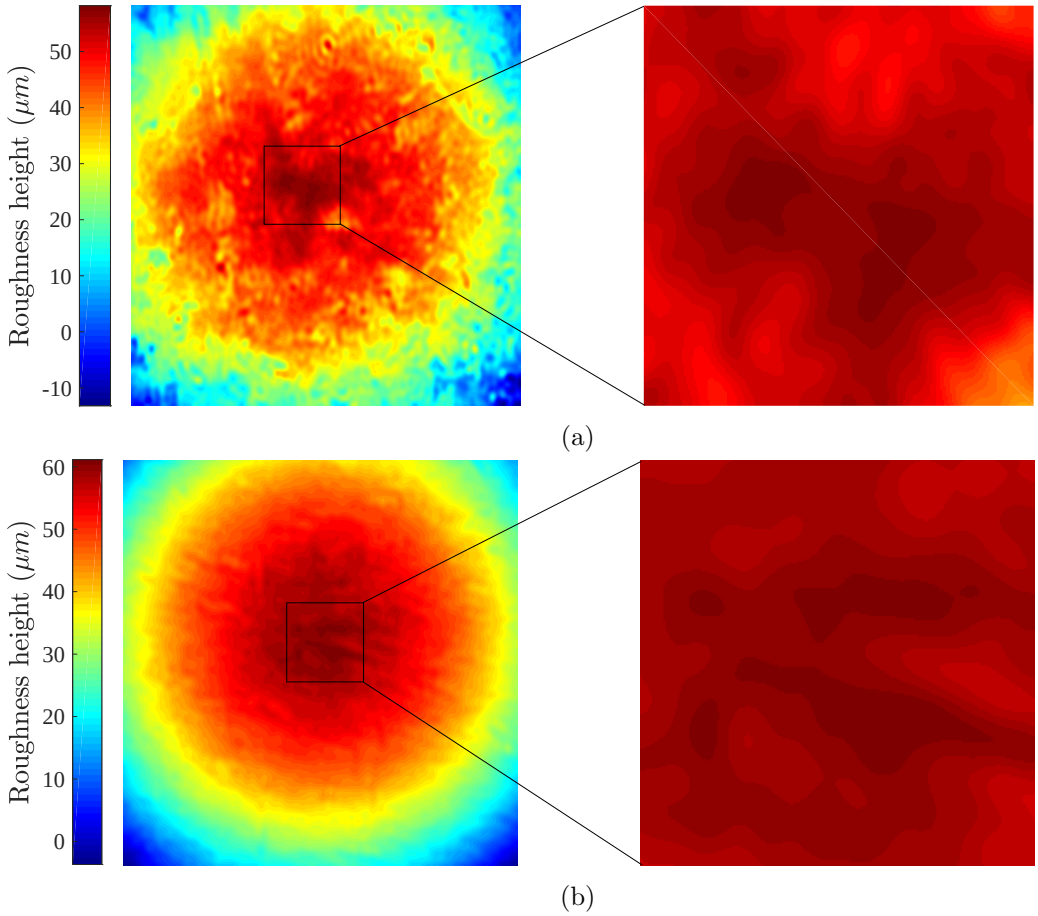

Figure 3.20: Roughness height of the balls ($1.1mm \times 1.1mm$ area): (a) HDPE and (b) POM.

the frictional contact of two rough polymeric balls, HDPE (High Density Polyethylene) and POM (Polyoxymethylene), against a smooth silicon wafer at three normal loads ($25mN, 50mN$ and $75mN$) and five spots is experimentally studied. The friction coefficient and sliding stroke for each set of measurement are extracted from experiments to be considered inputs to the developed BEM model along with the measured surface roughness of the balls and their mechanical properties.

The roughness height of the balls are depicted in Figure 3.20. with a zoomed view to see the highest asperities where the contact patches form. Four friction loops are simulated using the sliding path (instead of loading path) as show in Figure 3.21.

As, in the case of contact between dissimilar materials, friction takes a few loops to converge to a stable one, therefore only the last simulated loop is compared with the

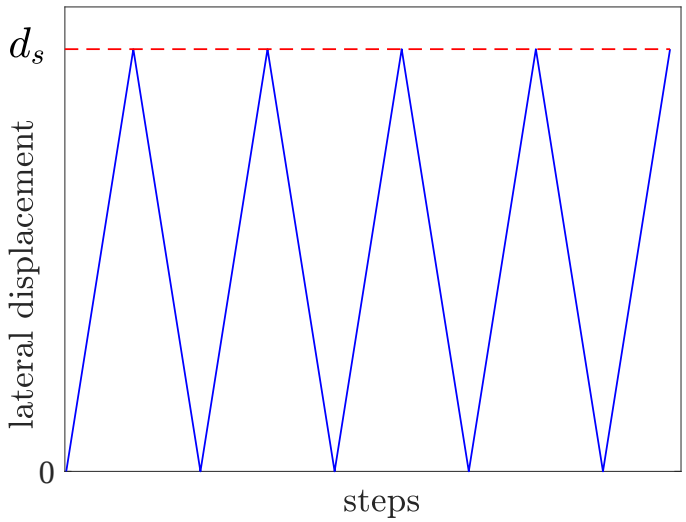

Figure 3.21: Displacement path.

last loop of experiments. Figures 3.22 and 3.23 depict the development of slipping area and shrinking of the sticking zone within the contact area for three spots (A, B and C) on the pre-sliding part of the friction hysteresis loop (with $F_x/\mu_f F_0 = -0.5, 0,$ and 0.5, respectively).

Figures 3.24 and 3.25 compare the experimental and numerically predicted friction hysteresis loops for both contacts (HDPE and POM balls against a silicon wafer) at three normal loads. There is rather good agreement between the experiments and simulations.

To have a quantitative comparison between experiments and simulations, the lateral contact stiffness, defined as the local slope of the friction-displacement curve, is calculated (using a power-law curve fitting) at the mentioned three points on the hysteresis loop (see Figure 3.26). Except for the case of the POM ball contact at point A for normal loads of $25mN$ and $75mN$, the rest of numerically predicted values for the lateral stiffness are in good agreement with those of the experiments. It is confirmed that from point A to C, the lateral stiffness decreases since a larger part of the contact area is slipping and experiencing a greater relative displacement and thus, the contact becomes laterally more compliant.

In general, the higher lateral stiffness of the POM contact compared to HDPE is due to the larger elastic modulus of POM ($1.38GPa$) than that of HDPE ($0.98GPa$) and the smoother surface of POM.

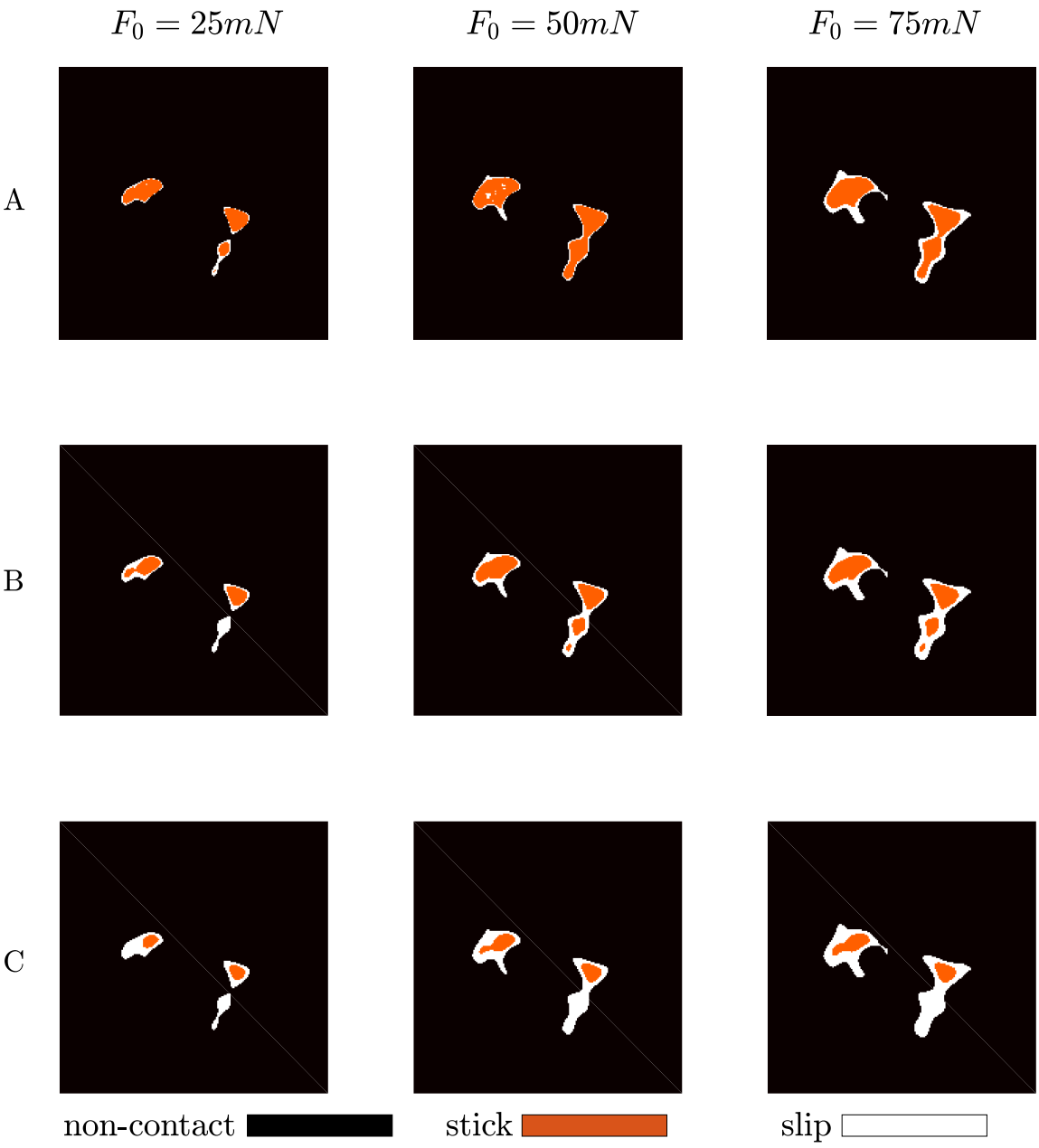

Figure 3.22: Stick-slip transition from point A to C for three different normal loads: HDPE ball-silicon wafer contact (the size of each image is $0.2\mu m \times 0.2\mu m$).

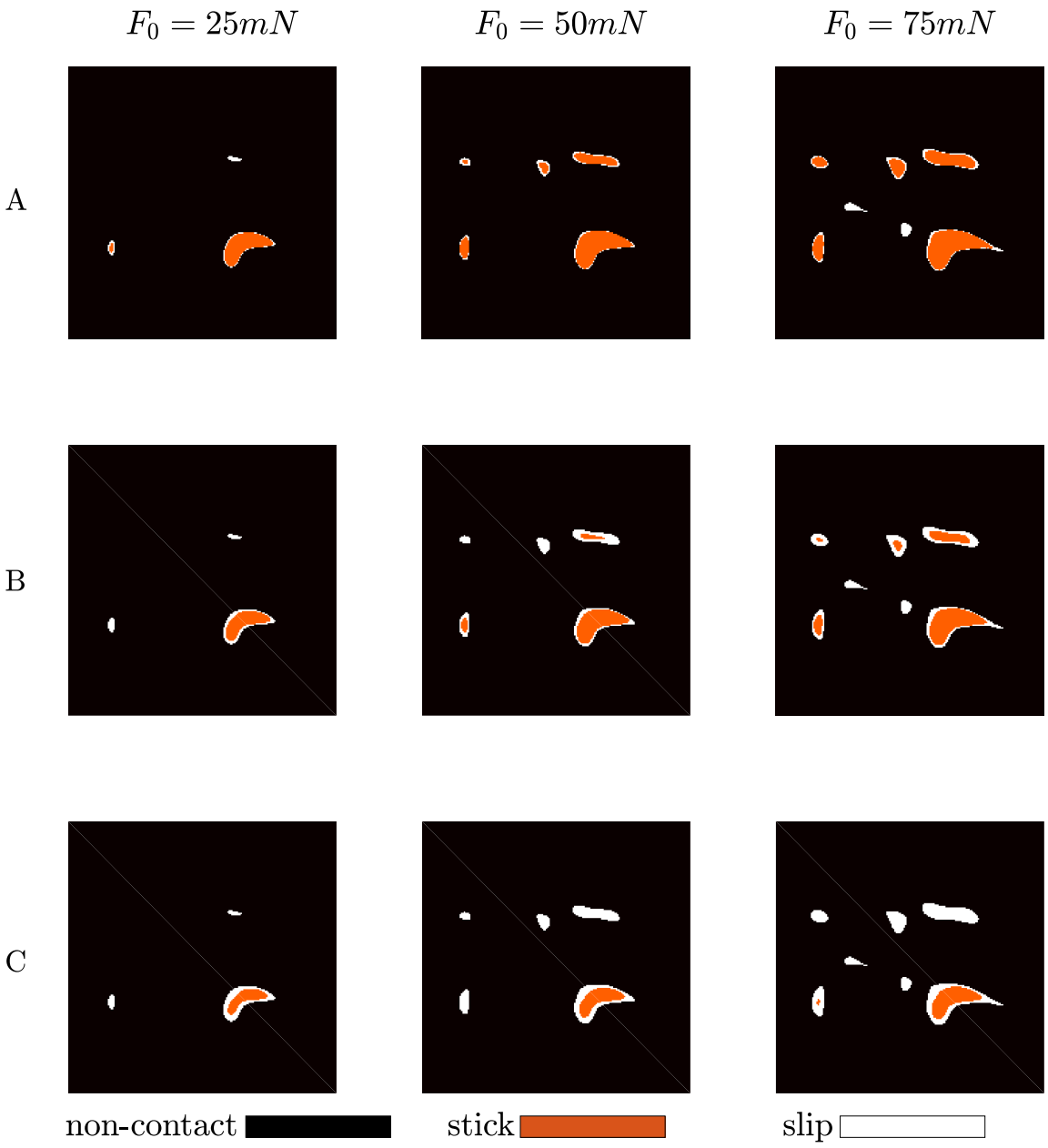

Figure 3.23: Stick-slip transition from point A to C for three different normal loads: POM ball-silicon wafer contact (the size of each image is $0.2\mu m \times 0.2\mu m$)

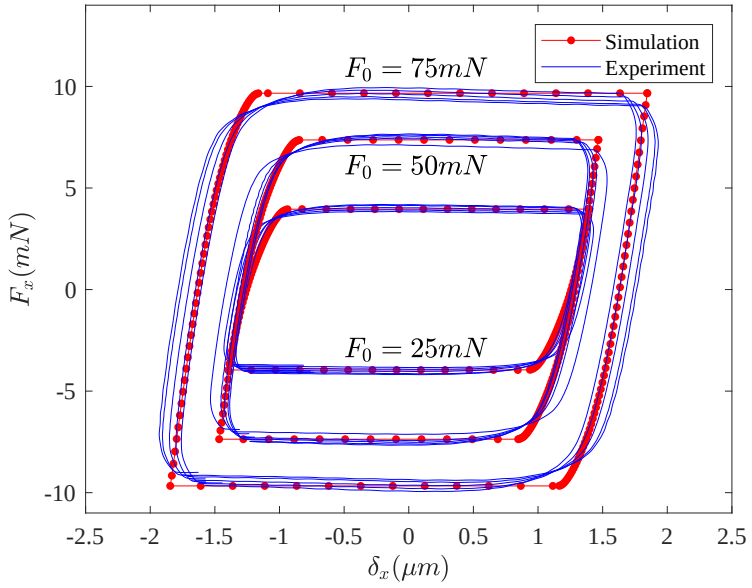

Figure 3.24: Comparison of simulation and experimental friction hysteresis loops for HDPE ball - silicon wafer contact.

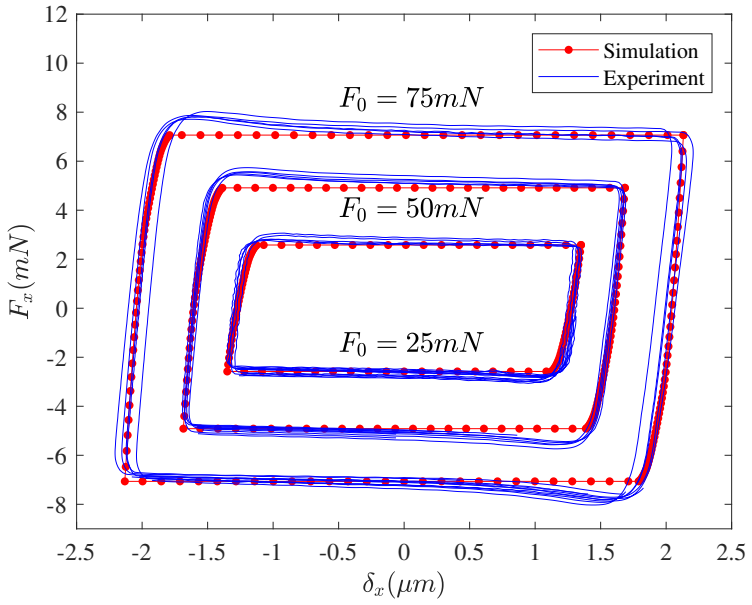

Figure 3.25: Comparison of simulation and experimental friction hysteresis loops for POM ball - silicon wafer contact.

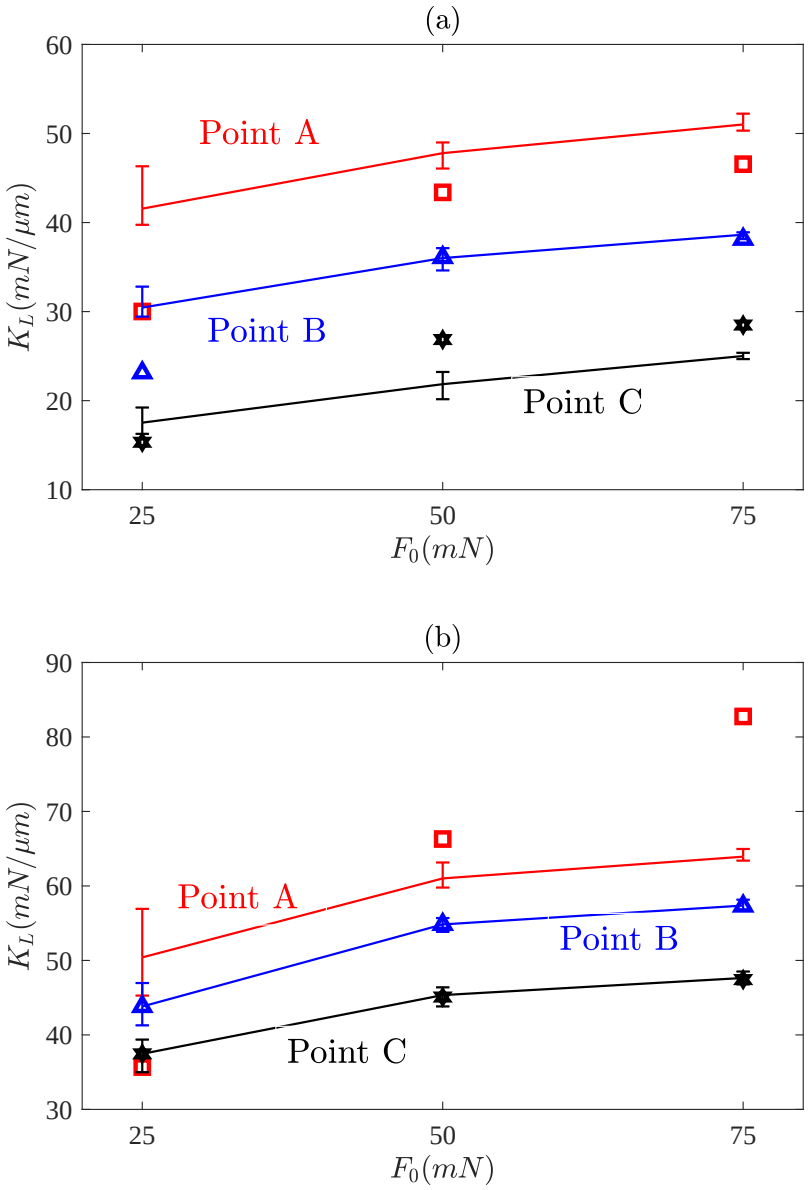

Figure 3.26: Comparison of the experimental (solid lines) and numerical (markers) lateral stiffness at points A, B, and C for (a) HDPE and (b) POM contact on the silicon wafer.

Chapter 4

CONCLUSION AND RECOMMENDATIONS

4.1 Conclusion

In this thesis, a BEM model for the adhesive pre-sliding behavior at a rough interface of two contacting surfaces was proposed. The complete model is developed in a number of steps. At first, the model is developed for the adhesive normal contact where the adhesion originates from the van der Waals forces. Similar to the Maugis-Dugdale model of adhesion of a ball on a flat, the Lennard-Jones potential, which is used to describe the separation-dependence of these forces, is estimated by a Dugdale approximation, based on which, the adhesion is present as long as the local separation does not exceed a critical value. Local regions surrounding the contact patches at an interface, meeting this separation rule, experience a constant negative stress which is the maximum negative stress of the Lennard-Jones potential. The existing CGM algorithm for the non-adhesive contact problem between two surfaces of arbitrary geometries is extended to capture this definition of adhesive stress.

The model was first verified through comparing the numerical results with analytical expressions for two well-known cases of adhesive contact, namely the ball on a flat half-space and ball on a wavy half-space. In addition, the pull-off force from a bi-sinusoidal interface was considered and numerically solved for various values of the elastic modulus, work of adhesion, radius of curvature and wavelength ratio. In the end, an expression was fitted on the numerically predicted values to give a very good analytical approximation of the pull-off force at this interface. The pull-off force was found to be linearly proportional to the work of adhesion and radius of curvature of the contacting summits, similar to JKR and DMT theories of adhesion. Further, the adhesive contact of a smooth ball on a rough surface with several values of rms roughness ranging from 0 (for an ideally smooth surface) to $100z_0$ was investigated. It was shown that a

small change in rms roughness can increase the pull-off force, adhesive force, and area ratio.

Secondly, the model is extended to include the effect of the capillary force as the dominating component of the total adhesive force in the ambient conditions. Thin water films, whose thickness depends on the relative humidity of the environment, are adsorbed on the surfaces and considered to mediate the formation of micro-menisci islands around the contacting and at the near-contacting asperities. The uneven distribution of these films over the contacting rough surfaces is calculated by numerically solving the equations of mechanical equilibrium and rheology of the water. In areas, where a micro-meniscus has formed, a constant humidity-dependent negative stress exists.

It was found that the capillary force first increases with RH and then decreases as a results of variation in both capillary area and capillary pressure. The maximum of the capillary force was found to be larger and at a lower RH for surfaces with smaller curvatures (here longer auto-correlation length and or smaller rms roughness). The normal force appeared to be a key factor as it can change not only the maximum capillary force but also the entire curve of capillary force versus RH.

At the last step of this block, the adhesive normal contact model was experimentally evaluated by performing pull-off force measurements using an AFM for the contact between an SiO_2 colloidal probe and two substrates in vacuum and ambient conditions. The measurements were performed initially in ambient, followed by vacuum and then ambient again. Results showed there is a sharp increase in the pull-off force due to removal of the hydrocarbon contamination from the substrates and or the change in the topography of the colloidal probe. The presence of contamination was confirmed by the curvy snap-in behavior in the approach part of the force-distance curve of the measurements. Although the predicted pull-off force for the ambient conditions was in good agreement with experiments, the model predicted lower forces for the vacuum conditions as it neglects the presence of water monolayers on the substrates even under vacuum conditions.

The next block is the stick-slip behavior and the effect of adhesion and roughness on it. Adhesion, coming from the van der Waals force, is modeled by means of a Dugdale approximation of the total work of adhesion. The contact area is divided into stick and slip regions, distinguished by the local values of the shear stress components and normal pressure, and the relative displacement at the interface. The CGM algorithm is implemented to find the optimum solution for the shear stress components and stick and slip regions, meeting the mentioned conditions.

The numerical results suggest that, for an adhesive contact, it is the contact repulsive force that controls the start of gross-sliding and not the external normal force. This repulsive force increases with adhesion. It was also shown that the adhesion increases

both pre-sliding displacement and static friction force, while roughness can only increase the former one. However, the combined effect of roughness and adhesion is not cumulative as these two parameters are found to be interdependent and any change in the roughness significantly changes the adhesive behavior and thus, the normal pressure distribution.

At this stage, since the tangential load was applied in a single-step, it could not include the history of friction and thus, it could not simulate the friction hysteresis behavior. The definition of the stick and slip regions changed accordingly. Then, rather than merely the relative displacement, the rate of relative displacement was used to distinguish between the stick and slip. In the stick region, this rate was zero, while it was non-zero in the slip region. Then, the amplitude of the oscillating tangential force to capture the hysteresis behavior, was set to be smaller than the static friction force. It was shown that, the contact of dissimilar materials does not obey the well-known Mindlin solution, and there is a remarkable difference and asymmetry in the results due to the difference in the mechanical properties of the bodies in contact. Results also suggested that adhesion can exclusively increase the static friction force and pre-sliding displacement at a smooth interface. On the other hand, roughness can only increase the pre-sliding displacement for a non-adhesive contact. For an adhesive contact at a rough interface, however, the effect of combined adhesion and roughness is not cumulative.

The last step was to experimentally evaluate the effect of adhesion on the pre-sliding behavior. Since performing measurement to see the effect of adhesion was not possible with the available equipment, the friction behavior at a rough interface of two elastic polymeric balls (HDPE and POM) against the smooth surface of a silicon wafer at three normal loads and at five spots was measured using an in-house built-in setup. Extracting the friction coefficient and stroke from the experiments and using them as inputs to a BEM model, the same friction hysteresis loops were predicted compared with experiments. The lateral stiffness of the contact was also calculated at three points on the friction loop both experimentally and numerically to quantitatively compare the results. The difference in lateral stiffness between the HDPE and POM is attributed to the difference in elastic modulus, friction coefficient, and their surface roughness.

4.2 Recommendations

There are a number of points to be addressed for future research.

- The current simulations are conducted on micro-scale, where the sizes of the scanned area is $2 - 10\mu m$. The question, left open here, is that whether these results can be extended to macroscopic level. In other words, can such a small measured area represent the topography of the entire microscopic contact? This is even more crucial

for surfaces with roughness inhomogeneities, where roughness properties varies over the surface from point to point. Here, a multi-scale study could help. Larger area measurements can detect areas with higher asperities or higher patches compared to the rest of the surface and then, the focus can be put to such areas.

- One of the major steps in the calculation of the capillary force is to find the uneven distribution of the water films on the contacting surfaces. This step is basically solving a very complex PDE and takes a long time for the film to reach a stable state. Since only this stable state is needed, the PDE can be converted to a large number of algebraic equations. Yet, this large system of algebraic equations needs to be solved efficiently. As conventional methods like Gaussian elimination and LU decomposition are pretty slow and occupy too much memory, faster algorithms, which are typically iterative-based, are needed [110].

- In the pre-sliding model, the deformation in vertical direction induced by the shear stress components is taken into account. This deformation can change the interfacial profile and consequently, the contact pressure distribution. Another factor that can change this profile is when the tangential displacement is larger than the measurement resolution which forms new contact pairs and probably, local stick-slip behavior. This behavior normally appears in friction experiments as a saw-tooth shape in the sliding regime. Future research can include this change in the interfacial profile to capture this local stick-slip transitions. The starting point, in this regard, could be surface updating by including the tangential displacements caused by the contact stresses.

- An approach to experimentally see the effect of adhesion on pre-sliding is to perform friction measurements with the AFM. The cantilevers with colloidal probes can be also used to make a large nominal contact area and therefore higher friction forces. A challenge, however, is the torsional calibration of the cantilever. There are theoretical and experimental methods to precisely calibrate the cantilevers with sharp tips. For colloidal probes, however, theoretical approaches are not reliable as they cannot consider the true effect of the glue, binding the sphere to the cantilever. On the other hand, experimental methods are also pretty demanding.

Appendices

Appendix A

SINGLE-ASPERITY CONTACT

A.1 Non-adhesive contact: Hertzian theory

When two elastic bodies with non-conforming curved surfaces are brought into contact, point or line contact between them changes to area contact leading to 3D stresses at this area. In 1882, using the theory of elasticity, Heinrich Hertz developed an analytical strategy to find these contact stresses by means of considering the shape of the contact and the deformation of the contacting bodies. The Hertzian contact theory assumes the half-space approximations [52]:

- Contact area is small compared to the size of contacting bodies.
- Contact stresses are concentrated in the proximity of the contact region and their intensity rapidly decreases with the distance from the contact point.
- Contact stresses are not critically dependent on the shape of bodies distant from the contact region. Therefore, the shape of the bodies can be well approximated with parabolic shapes.
- All the assumptions of the classical theory of elasticity apply (small strain, homogeneous material)

Figure A.1 illustrates the frictionless contact of an elastic sphere of radius R and elastic properties of E_1 and ν_1 against an elastic half-space with elastic properties of E_2 and ν_2 under a normal force F_0.

The Hertz solution for this problem leads to the contact radius, a, pressure profile, $P(r)$, and indentation, δ, as:

$$a = \left(\frac{3RF_0}{4E_s}\right)^{1/3} \tag{A.1}$$

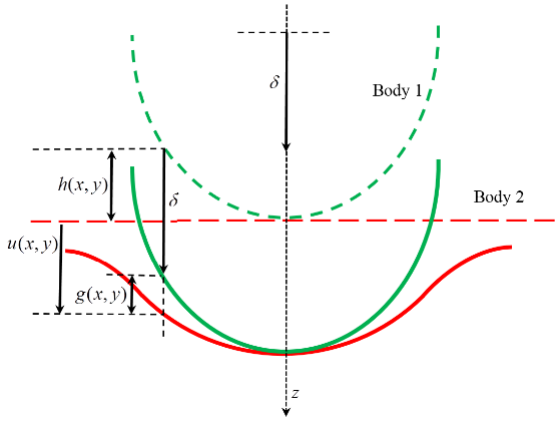

Figure A.1: Two elastic bodies in contact before and after the contact.

$$P(r) = P_0 \left(1 - \frac{r^2}{a^2}\right)^{1/2}, \quad P_0 = \frac{3F_0}{2\pi a^2} \tag{A.2}$$

$$\delta = \frac{a^2}{R} \tag{A.3}$$

in which, the reduced elastic modulus, E_s, is expressed as:

$$\frac{1}{E_s} = \frac{1-\nu_1^2}{E_1} + \frac{1-\nu_2^2}{E_2} \tag{A.4}$$

and the distance from the center of contact, r, is expressed as a function of the spatial coordinates, x and y:

$$r = \sqrt{x^2 + y^2} \tag{A.5}$$

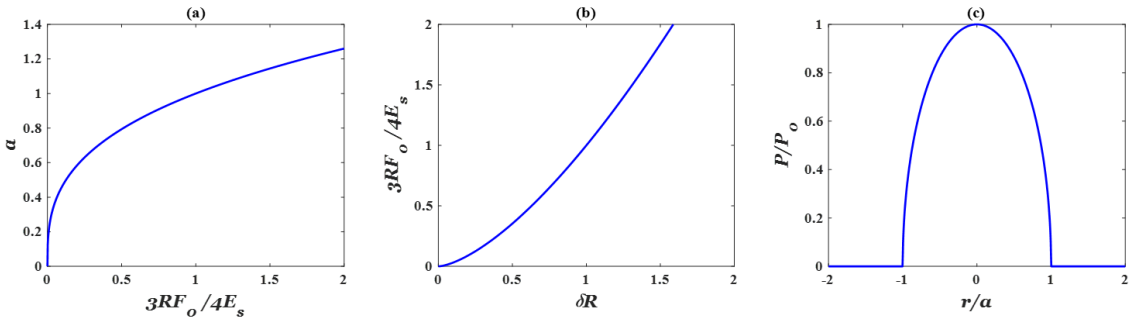

Figure A.2: Hertzian solution for a ball on flat contact.

Figure A.2(a) displays the variation of contact radius vs. the scaled normal force (by $4E_s/3R$). The scaled normal force vs. scaled indentation (by $1/R$) is also shown in Figure A.2(b). The normalized pressure profile, shown in Figure A.2(c), implies that the contact pressure within the contact area is parabolic with its maximum in the contact center and its minimum at the contact edge. Outside the contact, there is no contact pressure.

A.2 Adhesive contact

According to the Hertzian theory, when the normal force is removed from the contact, the contact area reduces to zero. This means that the two surfaces require no force to separate. In reality, however, the surfaces stick to the contact even after the force is removed. This is due to the adhesion at the interface. Therefore, a negative (pulling) normal force is required to separate the two surfaces, referred to the pull-off force. There are different types of adhesive forces at the interface of two contacting (or near-contacting) bodies which contribute to the total adhesive force depending on the material properties and the medium through which the contact is formed. Van der Waals, capillary, electrostatic, as well as hydrogen-bond forces, are examples of the contributors to the total adhesive force.

A.2.1 van der Waals forces

Van der Waals forces are the results of (weak) short-range electrostatic interactions between uncharged molecules or atoms due to the interaction of permanent or transient electric dipole moments. The Lennard-Jones (LJ) potential is typically used to express the distance dependency of these forces. The LJ potential describes the pressure between two atoms, separated by a distance z_0, as:

$$p = \frac{8\Delta\gamma}{3z_0}\left[\left(\frac{z_0}{z}\right)^9 - \left(\frac{z_0}{z}\right)^3\right] \tag{A.6}$$

where $\Delta\gamma$ and z_0 are the total work of adhesion and the equilibrium separation, respectively. In Eq.A.6, z is the separation between surfaces in the atomic description of the surfaces which differs from its continuum counterparts, g. In the atomic description, the zero-pressure conditions takes place at $z = z_0$ as equilibrium. In the continuum description, however, the equilibrium occurs at $g = 0$. Therefore, these two description can be easily related by:

$$g = z - z_0 \tag{A.7}$$

Substituting Eq.A.7 in Eq.A.6, gives rise to the continuum description of the LJ potential separation dependence as:

$$p = \frac{8\Delta\gamma}{3z_0}\left[\left(\frac{z_0}{g+z_0}\right)^9 - \left(\frac{z_0}{g+z_0}\right)^3\right] \tag{A.8}$$

Bradley's model

50 years after Hertz developed his non-adhesive contact theory, Bradley provided an exact solution for the potential between two rigid spheres of radii R_1 and R_2 with perfectly smooth surfaces. He showed that these two spheres adhere to one another with the force of $2\pi R\Delta\gamma$, where $R = R_1R_2/(R_1 + R_2)$ is the equivalent radius.

Johnson, Kendall, and Roberts (JKR) model

The first classical theory of adhesion for an elastic contact was proposed by Johnson, Kendall, and Roberts [105]. This model is based on the balance between the stored elastic energy and the loss of surface energy. This model confines the entire surface energy inside the contact area. The pressure description of this model is expressed as:

$$p(r) = \frac{2aE_s}{\pi R}\left(1 - \frac{r^2}{a^2}\right)^{1/2} - \left(\frac{2\Delta\gamma E_s}{\pi a}\right)^{1/2}\left(1 - \frac{r^2}{a^2}\right)^{-1/2} \tag{A.9}$$

where the contact radius, a, is related to the normal force, F_0, by:

$$a^3 = \frac{3R}{4E_s}\left(F_0 + 3\pi R\Delta\gamma + \sqrt{6\pi R\Delta\gamma F_0 + (3\pi R\Delta\gamma)^2}\right) \tag{A.10}$$

This contact radius is larger than the one predicted by the Hertzian theory, as in the case of zero normal force, in contrast to the Hertzian contact predicting a zero contact radius, the JKR model give a non-zero contact radius as:

$$a^3 = \frac{9\pi R^2\Delta\gamma}{2E_s} \tag{A.11}$$

The largest negative force that the interface can tolerate before the full separation, known as the pull-of force, is given by:

$$F_{pull-off}^{JKR} = \frac{3}{2}\pi R\Delta\gamma \tag{A.12}$$

Derjaguin, Muller, and Toporov (DMT) model

Derjaguin, Muller, and Toporov (DMT) proposed another model of adhesion for a single asperity contact by assuming a compressive Hertzian pressure distribution inside the contact area and adhesive pressure outside the contact area [106]. This model neglects

the effect of adhesion on the contact area. The contact radius is related to the normal force as:

$$a^3 = \frac{3R}{4E_s}(F_0 + 2\pi R\Delta\gamma) \tag{A.13}$$

which leads to the pull-off force as:

$$F_{pull-off}^{DMT} = 2\pi R\Delta\gamma \tag{A.14}$$

Maugis-Dugdale (MD) model

Although JKR and DMT models take different approaches and make significantly different assumptions, they are both true. It was shown by Tabor that these two models are the two opposite extreme limits of a single theory characterized by the Tabor parameter [107]:

$$\mu_T = \left(\frac{R\Delta\gamma^2}{E_s^2 z_0^3}\right)^{1/3} \tag{A.15}$$

The JKR model is valid for large values of the Tabor parameter, as in the case of large and compliant contacts. The DMT model, however, is suitable for low values of this parameter, as for small and stiff contacts. Physically it is not realistic to confine adhesion to either inside or outside of the contact area. The contribution of adhesion from both inside and outside of the contact was first considered by Muller et al. [108]. They developed a numerical solution for the adhesion interaction by integrating the Lennard-Jones potential and characterizing the transition from DMT to JKR by adjusting the Tabor parameter. Subsequently, Maugis implemented the principles of elasticity and fracture mechanics to derive an analytical transition from DMT to JKR model by means of a Dugdale approximation of the LJ representation of the adhesion [108]. Maugis represented the surface force in terms of a Dugdale cohesive zone and stated that adhesion is present up to a specific value of separation, between the two contacting bodies, named h_0. Over this separation the attractive pressure of σ_0, which is the maximum attractive pressure of the LJ potential, is applied such that [109] (Figure A.3):

$$\Delta\gamma = \sigma_0 h_0 \tag{A.16}$$

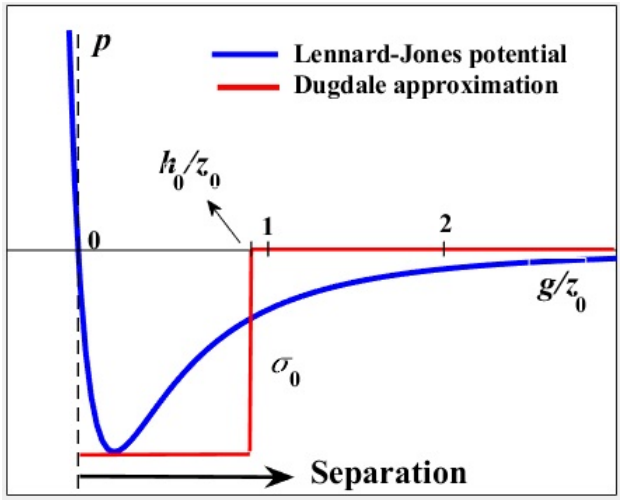

Figure A.3: Dugdale approximation of the LJ potential.

This results in $\sigma_0 = 16\Delta\gamma/9\sqrt{3}z_0$ and $h_0/z_0 = 9\sqrt{3}/16 = 0.974$. Based on the definition of the MD model, the pressure inside the contact region is the superposition of the positive Hertzian pressure of radius a and the negative adhesive pressure. Outside the contact region, the attractive pressure is constant for $z_0 \leq z \leq z_0 + h_0$, or equivalently, over a ring of inner and outer radii of a and c, in which the separation is:

$$\phi = \begin{cases} 0, & \text{at } r = a \\ h_0, & \text{at } r = c \end{cases} \tag{A.17}$$

For such a contact, the normalized contact radius, A_M, the normalized normal force, F_M, and the adhesive parameter, λ, are defined as:

$$A_M = a\left(\frac{4E_s}{3\pi\Delta\gamma R^2}\right)^{1/3} \tag{A.18}$$

$$F_M = \frac{F_0}{\pi R\Delta\gamma} \tag{A.19}$$

$$\lambda = 2\sigma_0\left(\frac{9R}{16\pi\Delta\gamma E_s^2}\right)^{1/3} \simeq 1.16\mu_T \tag{A.20}$$

Given a normal force, one must simultaneously solve Eqs. A.21 and A.22 for A_M and m:

$$F_M = A_M^3 - \lambda A_M^2 \left(\sqrt{m^2-1} + m^2 \tan^{-1} \sqrt{m^2-1} \right) \tag{A.21}$$

$$\begin{aligned} &\frac{\lambda A_M^2}{2} \left[\sqrt{m^2-1} + (m^2-2) \tan^{-1} \sqrt{m^2-1} \right] + \\ &\frac{4\lambda^2 A_M}{3} \left[\sqrt{m^2-1} \tan^{-1} \sqrt{m^2-1} - m + 1 \right] = 1 \end{aligned} \tag{A.22}$$

Finally, the pressure profile, $P(r)$ and the normalized indentation, Δ_m, are given as:

$$P(r) = \begin{cases} \frac{2E_s a}{\pi R}(1 - r^2/a^2)^{1/2} - \frac{2\sigma_0}{\pi} \tan^{-1} \left(\frac{m^2-1}{1-r^2/a^2} \right)^{1/2}, & r \le a \\ -\sigma_0, & a < r \le c \end{cases} \tag{A.23}$$

$$\Delta_M = \delta \left(\frac{16 E_s}{9\pi^2 \Delta\gamma^2 R} \right)^{1/3} = A_M^2 - \frac{4}{3} A_M \lambda \sqrt{m^2-1} \tag{A.24}$$

Figure A.4 compares the pressure profiles of the Hertzian contact and the three adhesive models. The variation of the normalized contact radius vs. normalized normal force and normalized normal force vs. normalized indentation are illustrated in Figure A.5. This figure implies that when the normal force is removed from the contact, in contrast to the Hertzian contact, the surfaces stick to one another as there is a non-zero contact radius and a positive indentation. Applying a negative normal force reduces the contact radius and indentation. Further increasing the negative force starts the pull-off process and as soon as the negative force reaches its maximum tolerable value by the contact interface, adhesive bonds are broken and the two surfaces abruptly separate while the contact radius, right before the full separation, was non-zero. The higher the work of adhesion, the higher the pull-off force. Moreover, for higher values of the work of adhesion, corresponding to higher values of λ, the contact radius at the separation moment is smaller and the indentation is more negative which means that the interface deforms more significantly before the separation.

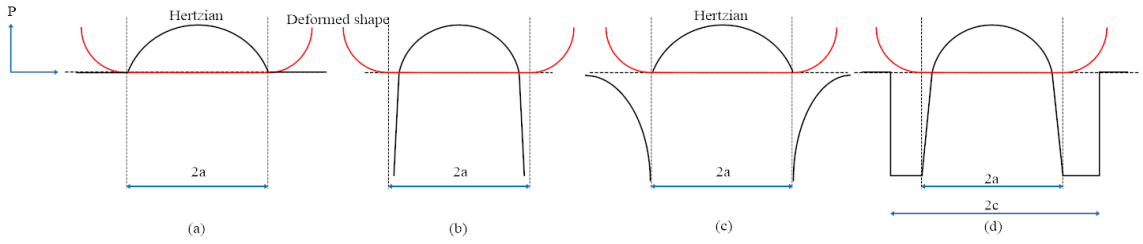

Figure A.4: Pressure profiles based on (a) Hertzian model, (b) JKR model, (c) DMT model, and (d) MD model.

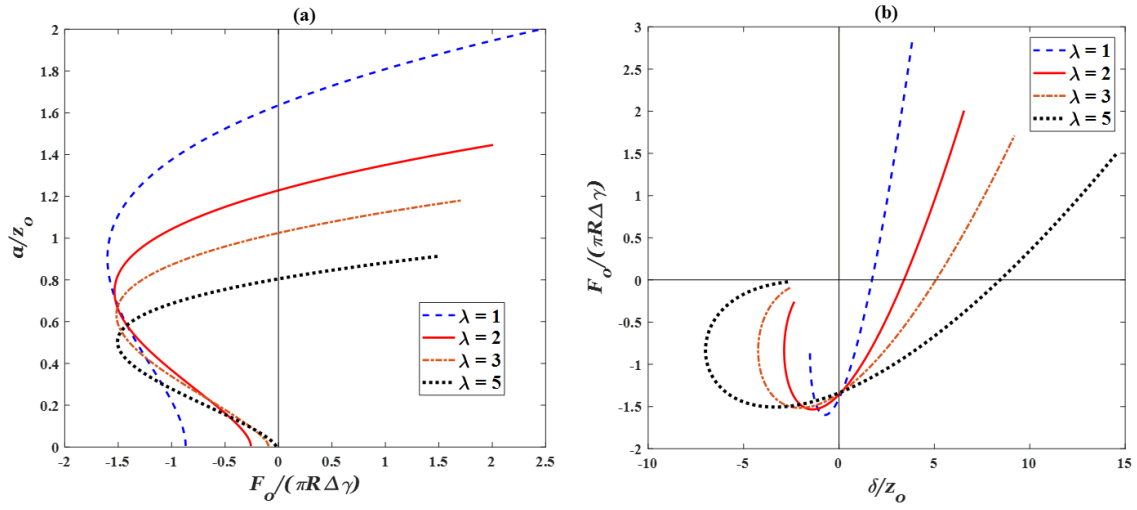

Figure A.5: Variation of (a) normalized contact radius vs. normalized normal force and (b) normalized normal force vs. normalized indentation for different values of the adhesive parameter.

Johnson and Greenwood constructed an adhesion map for the elastic adhesive contact of a ball against a flat based on the MD model (Figure A.6). It can be confirmed that the JKR model is suitable for large values of λ (or equivalently the Tabor parameter μ_T), whereas it is appropriate to consider the DMT model for low values of this parameter.

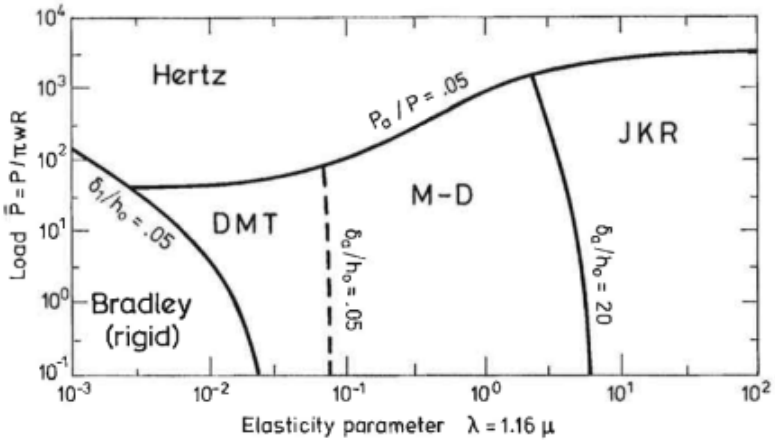

Figure A.6: Adhesion map [110].

A.2.2 Capillary force

Liquids with small contact angles condense from humid environment to fill in cracks and pores. At a dry and smooth ball-on-flat interface, water condenses to form a meniscus outside the contact area (Figure A.7). At thermodynamic equilibrium, the meniscus radius of curvature or namely Kelvin radius, r_k, is directly controlled by the relative humidity (RH) as [111]:

$$\left(\frac{1}{r_1}-\frac{1}{r_2}\right)^{-1} = r_k = \frac{\gamma V}{R_g T \log RH} \tag{A.25}$$

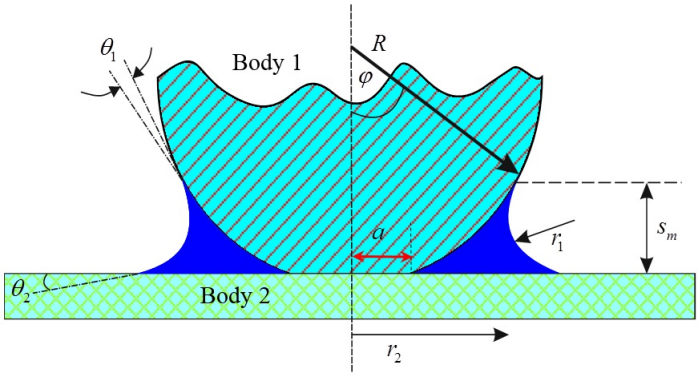

Figure A.7: Meniscus formation at a smooth ball-on-flat interface.

where $1/r_1$ and $1/r_2$ are the meniscus curvatures, V the molar volume of water, R_g the universal gas constant, and T the absolute temperature. The capillary pressure inside the meniscus is then given by:

$$\Delta P_{cap} = \frac{\gamma}{r_k} = \frac{R_g T \log RH}{V} \tag{A.26}$$

Figure A.8 displays the formation of a meniscus at the interface of a ball-on-flat configuration in the presence of a thin adsorbed water film. The curvature of the meniscus does not significantly change the thickness of the adsorbed film [112].

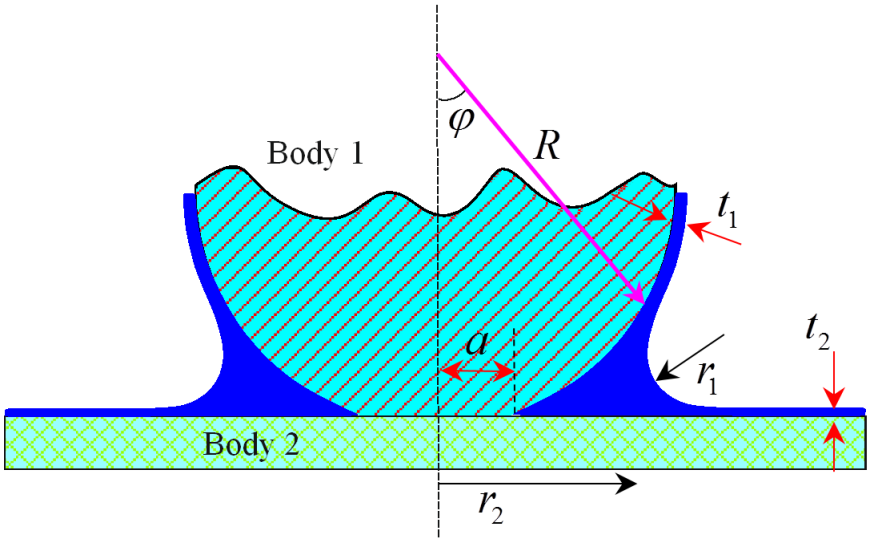

Figure A.8: Meniscus formation at a smooth ball-on-flat interface in the presence of an adsorbed water film.

The meniscus radii of curvature in the presence of a thin adsorbed water film with thickness of t_1 and t_2 on the ball and flat, respectively, can be simply obtained as:

$$r_1 = \frac{R(1-\cos\phi) - a^2/R - (t_1\cos\phi + t_2)}{1+\cos\phi} \tag{A.27a}$$

$$r_2 = R\sin\phi \tag{A.27b}$$

where a and ϕ are the contact radius and the meniscus filling angle, respectively. The term a^2/R counts as the normal indentation. Substituting Eq.A.27 in Eq.A.25 reads:

$$\frac{1}{R\sin\phi} - \frac{1+\cos\phi}{R(1-\cos\phi) - a^2/R - (t_1\cos\phi + t_2)} = \frac{R_g T}{\gamma V}\log RH \tag{A.28}$$

Solving this equation for the filling angle, ϕ, gives the capillary force as:

$$F_{cap} = \pi\left(R^2\sin^2\phi - a^2\right)\Delta P_{cap} \tag{A.29}$$

It is worth noting that the contact radius, a, in Eq.A.28 is unknown and dependent on the capillary force (and the filling angle) as well as some other parameters which needs to be numerically obtained.

Appendix B

LEVELING OF A THIN LIQUID FILM

This appendix presents the numerical procedure to solve the leveling problem of a thin liquid film on a rough surface. Given the rough profile as $h_s(x, y)$ and the initial uniform film thickness as e_0, the dynamics of this problem expresses the height of the film free surface, $h_w(x, y, t)$, as [86]:

$$\begin{aligned}\frac{\partial h_w}{\partial t} = &-\frac{\gamma}{3\eta}\frac{\partial}{\partial x}\left[(h_w - h_s)^3\left(\frac{\partial^3 h_w}{\partial x^3} + \frac{\partial^3 h_w}{\partial x \partial y^2}\right)\right] \\ &-\frac{\gamma}{3\eta}\frac{\partial}{\partial y}\left[(h_w - h_s)^3\left(\frac{\partial^3 h_w}{\partial y^3} + \frac{\partial^3 h_w}{\partial y \partial x^2}\right)\right]\end{aligned} \tag{B.1}$$

where the initial condition is given by:

$$h_w(x, y, t = 0) = h_s(x, y) + e_0 = h_{w_0} \tag{B.2}$$

Eq. B.1 can be summarized as:

$$\frac{\partial h_w}{\partial t} = f(t, h_w) = c_0\left(D_x + D_y\right) \tag{B.3}$$

with $c_0 = -\gamma/3\eta$ and:

$$D_x = \frac{\partial}{\partial x}\left[(h_w - h_s)^3\left(\frac{\partial^3 h_w}{\partial x^3} + \frac{\partial^3 h_w}{\partial x \partial y^2}\right)\right] \tag{B.4a}$$

$$D_y = \frac{\partial}{\partial y}\left[(h_w - h_s)^3\left(\frac{\partial^3 h_w}{\partial y^3} + \frac{\partial^3 h_w}{\partial y \partial x^2}\right)\right] \tag{B.4b}$$

The 4th-order Runge-Kutta scheme can be implemeneted to solve the ordinary differential equation of Eq. B.3 with the suitable time increment of s as:

$$h_{w_{n+1}} = h_{w_n} + \frac{1}{6}\left(k_1 + 2k_2 + 2k_3 + k_4\right) \tag{B.5a}$$

$$t_{n+1} = t_n + s \tag{B.5b}$$

for $n = 0, 1, 2, ...$, where:

$$k_1 = s\ f(t_n, h_{w_n}) \tag{B.6a}$$

$$k_2 = s\ f\left(t_n + \frac{s}{2}, h_{w_n} + \frac{k_1}{2}\right) \tag{B.6b}$$

$$k_3 = s\ f\left(t_n + \frac{s}{2}, h_{w_n} + \frac{k_2}{2}\right) \tag{B.6c}$$

$$k_4 = s\ f\left(t_n + s, h_{w_n} + k_3\right) \tag{B.6d}$$

An important step in solving Eq. B.3 is to evaluate the f function, or equivalently D_x and D_y, at each time step. For a rough substrate, assuming a periodic solution for h_w at each step, the derivative property of the Fourier transform can be exploited to convert the complex derivatives of Eq. B.1 to algebraic values in the frequency domain. This property states that for a function $g(x)$:

$$\mathcal{F}[g(x)] = G(\omega) \rightarrow \mathcal{F}[\frac{dg}{dx}] = j\omega G(\omega) \tag{B.7}$$

where $\mathcal{F}$ is the Fourier transform operator. ω and j are the radial frequency and the imaginary unity, respectively.
Another property of the Fourier transform that is used here is the convolution property, stating that for functions $g_1(x)$ and $g_2(x)$:

$$\mathcal{F}[g_1(x)\ g_2(x)] = G_1(\omega) * G_2(\omega) \tag{B.8}$$

where the symbol $*$ means convolution. This property means that the Fourier transform of the product of two functions is the convolution of their individual Fourier transform.

Now, the derivative and convolution properties of the Fourier transform are implemented to simplify the D_x and D_y functions in the frequency domain as:

$$\mathcal{F}[D_x] = j\omega_x \left[(H_w - H_s) * (H_w - H_s) * (H_w - H_s) * \left(-j\omega_x(\omega_x^2 + \omega_y^2)H_w\right)\right] \tag{B.9a}$$
$$\mathcal{F}[D_y] = j\omega_y \left[(H_w - H_s) * (H_w - H_s) * (H_w - H_s) * \left(-j\omega_y(\omega_x^2 + \omega_y^2)H_w\right)\right] \tag{B.9b}$$

in which H_w and H_s are the Fourier transform of h_w and h_s. Moreover, ω_x and ω_y are the radial frequencies corresponding to the x and y directions in the spatial domain.

At this stage, suppose that the discretized rough profile of h_s of length L is given by a square matrix of N^2 elements and so does the h_{w_0}. Therefore, h_w also has the same size. The frequency range for $-L/2 < x, y < L/2$ is then, $-2\pi N/L < \omega_x, \omega_y < 2\pi N/L$.

The main step in the leveling problem is to evaluate $f(t, h_w)$ at each time step. Due to its complex structure, it has been simplified in the frequency domain. Therefore, it is evaluated in this domain, or simply $\mathcal{F}[D_x]$ and $\mathcal{F}[D_y]$ need to be calculated and then at each step:

$$f(t, h_w) = c_0 \, \mathcal{F}^{-1} \left[\mathcal{F}[D_x] + \mathcal{F}[D_y]\right] \tag{B.10}$$

in which $\mathcal{F}^{-1}$ is the inverse Fourier transform operator.

Bibliography

[1] F. Bowden and D. Tabor, *The Friction and Lubrication of Solids*. New York: Oxford University Press, 1950.

[2] D. Dowson, *History of Tribology*. London, New York: Longman, 1978.

[3] B. Bhushan, *Introduction to Tribology*. Wiley, 2nd ed., 2013.

[4] J. Greenwood and J. Williamson, "Contact of Nominally Flat Surfaces," *Proceedings of the Royal Society of London. Series A. Mathematical and Physical Sciences*, vol. 295, no. 1442, pp. 300–319, 1966.

[5] A. W. Bush, R. D. Gibson, and T. R. Thomas, "The elastic contact of a rough surface," *Wear*, vol. 35, no. 1, pp. 87–111, 1975.

[6] J. I. McCool, "Non-Gaussian effects in microcontact," *International Journal of Machine Tools and Manufacture*, vol. 32, no. 1, pp. 115–123, 1992.

[7] J. A. Greenwood, "A simplified elliptic model of rough surface contact," *Wear*, vol. 261, no. 2, pp. 191–200, 2006.

[8] G. Carbone and F. Bottiglione, "Asperity contact theories: Do they predict linearity between contact area and load?," *Journal of the Mechanics and Physics of Solids*, vol. 56, no. 8, pp. 2555–2572, 2008.

[9] G. Carbone, "A slightly corrected Greenwood and Williamson model predicts asymptotic linearity between contact area and load," *Journal of the Mechanics and Physics of Solids*, vol. 57, no. 7, pp. 1093–1102, 2009.

[10] M. Ciavarella, J. A. Greenwood, and M. Paggi, "Inclusion of "interaction" in the Greenwood and Williamson contact theory," *Wear*, vol. 265, no. 5-6, pp. 729–734, 2008.

[11] S. Chandrasekar, M. Eriten, and A. A. Polycarpou, "An Improved Model of Asperity Interaction in Normal Contact of Rough Surfaces," *Journal of Applied Mechanics*, vol. 80, no. 1, p. 011025, 2012.

[12] A. I. Vakis, "Asperity Interaction and Substrate Deformation in Statistical Summation Models of Contact Between Rough Surfaces," *Journal of Applied Mechanics*, vol. 81, no. 4, p. 041012, 2013.

[13] M. Ciavarella, "A Comment on "Meeting the Contact-Mechanics Challenge" by Muser et al. [1]," *Tribology Letters*, vol. 66, no. 1, pp. 18–20, 2018.

[14] R. Heise and V. L. Popov, "Adhesive contribution to the coefficient of friction between rough surfaces," *Tribology Letters*, vol. 39, no. 3, pp. 247–250, 2010.

[15] W. Zhang, F. Jin, S. Zhang, and X. Guo, "Adhesive Contact on Randomly Rough Surfaces Based on the Double-Hertz Model," *Journal of Applied Mechanics*, vol. 81, no. 5, p. 051008, 2013.

[16] G. Haiat and E. Barthel, "An approximate model for the adhesive contact of rough viscoelastic surfaces," *Langmuir*, vol. 23, no. 23, pp. 11643–11650, 2007.

[17] P. Sahoo, A. Mitra, and K. Saha, "Elastic-plastic adhesive contact of rough surfaces using n-point asperity model," *Journal of Physics D: Applied Physics*, vol. 42, no. 6, 2009.

[18] G. G. Adams and M. Nosonovsky, "Contact modeling - forces," *Tribology International*, vol. 33, no. 5, pp. 431–442, 2000.

[19] M. Ciavarella, "A very simple estimate of adhesion of hard solids with rough surfaces based on a bearing area model," *Meccanica*, pp. 1–10, 2017.

[20] Z. Song and K. Komvopoulos, "Adhesive contact of an elastic semi-infinite solid with a rigid rough surface: Strength of adhesion and contact instabilities," *International Journal of Solids and Structures*, vol. 51, no. 6, pp. 1197–1207, 2014.

[21] P. Prokopovich and V. Starov, "Adhesion models: From single to multiple asperity contacts," *Advances in Colloid and Interface Science*, vol. 168, no. 1-2, pp. 210–222, 2011.

[22] S. You and M. P. Wan, "Mathematical models for the van der waals force and capillary force between a rough particle and surface," *Langmuir*, vol. 29, no. 29, pp. 9104–9117, 2013.

[23] N. Zarate, A. Harrison, J. Litster, and S. Beaudoin, "Effect of relative humidity on onset of capillary forces for rough surfaces," *Journal of Colloid and Interface Science*, vol. 411, pp. 265–272, 2013.

[24] M. P. Boer, "Capillary adhesion between elastically hard rough surfaces," *Experimental Mechanics*, vol. 47, no. 1, pp. 171–183, 2007.

[25] Y. F. Peng, Y. B. Guo, and Y. Q. Hong, "An Adhesion Model for Elastic-Contacting Fractal Surfaces in the Presence of Meniscus," *Journal of Tribology*, vol. 131, no. 2, p. 024504, 2009.

[26] P. Lu and S. J. O'Shea, "Mechanical contact between rough surfaces at low load," *Journal of Physics D: Applied Physics*, vol. 45, no. 47, 2012.

[27] H. M. Stanley and T. Kato, "An FFT-Based Method for Rough Surface Contact," *Journal of Tribology*, vol. 119, no. 3, pp. 481–485, 1997.

[28] B. N. Persson, "Contact mechanics for randomly rough surfaces," *Surface Science Reports*, vol. 61, no. 4, pp. 201–227, 2006.

[29] B. N. Persson, "Adhesion between an elastic body and a randomly rough hard surface," *European Physical Journal E*, vol. 8, no. 4, pp. 385–401, 2002.

[30] B. N. J. Persson, "Theory of rubber friction and contact mechanics," *The Journal of Chemical Physics*, vol. 115, no. 8, pp. 3840–3861, 2001.

[31] B. N. J. Persson and M. Scaraggi, "Theory of adhesion: Role of surface roughness," *Journal of Chemical Physics*, vol. 141, no. 12, pp. 1–18, 2014.

[32] W. B. Dapp, N. Prodanov, and M. H. Müser, "Systematic analysis of Persson's contact mechanics theory of randomly rough elasticsurfaces," *Journal of Physics Condensed Matter*, vol. 26, no. 35, 2014.

[33] C. Campañá and M. H. Müser, "Contact mechanics of real vs. randomly rough surfaces: A Green's function molecular dynamics study," *Europhysics Letters (EPL)*, vol. 77, no. 3, p. 38005, 2007.

[34] S. Hyun, L. Pei, J. F. Molinari, and M. O. Robbins, "Finite-element analysis of contact between elastic self-affine surfaces," *Physical Review E - Statistical Physics, Plasmas, Fluids, and Related Interdisciplinary Topics*, vol. 70, no. 2, p. 12, 2004.

[35] L. Pei, S. Hyun, J. F. Molinari, and M. O. Robbins, "Finite element modeling of elasto-plastic contact between rough surfaces," *Journal of the Mechanics and Physics of Solids*, vol. 53, no. 11, pp. 2385–2409, 2005.

[36] V. A. Yastrebov, J. Durand, H. Proudhon, and G. Cailletaud, "Rough surface contact analysis by means of the Finite Element Method and of a new reduced model," *Comptes Rendus - Mecanique*, vol. 339, no. 7-8, pp. 473–490, 2011.

[37] S. Hyun and M. O. Robbins, "Elastic contact between rough surfaces: Effect of roughness at large and small wavelengths," *Tribology International*, vol. 40, no. 10-12 SPEC. ISS., pp. 1413–1422, 2007.

[38] R. A. Sauer, "A Survey of Computational Models for Adhesion," *The Journal of Adhesion*, vol. 92, no. 2, pp. 81–120, 2015.

[39] R. A. Sauer and S. Li, "An atomic interaction-based continuum model for adhesive contact mechanics," *Finite Elements in Analysis and Design*, vol. 43, no. 5, pp. 384–396, 2007.

[40] R. A. Sauer and P. Wriggers, "Formulation and analysis of a three-dimensional finite element implementation for adhesive contact at the nanoscale," *Computer Methods in Applied Mechanics and Engineering*, vol. 198, no. 49-52, pp. 3871–3883, 2009.

[41] R. A. Sauer, "A Computational Model for Nanoscale Adhesion between Deformable Solids and Its Application to Gecko Adhesion," *Journal of Adhesion Science and Technology*, vol. 24, no. 11-12, pp. 1807–1818, 2010.

[42] C. Campana and M. H. Muser, "Practical Green's function approach to the simulation of elastic semi-infinite solids," *Physical Review B - Condensed Matter and Materials Physics*, vol. 74, no. 7, pp. 1–15, 2006.

[43] N. Prodanov, W. B. Dapp, and M. H. Müser, "On the Contact Area and Mean Gap of Rough, Elastic Contacts: Dimensional Analysis, Numerical Corrections, and Reference Data," *Tribology Letters*, vol. 53, no. 2, pp. 433–448, 2014.

[44] M. H. Muser, W. B. Dapp, R. Bugnicourt, P. Sainsot, N. Lesaffre, T. A. Lubrecht, B. N. Persson, K. Harris, A. Bennett, K. Schulze, S. Rohde, P. Ifju, W. G. Sawyer, T. Angelini, H. Ashtari Esfahani, M. Kadkhodaei, S. Akbarzadeh, J. J. Wu, G. Vorlaufer, A. Vernes, S. Solhjoo, A. I. Vakis, R. L. Jackson, Y. Xu, J. Streator, A. Rostami, D. Dini, S. Medina, G. Carbone, F. Bottiglione, L. Afferrante, J. Monti, L. Pastewka, M. O. Robbins, and J. A. Greenwood, "Meeting the Contact-Mechanics Challenge," *Tribology Letters*, vol. 65, no. 4, 2017.

[45] M. H. Muser, "A dimensionless measure for adhesion and effects of the range of adhesion in contacts of nominally flat surfaces," *Tribology International*, vol. 100, pp. 41–47, 2016.

[46] L. Pastewka and M. O. Robbins, "Contact between rough surfaces and a criterion for macroscopic adhesion.," *Proceedings of the National Academy of Sciences of the United States of America*, vol. 111, no. 9, pp. 3298–303, 2014.

[47] C. Putignano, W. Dapp, and M. H. Müser, "A Green's Function Molecular Dynamics Approach to the Mechanical Contact between Thin Elastic Sheets and Randomly Rough Surfaces," *Biomimetics*, vol. 1, no. 1, p. 7, 2016.

[48] C. Yang, U. Tartaglino, and B. N. J. Persson, "A multiscale Molecular Dynamics approach to Contact Mechanics," *The European Physical Journal E*, vol. 58, pp. 47–58, 2006.

[49] S. Medina and D. Dini, "A numerical model for the deterministic analysis of adhesive rough contacts down to the nano-scale," *International Journal of Solids and Structures*, vol. 51, no. 14, pp. 2620–2632, 2014.

[50] M. H. Muser, "Single-asperity contact mechanics with positive and negative work of adhesion: Influence of finite-range interactions and a continuum description for the squeeze-out of wetting fluids," *Beilstein Journal of Nanotechnology*, vol. 5, no. 1, pp. 419–437, 2014.

[51] X. Tian and B. Bhushan, "A numerical three-dimensional model for the contact of rough surfaces by variational principle," *J. Tribol.*, vol. 1, no. January, 1996.

[52] K. L. Johnson, *Contact Mechanics*. Cambridge: Cambridge University Press, 1985.

[53] T. F. Conry and A. Seireg, "A Mathematical Programming Method for Design of Elastic Bodies in Contact," *Journal of Applied Mechanics*, no. 70, pp. 387–392, 1971.

[54] J. Kalker and Y. V. RANDEN, "A Minimum Principle for Frictionless Elastic Contact with Application to Non-Hertzian Half-Space Contact Problems," *Journal of Engineering Mathematics*, vol. 6, no. 2, pp. 193–206, 1972.

[55] C. Y. Poon and R. S. Sayles, "Numerical contact model of a smooth ball on an anisotropic rough surface," *Journal of Tribology*, vol. 116, no. 2, pp. 194–201, 1994.

[56] A. Kubo, T. Okamoto, and N. Kurokawa, "Contact Stress Between Rollers With Surface Irregularity," *Journal of Mechanical Design*, vol. 103, no. 2, p. 492, 1981.

[57] H. A. Francis, "The accuracy of plane strain models for the elastic contact of three-dimensional rough surfaces," *Wear*, vol. 85, no. 2, pp. 239–256, 1983.

[58] A. Brandt and A. Lubrecht, "Multilevel matrix multiplication and fast solution of integral equations," *Journal of Computational Physics*, vol. 90, pp. 348–370, oct 1990.

[59] I. A. Polonsky and L. M. Keer, "A numerical method for solving rough contact problems based on the multi-level multi-summation and conjugate gradient techniques," *Wear*, vol. 231, no. 2, pp. 206–219, 1999.

[60] T. Nogi and T. Kato, "Influence of a Hard Surface Layer on the Limit of Elastic Contact—Part I: Analysis Using a Real Surface Model," *Journal of Tribology*, vol. 119, no. July, pp. 493–500, 1997.

[61] S. Liu, Q. Wang, and G. Liu, "A versatile method of discrete convolution and FFT (DC-FFT) for contact analyses," *Wear*, vol. 243, no. 1-2, pp. 101–111, 2000.

[62] L. He and T. C. Ovaert, "Three-Dimensional Rough Surface Contact Model for Anisotropic Materials," *Journal of Tribology*, vol. 130, pp. 1–6, 2008.

[63] D. Nelias, E. Antaluca, V. Boucly, and S. Cretu, "A Three-Dimensional Semianalytical Model for Elastic-Plastic Sliding Contacts," *Journal of Tribology*, vol. 129, pp. 761–771, 2007.

[64] E. A. H. Vollebregt, "A new solver for the elastic normal contact problem using conjugate gradients, deflation, and an FFT-based preconditioner," *Journal of Computational Physics*, vol. 257, pp. 331–351, 2014.

[65] T. jian Wang, L. qin Wang, L. Gu, and X. li Zhao, "Numerical analysis of elastic coated solids in line contact," *Journal of Central South University*, vol. 22, no. 7, pp. 2470–2481, 2015.

[66] Z. J. Wang, W. Z. Wang, H. Wang, D. Zhu, and Y. Z. Hu, "Partial Slip Contact Analysis on Three-Dimensional Elastic Layered Half Space," *Journal of Tribology*, vol. 132, no. 2, p. 021403, 2010.

[67] K. Zhou, W. W. Chen, L. M. Keer, X. Ai, K. Sawamiphakdi, P. Glaws, and Q. J. Wang, "Multiple 3D inhomogeneous inclusions in a half space under contact loading," *Mechanics of Materials*, vol. 43, no. 8, pp. 444–457, 2011.

[68] R. Pohrt and Q. Li, "Complete Boundary Element Formulation for Normal and Tangential Contact Problems," *Physical Mesomechanics*, vol. 17, no. 4, pp. 334–340, 2014.

[69] A. Almqvist, C. Campañá, N. Prodanov, and B. N. Persson, "Interfacial separation between elastic solids with randomly rough surfaces: Comparison between theory and numerical techniques," *Journal of the Mechanics and Physics of Solids*, vol. 59, no. 11, pp. 2355–2369, 2011.

[70] V. A. Yastrebov, G. Anciaux, and J. F. Molinari, "On the accurate computation of the true contact-area in mechanical contact of random rough surfaces," *Tribology International*, vol. 114, no. December 2016, pp. 161–171, 2017.

[71] J. Q. Feng, "Contact behavior of spherical elastic particles: A computational study of particle adhesion and deformations," *Colloids and Surfaces A: Physicochemical and Engineering Aspects*, vol. 172, no. 1-3, pp. 175–198, 2000.

[72] Y. Yamamoto, M. Inui, and H. Koguchi, "Adhesion analysis considering van der waals force in a nanosized region using the boundary element method," *Tribology Letters*, vol. 53, no. 1, pp. 225–235, 2014.

[73] H. Koguchi and K. Seki, "BOUNDARY ELEMENT ANALYSIS OF ADHESION CONSIDERING VAN DER WAALS FORCE," in *Proceedings of the ASME 2013 International Mechanical Engineering Congress and Exposition*, 2013.

[74] G. Carbone, M. Scaraggi, and U. Tartaglino, "Adhesive contact of rough surfaces: Comparison between numerical calculations and analytical theories," *European Physical Journal E*, vol. 30, no. 1, pp. 65–74, 2009.

[75] V. Rey, G. Anciaux, and J.-F. Molinari, "Normal adhesive contact on rough surfaces: efficient algorithm for FFT-based BEM resolution," *Computational Mechanics*, vol. 60, no. 1, pp. 69–81, 2017.

[76] R. Bugnicourt, P. Sainsot, D. Dureisseix, C. Gauthier, and A. A. Lubrecht, "FFT-Based Methods for Solving a Rough Adhesive Contact: Description and Convergence Study," *Tribology Letters*, vol. 66, no. 1, pp. 1–12, 2018.

[77] J.-j. Wu, "Numerical Simulation on the Adhesive Contact between Rough Surfaces with Bi-Conjugate Gradient Stabilized Method," *Tribology Letters*, vol. 65, pp. 150–156, 2017.

[78] M. Bazrafshan, M. B. de Rooij, M. Valefi, and D. J. Schipper, "Numerical method for the adhesive normal contact analysis based on a Dugdale approximation," *Tribology International*, vol. 112, no. April, pp. 117–128, 2017.

[79] A. Rostami and J. L. Streator, "Study of liquid-mediated adhesion between 3D rough surfaces: A spectral approach," *Tribology International*, vol. 84, pp. 36–47, 2015.

[80] S. E. Orchard, "On surface levelling in viscous liquids and gels," *Applied Scientific Research, Section A*, vol. 11, no. 4-6, pp. 451–464, 1963.

[81] G. Ahmed, M. Sellier, Y. C. Lee, M. Jermy, and M. Taylor, "Rheological effects on the levelling dynamics of thin fluid films," *International Journal of Numerical Methods for Heat and Fluid Flow*, vol. 25, no. 8, pp. 1850–1867, 2015.

[82] F. Seeler, C. Hager, O. Tiedje, and M. Schneider, "Simulations and experimental investigation of paint film leveling," *Journal of Coatings Technology and Research*, vol. 14, pp. 767–781, jul 2017.

[83] M. H. Eres, D. E. Weidner, and L. W. Schwartz, "Three-Dimensional Direct Numerical Simulation of Surface-Tension-Gradient Effects on the Leveling of an Evaporating Multicomponent Fluid," *Langmuir*, vol. 15, pp. 1859–1871, mar 1999.

[84] D. E. Weidner, L. W. Schwartz, and R. R. Eley, "Role of surface tension gradients in correcting coating defects in corners," *Journal of Colloid and Interface Science*, 1996.

[85] L. W. Schwartz, R. V. Roy, R. R. Eley, and S. Petrash, "Dewetting patterns in a drying liquid film," *Journal of Colloid and Interface Science*, 2001.

[86] B. Figliuzzi, D. Jeulin, A. Lemaître, G. Fricout, J.-J. Piezanowski, and P. Manneville, "Numerical simulation of thin paint film flow," *Journal of Mathematics in Industry*, vol. 2, no. 1, p. 1, 2012.

[87] Cattaneo C., "Sul Contatto Di Due Corpi Elastici: Distribuzione Locale Degli Sforzi," *Atti Accad Naz Lincei*, vol. 27, pp. 342–348, 1938.

[88] R. Mindlin, "Compliance of elastic bodies in contact," *Journal of Applied Mechanics*, vol. 16, no. 1945, pp. 259–268, 1949.

[89] R. Mindlin and H. Deresiewicz, "Elastic Spheres in Contact Under Varying Oblique Force," *Journal of Applied Mechanics*, vol. 20, pp. 327–344, 1953.

[90] L. Kogut and I. Etsion, "A Semi-Analytical Solution for the Sliding Inception of a Spherical Contact," *Journal of Tribology*, vol. 125, no. 3, pp. 499–506, 2003.

[91] R. H. Wang, V. K. Jain, and S. Mall, "A non-uniform friction distribution model for partial slip fretting contact," *Wear*, vol. 262, no. 5-6, pp. 607–616, 2007.

[92] T. Yue and M. Abdel Wahab, "Finite element analysis of fretting wear under variable coefficient of friction and different contact regimes," *Tribology International*, vol. 107, no. December 2016, pp. 274–282, 2017.

[93] W. W. Chen, S. Liu, and Q. J. Wang, "Fast Fourier Transform Based Numerical Methods for Elasto-Plastic Contacts of Nominally Flat Surfaces," *Journal of Applied Mechanics*, vol. 75, no. 1, p. 011022, 2008.

[94] Z.-j. Wang, W.-z. Wang, F.-m. Meng, and J.-x. Wang, "Fretting Contact Analysis on Three-Dimensional Elastic Layered Half Space," *Journal of Tribology*, vol. 133, no. 3, p. 031401, 2011.

[95] L. Rodríguez-Tembleque, R. Abascal, and M. H. Aliabadi, "A boundary elements formulation for 3D fretting-wear problems," *Engineering Analysis with Boundary Elements*, vol. 35, no. 7, pp. 935–943, 2011.

[96] L. Gallego, D. Nélias, and S. Deyber, "A fast and efficient contact algorithm for fretting problems applied to fretting modes I, II and III," *Wear*, vol. 268, no. 1, pp. 208–222, 2010.

[97] J. Archard, "Elastic deformation and the laws of friction," *Proceedings of the Royal Society of London. Series A. Mathematical and Physical Sciences*, vol. 243, pp. 190 LP – 205, dec 1957.

[98] W. W. Chen and Q. J. Wang, "A numerical model for the point contact of dissimilar materials considering tangential tractions," *Mechanics of Materials*, vol. 40, no. 11, pp. 936–948, 2008.

[99] M. Paggi, R. Pohrt, and V. L. Popov, "Partial-slip frictional response of rough surfaces.," *Scientific reports*, vol. 4, p. 5178, 2014.

[100] B. Grzemba, R. Pohrt, E. Teidelt, and V. L. Popov, "Maximum micro-slip in tangential contact of randomly rough self-affine surfaces," *Wear*, vol. 309, no. 1-2, pp. 256–258, 2014.

[101] A. T. Kasarekar, N. W. Bolander, F. Sadeghi, and S. Tseregounis, "Modeling of fretting wear evolution in rough circular contacts in partial slip," *International Journal of Mechanical Sciences*, vol. 49, no. 6, pp. 690–703, 2007.

[102] S. C. Chen, P. J. Wei, and J. F. Lin, "A model developed for the adhesion forces formed between an atomic force microscopy tip and a rough surface under different humidity levels," *Japanese Journal of Applied Physics*, vol. 48, no. 5, pp. 0550011–0550015, 2009.

[103] O. T. Sari, G. G. Adams, and S. Muftu, "Nano-Scale Effects in the Sliding and Rolling of a Cylinder on a Substrate," *Journal of Applied Mechanics*, vol. 72, no. 5, p. 633, 2005.

[104] G. G. Adams, "Stick, partial slip and sliding in the plane strain micro contact of two elastic bodies.," *Royal Society open science*, vol. 1, no. 3, p. 140363, 2014.

[105] K. L. Johnson, K. Kendall, and A. D. Roberts, "Surface Energy and the Contact of Elastic Solids," *Proceedings of the Royal Society of London. Series A, Mathematical and Physical Sciences*, vol. 324, pp. 301–313, 1971.

[106] B. Derjaguin, V. Muller, and Y. Toporov, "Effect of contact deformations on the adhesion of particles," *Journal of Colloid and Interface Science*, vol. 53, no. 2, pp. 314–326, 1975.

[107] D. Tabor, "Surface forces and surface interactions," *Journal of Colloid and Interface Science*, vol. 58, no. 1, pp. 2–13, 1977.

[108] V. M. Muller, V. S. Yushchenko, and B. V. Derjaguin, "On the influence of molecular forces on the deformation of an elastic sphere and its sticking to a rigid plane," *Journal of Colloid and Interface Science*, vol. 77, pp. 91–101, 1980.

[109] D. Maugis, "Adhesion of spheres: The JKR-DMT transition using a dugdale model," *Journal of Colloid And Interface Science*, vol. 150, no. 1, pp. 243–269, 1992.

[110] J. A. Greenwood, "Adhesion of elastic spheres," *Proceedings of the Royal Society A: Mathematical, Physical and Engineering Sciences*, vol. 453, no. 1961, pp. 1277–1297, 1997.

[111] J.N. Israelachvili, *Intermolecular and surface forces*. Elsevier, 2013.

[112] F. W. DelRio, M. L. Dunn, and M. P. de Boer, "Capillary adhesion model for contacting micromachined surfaces," *Scripta Materialia*, vol. 59, no. 9, pp. 916–920, 2008.

Part II

Paper A

Numerical Method for the Adhesive Normal Contact Analysis Based on a Dugdale Approximation

M. Bazrafshan[1,2*], M.B. de Rooij[2], M. Valefi[3], and D.J. Schipper[2]

[1] *Materials innovation institute (M2i), P.O. box 5008, 2600GA, Delft, Netherlands*
[2] *Laboratory for Surface Technology and Tribology, Department of Engineering Technology, University of Twente, P.O. box 217, 7500AE, Enschede, Netherlands*
[3] *Research Department, ASML Netherlands B.V., De Run 6501, 5504DR Veldhoven, Netherlands*

Abstract

Modeling adhesion between two contacting surfaces plays a vital role in nano-tribology. However, providing analytical models, although desirable, is mostly impossible, in particular for complex geometries. Therefore, much attention has to be paid to numerical modeling of this phenomenon. Based on the adhesive stress description of the Maugis-Dugdale model of adhesion, which is credible over a broad range of engineering applications, an extended Conjugate Gradient Method (CGM) has been developed for adhesive contact problems. To examine the accuracy of the proposed method, the common case of the adhesive contact of a rigid sphere on an elastic half-space is investigated. To further evaluate the accuracy of this method, the adhesive contact of a rigid sphere over a wavy elastic half-space is also studied for different combinations of the amplitude and wavelength. There is good agreement between the analytical solution and the values predicted by the proposed method in the force-approach curves. Moreover, the calculation of pull-off force at a bisinusoidal interface between two surfaces is carried out for various cases to study the effects of different influential parameters including work of adhesion, elastic modulus, radius curvature at a crest, and the wavelength ratio. A curve is fitted on the calculated pull-off force in order to express it as an analytical relation. Similar to the JKR and DMT expressions for the pull-off force of a rigid ball on an elastic half-plane, the fitted curve is not affected by the elastic modulus and is linearly dependent on the radius of curvature and the work of adhesion. In addition, a power law governs the relation between pull-off force and the wavelength ratio. In the end, it is shown that roughness can either increase or decrease the adhesive force at a rough interface depending on the degree of the roughness.

Keywords: Adhesion, Numerical modeling, Conjugate Gradient Method, Pull-off force, Roughness

1 Introduction

Adhesion plays a significant role in several technological fields and serves as one of the main reliability issues while dealing with smooth surfaces in contact under relatively low normal loads such as the case of micro/nano

devices [1, 2]. The early research on adhesion in contact mechanics was done by Bradley who studied the adhesive contact of rigid spheres [3]. Later on, two opposing classical theories of adhesion, JKR [4], and DMT [5], for single spherical elastic contacts were presented. Although these two models take different approaches and make significantly different assumptions, they are both true. It was shown by Tabor that these two models are the two opposite extreme limits of a single theory characterized by the Tabor parameter [6]:

$$\mu = (\frac{R\Delta\gamma^2}{E^{*2}z_0^2})^{1/3} \tag{1}$$

where $R, \Delta\gamma, E^*, z_0$ are the radius of the sphere, work of adhesion, the effective elastic modulus, and the equilibrium separation. The JKR model is valid for large values of the Tabor parameter, as in the case of large and compliant contacts. The DMT model, however, is suitable for low values of this parameter, as for small and stiff contacts. Following these two models, Muller et al developed a numerical solution to the adhesion interaction by integrating the Lennard-Jones potential and characterized the transition from DMT to JKR by adjusting the Tabor parameter [7]. Subsequently, Maugis provided a solution to this contact problem through assuming the contribution of adhesion inside and outside the contact area, by means of a Dugdale approximation and is known as Maugis-Dugdale (MD) model [8]. Based on the MD model, Johnson and Greenwood constructed an adhesion map for the contact of elastic spheres [9, 10]. Although the mentioned analytical models provide exact solutions to the adhesion problem, they are limited to simple and smooth geometries. Thus, researchers have resorted to numerical approaches for surfaces with a more complex geometry [11–13]. Several authors have attempted to numerically evaluate the adhesion between two rough surfaces through multi-asperity and finite element approaches. In multi-asperity models, the surface is described merely in terms of the summit geometry and the rest of the surface is discarded [14–16]. As the main limitation of this model, next to the simplified summit geometry, is the assumption of a Gaussian distribution of roughness height, which is not valid for many engineering applications, different height distributions have been implemented, all of which still have the limitation to a specific application [16–19]. Finite element models for adhesive contact problems, incorporating the Lennard-Jones potential into the framework of nonlinear continuum mechanics, have also been

developed [20, 21].

The roughness of a surface could be described by means of surface models, such as fractals and Fourier transforms [22–25]. In these cases, numerical simulation of an adhesive contact has been considered while taking into account the regenerated topography of the contacting surfaces and not the original topography as it is measured. Here, the measured topography of a surface can be different from the roughness details regenerated or approximated by stochastic parameters. Consequently, since the adhesion force is a function of the exact local distance between the asperities of the two contacting surfaces, changing this distance influences the corresponding local adhesive force, and thus, deviation in the adhesive behavior is expected. Therefore, the core purpose of the current study is to develop a numerical adhesive contact solver between two elastic surfaces without any assumption on or restriction to the topography of the surfaces. Restricting ourselves to this goal, the Conjugate Gradient Method (CGM) is considered. CGM is a fast and accurate numerical algorithm typically implemented for a system of linear equations and is often used in an iterative scheme [26]. Polonsky and Keer first implemented this method for non-adhesive normal contact problems [27]. Ever since, this method has been extensively exploited for various non-adhesive contact problems in order to determine the normal and tangential contact stresses and contact area [28–33].

In the present study, the CGM is extended to include a Dugdale approximation, similar to MD model of adhesion, for the adhesive stress. In this way, it is used for the adhesive contact analysis between two elastic bodies with a general complex surface geometry.

2 Adhesive parameters

Maugis represented the surface force in terms of a Dugdale cohesive zone and stated that adhesion is present up to a specific value of the separation between the two contacting bodies, named h_0. Within this separation, the attractive pressure of σ_0, which is the maximum attractive pressure of Lennard-Jones potential, is applied such that [8]:

$$\Delta\gamma = \sigma_0 h_0, \quad \sigma_0 = \frac{16\Delta\gamma}{9\sqrt{3}z_0} \tag{2}$$

This results in $h_0 = 9\sqrt{3}z_0/16 = 0.974z_0$. In the equation above, z_0 is the equilibrium separation, ranging from $0.2nm$ to $0.4nm$. Based on the

definition of the MD model, the pressure inside the contact region is the superposition of the positive Hertzian pressure of radius a and the negative adhesive pressure. Outside the contact region, the attractive pressure is constant over a ring of inner and outer radii of a and c, in which:

$$separation = \begin{cases} 0 & at \quad r = a \\ h_0 & at \quad r = c \end{cases} \tag{3}$$

The Dugdale stress, $-\sigma_0$, and the maximum separation, h_0, are the two adhesive parameters that will be used in the proposed algorithm for the adhesive normal contact between two bodies.

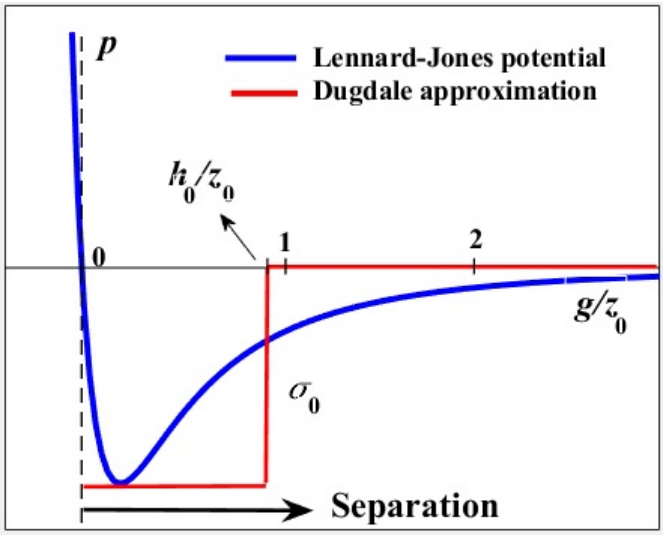

Figure 1: Dugdale approximation (red line) of Lennard-Jones potential (blue line)

3 Problem definition

When two rough surfaces are brought into contact, the generated normal stress (pressure) deforms the surfaces. The composite deformation of the two surfaces, $u(x, y)$ due to the applied pressure, $P(x, y)$, over the region Ω is given by:

$$u(x, y) = \int_{\Omega} k(x - \zeta, y - \eta) P(\zeta, \eta) d\zeta d\eta \tag{4}$$

where x and y are the spatial coordinates and $k(x, y)$ is the Boussinesq kernel function and is expressed as [34]:

$$k(x,y) = \frac{1}{\pi E^*} \frac{1}{\sqrt{x^2+y^2}}, \quad \frac{1}{E^*} = \frac{1-\nu_1^2}{E_1} + \frac{1-\nu_2^2}{E_2} \tag{5}$$

in which $E_i, \nu_i, i = 1, 2$ are the elastic moduli and Poisson ratios of the two contacting surfaces. If the separation between these two surfaces before and after the deformation are denoted by $h(x, y)$ and $g(x, y)$, they can be related to the deformation as:

$$g(x,y) = u(x,y) + h(x,y) - \delta \tag{6}$$

where δ is the rigid approach of the two surfaces (Fig. 2). The non-adhesive contact problem necessitates the pressure to be positive at contacting areas, where there is no separation between the two surfaces (where $g(x, y) = 0$). On the other hand, at separated areas (where $g(x, y) > 0$), the pressure must be zero. Moreover, the pressure distribution must balance the applied normal load, F_0. In other words:

$$P(x,y) > 0 \quad at \quad g(x,y) = 0 \tag{7a}$$

$$P(x,y) = 0 \quad at \quad g(x,y) > 0 \tag{7b}$$

$$\int_\Omega P(x,y)dxdy = F_0 \tag{7c}$$

The adhesive contact problem is, nevertheless, different from the definition by Eq. (7). For an adhesive contact problem, there is a negative stress between separated areas described by the Lennard-Jones potential as an explicit function of the local separation. As stated in the previous section, the MD model of adhesion assumes this dependence to be a step function of the local separation (by means of a Dugdale approximation of the Lennard-Jones expression). Based on this description, the negative stress due to adhesion at separated areas is a constant value ($-\sigma_0$, the Dugdale stress which is the maximum negative stress of the Lennard-Jones potential) as long as the local separation does not exceed a specific value (named h_0 as defined in the previous section). At all other separated areas, there is no adhesive stress. It is also important to note that the pressure may take negative values at contacting areas but it is never smaller than $-\sigma_0$ (therefore, the pressure transition between contacting and separate areas is continuous). This model could be mathematically summarized as:

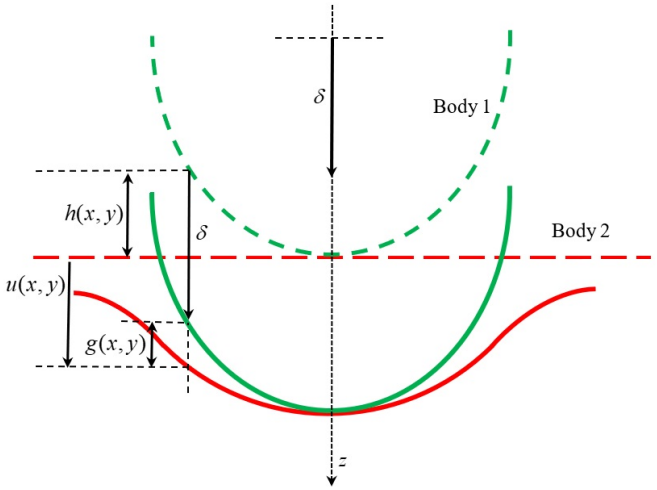

Figure 2: The normal contact between two bodies; undeformed (dash lines) and deformed (solid lines)

$$P(x,y) > -\sigma_0 \quad at \quad g(x,y) = 0 \tag{8a}$$
$$P(x,y) = -\sigma_0 \quad at \quad 0 < g(x,y) < h_0 \tag{8b}$$
$$P(x,y) = 0 \quad at \quad g(x,y) > h_0 \tag{8c}$$
$$\int_\Omega P(x,y)dxdy = F_0 \tag{8d}$$

The aim of the current study is to solve Eq. (8) for $P(x, y)$ at a general topography between two surfaces provided that the geometry of the contacting bodies ($h(x, y)$), the normal load (F_0), the mechanical properties (E and ν), and the work of adhesion ($\Delta\gamma$) are all known.

4 Numerical technique

As it was stated before, providing an analytical solution for the problem defined in previous section is only limited to simple geometries and therefore, this section aims at developing a numerical algorithm for more complex geometries.

4.1 Discretization

The first step to numerically solve Eq. (8) is to discretize the calculation area. Thus, the area Ω is divided into N^2 rectangular surface elements with grid sizes of Δx and Δy. Therefore, one can assume a piecewise constant function within each surface element for the contact pressure distribution. The discrete form of the convolution integral of Eq. (4) is then given by:

$$u_{ij} = \sum_{k=1}^{N} \sum_{l=1}^{N} K_{i-k,j-l} p_{kl} \quad i,j = 1,2,...,N \tag{9}$$

where u_{ij} is the surface deformation at node (i,j), p_{kl} is the uniform pressure acting upon the element centered at node (k,l), and K_{ij} are the influence coefficients, expressed as (x_i and y_j are the spatial coordinates of the node (i,j)):

$$K_{ij} = \int_{-\Delta x/2}^{\Delta x/2} \int_{-\Delta y/2}^{\Delta y/2} k(x_i - \xi, y_j - \eta) d\eta d\xi \quad i,j = 1,2,...,N \tag{10}$$

In practice, the DC-FFT algorithm developed by Liu et al can be used to evaluate the linear convolution of Eq. (9), efficiently [34]. If the FFT of K_{ij} and p_{ij} are respectively denoted by $\tilde{K}_{ij}$ and $\tilde{p}_{ij}$, the convolution summation of Eq. (9) is performed as follows:

$$u_{ij} = IFFT[\tilde{K}_{ij}.\tilde{K}_{ij}] \quad i,j = 1,2,...,N \tag{11}$$

where $IFFT$ stands for Inverse Fast Fourier Transform. This method has been used by many authors [35–37]. One should, however, note that the FFT-based convolution leads to periodicity errors which are, due to the non-periodic nature of the contact problem, more prominent close to the boundaries of the target area. One approach to minimize this error is to expand the calculation domain by zero-padding the applied pressure outside the target area. In the present study, where needed, the calculation domain is chosen to be 2 times greater than the target domain (contact domain) [34].

4.2 CGM-based iteration scheme

Due to the fact that the only inputs to the general elastic contact problem are mechanical properties, normal force, and contacting surfaces geometry, the aim of the non-adhesive contact problem is to find the set of grid points

pressure, p_{ij}, which satisfies the Kuhn-Tucker complementary conditions over the target area Ω:

$$p_{ij} \geq 0,\ g_{ij} \geq 0,\ p_{ij}g_{ij} = 0, \quad i,j = 1,2,...,N \tag{12}$$

Various methods have been proposed to solve this nonlinear optimization problem, among which, Conjugate Gradient Method (CGM) is regarded as one of the most prominent ones in terms of simplicity, accuracy, and convergence (readers are referred to [27] for details). To include the effect of adhesion, the definition of the mentioned problem, according to the adhesive stress description of MD model, must change as follows (the problem proposed in section 3 is here mimicked in the discrete format):

$$p_{ij} > -\sigma_0 \quad at \quad g_{ij} = 0 \tag{13a}$$
$$p_{ij} = -\sigma_0 \quad at \quad 0 < g_{ij} < h_0 \tag{13b}$$
$$p_{ij} = 0 \quad at \quad g_{ij} > h_0 \tag{13c}$$
$$\Delta x \Delta y \sum_{i=1}^{N}\sum_{j=1}^{N} = F_0 \tag{13d}$$

The following CGM algorithm is based on the one proposed by Polonsky and Keer [27]. However, in some steps, changes have been made to satisfy the conditions imposed by the presence of adhesion (described by Eq.(13)). The following procedure is an optimization algorithm to minimize the separation at contact nodes (defined as the objective function of the problem to be minimized). The whole process, as will be described, is summarized in Fig. 3 (the mathematical background of this algorithm is beyond the scope of this study and the readers are referred to [34] for details). The detailed description of this algorithm is provided next and is suitable for the readers who wish to implement it for computer programming.

Step 1. Set the initial pressure and balance the force using the approach presented in step 6. A constant pressure over the target area is a suitable initial choice.

Step 2. Initiate the iteration and calculate the deformation, u_{ij}, by means of Eq. (11) and set the separation and subtract its mean value as follows:

$$g_{ij} = u_{ij} + h_{ij} \tag{14a}$$

$$\bar{g} = \frac{1}{N_c} \sum_{(i,j)\in I_c} g_{ij} \tag{14b}$$

$$g_{ij} = g_{ij} - \bar{g} \tag{14c}$$

In the equation above, N_c is the number of nodes in the contact region, I_c, for which $p_{ij} > -\sigma_0$. To exclude the points with zero pressure but separation greater than h_0 from this definition for the contacting nodes, we later set the pressure at such nodes to a very high negative value such as $-1000\sigma_0$.

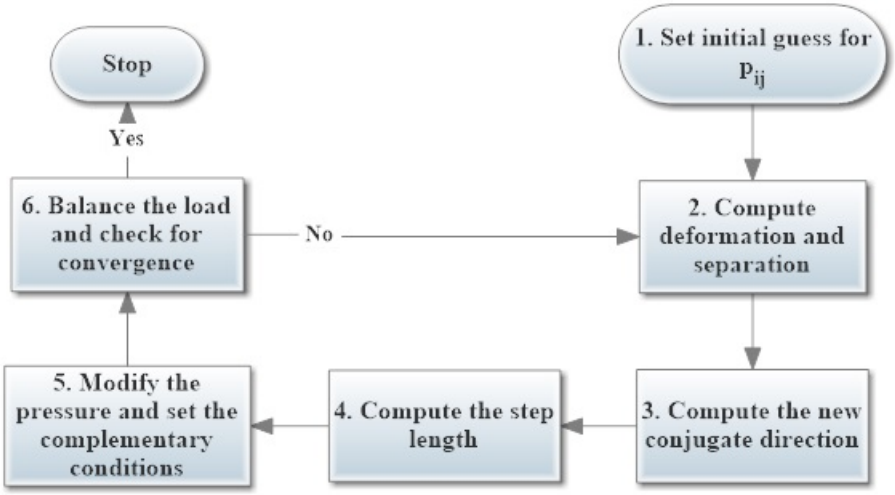

Figure 3: Numerical algorithm, the extended CGM

As stated by Polonsky and Keer, a precious feature of CG algorithm is the force balance which obviates the need for including the approach (also called penetration) between the two surfaces while computing the surface separation and therefore, enables the problem to be solved within only one level of iteration [27]. In other words, the approach is claimed to be $\bar{g}$, which is updated in each iteration.

Step 3. Compute the new conjugate direction t_{ij} as:

$$t_{ij} = g_{ij} + \delta \frac{G}{G_{old}} t_{ij}, \quad (i,j) \in I_c \tag{15}$$

where:

$$G = \sum_{(i,j)\in I_c} g_{ij}^2 \tag{16}$$

In this algorithm, the subscript old refers to the parameter value at the previous iteration. Therefore, G_{old} and δ are respectively set to 1 and 0 before the iteration starts.

Step 4. Store the current value of G for the next iteration by setting $G_{old} = G$. Then, do the following convolution and subtract the mean value of r_{ij} as follows:

$$r_{ij} = \sum K_{i-k,j-l} t_{kl} \tag{17a}$$

$$\bar{r} = \frac{1}{N_c} \sum_{(i,j)\in I_c} r_{ij} \tag{17b}$$

$$r_{ij} = r_{ij} - \bar{r} \tag{17c}$$

This convolution can be also carried out through Eq. (11). Then, calculate the step length, τ as:

$$\tau = \frac{\sum_{(i,j)\in I_c} g_{ij} t_{ij}}{\sum_{(i,j)\in I_c} r_{ij} t_{ij}} \tag{18}$$

Step 5. Store the current pressure, p_{ij} as $p_{ij_{old}}$ to be used in the next step for error estimation. At this stage, the pressure is updated by making a step in the direction t_{ij}:

$$p_{ij} = p_{ij} - \tau t_{ij}, \quad (i,j) \in I_c \tag{19}$$

Next, instead of setting all negative values of p_{ij} to zeros, as it is done for a non-adhesive elastic contact problem, set all $p_{ij} < -\sigma_0$ to $-\sigma_0$. Also, nodes with non-positive pressure and separation greater than h_0 must be set to $-1000\sigma_0$. Polonsky and Keer defined the overlap area as the set of all non-contacting nodes ($p_{ij} = 0$) at which separation is negative [27]. However, these nodes are defined here as the ones with negative pressure and separation:

$$I_{ol} = \{(i,j) : \ \ p_{ij} < 0, \ \ g_{ij} < 0\} \tag{20}$$

If $I_{ol} = \varnothing$, then $\delta = 1$. Otherwise, δ is set to zero and the following correction at these nodes is performed:

$$p_{ij} = p_{ij} - \tau g_{ij}, \quad (i,j) \in I_{ol} \tag{21}$$

Since τ is always positive, the nodes in overlap area will enter the contact region by this correction.

Step 6. To balance the force, in the general elastic contact problem, the total force, F is determined by multiplying the grid area by the summation of the pressure over the whole area and then, the pressure at this stage is multiplied by the ratio F_0/F, where F_0 is the external normal load. In the present algorithm, however, we seek to keep the constant negative pressure,$-\sigma_0$, unchanged. Therefore, before applying the multiplication, the constant value of $-\sigma_0$ is added to the pressure at nodes with non-zero pressure (shifted to zero) in order to keep the nodes with the constant negative pressure unaffected. Finally, the pressure is subtracted by beforehand added $-\sigma_0$:

$$c_p = \frac{F_0 + \Delta x \Delta y \sum_{p_{ij} > -\sigma_0} \sigma_0}{\Delta x \Delta y \sum_{p_{ij} > -\sigma_0} (p_{ij} + \sigma_0)} \tag{22a}$$

$$p_{ij} = c_p(p_{ij} + \sigma_0) - \sigma_0, \text{ at nodes with } p_{ij} > -\sigma_0 \tag{22b}$$

where Δx and Δy are the grid element sizes. It can be easily proven that Eq. (22) balances the force and the force corresponding the updated pressure distribution is the same as applied external one. Eventually, the relative error is estimated as:

$$\epsilon = \Delta x \Delta y \sum |p_{ij_{old}} - p_{ij}| \tag{23}$$

If the relative error is smaller than the specified tolerance, the iteration stops. Otherwise, another iteration must be performed. It should be noted that one must set all pressures less than $-\sigma_0$ to zero before calculating the deformation in step 2 and relative error in step 6. In the end, it is very important to note that since the CGM algorithm is based on minimizing the local separation at contact points as the residual, it is not necessary to

check whether this local separation is zero when the convergence is reached. In the present algorithm, the contribution of each element in the pressure distribution and deformation is considered separately and thus, there is no assumption in terms of the geometry. Therefore, this algorithm can be utilized at any geometry between two contacting bodies.

5 Numerical example

In this section, to demonstrate the accuracy of the proposed method, two cases, for which the analytical solutions are available in the literature, will be numerically investigated. First, the well-known case of the adhesive contact of a rigid sphere and a flat elastic half-space will be studied. And second, the contact of a rigid sphere over a wavy half-space will be investigated. Inserting the normal force and the geometry of the contacting surfaces into the algorithm, it is expected to predict the true contact pressure and radius and then other required outputs. For the first case, the problem reduces to original MD model of adhesion for a ball-on-flat contact.

5.1 Adhesive contact of a rigid sphere over a flat elastic half-space

In this section, the ball-on-flat contact will be numerically analyzed and the results including the contact pressure, contact radius, and the imposed approach of the two bodies are compared to their analytical counterparts provided in [38]. The geometry of the sphere, as one of the inputs to the numerical algorithm, is estimated to be a parabola (as long as $r << R$) as:

$$h = \frac{r^2}{2R} \tag{24}$$

in which r is the distance from the center of the contact plane and R is the sphere radius. The other input to the numerical algorithm is the external normal force. The analytical contact radius corresponding to this force is then determined. The calculation area is extended to 2 times farther than the analytical contact radius to minimize the periodicity error to an acceptable level (as described in [34]). The whole calculating area is divided into 512×512 uniform square elements for this example. The parameter values are chosen as $E = 73GPa,\ \nu = 0.17,\ R = 2.5mm$. Fig.

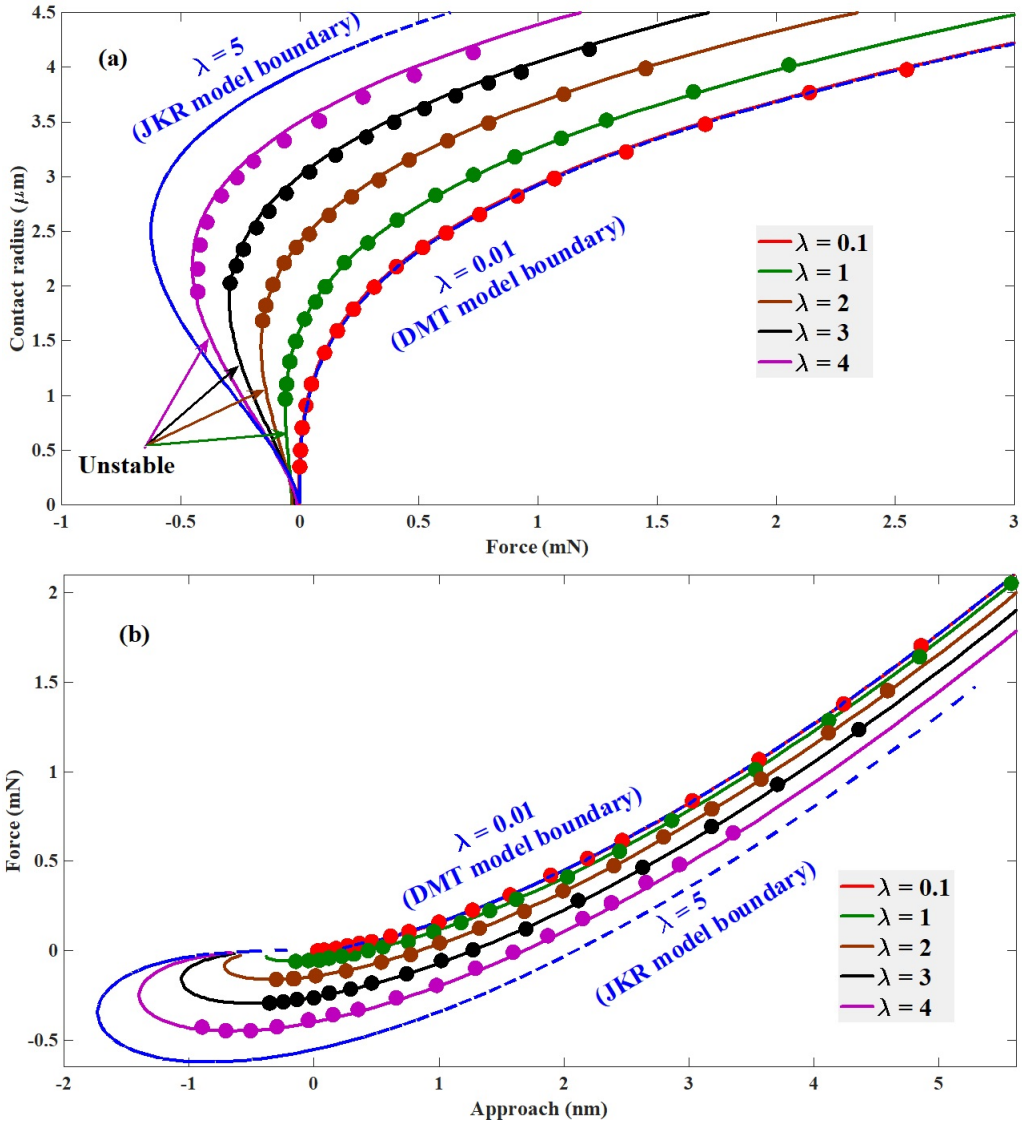

Figure 4: (a) Variation of contact radius with normal force, (b) Variation of normal force with approach, for different values of λ. Solid lines and dots are respectively due to the MD model and (current) numerical expressions for pressure

4(a) depicts the normal force vs. contact radius for various values of λ within the boundaries of JKR and DMT theories. Based on the nature of adhesion, when the normal force continuously goes down toward zero, the contact radius decreases as well, up to the point at which this force reaches zero. At this point, in contrast to the Hertzian contact model, the contact radius is non-zero. Following this trend (as shown in Fig. 4), applying a negative (pulling) force decreases the contact radius up to the complete separation of the contacting bodies. The (pulling) force required to separate the two bodies is named pull-off force. Further, the separation will be called jump-off since at this certain point, the molecular links between the surfaces of the bodies are abruptly broken (while the contact radius is still greater than zero). The reverse phenomenon, which is named jump-in and is literally unstable, occurs when the two bodies approach one another and at a certain separation, they jump into contact. As it is shown in Fig. 4(a), the proposed numerical approach is capable of tracking the contact behavior from a comparatively high applied force to jump-off point. However, due to its unstable nature of the contact under such conditions, this algorithm does not give a solution at the areas specified by arrows, which can be expected. This instability may also be interpreted through contact radius. It is apparent in Fig. 4(a) that for every negative force, there are two corresponding contact radii and only is the greater one stable due to its lower level of potential.
The other parameter to be evaluated is the approach. In [38], an analytical expression for this parameter as a function of contact radius was presented. Fig. 4(b) displays this relation for various values of λ. It is apparent that there is good agreement between the analytical curve and the values predicted by the numerical algorithm.

5.2 Adhesive contact of a rigid sphere over a wavy elastic half-space

In the following, the adhesive contact of a rigid sphere over a wavy elastic half-space is briefly investigated and the present numerical algorithm is employed to predict the analytical expressions provided for this problem. Fig. 5 depicts the geometry of the contact of a rigid sphere and a wavy elastic half-space. The total separation between these two surfaces is given by:

$$h(r) = \frac{r^2}{2R} + A\left(1 - \cos\frac{2\pi r}{\xi}\right) \tag{25}$$

where r, R, ξ, and A are the distance from the center of contact, the radius of sphere, the wavelength and the amplitude of the wavy surface, respectively. The governing equation to find the cohesive zone , based on MD model of adhesion, is as follows [39]:

$$\begin{aligned} 1 &= 2\lambda\bar{a}^2\left(\frac{\beta}{3}\right)^{2/3}[\sqrt{m^2-1}+(m^2-2)\tan^{-1}\sqrt{m^2-1}] \\ &+ \frac{8}{3}\lambda^2\bar{a}\left(\frac{\beta}{3}\right)^{1/3}[\sqrt{m^2-1}\tan^{-1}\sqrt{m^2-1}-m+1] \\ &+ 2\pi\lambda\alpha\left(\frac{\beta}{3}\right)^{2/3}[1-\cos 2\pi\bar{a}m-\pi^2\bar{a}H_0(2\pi\bar{a}) \\ &+ 2\pi\bar{a}H_0(2\pi\bar{a}\sin^{-1}\frac{1}{m}-2\pi\bar{a}\int_0^1\frac{tH_0(2\pi\bar{a}t)}{\sqrt{m^2-t^2}})] \end{aligned} \tag{26}$$

The dimensionless normal force and approach are expressed as:

$$\bar{P}_m(\bar{a}) = \bar{P}_1(\bar{a}) - 4\lambda\bar{a}^2\left(\frac{\beta}{3}\right)^{2/3}[\sqrt{m^2-1}+m^2\tan^{-1}\sqrt{m^2-1}], \tag{27}$$

$$\bar{\Delta}_m = \bar{a}^2 + \bar{a}\left[\pi^2\alpha H_0(2\pi\bar{a}) - 2\lambda\left(\frac{1}{9\beta}\right)^{1/3}\sqrt{m^2-1}\right] \tag{28}$$

where,$\bar{P}_1(\bar{a})$, the Hertzian contribution in normal force, is given by:

$$\bar{P}_1(\bar{a}) = 4\beta\left[\frac{2\bar{a}}{3}+\alpha\left(\frac{4\pi^2\bar{a}^3}{3}+\frac{\pi\bar{a}}{2}H_1(2\pi\bar{a})-\bar{a}^2H_2(2\pi\bar{a})\right)\right] \tag{29}$$

In Eqs. (26, 28-29), H_i is the Struve function of order i (the Struve functions are the solutions of the non-homogeneous Bessel's differential equation) and the following dimensionless parameters have been employed:

$$\bar{P} = \frac{P}{\pi\Delta\gamma R},\ \ \beta = \frac{\xi^3E^*}{2\pi\Delta\gamma R^2},\ \ \bar{a} = \frac{a}{\xi},\ \ \bar{\Delta} = \frac{\Delta R}{\xi^2},\ \ \alpha = \frac{AR}{\xi^2} \tag{30}$$

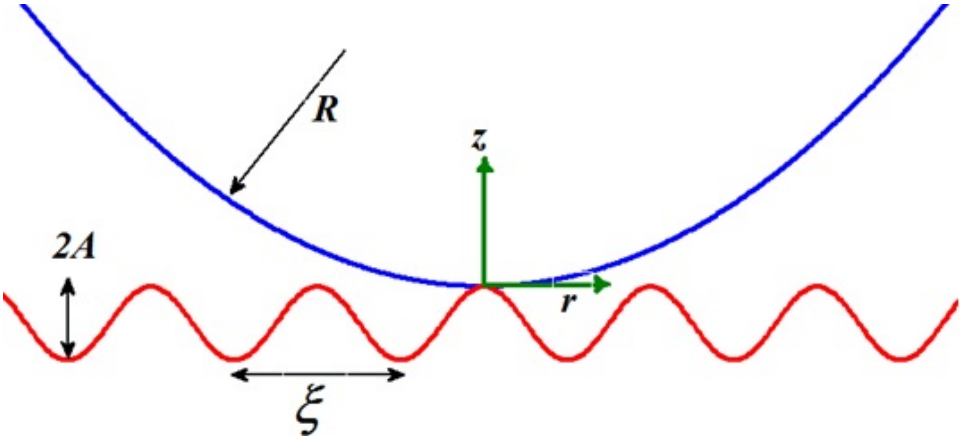

Figure 5: Schematic representation of the contact of a rigid sphere over a wavy elastic half-space

Eqs. (26-29) fully describe the MD adhesive contact problem between a rigid sphere and a wavy elastic half-space. Having in hand the external normal force, one must solve Eqs. (26-27) for m and $\bar{a}$, then, Eq. (28) is used to compute the normal approach (for more details refer to [39]).
To examine the accuracy of the present numerical algorithm, the external normal force and the geometrical characteristics of this type of contact are inserted into it and it is expected to predict the contact radius and approach given by the analytical expressions of Eqs. (26-29). The numerical values for parameters in this problem are considered the same as those of section 5.1. The wavelength of the wavy surface is also chosen to be $0.8\mu m$. Fig. 6 shows the variation of normal force with approach for different values of λ for three different geometries of the wavy surface, specified by $\alpha = 0.1$, $\alpha = 0.2$, and $\alpha = 0.3$. As it can be seen in this figure, there is good agreement between the analytical solution and results by the numerical algorithm. Again, for every negative force, similar to the case of the ball-on-flat contact, theoretically, there are more than one corresponding approaches, only one of which is physically stable and the numerical algorithm can only capture this stable state. This behavior is observable in Fig. 6 through a number of jumps in each curve. This phenomenon, which causes energy dissipation and toughening of the contact interface, indicates that models which assume reversible approach

and separation processes neglect a principal mechanism for interface toughening [39].

6 Pull-off force of a bisinusoidal interface

One of the simplest analytical representations for topography between two rough surfaces is the bisinusoidal profile which expresses a mono-modal distribution of asperities with two crossing rough waves. This combined interface could be created when one of the contacting surfaces is flat and the other one has a bisinusoidal roughness. For those tribological applications in which adhesion needs to be taken into account, providing a precise modeling is crucial. For detachment process, specifically, it is highly required to have an estimation of the pulling force needed to detach the contacting surfaces. This section aims at proposing an analytical expression for the pull-off force at a bisinusoidal interface as a function of mechanical and geometrical properties of the contacting bodies. This aim will be achieved through fitting a curve on the calculated pull-off forces by means of the developed numerical algorithm.

6.1 Geometry of a bisinusoidal interface

A typical bisinusoidal profile, with wavelengths λ_x and λ_y in x and y directions and amplitude S, is depicted in Fig. 7. It is worth noting that while adhering to the counter surface, the area in contact will be an ellipse whose dimensions are related to the wavelengths λ_x and λ_y (See [40] for more details). The height of this profile is described as:

$$h(x,y) = S\cos\left(\frac{2\pi x}{\lambda_x}\right)\cos\left(\frac{2\pi y}{\lambda_y}\right), \quad -\frac{\lambda_x}{2} < x < \frac{\lambda_x}{2},\ -\frac{\lambda_y}{2} < y < \frac{\lambda_y}{2} \tag{31}$$

It must be noted that since this profile is originally periodic, there is no need to expand the computation domain before using DFT. The effective radius of curvature of this profile is also expressed as:

$$R_c = \sqrt{R_x R_y} \tag{32}$$

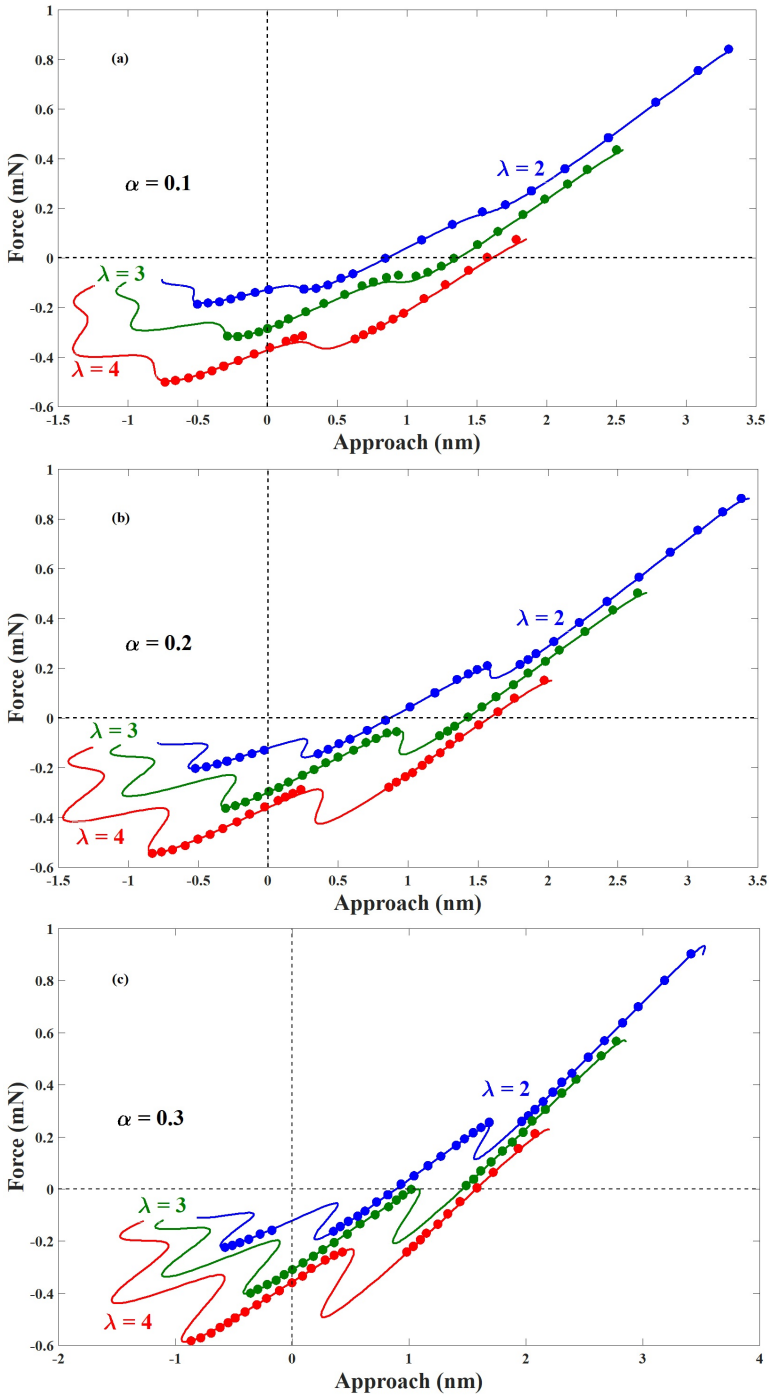

Figure 6: Variation of normal force with approach for different values of λ in the contact of a sphere over a wavy surface, (a) $\alpha = 0.1$, (b) $\alpha = 0.2$, (c) $\alpha = 0.3$. Solid lines and dots are respectively due to the M and (current) numerical expressions for pressure

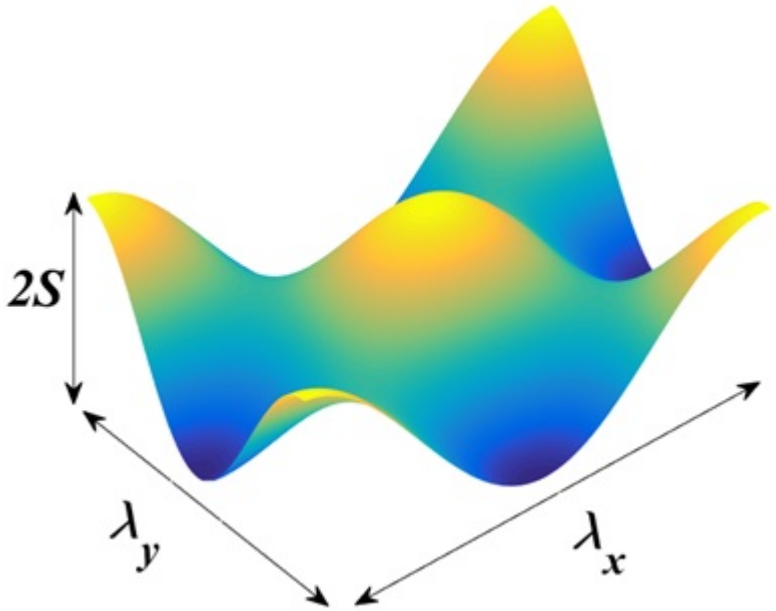

Figure 7: A typical bisinusoidal profile

where R_x and R_y are the radii of curvature in x and y directions, respectively and are obtained through the second derivative of the surface profile as [41]:

$$R_x = \frac{\lambda_x^2}{4\pi^2 S}, \quad R_y = \frac{\lambda_y^2}{4\pi^2 S} \tag{33}$$

The wavelength ratio is also defined as:

$$k = \frac{\lambda_y}{\lambda_x}, \quad \lambda_y \leq \lambda_x \tag{34}$$

6.2 Analysis

The pull-off condition that is dealt with in this section assumes the contact to be only at the crests. To include any possible effect of the mechanical and geometrical parameters on the pull-off force, various values are chosen for the work of adhesion, elastic modulus, radius of curvature at a crest, and the wavelength ratio. These values are presented in Table 1. It is very important to note that S, R_c, and k fully define a unique bisinusoidal interface geometry. Each of the parameters in Table 1 takes 5 different

Table 1: Parameter values for the calculation of pull-off force at a bisinusoidal interface, $S = 5nm$

Parameter	**Values**
$\Delta\gamma(mJ/m^2)$	30,40,50,60,70
$R(\mu m)$	100,200,300,400,500
$E^*(GPa)$	80,90,100,110,120
k	0.1,0.3,0.5,0.7,0.9

values. Therefore, there are $5^4 = 625$ different combinations of these parameters. One should, of course, note that the Tabor parameter for any of these combinations is within the MD boundaries. By means of the proposed numerical algorithm, the pull off force is calculated through generating the force-approach curve and finding the largest negative force on the curve for all these combinations.

6.3 Curve fitting on the pull-off force results

For the mentioned 625 different combinations of mechanical and geometrical parameters, presented in Table 1, the pull-off force at the bisinusoidal interface is calculated. At this stage, we aim at fitting a curve on these calculated values to express the pull-off force at such an interface as an explicit function of the mentioned parameters. The general form of the curve is chosen to be:

$$f_{pull-off} = aE^{*\beta}R_c^{1+\beta}\Delta\gamma^{1-\beta}k^b \tag{35}$$

where a, b, β are unknown constants to be identified. The powers of $E^*, R_c, \Delta\gamma$ terms are expressed as functions of β in such a way to keep the physical dimension in both sides the same, i.e. Newton. Through an optimization algorithm, one can find the optimum set of the mentioned constants which makes the general function of Eq. (35) fit best to the calculated pull-off forces. The resulting constants are presented in Table 2. The identified values imply that the pull-off force is not dependent on the effective elastic modulus of the contacting bodies. In addition, this pull-off force is linearly dependent on both radius of curvature and work of adhesion which is identical to the JKR and DMT predictions of the pull-off force of a rigid ball over an elastic half-space. For the contact of a sphere of

Table 2: Identified values for the unknown constants of Eq. (43) through Genetic Algorithm optimization algorithm

Parameter	β	a	b
value	0.0	10.390	0.041

radius R and a half-plane, if we define $f_{pull-off} = n_{model} R\Delta\gamma$, we will have $n_{JKR} = 3\pi/2 = 4.71$, $n_{DMT} = 2\pi = 6.28$ and $n_{JKR} < n_{MD} < n_{DMT}$ [41]. Similarly, considering the fact that the surface investigated in this section (Fig. 7) effectively includes 2 crests (1 in the center and 4 quarters in the corners), the mentioned linearity constant for a circular area in contact when $k = 1$, caused at a single crest, is $a/2 = 5.20$. Hence, for $k = 1$ we have $n_{JKR} < n_{MD}^{Bi-sinusoidal} < n_{DMT}$. This consistence ascertains the validity of the fitted curve. Further, this value implies that if this relation is used to estimate the pull-off force in case of very large or small values of the Tabor parameter (corresponding to the JKR and DMT theories, respectively), the absolute value for error will be 10.4% and 16.1%, respectively.

7 The roll of roughness in the contact pressure

As stated before, the proposed algorithm does not make any assumption about how roughness is distributed over the contacting surfaces. The roughness could be either a measured roughness or a generated surface texture. The former one is applicable when the surface roughness is measured, for instance, by an Atomic Force Microscope (AFM). The latter one could be implemented to design a surface roughness and study the effects of different roughness parameters such as rms, skewness, and kurtosis. In both cases, the proposed algorithm can be used to study the adhesive behavior. In this section, we aim at studying the effect of roughness rms on the adhesive contact between a smooth ball of radius $R_b = 100\mu m$ and a rough half-space. The method proposed by Hu and Tonder has been implemented to numerically generate a Gaussian rough surface [42]. The rough profile is first subtracted by its arithmetic average value and then scaled in the vertical direction to create rough surfaces with different values of rms and keep the spatial distribution of peaks and valleys the same [12]. The mentioned subtraction is necessary in order to keep higher order statistical parameters such as skewness and kurtosis

unaffected. This technique enables one to isolate the effect of varying roughness rms and maintain the same distribution of asperities, since different distributions of asperities (even with same rms) lead to different adhesive behaviors.

Fig. 8 depicts the normalized contact pressure at this contact for different values of the roughness rms at the same normal load and for Tabor parameter $\mu = 2$. It is well-known that the roughness can reduce the adhesive force. However, it is apparent that the small amount of roughness rms can cause a large zone within the macro contact (and especially close to the contact boundary) to experience a small separation (smaller than h_0), where the adhesive stress is maximum. As we further increase the roughness rms, the majority of the contact zone is separated by greater distances (greater than h_0), and experiences no adhesive forces. Only local areas surrounding the asperities with a positive pressure are in the zone for a high adhesive force. This trend can be realized through the adhesive area and force ($A_{adhesive}$ and $F_{adhesive}$) in Fig. 8. A similar behavior is observed in Fig. 9 which shows the variation of pull-off force for this configuration versus roughness rms for two different values of Tabor parameter. It can be seen that the pull-off force first increases with the roughness rms and then decreases. Fig. 10 depicts the effect of roughness rms on the contact pressure distribution at $F_0 = 10\mu N$. As the rms increases, the positive contact pressure scales up since the asperities locations remain the same (unless the increase in the roughness rms makes the asperity separate from the counter surface and experience a negative or zero stress depending on the local separation). However, at nodes with a negative pressure, the pressure scales down to $-\sigma_0$ and then disappears as soon as the local separation exceeds h_0.

The effect of roughness rms on the adhesive force normalized by the total normal force ($F_0 = 10\mu N$) is shown in Fig. 11(a) for two different values of the Tabor parameter. Increasing the roughness rms, as discussed for Fig. 8, first increases and then decreases the adhesive force. Fig. 11(b) depicts the effect of roughness rms on the area ratio, defined as the ratio of integral of the area with a negative stress to the contact area. As the roughness increases, the adhesive area decreases; yet, the decrease in the contact area is greater which, in total, leads to an increase in this ratio. It is worth noting that at all rms values, a higher Tabor parameter predicts a lower area ratio since a higher Tabor parameter corresponds to a higher work of adhesion and thus a higher contact area, which leads to a lower area ratio.

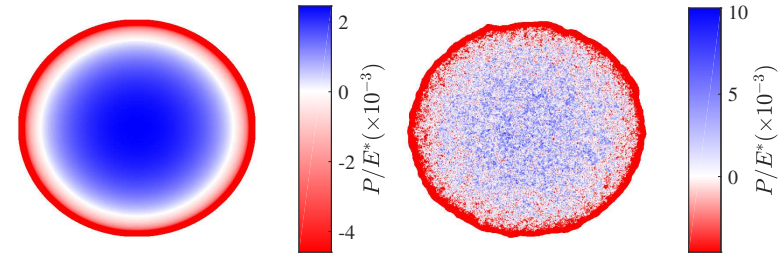

(a) $rms/z_0 = 0$
$A_{Adhesive} = 0.355\mu m^2$
$F_{Adhesive} = 62.4\mu N$

(b) $rms/z_0 = 5$
$A_{Adhesive} = 0.445\mu m^2$
$F_{Adhesive} = 84.2\mu N$

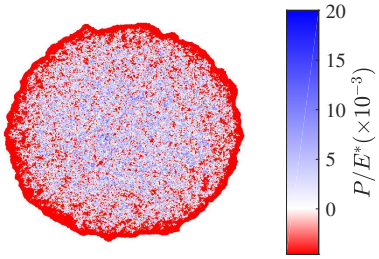

(c) $rms/z_0 = 10$
$A_{Adhesive} = 0.521\mu m^2$
$F_{Adhesive} = 125\mu N$

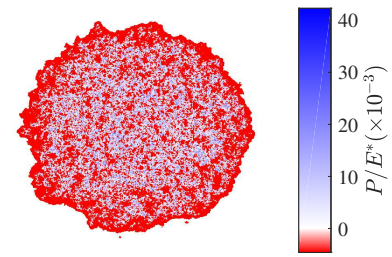

(d) $rms/z_0 = 20$
$A_{Adhesive} = 0.589\mu m^2$
$F_{Adhesive} = 179\mu N$

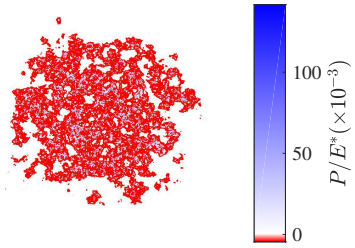

(e) $rms/z_0 = 50$
$A_{Adhesive} = 0.381\mu m^2$
$F_{Adhesive} = 130\mu N$

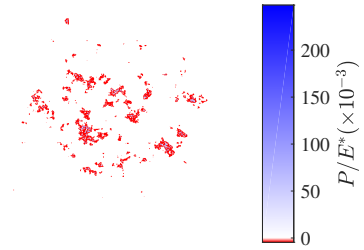

(f) $rms/z_0 = 100$
$A_{Adhesive} = 0.039\mu m^2$
$F_{Adhesive} = 13.5\mu N$

Figure 8: Contact pressure for a smooth and rough ball of different roughness rms on a smooth flat at the same normal load for $\mu = 2$.

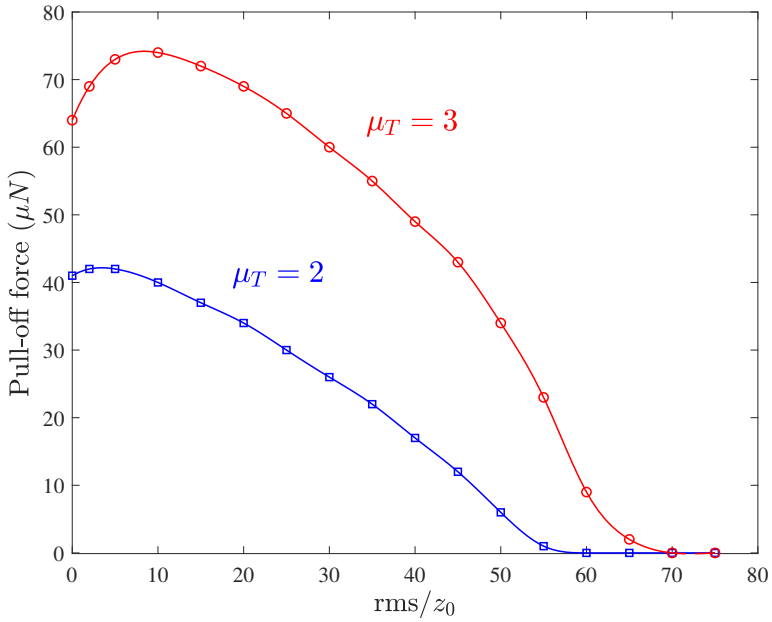

Figure 9: The variation of pull-off force vs the roughness rms

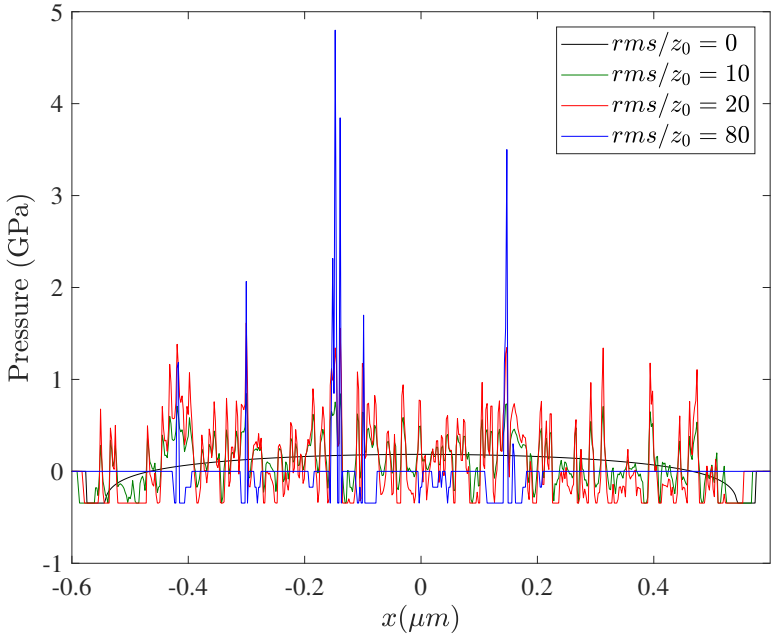

Figure 10: The effect of roughness rms on the contact pressure for $\mu = 2$

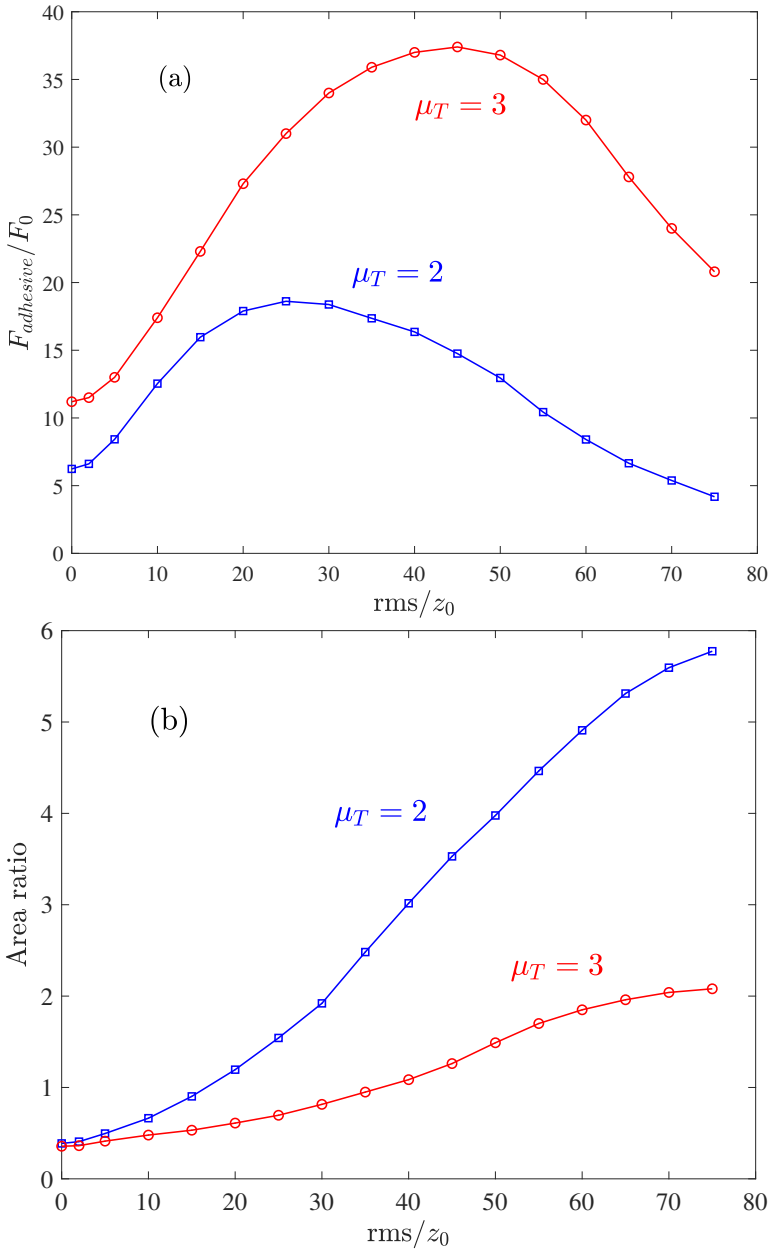

Figure 11: The effect of roughness rms on (a) the normalized adhesive force and (b) the area ratio

8 Conclusion

In this paper, the Conjugate Gradient Method (CGM) was extended for adhesive contact analyses between two elastic bodies with a general geometry (either rough or smooth of any shape) based on the assumptions of the Maugis-Dugdale model of adhesion. The accuracy of the proposed algorithm was examined through the conventional case of ball-on-flat adhesive contact and later, the contact of a ball over a wavy surface. Then, by means of the proposed algorithm, the pull-off force at a bisinusoidal interface was calculated for various cases of different geometrical and mechanical properties and a curve as a function of all these parameters was fitted on the calculated pull-off forces. The fitted curve showed no dependence on the elastic modulus, but a linear trend vs. radius of curvature and work of adhesion. In the end, the contact between a smooth flat and a rough ball was considered. It was shown that small degrees of roughness can increase the pull-off force, adhesive force, and area ratio.

9 Acknowledgment

The authors would like to express their gratitude to ASML Company, Veldhoven, the Netherlands (www.asml.com) for the financial support of this research project. This research was carried out under project number S61.7.13492 in the framework of the Partnership Program of the Materials Innovation Institute M2i (www.m2i.nl) and the Technology Foundation STW (www.stw.nl), which is a part of the Netherlands Organization for Scientific Research (www.nwo.nl).

Bibliography

[1] K. Stamatakis and C. Tien., "A simple model of cross-flow filtration based on particle adhesion," *AIChE Journal*, vol. 39, pp. 1292–1302, 1993.

[2] J. C. Horton, C. S. German, S. Allen, M. C. Davies, C. J. Roberts, S. J. Tendler, and P. M. Williams, "Characterization of particle-interactions by atomic force microscopy: Effect of contact area," *Pharmacological Research*, vol. 20, pp. 508–514, 2003.

[3] R. S. Bradley, "The cohesive force between solid surfaces and the surface energy of solids," *Philosophical Magazine and Journal of Science*, vol. 86, pp. 853–862, 1932.

[4] K. L. Johnson, K. Kendall, and A. D. Roberts, "Surface Energy and the Contact of Elastic Solids," *Proceedings of the Royal Society of London. Series A, Mathematical and Physical Sciences*, vol. 324, pp. 301–313, 1971.

[5] B. Derjaguin, V. Muller, and Y. Toporov, "Effect of contact deformations on the adhesion of particles," *Journal of Colloid and Interface Science*, vol. 53, no. 2, pp. 314–326, 1975.

[6] D. Tabor, "Surface forces and surface interactions," *Journal of Colloid and Interface Science*, vol. 58, no. 1, pp. 2–13, 1977.

[7] V. M. Muller, B. V. Derjaguin, and Y. P. Toporov, "On two methods of calculation of the force of sticking of an elastic sphere to a rigid plane," *Journal of Colloids and Interface Science*, vol. 7, no. 3, pp. 251–259, 1983.

[8] D. Maugis, "Adhesion of spheres: The JKR-DMT transition using a dugdale model," *Journal of Colloid And Interface Science*, vol. 150, no. 1, pp. 243–269, 1992.

[9] K. Johnson and J. A. Greenwood, "An Adhesion Map for the Contact of Elastic Spheres," *Journal of Colloid and Interface Science*, vol. 192, no. 2, pp. 326–333, 1997.

[10] K. Johnson, "Mechanics of adhesion," *Tribology International*, vol. 31, no. 8, pp. 413–418, 1998.

[11] G. Carbone and L. Mangialardi, "Adhesion and friction of an elastic half-space in contact with a slightly wavy rigid surface," *Journal of the Mechanics and Physics of Solids*, vol. 52, no. 6, pp. 1267–1287, 2004.

[12] S. Medina and D. Dini, "A numerical model for the deterministic analysis of adhesive rough contacts down to the nano-scale," *International Journal of Solids and Structures*, vol. 51, no. 14, pp. 2620–2632, 2014.

[13] B. N. Persson, "Contact mechanics for randomly rough surfaces," *Surface Science Reports*, vol. 61, no. 4, pp. 201–227, 2006.

[14] J. Archard, "Elastic deformation and the laws of friction," *Proceedings of the Royal Society of London. Series A. Mathematical and Physical Sciences*, vol. 243, pp. 190 LP – 205, dec 1957.

[15] J. Greenwood and J. Williamson, "Contact of Nominally Flat Surfaces," *Proceedings of the Royal Society of London . Series A , Mathematical and Physical Published*, vol. 295, no. 1442, pp. 300–319, 1966.

[16] M. Götzinger and W. Peukert, "Particle adhesion force distributions on rough surfaces," *Langmuir*, vol. 20, no. 13, pp. 5298–5303, 2004.

[17] N. Yu and A. a. Polycarpou, "Combining and Contacting of Two Rough Surfaces with Asymmetric Distribution of Asperity Heights," *Journal of Tribology*, vol. 126, no. April, p. 225, 2004.

[18] C. A. Kotwal and B. Bhushan, "Contact Analysis of Non-Gaussian Surfaces for Minimum Static and Kinetic Friction and Wear," *Tribology Transactions*, vol. 39, pp. 890–898, jan 1996.

[19] R. Ardito, A. Frangi, F. Rizzini, and A. Corigliano, "Evaluation of adhesion in microsystems using equivalent rough surfaces modeled with spherical caps," *European Journal of Mechanics, A/Solids*, vol. 57, pp. 121–131, 2016.

[20] S. S. Cho and S. Park, "Finite element modeling of adhesive contact using molecular potential," *Tribology International*, vol. 37, no. 9, pp. 763–769, 2004.

[21] R. A. Sauer, "A Computational Model for Nanoscale Adhesion between Deformable Solids and Its Application to Gecko Adhesion," *Journal of Adhesion Science and Technology*, vol. 24, no. 11-12, pp. 1807–1818, 2010.

[22] N. Mulakaluri and B. N. J. Persson, "Adhesion between elastic solids with randomly rough surfaces: Comparison of analytical theory with molecular-dynamics simulations," *EPL (Europhysics Letters)*, vol. 96, no. 6, p. 66003, 2011.

[23] G. Carbone and E. Pierro, "The Influence of the Fractal Dimension of Rough Surfaces on the Adhesion of Elastic Materials," *Journal of Adhesion Science and Technology*, vol. 26, no. 22, pp. 2555–2570, 2012.

[24] C. Yang, B. N. J. Persson, J. N. Israelachvili, and K. Rosenberg, "Contact mechanics with adhesion: Interfacial separation and contact area," *Europhysics Letters (EPL)*, vol. 84, no. 4, p. 5, 2008.

[25] M. H. Muser, "Single-asperity contact mechanics with positive and negative work of adhesion: Influence of finite-range interactions and a continuum description for the squeeze-out of wetting fluids," *Beilstein Journal of Nanotechnology*, vol. 5, no. 1, pp. 419–437, 2014.

[26] M. R. Hestenes and E. Stiefel, "Methods of Conjugate Gradients for Solving Linear Systems," *Journal of Research of the National Bureau of Standards*, vol. 49, pp. 409–436, 1952.

[27] I. A. Polonsky and L. M. Keer, "A numerical method for solving rough contact problems based on the multi-level multi-summation and conjugate gradient techniques," *Wear*, vol. 231, no. 2, pp. 206–219, 1999.

[28] L. He and T. C. Ovaert, "Three-Dimensional Rough Surface Contact Model for Anisotropic Materials," *Journal of Tribology*, vol. 130, pp. 1–6, 2008.

[29] D. Nelias, E. Antaluca, V. Boucly, and S. Cretu, "A Three-Dimensional Semianalytical Model for Elastic-Plastic Sliding Contacts," *Journal of Tribology*, vol. 129, pp. 761–771, 2007.

[30] E. A. H. Vollebregt, "A new solver for the elastic normal contact problem using conjugate gradients, deflation, and an FFT-based preconditioner," *Journal of Computational Physics*, vol. 257, pp. 331–351, 2014.

[31] T. jian Wang, L. qin Wang, L. Gu, and X. li Zhao, "Numerical analysis of elastic coated solids in line contact," *Journal of Central South University*, vol. 22, no. 7, pp. 2470–2481, 2015.

[32] Z. Wang, W. Wang, Y. Hu, and H. Wang, "A Numerical ElasticPlastic Contact Model for Rough Surfaces," *Tribology Transactions*, vol. 53, no. 2, pp. 224–238, 2010.

[33] K. Zhou, W. W. Chen, L. M. Keer, X. Ai, K. Sawamiphakdi, P. Glaws, and Q. J. Wang, "Multiple 3D inhomogeneous inclusions in a half space under contact loading," *Mechanics of Materials*, vol. 43, no. 8, pp. 444–457, 2011.

[34] S. Liu, Q. Wang, and G. Liu, "A versatile method of discrete convolution and FFT (DC-FFT) for contact analyses," *Wear*, vol. 243, no. 1-2, pp. 101–111, 2000.

[35] A. A. Elsharkawy and B. J. Hamrock, "A Numerical Solution for Dry Sliding Line Contact of Multilayered Elastic Bodies," *Journal of Tribology*, vol. 115, no. 2, pp. 237–245, 1993.

[36] H. M. Stanley and T. Kato, "An FFT-Based Method for Rough Surface Contact," *Journal of Tribology*, vol. 119, no. 3, pp. 481–485, 1997.

[37] Z. J. Wang, W. Z. Wang, H. Wang, D. Zhu, and Y. Z. Hu, "Partial Slip Contact Analysis on Three-Dimensional Elastic Layered Half Space," *Journal of Tribology*, vol. 132, no. 2, p. 021403, 2010.

[38] X. Shi and A. A. Polycarpou, "Adhesive transition from noncontacting to contacting elastic spheres: Extension of the Maugis-Dugdale model," *Journal of Colloid and Interface Science*, vol. 281, no. 2, pp. 449–457, 2005.

[39] J. F. Waters, S. Lee, and P. R. Guduru, "Mechanics of axisymmetric wavy surface adhesion: JKR-DMT transition solution," *International Journal of Solids and Structures*, vol. 46, no. 5, pp. 1033–1042, 2009.

[40] Y. Xu, A. Rostami, and R. L. Jackson, "Elastic Contact Between a Geometrically Anisotropic Bisinusoidal Surface and a Rigid Base," *Journal of Tribology*, vol. 137, no. 2, p. 021402, 2015.

[41] K. L. Johnson, *Contact Mechanics*. Cambridge: Cambridge University Press, 1985.

[42] Y. Hu and K. Tonder, "Simulation of 3-D random rough surface by 2-D digital filter and Fourier analysis," *International Journal of Machine Tools and Manufacture*, vol. 32, no. 1-2, pp. 83–90, 1992.

Paper B

Adhesive force model at a rough interface in the presence of thin water films: the role of relative humidity

M. Bazrafshan[1,2*], M.B. de Rooij[2], and D.J. Schipper[2]

[1] *Materials innovation institute (M2i), P.O. box 5008, 2600GA, Delft, Netherlands*
[2] *Laboratory for Surface Technology and Tribology, Department of Engineering Technology, University of Twente, P.O. box 217, 7500AE, Enschede, Netherlands*

Abstract

This paper proposes a Boundary Element Model (BEM) for the adhesive contact at the rough interface of two contacting bodies, where a thin water film is adsorbed on the surfaces due to the condensation from the humid environment. Three adhesive components contribute to the total adhesive force: solid-solid and liquid-solid van der Waals interactions and capillary force. Rather than a film with uniform thickness, the true distribution of the water film over the surfaces is considered. The capillary component of the adhesive force is first verified through the well-known capillary force model at the smooth contact of a rigid ball-on-flat configuration for different values of the Relative Humidity (RH) of the environment. Then, the adhesive contact at a rough interface with three different relative auto-correlation lengths under different normal loads is considered. It is found that the capillary force dominates the total adhesive force and it increases with RH, while the other two adhesive components are rather constant. In addition, the capillary force appears to first increase with RH and then decrease as almost the entire non-contact area of the interface is covered by a meniscus. This variation in the capillary force depends on the auto-correlation length, roughness rms of the rough interface, and the normal load. Furthermore, it is confirmed that the capillary force, while employing a water film with uniform thickness, deviates that of the true distribution of this film.

Keywords: Adhesion, Capillary, Thin water film, Boundary element method

Nomenclature

A	area of target domain
A_{1w2}	Hamaker constant for bodies 1 and 2 contacting across medium w
a	contact radius
E^*	reduced elastic modulus
e	film thickness
e_a	air gap
F_0	external normal force
F_{adh}	adhesion force
F_{cap}	capillary force

F_{el}	electro-static force
F_{total}	total adhesive force
F_{vdW}	van der Waals adhesive force
g	local gap
h_0	maximum allowable gap for adhesion
h_s	roughness height
h_w	water film free surface
L	size of the target domain
L_{ac}	auto-correlation length
N	no. of grid points in each direction
p	pressure
p_{ss}	solid-solid adhesive pressure
R	ball radius
R_g	universal gas constant
RH	Relative Humidity
$r_{1,2}$	meniscus radii
r_k	Kelvin radius
S	equivalent meniscus height
s_m	meniscus height
T	Temperature
$t_{1,2}$	film thickness on bodies 1 and 2
V	Molar volume of water
V_{adh}	adsorbed water volume
z_0	Equilibrium distance
ΔP_{cap}	capillary pressure
$\Delta\gamma$	work of adhesion
Ω	Computation domain
Ω_{ws}^1	water-solid interaction area, scenario 1
Ω_{ws}^2	water-solid interaction area, scenario 2
Ω_{wetted}	meniscus-wetted areas
γ	surface tension
η	viscosity
σ	roughness rms
$\theta_{1,2}$	contact angles of bodies 1 and 2
η	viscosity
ϕ	filling angle

1 Introduction

Along with the rapid development of micro-nano electromechanical systems (MEMs/NEMs), intermolecular adhesive interactions between two surfaces has attracted a lot of attention among the researchers. In such devices, adhesion is a common failure mechanism and a major reliability concern since strong adhesive forces arise due to the high surface energies of the contacting solids and or the formation of liquid menisci between contacting surfaces leading to undesirable friction forces. Prediction of these adhesive forces is crucial for the design of micro/nano devices. To reach this purpose, providing analytical models is, although desirable, almost impossible due to the complexity of the geometry of the contacting surfaces. Thus, numerical modeling is a suitable alternative for such cases. Bradley was the first in studying adhesion in contact mechanics by looking at the adhesive contact between two rigid spheres [1]. Then, two opposing models, JKR [2] and DMT [3], were proposed for spherical elastic contacts. It was shown by Tabor that, regardless of their different approaches and assumptions, both models were correct as they were two opposite extremes of a single theory. The JKR model is valid for the case of large and compliant contacts. The DMT model, whereas, is suitable for the small and stiff contacts. Following these two models, Maugis proposed an adhesive model (known as Maugis-Dugdale (MD) model) for this spherical contact through a Dugdale approximation of the Lennard-Jones potential (which defines the adhesive energy) [4].

Although such analytical models provide exact solution to the adhesive problem, they are limited to smooth contacts with simple shapes. For the adhesive contact of rough surfaces, however, numerical methods are essential. Several authors have attempted to numerically evaluate the adhesion between two rough surfaces through multi-asperity [5, 6], finite element [7, 8], statistical [9–11], molecular dynamics [12–14], and boundary element models (BEM) [15, 16]. Yet, there is a lot of discussion in the scientific community in this regard [17–22]. Vakis et al recently conducted a very comprehensive review of these methods along with the tribological applications in different scales [23].

The strong adhesion bond between the sand particles in a sandcastle, powders and sand in granular materials, and so forth is due to the liquid menisci forming around the contact area of two adjacent particles. The corresponding force caused by this phenomenon is called meniscus or capillary force. Understanding this phenomenon is important in granular materials, adhesion of insects, geckos, and spiders, and micro-nano electromechanical systems. Haines [24] and then Fisher [25] were among

the first who realized the importance of capillary forces.

Investigation of the meniscus formation between smooth surfaces of different configurations such as sphere-sphere, sphere-plane, plane-plane, cone-cone, cone-plane and so on can be found frequently in literature [26–32]. The transition of water from ordered to bulk form as a function of the relative humidity has been investigated for a ball-on-flat configuration in [33–35]. It was shown that for low values of relative humidity (RH $< 30\%$), 1 to 3 monolayers of water molecules are adsorbed on the surface behaving like ice and therefore, no meniscus forms. Consequently, the adhesive force is only contributed by the van der Waals force due to the solid-solid and liquid-solid interactions. At higher levels of relative humidity, however, the capillary force is responsible for the adhesive force.

To study the meniscus formation and capillary force between rough surfaces, researchers have pursued different numerical approaches such as multi-asperity, statistical, and boundary element approaches. Xue and Polycarpou coupled a single asperity meniscus model, based on the extended Maugis-Dugdale elastic theory, with a statistical roughness surface and presented an improved multi-asperity meniscus force model for rough contacts [36]. de Boer proposed a multi-asperity model by extending the Greenwood-Williamson model of rough surfaces [37]. Wang and Regnier developed a capillary adhesion model for the contact of a single asperity of a power law shape with a flat surface and extended it to the contact between rough surfaces [38]. Based on the fractal theory, describing the behavior of multiple roughness scales and the Gaussian roughness distribution, You and Wan proposed a model to account for the van der Waals and capillary forces between a rough particle and surface [39]. Peng et al studied the capillary adhesion of rough fractal surfaces [40]. They implemented a Dugdale approximation of the Laplace pressure to express adhesive interaction at the contact interface. As the main limitations of such multi-asperity models, one should note that merely the summits are considered and the rest of the surface is discarded.

Tian and Bhushan proposed a numerical algorithm to study the micro-meniscus effect of a very thin liquid film on the static friction of rough surface contacts [41]. They modified the classical meniscus theory of a single-sphere contact to include the effect of multi-asperity contacts in the presence of an ultra-thin liquid film adsorbed on the contacting surfaces. In their calculation, however, they did not incorporate the elastic deformations due to the adhesive pressure. Lin and Chen developed a model for the adhesive meniscus force at the interface of a rough surface and a smooth surface

covered by a thin water film [42]. They also considered the variation of the water film as a normal load is applied. Rostami and Streator proposed a deterministic approach to study the liquid-mediated adhesion between rough surfaces [43]. Based on the liquid volume available at the interface, they defined a wetting radius and the non-contact areas inside the wetting radius would experience a constant capillary pressure. They, however, neglected the contribution of mobile liquid at the interface, which indeed contributes to the meniscus formation. Hence, a comprehensive model to predict the adhesive force between two rough surfaces in the presence of the adsorbed liquid films is still in need.

In this paper, we present a boundary element model to analyze the adhesive contact between two rough surfaces where thin films of water are adsorbed on the contacting surfaces mediating the formation of meniscus. The total volume of adsorbed water depends on the contacting materials and increases with relative humidity. The thickness of the water films varies over the interface in such a way to fulfill the mechanical equilibrium and Newtonian rheology of water. Three components contribute to the total adhesive force: solid-solid and water-solid van der Waals interactions and capillary force. The deformation due to the adhesive pressure is also included in the total deformation of the interface. The next section introduces these components and formulates their contribution to the total adhesive force.

2 Theory and modeling

When two surfaces are brought into contact under an external normal load, an attractive force pulls the two surfaces together. This adhesive force might originate from different sources: van der Waals interactions between the opposing molecules on the two surfaces, a capillary force due to the meniscus pressure, an electrostatic force due to a possible electric charge on the surfaces, and so forth. The total work of adhesion is the work required to put into the system to separate these two surfaces from equilibrium to an infinite distance. In general, the total adhesive force is the summation of all these attractive forces:

$$F_{adh} = F_{vdW} + F_{cap} + F_{el} + ... \tag{1}$$

In this paper, we study the van der Waals and capillary forces as the main

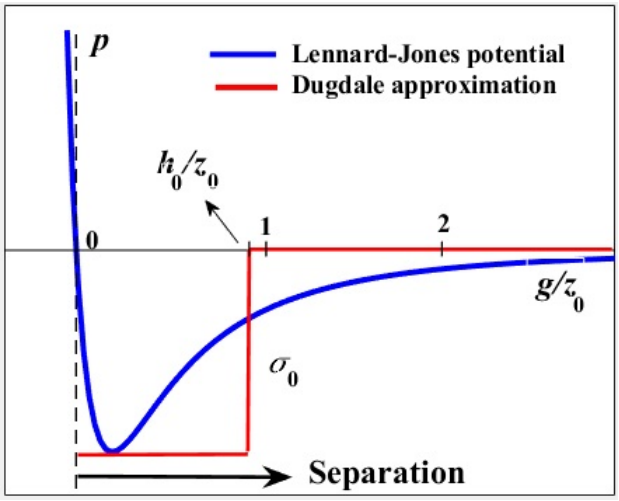

Figure 1: Dugdale approximation of Lennard-Jones potential

contributors to the adhesive force between two rough surfaces. The total van der Waals force comes from two types of interaction: solid-solid and water-solid interaction. In the following, these two interactions as well as the capillary force are modeled.

2.1 van der Waals forces

The van der Waals forces are distance dependent interactions between atoms which are divided into three categories: dipole-dipole interactions, randomly induced dipole interactions, and interaction between non-polar molecules [44]. The adhesive pressure, p_{ss}, due to van der Waals interactions is expressed through the Lennard-Jones potential (neglecting any capillary or electrostatic forces) as an explicit function of the separation, g:

$$p_{ss} = \frac{8\Delta\gamma}{3z_0}\left(\left(\frac{z_0}{g+z_0}\right)^9 - \left(\frac{z_0}{g+z_0}\right)^3\right) \tag{2}$$

where $\Delta\gamma$ is the work of adhesion due to solid-solid van der Waals interaction (see Fig. 1). In the equation above, z_0 is the equilibrium separation, typically ranging from $0.2nm$ to $0.4nm$.

Bazrafshan et al proposed a CGM (Conjugate Gradient Method) based

BEM algorithm by means of a Dugdale approximation for the total work of adhesion to solve the adhesive normal contact between two bodies, given by [16]:

$$p > -\sigma_0 \quad \text{at} \quad g = 0 \tag{3a}$$
$$p = -\sigma_0 \quad \text{at} \quad 0 < g < h_0 \tag{3b}$$
$$p = 0 \quad \text{at} \quad g > h_0 \tag{3c}$$
$$\int_\Omega p dx dy = F_0 \tag{3d}$$

in which, $-\sigma_0$, the maximum attractive pressure of the Lennard-Jones potential, is applied such that [4]:

$$\Delta\gamma = \sigma_0 h_0, \quad \sigma_0 = \frac{16\Delta\gamma}{9\sqrt{3}z_0} \tag{4}$$

This results in $h_0 = 9\sqrt{3}z_0/16 = 0.974z_0$. The parameter h_0 is the maximum allowable gap for the presence of adhesion (the constant negative stress $-\sigma_0$ as a Dugdale approximation of adhesion energy). In other words, in non-contact regions, a constant negative stress $(-\sigma_0)$ is present as long as the local separation is smaller than h_0.

2.2 Capillary force

Liquids with small contact angles spontaneously condense from vapor to fill in cracks and pores. At a dry and smooth ball-on-flat interface, water condenses to form a meniscus outside the contact area (Fig. 2). At thermodynamic equilibrium, the meniscus radius of curvature or namely Kelvin radius, r_k, is directly controlled by the relative humidity (RH) as [44]:

$$\left(\frac{1}{r_1} - \frac{1}{r_2}\right)^{-1} = r_k = \frac{\gamma V}{R_g T \log RH} \tag{5}$$

where $1/r_1$ and $1/r_2$ are the meniscus curvatures, V the molar volume of water, R_g the universal gas constant, and T the absolute temperature. When two rough surfaces are brought into contact under a light normal load, only a few pairs of asperities come into contact. In the presence of a thin adsorbed water film, a meniscus forms around the contacting and near-contacting

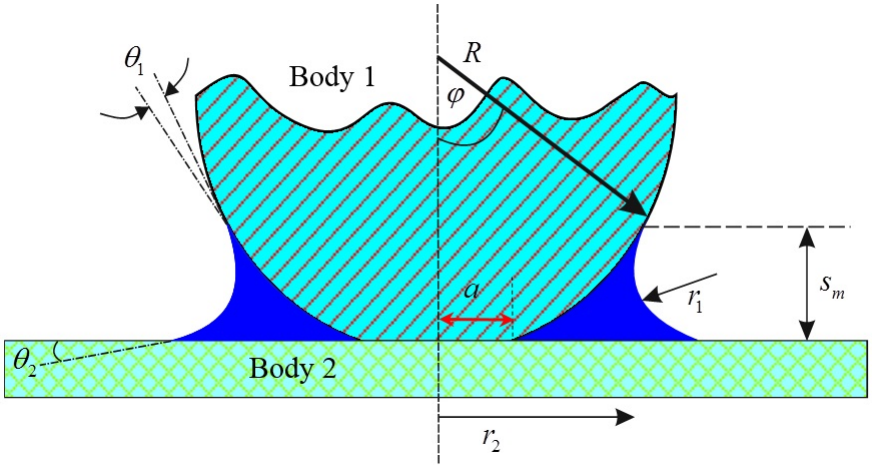

Figure 2: Meniscus formation at a smooth ball-on-flat interface.

asperities [44]. The pressure inside the meniscus is smaller than that outside the meniscus, resulting in an additional pulling force acting on the contacting surfaces.

Leveling of a thin water film over a rough surface

A thin film of water over a rough surface is neither flat nor the form of the rough surface, but follows the form illustrated in Fig. 3. The uneven distribution of this film over a rough surface is due to Laplace-Young pressure difference at summits and valleys of the surface. Having the topography of the surface, $h_s(x, y)$, and the volume of adsorbed water on it, $V_{ads}(RH)$, one can find the true uneven distribution by numerically solving the equations of mechanical equilibrium and rheology of the water. To do this, suppose that the water film is deposited on the surface at $t = 0$ and the initial thickness, $e(x, y, 0)$, is assumed to be uniform all over the surface, computed as:

$$e(x, y, 0) = \frac{V_{ads}(RH)}{A} \tag{6}$$

The water film is then non-uniformly distributed on the surface as time passes to reach a stable level while the volume of water is constant, and the same as its initial value, at any time as:

$$\int_{\Omega} e(x, y, t)\, dxdy = V_{ads}(RH) \tag{7}$$

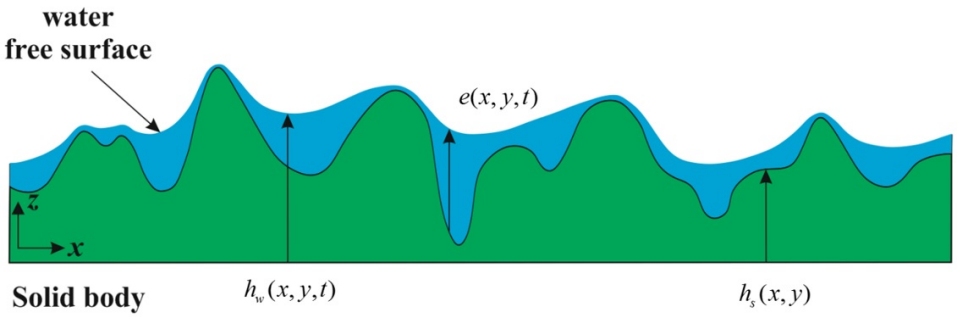

Figure 3: Leveling of a water film over a rough surface.

Combining the mechanical equilibrium and Newtonian rheology for water and neglecting the gravity reads [45]:

$$\begin{aligned}\frac{\partial h_w}{\partial t} = &-\frac{\gamma}{3\eta}\frac{\partial}{\partial x}\left[(h_w - h_s)^3\left(\frac{\partial^3 h_w}{\partial x^3} + \frac{\partial^3 h_w}{\partial x \partial y^2}\right)\right] \\ &-\frac{\gamma}{3\eta}\frac{\partial}{\partial y}\left[(h_w - h_s)^3\left(\frac{\partial^3 h_w}{\partial y^3} + \frac{\partial^3 h_w}{\partial y \partial x^2}\right)\right]\end{aligned} \tag{8}$$

where $h_w(x, y, t) = e(x, y, t) + h_s(x, y)$ is the height of the water free surface. When the water free surface reaches a stable level, it does not change with time. Eq. (7) is a set of high order non-linear partial differential equations which is numerically solved using the method of lines. If the input rough profile, h_s, has N^2 surface elements (and so does h_w), the method of lines converts Eq. (7) to a set of N^2 coupled ordinary differential equations of the first order. Since the roughness is assumed to be periodic, the derivation property of the Fourier Transform can be exploited to convert the derivatives to the function nodal values. Then, this set of N^2 ordinary differential equations are solved using the adaptive step-size Runge-Kutta scheme [45].

Meniscus formation between two rough surfaces

When the two surfaces approach one another, several isolated micro-menisci occur at the contact interface around the contacting asperities and also at near-contacting asperities (Fig. 4(a)). This formation is dependent on the relative humidity and roughness parameters.

It is first assumed in this study that there is no water flow between the contacting surfaces. We also neglect the squeezed water when two counter

asperities come into contact. This assumption underestimates the capillary force since this squeezed water can help to form larger menisci and thus, larger capillary force. This is even more significant for surfaces with long auto-correlation lengths as the available water film at the peaks is comparatively thicker due to smaller local gradients. For the sake of simplicity, however, we neglect the effect of this squeezed film. There are two mechanisms governing the formation of meniscus around an asperity contact. One is the condensation from the humid environment and the other one is surface migration-controlled growth [41]. These two mechanisms are distinguished by the source from which water required for the meniscus formation is supplied. Either or both of these mechanisms could be involved in the meniscus formation process. It is here assumed that water is supplied through capillary condensation from the humid environment to form the meniscus. This way, the original volume of adsorbed water is kept the same after the contact. As a result, the distribution of the thin water films does not change as the surfaces come into contact at a few asperities; at least it can be claimed that the film thickness changes much more in the valleys than in the summits (which is out of interest as the valleys have a lower contribution to the total adhesion). Therefore, one can keep the original distribution of water films (before the contact) for the calculations in the next section.

The total capillary force is a function of the meniscus shape and volume. Since determining the exact shape of meniscus is demanding, we conduct a simplified approach by approximating the effective section of a meniscus as an arc so that the meniscus height is given by [41]:

$$s_m = r_k \left(\cos\theta_1 + \cos\theta_2\right) \tag{9}$$

Here, θ_1 and θ_2 are the contact angles (see Fig. 2). It must be noted that, in the presence of water films, the curvature of the meniscus does not significantly change the thickness of the adsorbed film [46]. Therefore, the meniscus rises to $2r_k$ rather than the one expressed in Eq. (9). We also neglect the variation of the meniscus height around the irregular asperities. At this stage, it is required to locate the areas wetted by meniscus. These areas experience the capillary pressure. To do this, it is easier to first combine the heights of the two rough surfaces and put the summation of the thickness of the two water films on a smooth surface as shown in Fig. 4(b). It is first important to mention that the meniscus-wetted areas are the ones whose local gap from the counter surface is smaller than the

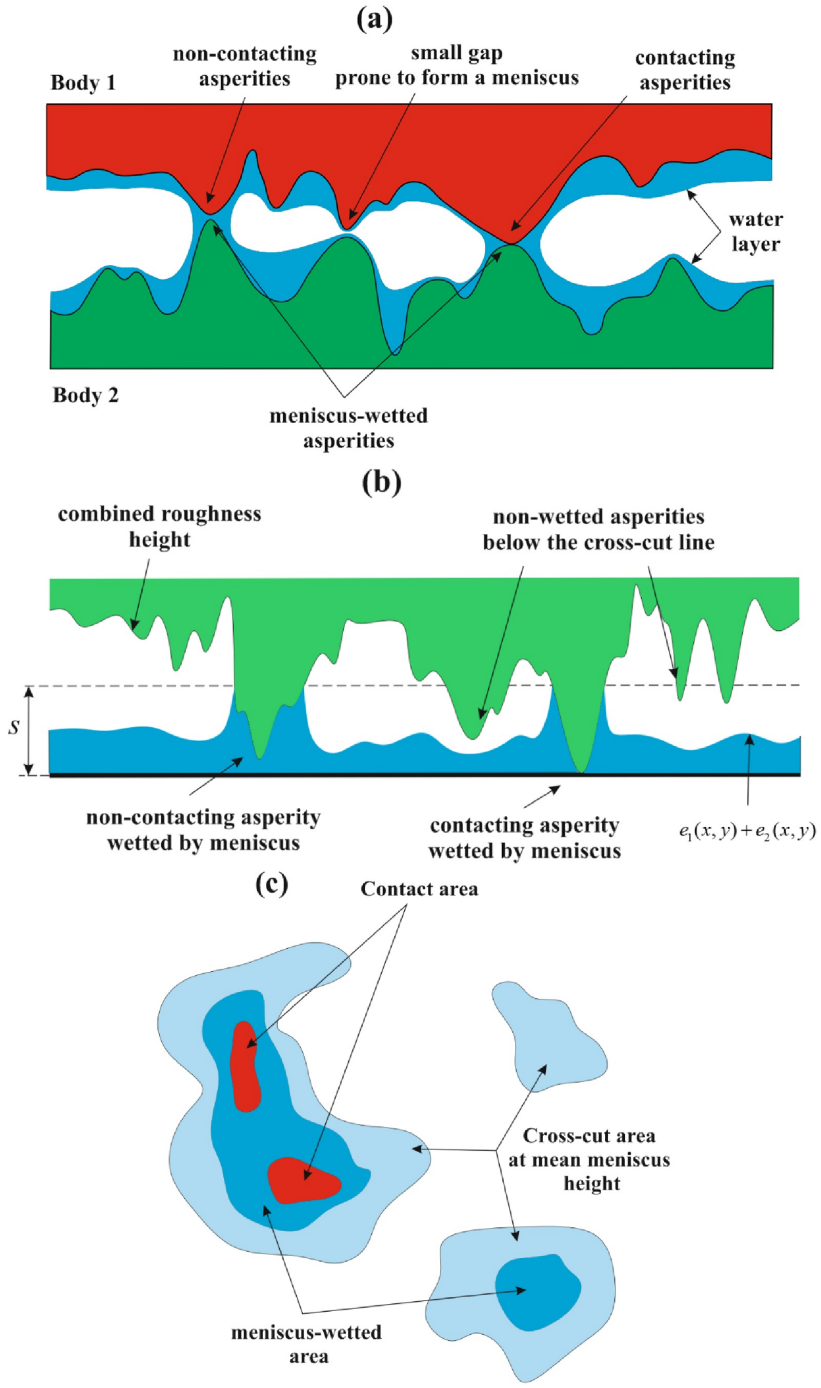

Figure 4: (a) Meniscus formation at the contact of two rough surfaces in the presence of adsorbed water films (b) strategy to find meniscus-wetted asperities (c) a schematic diagram of contact area, meniscus-wetted area, and cross-cut area at mean meniscus height

summation of the local thickness of the water films. The cross-cut areas of the combined roughness at the meniscus height of $S = 2r_k + e_1 + e_2$ (e_1 and e_2 are the local thickness of the water films on bodies 1 and 2 as obtained through the leveling procedure described in section 2.2.1) which are linked to the meniscus-wetted areas are considered to experience the capillary pressure. In other words, the cross-cut area at the meniscus height is first grouped into individual islands. Then, those islands, which overlap the meniscus-wetted areas, are selected to undergo the capillary pressure and the rest of the islands are discarded (see Fig. 4(c)).

Thermal fluctuations at molecular level can roughen the free surface of water films [46]. In addition, the van der Waals interaction between water films of the opposite sides at locations where the two films are very close to one another needs to be taken into account (see the small gap prone to form a meniscus in Fig. 4(a)). Combining these two effects at such locations, the two films can jump into contact and quickly form a meniscus similar to the one around the near-contacting asperities. To treat this behavior, we define a critical distance, d_{cr}, to distinguish whether such a meniscus forms or not. There is no strict criterion for the value of this parameter. However, it is expected to be in the order of 1-3 diameters of a water molecule. Here, we assume this parameter to be three times the size of a water molecule.

To put it all together, micro-menisci islands can form in three types of places at the interface while meeting either of the mentioned criteria: around the contacting asperities, at near contacting asperities, and at areas with a very small gap (smaller than d_{cr}) prone to form a micro-meniscus. In all these wetted areas, Ω_{wetted}, a capillary pressure of ΔP_{cap} exists:

$$\Delta P_{cap} = \frac{\gamma}{r_k} = \frac{R_g T \log RH}{V} \tag{10}$$

2.3 Water-Solid interaction

The other component in the adhesive force, which needs to be taken into consideration, is the interaction between the two solids through water and air (or vacuum) as media. In this case, two scenarios exist depending of the local gap between each two counter elements. The first scenario takes place where the local gap between these two nodes is smaller than the summation of the local thickness of the two water films (Fig. 5(a)). Therefore, the thickness of the trapped water, e_w, is the same as the local gap and the local adhesive stress is given by [44]:

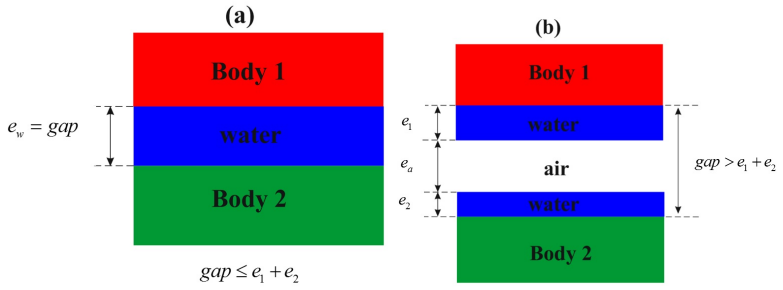

Figure 5: Two different scenarios for the water-solid interaction

$$P_{ws}^{1} = -\frac{A_{1w2}}{6\pi e_w^3} \tag{11}$$

where A_{1w2} is the Hamaker constant for media 1 and 2 interaction across water. The region at the interface eligible for this scenario is named Ω_{ws}^{1}.

The second scenario occurs where the local gap is larger than the summation of the local thickness of the two water films (Fig. 5(b)). The region at the interface eligible for this scenario is named Ω_{ws}^{2}. For this case, the local stress is expressed as [44]:

$$P_{ws}^{2} = -\frac{1}{6\pi}\left(\frac{A_{waw}}{e_a^3} - \frac{\sqrt{A_{1w1}A_{waw}}}{(e_a+e_1)^3} - \frac{\sqrt{A_{2w2}A_{waw}}}{(e_a+e_2)^3} + \frac{\sqrt{A_{1w1}A_{2w2}}}{(e_a+e_1+e_2)^3}\right) \tag{12}$$

where A_{ikj} is the Hamaker constant for media i and j interacting across medium k and a and w stand for air and water, respectively.
One needs to note that the largest and dominating term in Eq. (12) is A_{waw}/e_a^3 since the denominators of the other terms are comparatively much greater than e_a. On the other hand, considering the fact that e_a has to be larger than d_{cr}, the third power of e_a makes it very small compared to the case of Eq. (11). Therefore, it can be concluded that the water-solid interaction is dominated by scenario (a) in Fig. 5.

3 Numerical algorithm

This section summarizes the numerical scheme of the proposed approach. The present contact problem is the extension of Eq. (3) (which defines

the adhesive contact problem in the presence of only van der Waals forces) to include the capillary pressure and van der Waals water-solid interaction described in sections 2.2 and 2.3. This equation suggests that there is no pressure at areas where separation is greater than h_0. In presence of liquid films and capillary effect, however, such areas experience either or both of the capillary force and water-solid van der Waals interaction. Therefore, the present contact problem is given by:

$$p > -\sigma_0 \quad \text{at} \quad g = 0 \tag{13a}$$
$$p = -\sigma_0 \quad \text{at} \quad 0 < g < h_0 \tag{13b}$$
$$p = \Delta P_{cap} \text{ at} \quad \Omega_{wetted} \tag{13c}$$
$$p = P_{ws}^1 \quad \text{at} \quad \Omega_{ws}^1 \tag{13d}$$
$$p = P_{ws}^2 \quad \text{at} \quad \Omega_{ws}^2 \tag{13e}$$
$$\int_\Omega p dx dy = F_0 \tag{13f}$$

It is noted that for the solid-solid van der Waals interaction to be present, the local gap is required to be smaller than which is smaller than (or perhaps almost equal to) the size of a water molecule. In such areas, thus, no meniscus or water-solid interaction can exist.

In order to solve the contact problem of Eq. (13) for the unknown pressure, p, a BEM-based approach is implemented. The boundary element method (BEM) is a numerical method which transforms governing partial differential equations into integral equations over the surface or boundary of a domain [47]. Therefore, rather than discretizing the entire 3D domain, the boundary (here the contact interface) is divided into small patches where the unknown functions are approximated in terms of nodal values, and the integral equations are discretized and solved numerically. As all the approximations are transformed to the boundary, the BEM has better accuracy and efficiency (since the dimensionality reduces by one order) in contact of rough surfaces than other numerical methods such as finite element method and molecular dynamics.

Fig. 6 depicts the flowchart of the proposed numerical algorithm. In the first step, mechanical and surface properties of the contacting bodies as well as the loading conditions, surface topographies, and relative humidity are input to the algorithm. The relative humidity, along with the adsorption properties of the contacting surfaces, is used to estimate the volume of adsorbed water on the surfaces in a humid environment [48]. An

alternative to this is to measure this parameter at different values of the relative humidity of the environment which gives out an adsorption isotherm. Here, the volume of adsorbed water is used to calculate the distribution of the thin water films on the surfaces as explained in section 2.2.1.

In step 2, an initial guess is provided for the pressure. Using this initial pressure, in step 3, the corresponding deformation at the interface is computed as:

$$u(x,y) = \int_{\Omega} k(x-\zeta, y-\eta) p(\zeta,\eta)\, d\zeta d\eta \tag{14}$$

where x and y are the spatial coordinates and $k(x,y)$ is the Boussinesq kernel function and is expressed as [49]:

$$k(x,y) = \frac{1}{\pi E^*} \frac{1}{\sqrt{x^2+y^2}}, \quad \frac{1}{E^*} = \frac{1-\nu_1^2}{E_1} + \frac{1-nu_2^2}{E_2} \tag{15}$$

in which $E_i,\ \nu_i, i = 1,2$ are the elastic moduli and Poisson ratios of the two contacting surfaces. If the initial gap between these two surfaces before the deformation is denoted by $h(x,y)$, the gap after deformation can be calculated as:

$$g(x,y) = u(x,y) + h(x,y) - \delta \tag{16}$$

where δ is the rigid approach of the two surfaces. All the operations in Eqs. (13-15) are carried out numerically over the discretized domain [16]. All adhesive force components are (directly or indirectly) functions of the gap at the interface and are computed in step 4. According to Eq. (12), the solid-solid van der Waals interaction, given by a constant negative stress $-\sigma_0$, is present at areas with gap smaller than h_0. In all the meniscus wetted areas, the capillary pressure, ΔP_{cap} is set and finally, the water-solid van der Waals interaction is present in either of Ω_{ws}^1 or Ω_{ws}^2.

In step 5, the pressure is updated by balancing the force corresponding the current pressure (including the new adhesive components) with the external normal force. Step 6 checks whether the pressure has converged. If so, the iteration loop stops; otherwise, it starts over from step 3 using the new pressure. The base of this algorithm and the details for updating the pressure is presented in [16]. Here, however, the water-solid interaction and capillary forces in steps 4.2 and 4.3 are embedded in that algorithm.

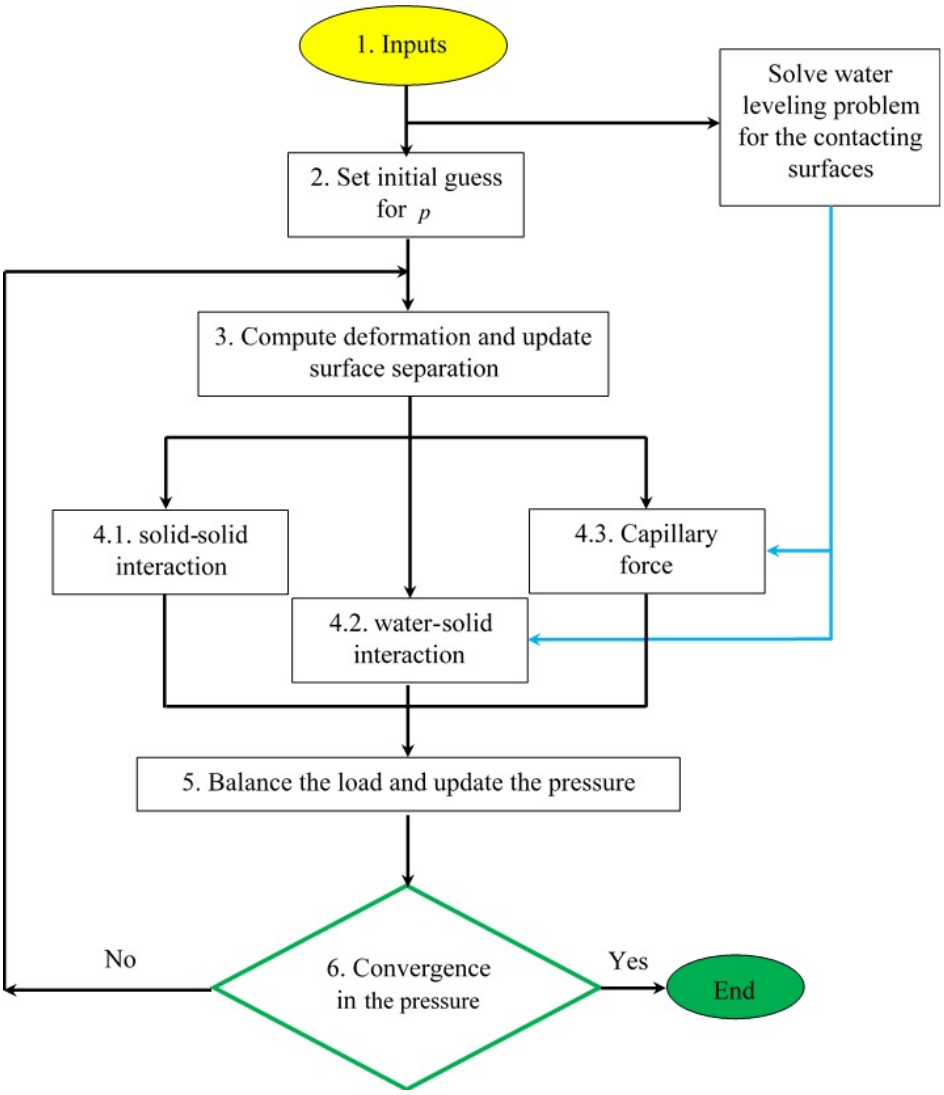

Figure 6: Numerical scheme to solve the adhesive normal contact problem

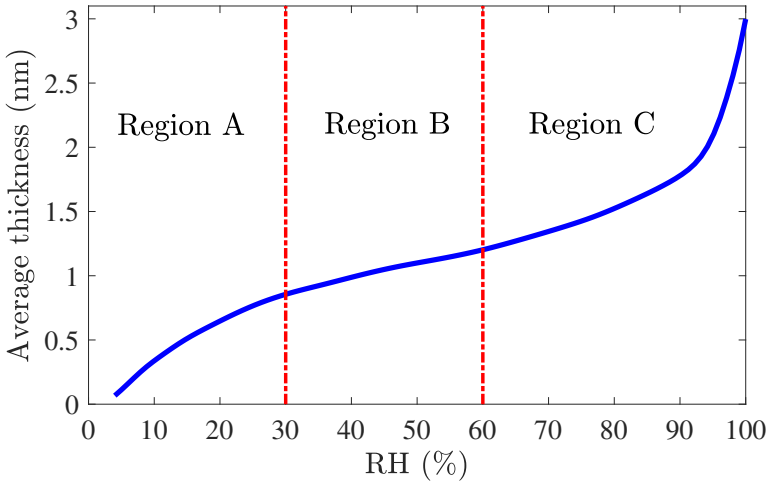

Figure 7: Adsorption isotherm of water on a silicon-oxide surface (redrawn from Ref. [50])

4 Numerical examples and discussion

This section provides two numerical examples. In both examples, the adsorption isotherm of water on the hydrophilic surface of Silicon-Oxide (SiO_2), measured by Asay and Kim [50], is used to express the average thickness of the water film as a function of RH. It is reported that at RH ranging from 0 to 30%, water grows up to three monolayers of hydrogen-bonded ice molecules (Region A in Fig. 7). Then, the liquid structure of water starts to appear and the ice-like structure grows to saturation for RH up to 60% (the transition regime, Region B in Fig. 7). Above 60% of RH, the adsorbed water is considered to be bulk and continues to increase in thickness (Region C in Fig. 7). The water meniscus is expected to form in this region.

In the following examples, we first examine the accuracy of the proposed BEM model by evaluating the well-known capillary force for the ball-on-flat configuration. Then, the formation of micro-menisci at a rough interface will be investigated.

4.1 Ball-on-flat configuration

Fig. 8 displays the formation of a meniscus at the interface of a ball-on-flat configuration in the presence of a thin adsorbed water film. As it was mentioned, the curvature of the meniscus does not significantly change the

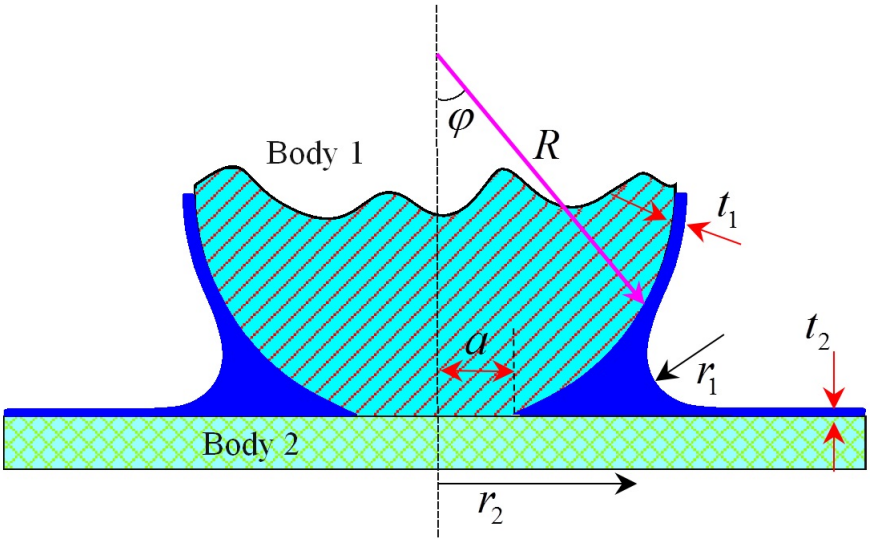

Figure 8: Meniscus formation at a smooth ball-on-flat interface in the presence of an adsorbed water film

thickness of the adsorbed film [51].

The meniscus radii of curvature in the presence of a thin adsorbed water film with thickness of t_1 and t_2 on the ball and flat, respectively, can be simply obtained as:

$$\begin{aligned} r_1 &= \frac{R(1-\cos\phi) - \frac{a^2}{R} - (t_1\cos\phi + t_2)}{1+\cos\phi} \\ r_2 &= R\sin\phi \end{aligned} \tag{17}$$

where a and ϕ are the contact radius and the meniscus filling angle, respectively. The term a^2/R counts as the normal indentation. Substituting Eq. (17) in Eq. (5) reads:

$$\frac{1}{R\sin\phi} - \frac{1+\cos\phi}{R(1-\cos\phi) - \frac{a^2}{R} - (t_1\cos\phi + t_2)} = \frac{R_g T}{\gamma V}\log RH \tag{18}$$

Solving this equation for the filling angle, ϕ, gives the capillary force as:

$$F_{cap} = \pi\left(R^2\sin^2\phi - a^2\right)\Delta P_{cap} \tag{19}$$

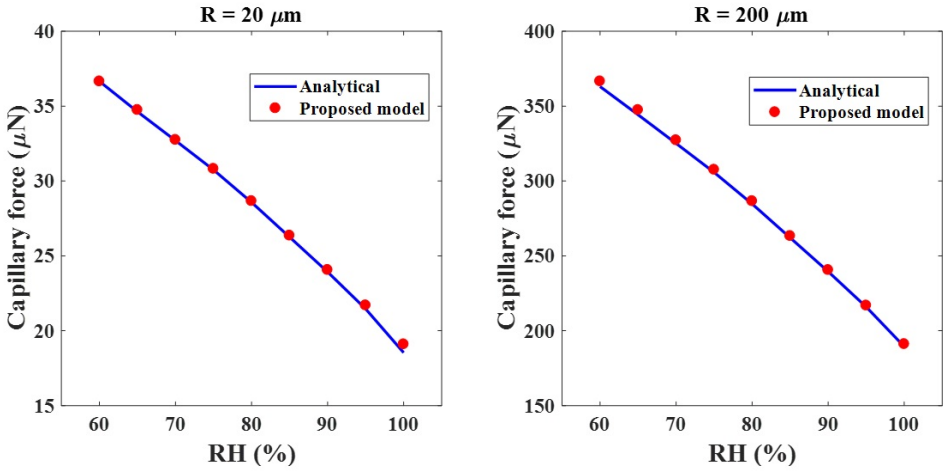

Figure 9: Comparison of the analytical and numerical solutions for the capillary force at different RH for two different ball radii (R)

It is worth noting that the contact radius, a, in Eq. (18) is unknown and dependent on the capillary force (and the filling angle) as well as some other parameters. To the best of our knowledge, however, there is no analytical solution for this problem in the presence of adsorbed films. Here we consider both the ball and flat to be rigid in order to have a zero contact radius and therefore, only does the filling angle remain to be solved and used in Eq. (19). The adsorption isotherms for the ball and flat are considered to be that of SiO_2. One must know that the effect of van der Waals forces in Eq. (18) is not considered. Therefore, we also neglect its contribution in the proposed model for this problem.

This problem is solved using the proposed model for two different values of the ball radius. Fig. 9 compares the capillary force obtained through the analytical solution of Eq. (18) and the proposed model. The relative error in both cases and at any RH value is negligible, implying that the numerical results are in good agreement with the analytical solution.

Here we conclude that the capillary problem for an elastic ball-on-flat configuration can be numerically solved using the proposed model where the contact radius and filling angle are both automatically derived from the numerical results.

4.2 Rough interface

This section aims at studying the adhesive contact at a rough interface. Three Gaussian rough surfaces with different autocorrelation lengths, L_{ac}, and the same rms value of σ, shown in Fig. 10, are generated. The size of each profile is $L \times L = 10\mu m \times 10\mu m$ and it includes 256×256 nodes which is typical of the surface topography measurement carried out by an Atomic Force Microscopy (the reader is referred to [52,53] for the effect of resolution on the contact area). Each of these surfaces comes into contact with a rigid flat surface. The properties of silicon-oxide (SiO_2) are used for the elastic rough surface and the water, for the case studied here, is assumed to be adsorbed only on the rough surface and thus, the flat surface is dry. For all of the following simulations, the external normal load is $500\mu N$ unless otherwise it is mentioned.

Fig. 11 shows a cross section of the leveled water film on top of the mentioned three rough surfaces at different RH levels. The film appears to be thicker at the peaks for surfaces with long auto-correlation length. In other words, the lower local gradients of the surface reduces the tendency of the water to flow towards the valleys.

The development of the meniscus area around the contacting regions at the three rough interfaces with increasing the relative humidity is shown in Fig. 12. It is apparent that the meniscus forms right around the contacting and at the near-contacting asperities and develops as the relative humidity increases. The micro-meniscus islands become larger and larger so that they can touch the neighboring micro-menisci and form a larger meniscus. At a high relative humidity level, at around 90%, all these islands are merged to form a single meniscus area which is developed all over the non-contact area. It is worth noting that from 90% to 100% of RH, some of the micro-contacts are lost. The reason is that, in this range, the capillary force decreases rapidly (it will be further on explained why) and therefore, the contact repulsive force (which is always larger than the external normal force due to the presence of adhesive forces) decreases accordingly and results in a lower contact area.

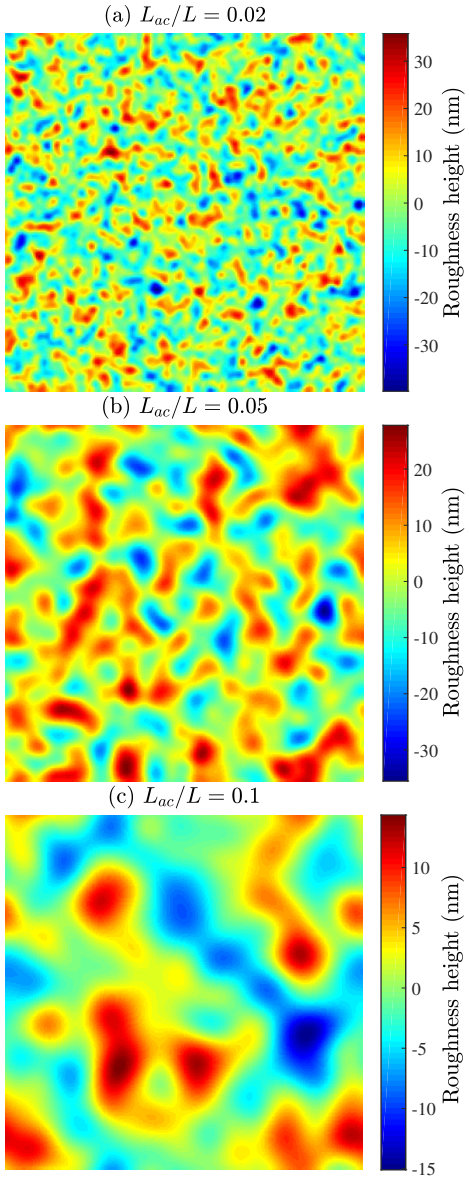

Figure 10: The roughness height (in nm) of the three generated Gaussian isotropic rough surfaces with different auto-correlation length ratio

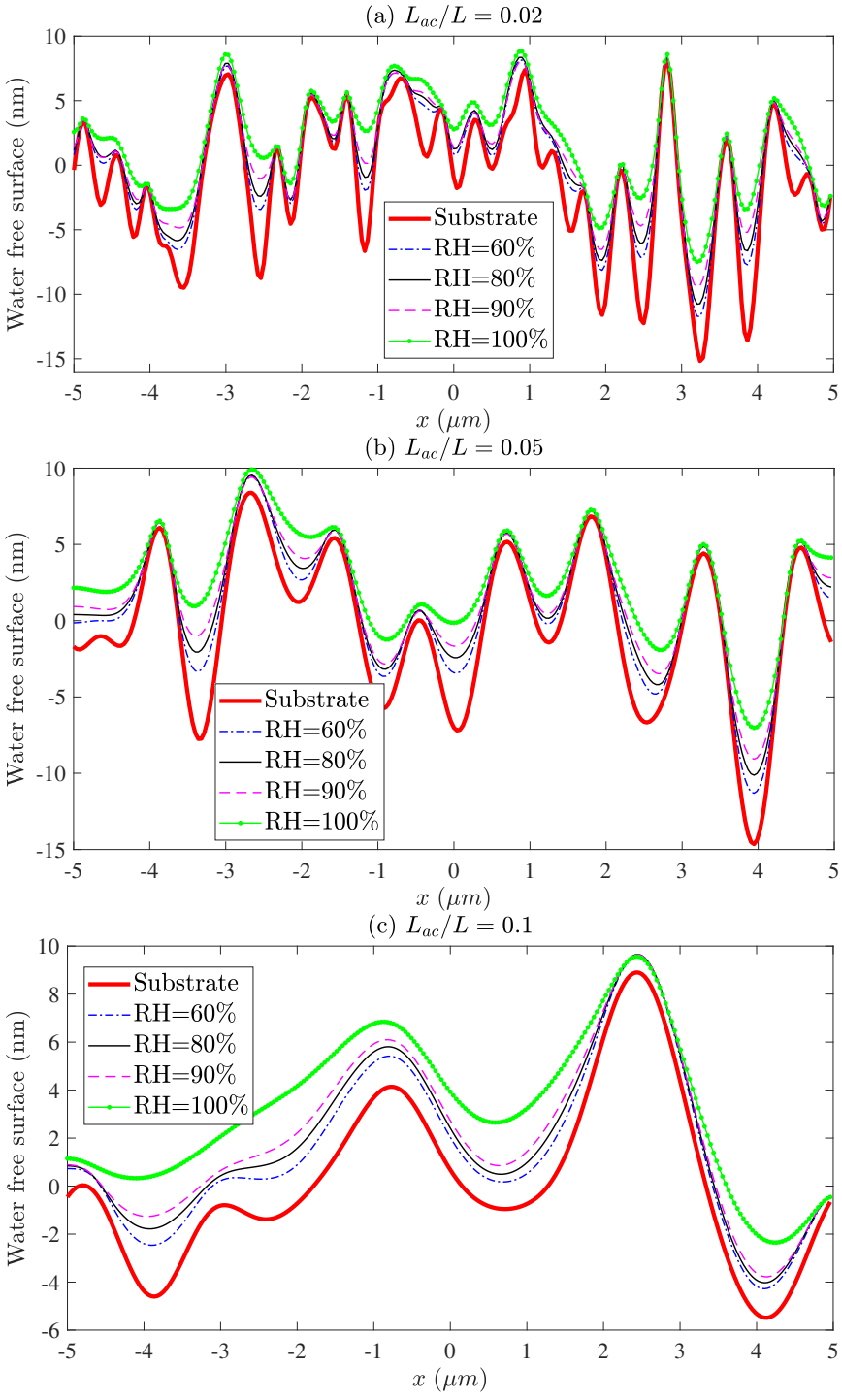

Figure 11: The leveled water film on the rough surfaces at different RH

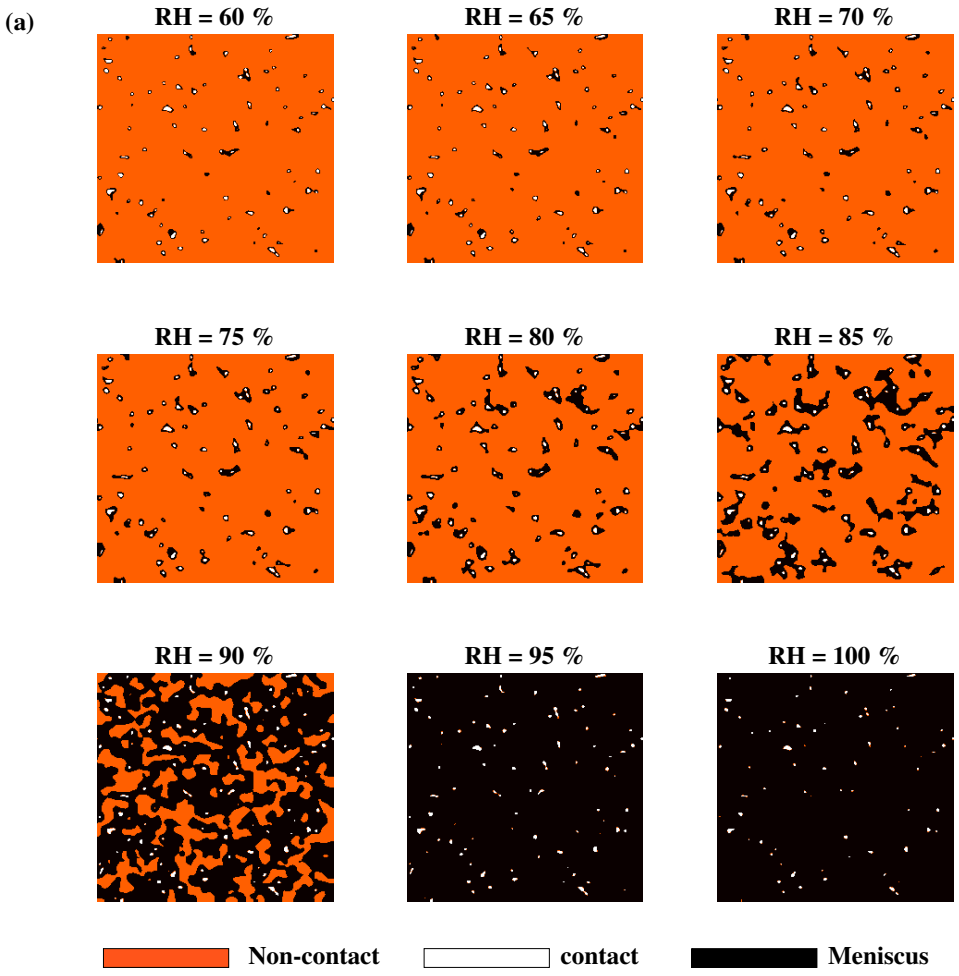
(a)
RH = 60 %
RH = 65 %
RH = 70 %
RH = 75 %
RH = 80 %
RH = 85 %
RH = 90 %
RH = 95 %
RH = 100 %
Non-contact
contact
Meniscus

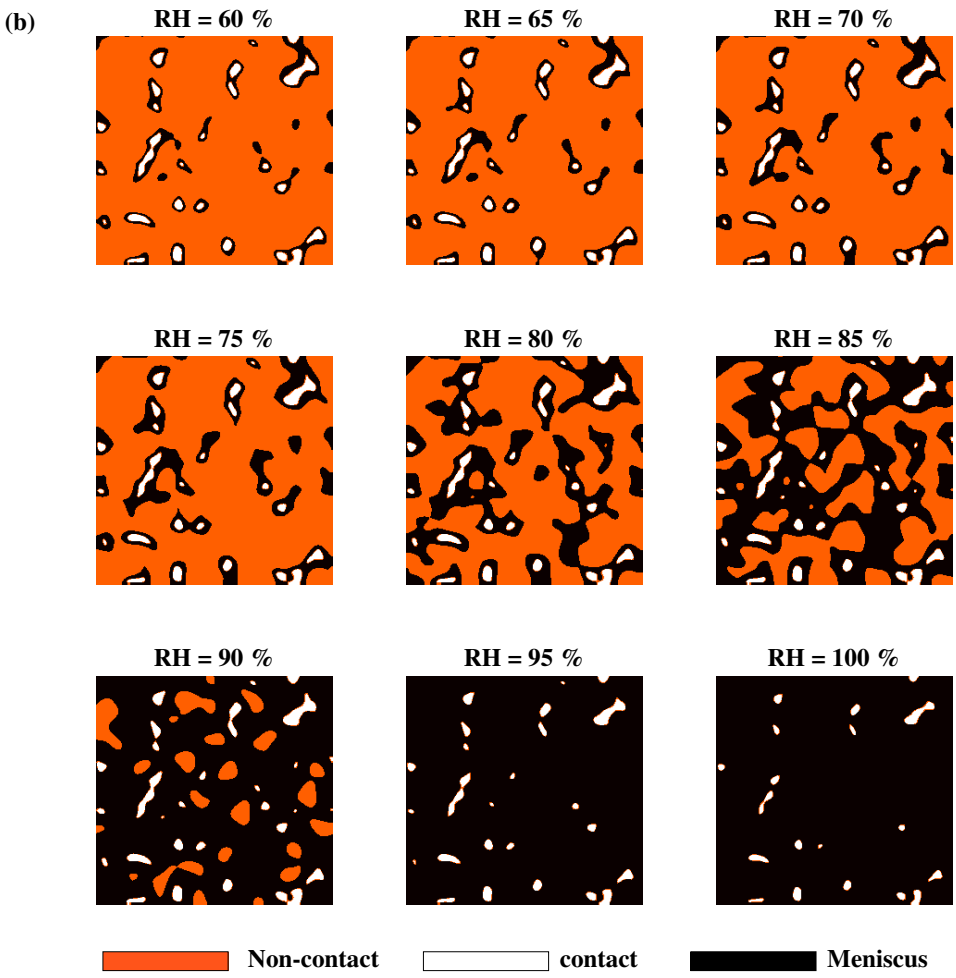
(b)
RH = 60 %
RH = 65 %
RH = 70 %
RH = 75 %
RH = 80 %
RH = 85 %
RH = 90 %
RH = 95 %
RH = 100 %
Non-contact
contact
Meniscus

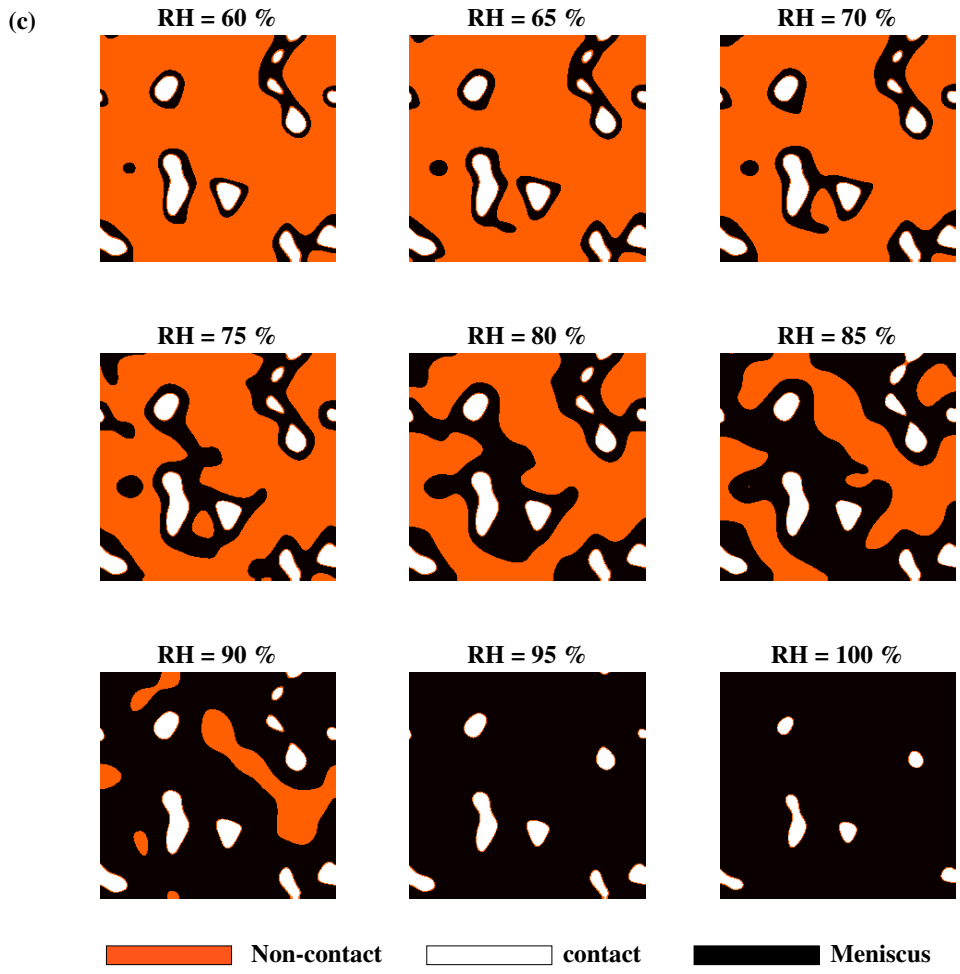

Figure 12: The development of meniscus area with increasing RH at the three rough interfaces with different auto-correlation lengths, (a) $Lac/L = 0.02$, (b) $L_{ac}/L = 0.05$, and (c) $L_{ac}/L = 0.1$

The variation of each of the adhesive force components and the total adhesive force at the rough interface with RH is depicted in Fig. 13(a-c). The capillary force first increases to reach its maximum at around 90% RH and then rapidly decreases to zero. To explain this behavior, one needs to note that in one hand, the capillary area increases and on the other hand, the capillary pressure, ΔP_{cap}, decreases with RH and therefore, the capillary force, which is the product of these two parameters, is a trade-off between these two changes. Initially, the increase of the capillary area

dominates the decrease in the capillary pressure. At higher levels of RH, where most of the non-contact area is covered by the merged micro-menisci, the capillary area does not increase noticeably with RH; specifically, after the whole non-contact area is covered with meniscus, there is no room for the capillary area to increase. This is the point where the decrease in the capillary pressure starts to dominate and thus, the capillary force steadily decreases to zero. Looking at Fig. 13(d), which compares the capillary force variation for rough interfaces with different auto-correlation lengths, reveals that the RH at which the maximum capillary force occurs, decreases with the auto-correlation length. In addition, the maximum capillary force increases (however not proportionally) with the auto-correlation length, too. The reason is that the water film is comparatively thicker for surfaces with longer auto-correlation lengths due to the smaller local gradients at the peaks. This figure also implies that at very large RH values, the capillary force is almost the same for all three surfaces and independent from the auto-correlation length due to the fact that all the non-contact area is covered by the meniscus and this parameter is, to a large extent, the same for all these three surfaces.

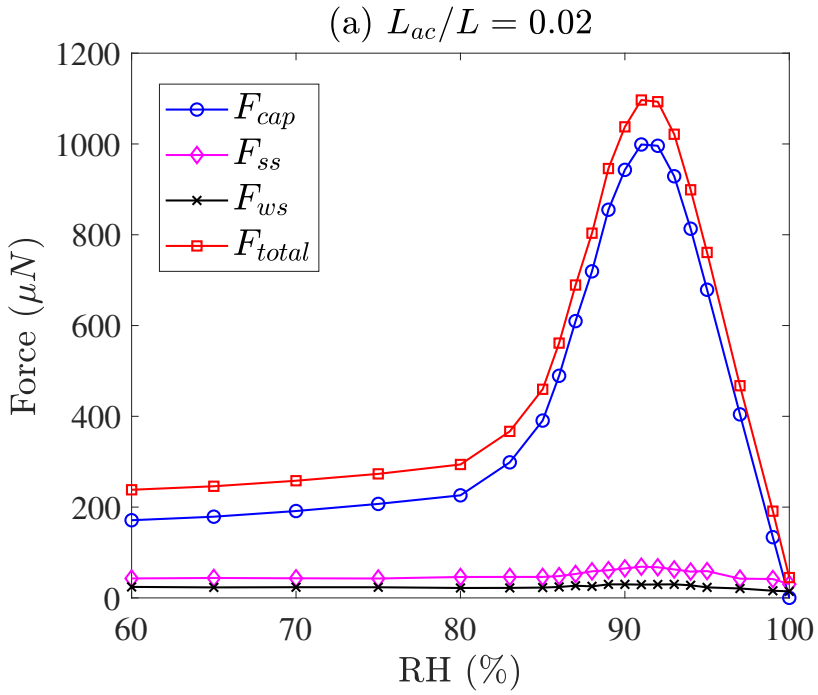
(a) $L_{ac}/L = 0.02$
F_{cap}
F_{ss}
F_{ws}
F_{total}
Force (μN)
RH (%)
0
200
400
600
800
1000
1200
60
70
80
90
100

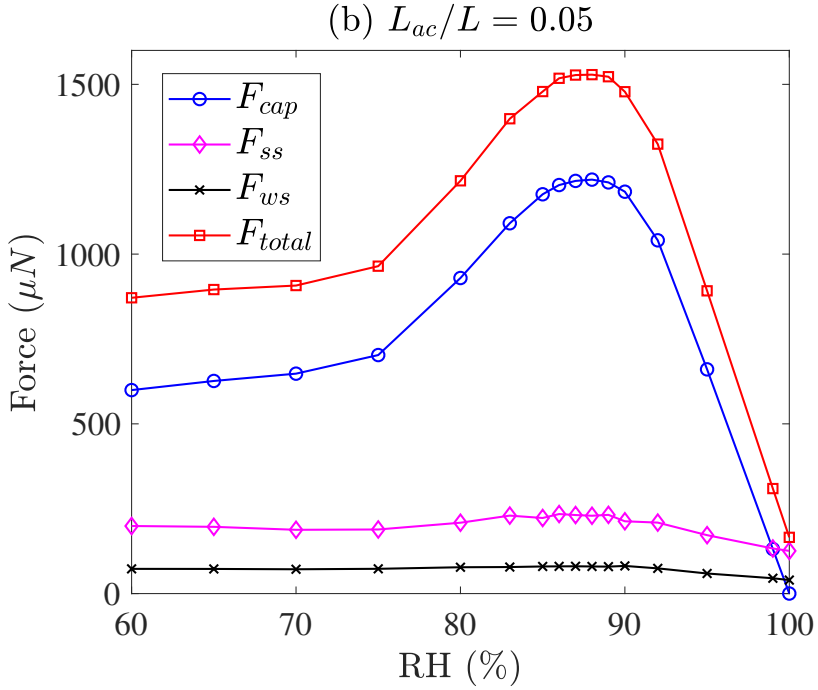
(b) $L_{ac}/L = 0.05$
F_{cap}
F_{ss}
F_{ws}
F_{total}
Force (μN)
RH (%)
0
500
1000
1500
60
70
80
90
100

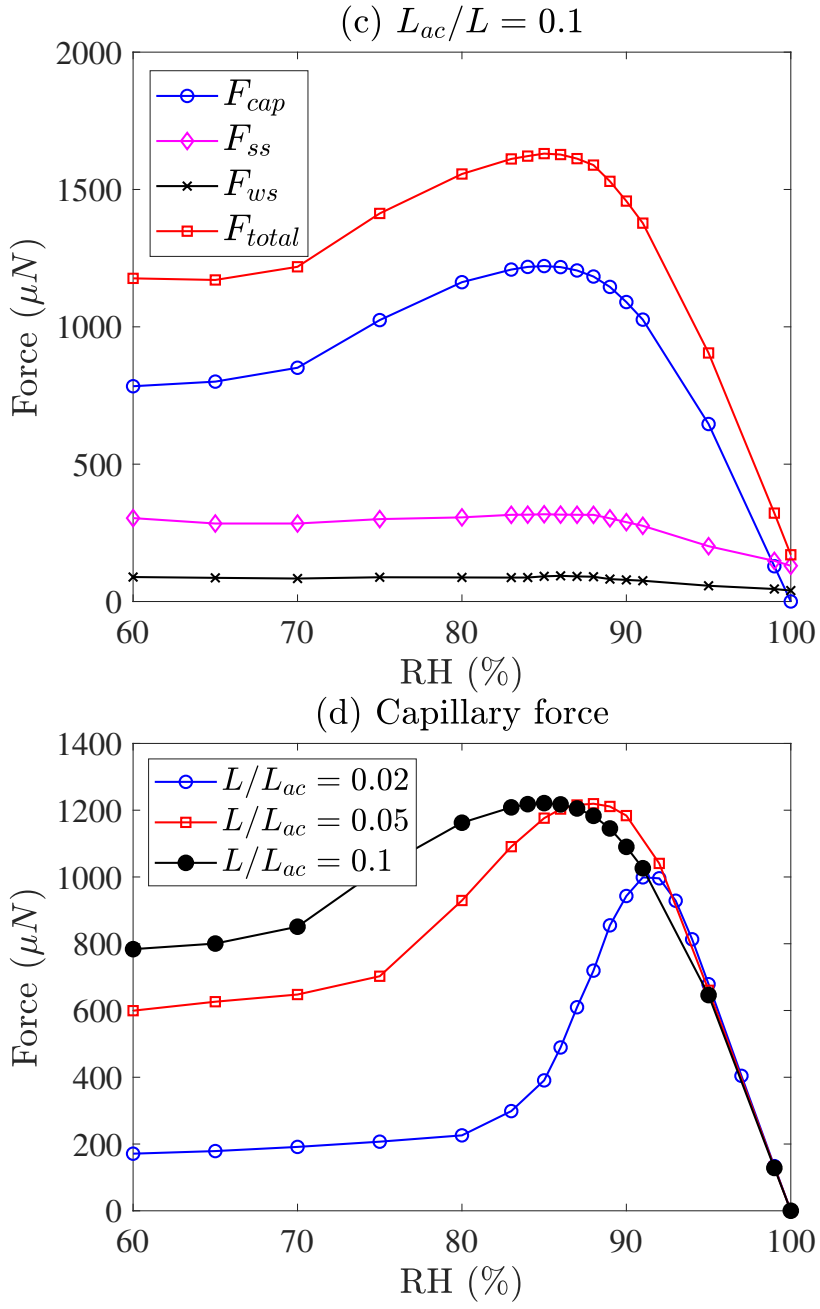

Figure 13: Variation of different adhesive components vs. RH at three different auto-correlation lengths (a-c) and (d) comparison of the capillary force component

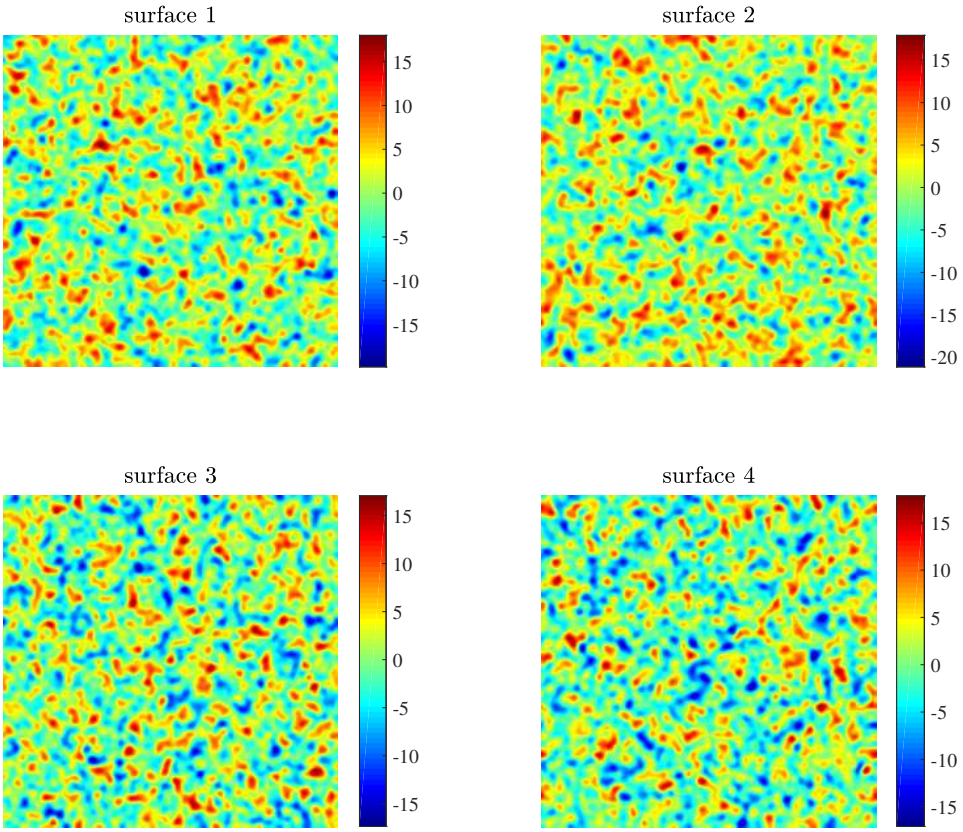

Figure 14: Roughness heights (in nm) of four different Gaussian rough surfaces with identical auto-correlation length ($L_{ac}/L = 0.02$), and RMS values ($\sigma = 5nm$); surface 1 is the same as Figure 10(a)

One should also note that the solid-solid and water-solid interaction forces (F_{ss} F_{ws} and respectively) are rather constant with RH, however larger for longer auto-correlation lengths. Furthermore, these two components are quite smaller than the capillary. In other words, the capillary force has the major contribution to the total adhesive force (F_{total}).

With the intention to confirm the repeatability of the presented simulations, the capillary development for three different realizations of the same statistical parameters of Fig. 10(a), shown in Fig. 14, is investigated. The variation of the capillary force with RH under $500\mu N$ of the normal load is depicted in Fig. 15. As it can be seen, the capillary force for each of the rough interfaces lies within a quite narrow band and they all follow the

same curve. Hence, one can conclude that the surface shown in Fig. 10(a) is representative of its corresponding statistical parameters and the observed trend for the capillary force holds for other similar surfaces. In addition, similar trends can be expected for surfaces shown in Fig. 10(b and c).

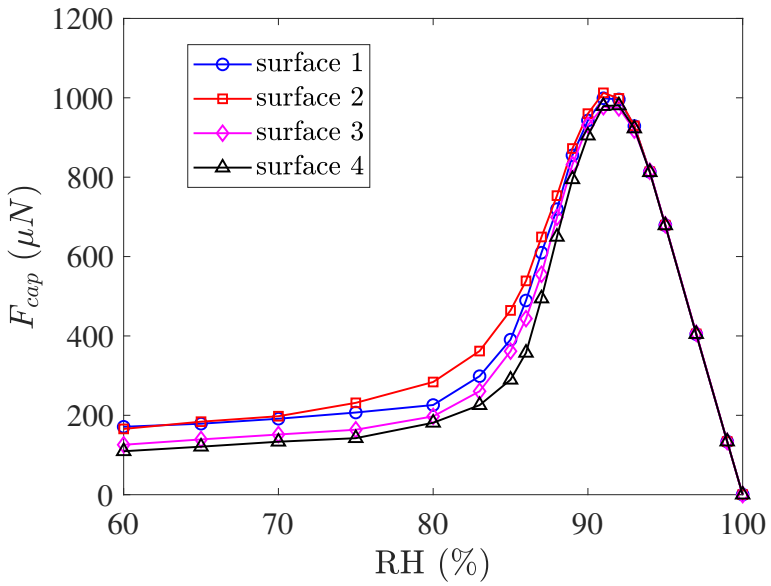

Figure 15: The comparison of the capillary force for 4 different Gaussian rough surfaces with identical auto-correlation lengths and RMS values ($L_{ac}/L = 0.02,\ \sigma = 5nm$)

In order to see how roughness RMS can affect the capillary force variation, the surface shown in Fig. 10(a) is scaled in vertical direction to generate surfaces with RMS values of $7.5nm$ and $10nm$ while the auto-correlation length is kept the same. It is noted that this scaling does not change higher order statistical parameters of the surface such as skewness and kurtosis as long as the arithmetic average of the roughness heights is zero. The variation of the capillary force with RH for these surfaces with different RMS values is illustrated in Fig. 16. This figure suggests that as the RMS values decreases, the capillary force increases and its peak is shifted to a lower RH value. This is, to some extent, similar to the effect of auto-correlation length (see Fig. 13(d)). In both cases, smaller local curvatures, due to smaller RMS value and or longer auto-correlation length, results in higher capillary force and shifting the

capillary peak to a lower RH value.

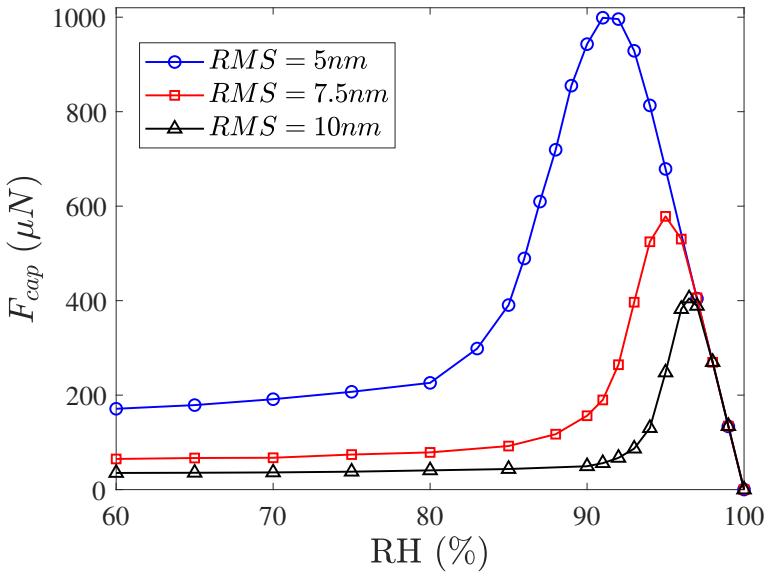

Figure 16: The comparison of the capillary force for a rough interface with different RMS values

Another parameter that affects the capillary force at the contact of two rough surfaces is surface deformation. The more the surfaces deform and get closer to one another, the higher chance for larger micro-menisci to form and thus, a larger capillary force. Fig. 17 shows the variation of the capillary force at the three rough interfaces of Fig. 10 for three quite different values of the external normal load. It appears conspicuous that the normal load can change not only the peak location (the corresponding RH value) and value of the capillary force but also the whole shape of the curve. In other words, it can change the width of the peak as well; specifically, Fig. 17(c) implies that there is no increase in the capillary force with RH for the normal load of $5000\mu N$ since the deformation is so large and the contacting surfaces get so close that even at 60% of RH the major part of the contact is covered by meniscus and any further increase in RH does not remarkably change it so that the decrease in the capillary pressure steadily decreases the capillary force, too. At very high RH values (over 90%), the capillary force due to different normal loads is slightly different which is due to the minor difference in the non-contact area.

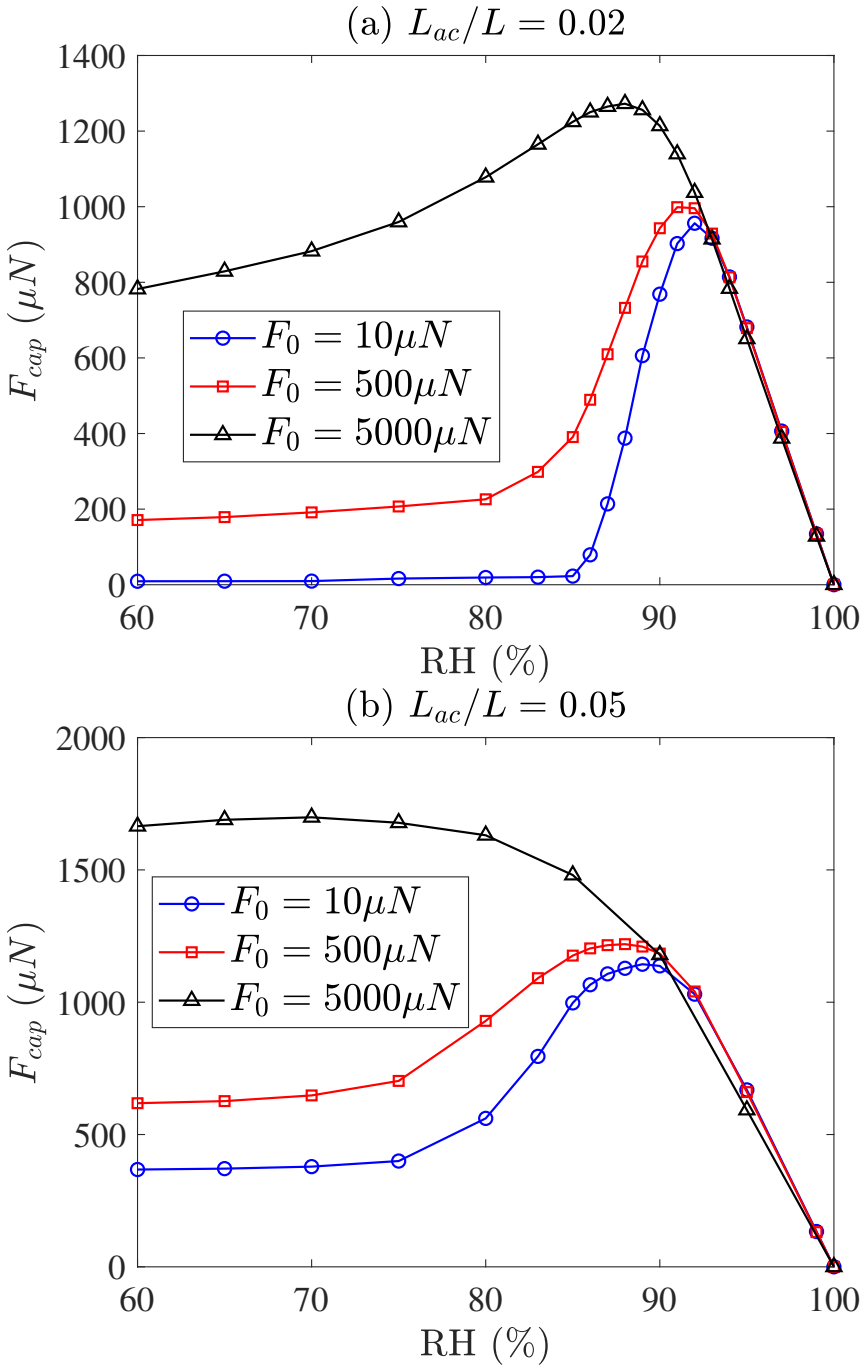
(a) $L_{ac}/L = 0.02$
F_{cap} (μN)
RH (%)
$F_0 = 10\mu N$
$F_0 = 500\mu N$
$F_0 = 5000\mu N$
(b) $L_{ac}/L = 0.05$
F_{cap} (μN)
RH (%)
$F_0 = 10\mu N$
$F_0 = 500\mu N$
$F_0 = 5000\mu N$

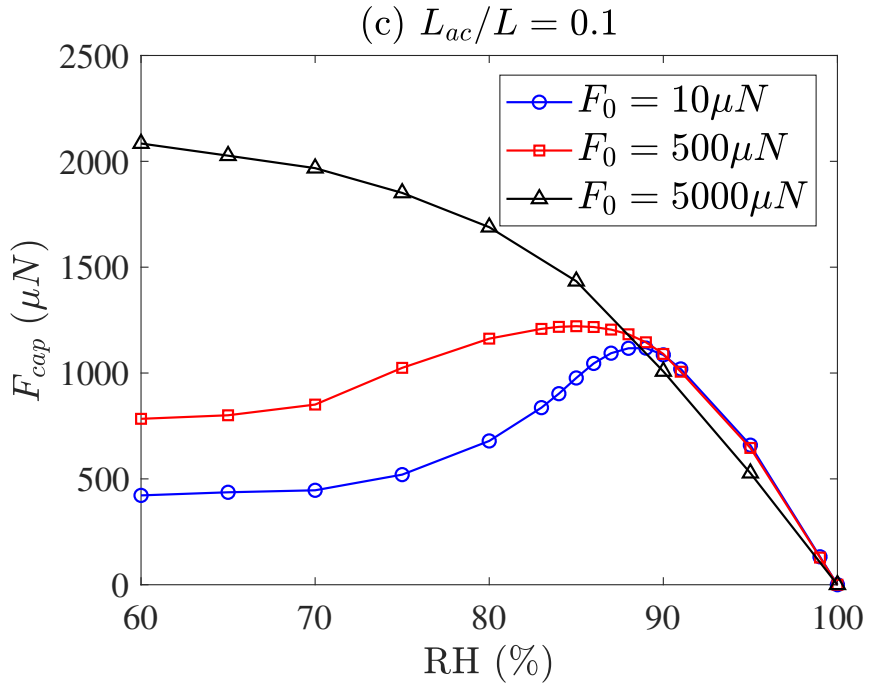

Figure 17: The effect of external normal load on the capillary force

One of the most significant steps in the proposed model is to find the uneven distribution of the water films on the contacting surfaces as described in section 2.2. Here, we are going to investigate how much the capillary force can deviate if we assume a uniform distribution of the water films. When the distribution is uniform, the water film is thicker at the high asperities. This is much more prominent for surfaces with shorter auto-correlation lengths due to the large local gradients which force the water flow towards the valleys. Consequently, at lower RH values, the probability of forming micro-menisci around non-contact asperities is higher. In addition, as the film is thicker around the contacting asperities (compared to the uneven distribution), the micro-menisci islands around these asperities develop to a farther distant. Combining these two effects, at lower RH values, a larger capillary force is expected when the water film distribution is uniform. This point can be easily noticed in Fig. 18 which compares the capillary force variation with RH between the variable and uniform thickness for the three rough interfaces of Fig. 13 under $500\mu N$ of the normal load. At larger RH values, micro-menisci become larger so that they can merge and form larger unified menisci. At such values, the

surface deformations are greater (due to larger capillary force) so that the accumulated water in the valleys can touch the counter surface and help menisci develop to a farther distant. Considering the fact that there is more water accumulated in the valleys when the uneven distribution of the water film is implemented, the resulting capillary area (and therefore the capillary force) is greater. These two regimes are less dominant as the auto-correlation lengths increase since the difference between uneven distribution and the uniform thickness is less (as explained before). For very large RH values, over 90%, there is no significant difference between the calculated capillary forces as almost all of the non-contact area is covered by a meniscus.

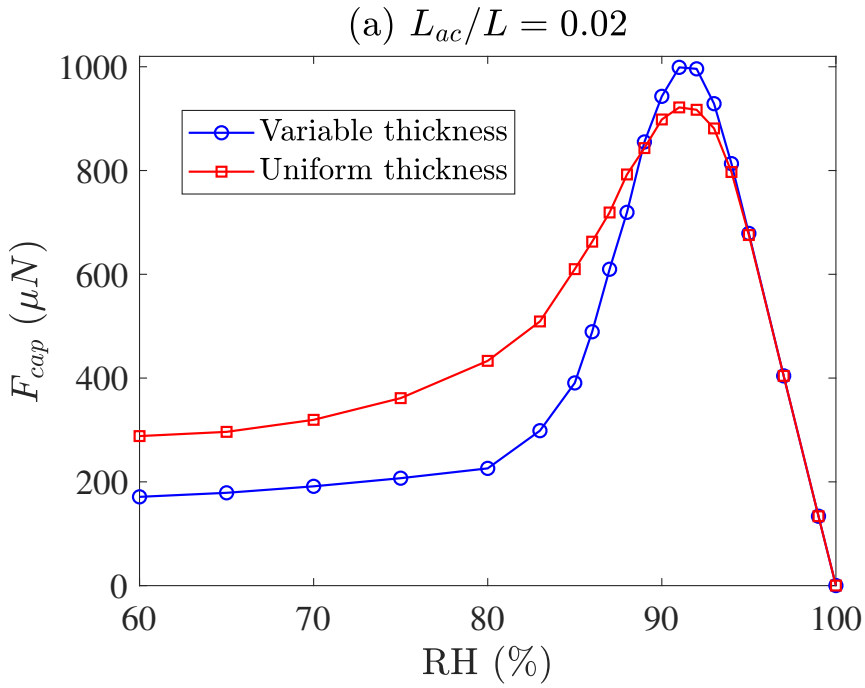

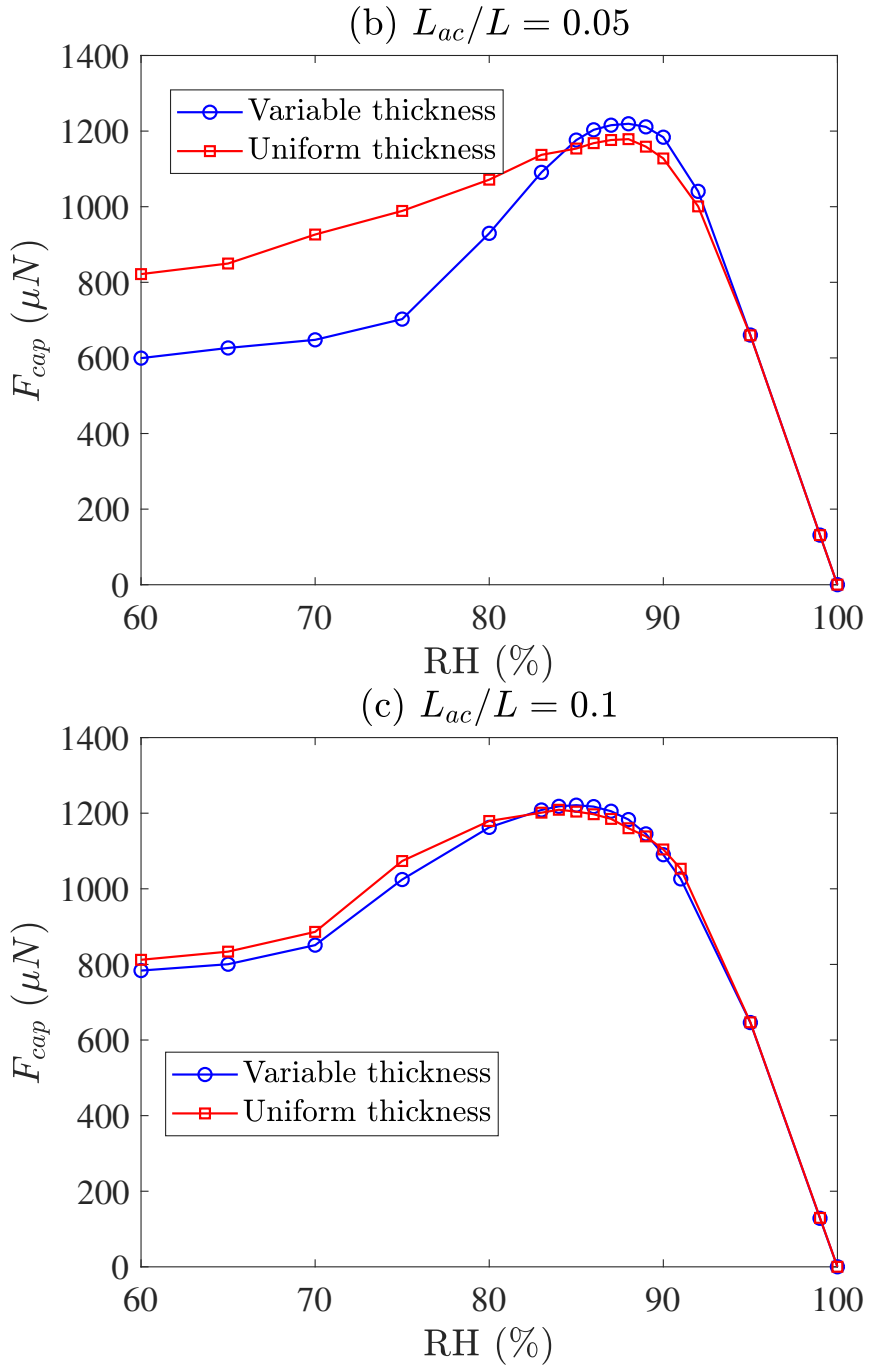

Figure 18: The comparison of the capillary force with uniform and variable thickness of the water film over the rough surfaces

5 Conclusions

A boundary element model for the adhesive contact of two rough surfaces in the presence of a thin water film adsorbed on the contacting surface is proposed. The distribution of this water film was considered to be uneven over the rough surface. Three different adhesive force components were considered. The capillary force, as the major contributor to the total adhesive force, appeared to dominate the solid-solid and water-solid interaction forces. In addition, the capillary force first increased with RH and then decreased as a results of variation in both capillary area and capillary pressure. The maximum of the capillary force was found to be larger and at a lower RH for surfaces with smaller curvatures (here longer auto-correlation length and or smaller roughness rms). The normal force also appeared to be a key factor as it can change not only the maximum capillary force and the corresponding RH but also the entire curve of capillary force versus RH.

6 Acknowledgment

The authors would like to express their gratitude to ASML Company, Veldhoven, the Netherlands (www.asml.com) for the financial support of this research project. This research was carried out under project number S61.7.13492 in the framework of the Partnership Program of the Materials innovation institute M2i (www.m2i.nl) and the Netherlands Organization for Scientific Research NWO (www.nwo.nl).

Bibliography

[1] R. S. Bradley, "The cohesive force between solid surfaces and the surface energy of solids," *Philosophical Magazine and Journal of Science*, vol. 86, pp. 853–862, 1932.

[2] K. L. Johnson, K. Kendall, and A. D. Roberts, "Surface Energy and the Contact of Elastic Solids," *Proceedings of the Royal Society of London. Series A, Mathematical and Physical Sciences*, vol. 324, pp. 301–313, 1971.

[3] B. Derjaguin, V. Muller, and Y. Toporov, "Effect of contact deformations on the adhesion of particles," *Journal of Colloid and Interface Science*, vol. 53, no. 2, pp. 314–326, 1975.

[4] D. Maugis, "Adhesion of spheres: The JKR-DMT transition using a dugdale model," *Journal of Colloid And Interface Science*, vol. 150, no. 1, pp. 243–269, 1992.

[5] Z. Song and K. Komvopoulos, "Adhesive contact of an elastic semi-infinite solid with a rigid rough surface: Strength of adhesion and contact instabilities," *International Journal of Solids and Structures*, vol. 51, no. 6, pp. 1197–1207, 2014.

[6] M. Gotzinger and W. Peukert, "Particle adhesion force distributions on rough surfaces," *Langmuir*, vol. 20, no. 13, pp. 5298–5303, 2004.

[7] S. S. Cho and S. Park, "Finite element modeling of adhesive contact using molecular potential," *Tribology International*, vol. 37, no. 9, pp. 763–769, 2004.

[8] R. A. Sauer, "A Computational Model for Nanoscale Adhesion between Deformable Solids and Its Application to Gecko Adhesion," *Journal of Adhesion Science and Technology*, vol. 24, no. 11-12, pp. 1807–1818, 2010.

[9] G. Carbone and E. Pierro, "The Influence of the Fractal Dimension of Rough Surfaces on the Adhesion of Elastic Materials," *Journal of Adhesion Science and Technology*, vol. 26, no. 22, pp. 2555–2570, 2012.

[10] M. Ciavarella, "A note on the possibility of roughness enhancement of adhesion in Persson's theory," *International Journal of Mechanical Sciences*, vol. 121, no. February 2016, pp. 119–122, 2017.

[11] J. Greenwood and J. Williamson, "Contact of Nominally Flat Surfaces," *Proceedings of the Royal Society of London . Series A , Mathematical and Physical Published*, vol. 295, no. 1442, pp. 300–319, 1966.

[12] M. H. Muser, "A dimensionless measure for adhesion and effects of the range of adhesion in contacts of nominally flat surfaces," *Tribology International*, pp. 1–7, 2015.

[13] N. Mulakaluri and B. N. J. Persson, "Adhesion between elastic solids with randomly rough surfaces: Comparison of analytical theory with molecular-dynamics simulations," *EPL (Europhysics Letters)*, vol. 96, no. 6, p. 66003, 2011.

[14] C. Yang and B. N. J. Persson, "Contact mechanics: contact area and interfacial separation from small contact to full contact," *Journal of Physics: Condensed Matter*, vol. 20, no. 21, 2008.

[15] V. Rey, G. Anciaux, and J.-F. Molinari, "Normal adhesive contact on rough surfaces: efficient algorithm for FFT-based BEM resolution," *Computational Mechanics*, vol. 60, no. 1, pp. 69–81, 2017.

[16] M. Bazrafshan, M. B. de Rooij, M. Valefi, and D. J. Schipper, "Numerical method for the adhesive normal contact analysis based on a Dugdale approximation," *Tribology International*, vol. 112, no. April, pp. 117–128, 2017.

[17] D. S. Rimai, D. J. Quesnel, L. P. DeMejo, and M. T. Regan, "Toner to photoconductor adhesion," *Journal of Imaging Science and Technology*, vol. 45, pp. 179–186, 2001.

[18] B. N. J. Persson, "Capillary adhesion between elastic solids with randomly rough surfaces," *Journal of Physics: Condensed Matter*, vol. 20, no. 31, p. 315007, 2008.

[19] R. Ardito, A. Frangi, F. Rizzini, and A. Corigliano, "Evaluation of adhesion in microsystems using equivalent rough surfaces modeled with spherical caps," *European Journal of Mechanics, A/Solids*, vol. 57, pp. 121–131, 2016.

[20] N. Zarate, A. Harrison, J. Litster, and S. Beaudoin, "Effect of relative humidity on onset of capillary forces for rough surfaces," *Journal of Colloid and Interface Science*, vol. 411, pp. 265–272, 2013.

[21] N. Prodanov, W. B. Dapp, and M. H. Müser, "On the Contact Area and Mean Gap of Rough, Elastic Contacts: Dimensional Analysis, Numerical Corrections, and Reference Data," *Tribology Letters*, vol. 53, no. 2, pp. 433–448, 2014.

[22] M. Ciavarella, "A very simple estimate of adhesion of hard solids with rough surfaces based on a bearing area model," *Meccanica*, pp. 1–10, 2017.

[23] A. I. Vakis, V. A. Yastrebov, J. Scheibert, C. Minfray, L. Nicola, D. Dini, A. Almqvist, M. Paggi, S. Lee, G. Limbert, J. F. Molinari, G. Anciaux, R. Aghababaei, S. Echeverri Restrepo, A. Papangelo, A. Cammarata, P. Nicolini, C. Putignano, G. Carbone, M. Ciavarella, S. Stupkiewicz, J. Lengiewicz, G. Costagliola, F. Bosia, R. Guarino, N. M. Pugno, and M. H. Müser, "Modeling and simulation in tribology across scales: An overview," *Tribology International*, 2018.

[24] W. B. Hanies, "Studies in the physical properties of soils: III. Observations on the electrical conductivity of soils," *The Journal of Agricultural Science*, vol. 15, pp. 536–543, 1925.

[25] R. A. Fisher, "On the capillary forces in an ideal soil; correction of formulae given by WB Haines," *The Journal of Agricultural Science*, vol. 16, no. 03, pp. 492–505, 1926.

[26] E. J. De Souza, M. Brinkmann, C. Mohrdieck, and E. Arzt, "Enhancement of capillary forces by multiple liquid bridges," *Langmuir*, vol. 24, no. 16, pp. 8813–8820, 2008.

[27] C. Gao, "Theory of menisci and its applications," *Applied physics letters*, vol. 13, no. 71, p. 1801, 1997.

[28] A. D. Lazzer, M. Dreyer, and H. J. Rath, "Particle - Surface Capillary Forces," no. 3, pp. 4551–4559, 1999.

[29] L. Sirghi, N. Nakagiri, and K. Sugisaki, "Effect of Sample Topography on Adhesive Force in Atomic Force Spectroscopy Measurements in Air," *Langmuir*, no. 10, pp. 0–4, 2000.

[30] Y. G. Tselishchev and V. A. Val'tsifer, "Influence of the type of contact between particles joined by a liquid bridge on the capillary cohesive forces," *Colloid Journal of the Russian Academy of Sciences: Kolloidnyi Zhurnal*, vol. 65, no. 3, pp. 385–389, 2003.

[31] C. D. Willett, M. J. Adams, S. A. Johnson, and J. P. K. Seville, "Capillary bridges between two spherical bodies," *Langmuir*, vol. 16, no. 24, pp. 9396–9405, 2000.

[32] C. Gao, P. Dai, A. Homola, and J. Weiss, "Meniscus Forces and Profiles: Theory and Its Applications to Liquid-Mediated Interfaces," *Journal of Tribology*, vol. 120, no. 2, pp. 358–368, 1998.

[33] X. Xiao and L. Qian, "Investigation of humidity-dependent capillary force," *Langmuir*, vol. 16, no. 21, pp. 8153–8158, 2000.

[34] M. A. Yaqoob, M. B. de Rooij, and D. J. Schipper, "Design of a vacuum based test rig for measuring micro adhesion and friction force," *High Performance Structure and Materials*, vol. 124, no. VI, pp. 261–274, 2012.

[35] D. B. Asay and S. H. Kim, "Effects of adsorbed water layer structure on adhesion force of silicon oxide nanoasperity contact in humid ambient," *Journal of Chemical Physics*, vol. 124, no. 17, 2006.

[36] X. Xue and A. A. Polycarpou, "An improved meniscus surface model for contacting rough surfaces," *Journal of Colloid and Interface Science*, vol. 311, no. 1, pp. 203–211, 2007.

[37] M. P. Boer, "Capillary adhesion between elastically hard rough surfaces," *Experimental Mechanics*, vol. 47, no. 1, pp. 171–183, 2007.

[38] L. Wang and S. Régnier, "A More General Capillary Adhesion Model Including Shape Index: Single-Asperity and Multi-Asperity Cases," *Tribology Transactions*, vol. 58, no. 1, pp. 106–112, 2014.

[39] S. You and M. P. Wan, "Mathematical models for the van der waals force and capillary force between a rough particle and surface," *Langmuir*, vol. 29, no. 29, pp. 9104–9117, 2013.

[40] Y. F. Peng, Y. B. Guo, and Y. Q. Hong, "An Adhesion Model for Elastic-Contacting Fractal Surfaces in the Presence of Meniscus," *Journal of Tribology*, vol. 131, no. 2, p. 024504, 2009.

[41] X. Tian and B. Bhushan, "A numerical three-dimensional model for the contact of rough surfaces by variational principle," *J. Tribol.*, vol. 1, no. January, 1996.

[42] J. F. Lin and S. C. Chen, "Calculations of the Meniscus Force and the Contact Force Formed in the Microcontacts of a Rough Surface and a Smooth, Rigid Surface with a Thin Water Film," *Journal of Mechanics*, vol. 24, no. 01, pp. 1–11, 2008.

[43] A. Rostami and J. L. Streator, "Study of liquid-mediated adhesion between 3D rough surfaces: A spectral approach," *Tribology International*, vol. 84, pp. 36–47, 2015.

[44] J.N. Israelachvili, *Intermolecular and surface forces*, vol. 53. 2013.

[45] B. Figliuzzi, D. Jeulin, A. Lemaître, G. Fricout, J.-J. Piezanowski, and P. Manneville, "Numerical simulation of thin paint film flow," *Journal of Mathematics in Industry*, vol. 2, no. 1, p. 1, 2012.

[46] K. R. Mecke, "Thermal fluctuations of thin liquid films," *J. Phys.: Condens. Matter*, vol. 13, pp. 4615–4636, 2001.

[47] Q. Wang and Y. Chung, *Encyclopedia of tribology*. 2013.

[48] H.-J. Butt, K. Graf, and M. Kappl, *Physics and chemistry of interfaces*. Weinheim: WILEY_VCH GmbH & Co. KGaA, 2003.

[49] K. L. Johnson, *Contact Mechanics*. Cambridge: Cambridge University Press, 1985.

[50] D. B. Asay and S. H. Kim, "Evolution of the adsorbed water layer structure on silicon oxide at room temperature.," *The journal of physical chemistry. B*, vol. 109, no. 35, pp. 16760–16763, 2005.

[51] F. W. DelRio, M. L. Dunn, and M. P. de Boer, "Capillary adhesion model for contacting micromachined surfaces," *Scripta Materialia*, vol. 59, no. 9, pp. 916–920, 2008.

[52] M. Ciavarella and A. Papangelo, "Discussion of Measuring and Understanding Contact Area at the Nanoscale: A Review (Jacobs, T. D. B.,

and Ashlie Martini, A., 2017, ASME Appl. Mech. Rev., 69 (6), p. 061101)," *Applied Mechanics Reviews*, vol. 69, no. 6, p. 065502, 2017.

[53] T. Jacobs and A. Martini, "Review : Measuring and Understanding Contact Area at the Nanoscale," *Applied Mechanics Reviews*, vol. 69, no. November 2017, 2017.

Paper C

The Effect of Surface Roughness on Adhesion: Experimental Evaluation of a BEM Model

M. Bazrafshan[1,2*], M.B. de Rooij[2], E.G. de Vries[2], and D.J. Schipper[2]

[1] *Materials innovation institute (M2i), van der Burghweg 1, 2628 CS Delft, Netherlands*
[2] *Laboratory for Surface Technology and Tribology, Department of Engineering Technology, University of Twente, P.O. box 217, 7500AE, Enschede, Netherlands*

Abstract

Atomic Force Microscopy (AFM) is an appropriate method to study the adhesion between two surfaces. Using a micron-size silicon dioxide colloidal probe, the adhesion at a rough interface of the probe and a substrate of either a silicon wafer (Si) or a thick silicon dioxide film (SiO_2) is investigated. Pull-off force, as an indicative of adhesion strength, is measured in ambient and vacuum conditions. Going from ambient to vacuum conditions, there is a steep increase in the measured pull-off force due to the removal of a hydrocarbon contamination film and or a change in the topography of the colloidal probe. Measurements in ambient after vacuum show a slight increase in the pull-off force due to the small increase in the water film thickness adsorbed on the substrate and probe after the samples are exposed to ambient conditions. In addition, a recently developed BEM (Boundary Element Method) model is implemented to predict the pull-off force at these interfaces using the measured topographies of the contacting surfaces and the humidity dependent adsorbed water film thickness. Although simulations are in agreement with experiments for the ambient conditions after vacuum, the BEM model predicts a lower pull-off force than experiments in vacuum.

Keywords: Adhesion, Roughness, Pull-off Force, Boundary Element Method, Atomic Force Microscopy

Nomenclature

A_{1w2}	Hamaker constant for bodies 1 and 2 contacting across medium w
A_c	contact area
e_w	water film thickness
F_0	external normal force
$F_{pull-off}$	pull-off force
$g(x, y)$	separation profile
h_0	maximum allowable gap for adhesion
$P(x, y)$	pressure profile
P_{ws}	water-solid adhesive pressure
R_g	universal gas constant
R_t	AFM cantilever tip radius of curvature

RH	Relative Humidity
r_k	Kelvin radius
S	equivalent meniscus height
T	Temperature
V	Molar volume of water
z_0	Equilibrium distance
ΔP_{cap}	capillary pressure
$\Delta\gamma$	work of adhesion
Ω	Computation domain
Ω_{ws}	water-solid interaction area
Ω_{wetted}	meniscus-wetted areas
γ	surface tension
$\gamma_{1,2}$	surface energy of bodies 1 and 2
γ_{12}	interfacial energy

1 Introduction

Along with the rapid development of MEMS/NEMS (Micro/Nano Electro-Mechanical Systems), the role of adhesion, as a dominant issue in achieving a high level of reliability and durability, is becoming more vital everyday. More specifically, controlling friction at the mating surfaces in such nanotribology applications is a challenge as it can be strongly affected by adhesion [1–8]. Therefore, a comprehensive understanding of this phenomenon at the interface of the mating components of such devices is a key step in designing such versatile devices.

The tendency of two surfaces to stick to one another is called adhesion. It can be due to one or a combination of physical interactions such as van der Waals, capillary, electrostatic forces, and chemical bonds like hydrogen bonding. The presence and strength of each of these contributors depend on the contacting materials and the medium through which the contact has formed. The energy and force required to separate two contacting surfaces are called work of adhesion, $\Delta\gamma$, and pull-off force, $F_{pull-off}$, respectively. Atomic Force Microscopy (AFM) is usually used to measure the pull-off force at the interface of the cantilever tip and the counter surface. Having the tip radius, R_t, JKR (Johnson-Kendall-Roberts) or DMT (Derjaguin-Muller-Toporov) are typically implemented (depending on the strength of adhesion compared to the elasticity of the contacting surfaces) to estimate the work

of adhesion due to van der Waals forces as [9, 10]:

$$\Delta\gamma_{JKR} = \frac{2F_{pull-off}}{3\pi R_t} \tag{1}$$

$$\Delta\gamma_{DMT} = \frac{F_{pull-off}}{2\pi R_t} \tag{2}$$

Van der Waals forces are the dominant contributor to the total adhesion force in a vacuum or a very dry environment. In ambient, however, the vapor in the humid environment condenses onto the surfaces and fills in the gaps and holes to form meniscus bridges. In such cases, the total adhesion force is dominated by the capillary force. Therefore, the strength of adhesion is in direct relation with the Relative Humidity (RH) of the environment as well as the hydrophilicity of the surfaces in contact. There are various research studies on AFM measurements of the pull-off force, with different tip materials such as Si, SiO_2, and Si_3N_4, either in vacuum or over a range of RH from 2% up to 100% [11–21]. They have observed different trends in the pull-off force versus RH.

To analyze the work of adhesion, no matter in which environment the experiments are conducted, the cantilever tip radius, which has to be known, is typically measured using a Scanning Electron-Microscope (SEM). However, the uncertainty in the measured radius of such nanosize tips is still an issue. Moreover, the resulting high contact pressures can deform the tip radius quickly and introduce an error to the measurements. Using cantilevers with a colloidal probe is an appropriate alternative to avoid such issues. For this, a micron-size sphere of desired material, such as SiO_2, is glued to the very end of a tipless cantilever. Ducker et al. were the first who implemented this technique by attaching a $3.5\mu m$ SiO_2 sphere to a cantilever to measure adhesion [22]. Fukunishi and Mori measured the pull-off force between an $8\mu m$ glass colloidal probe and two hydrophilic and hydrophobic substrates for several RH values ranging from 10% to 80% [23]. They observed a monotonic increase in the pull-off force as a function of RH for the hydrophilic substrate due to strong capillary condensation. For the hydrophobic substrate, however, the measured forces did not change with RH because of the weak capillary condensation. Biggs et al. observed no change in the measured pull-off force between a $15\mu m$ glass particle and a glass substrate for RH below 60% [24]. However, there was a jump in the measured forces right above 60% of RH resulting from the capillary force.

The mentioned studies have attempted to explain the variation of the pull-off force versus RH using an ideally smooth ball-on-flat configuration. In reality however, even such micron-size probes have rough surfaces which drastically influence the adhesion at the contact interface. In other words, the real area of contact at the snap-off moment is far smaller than the circular contact area calculated by such analytical models. This fact has been addressed in several research studies. Ata et al. measured the adhesion force between a glass colloidal probe and alumina, silica, and titanium-coated silicon wafers for several RH values [25]. They observed a difference between theoretically expected values for the pull-off force and the measured ones due to the roughness of the colloidal probe. Jones et al. studied the pull-off force at the interface of a flat glass or a silicon wafer and a silicon AFM tip or glass balls of different sizes for various RH values ranging from 5% up to 90% [26]. They found that the measured pull-off force by the sharp silicon tips was close to the predicted values by Laplace-Kelvin theory. Though, they measured lower values with the colloidal probes than the predicted forces due to the probe surface roughness. Using a flat silicon tip with $2\mu m$ of diameter, Colak et al. investigated the pull-off force from smooth and chemically etched silicon wafers over a range of RH [27]. The measured pull-off force at the rough surface of the etched wafer was an order of magnitude lower than that of the smooth wafer. Since the measured pull-off force for the contact of a silicon wafer and glass colloidal probes did not correlate with the radii of the probes, Yang et al. developed a multi-asperity elastic-plastic model to explain the effect of probe surface roughness on the measured pull-off force under dry conditions (RH $< 30\%$) [28]. Matope et al. fitted a roughness rms-dependent curve on the measured pull-off force for the contact of a silica particle and several rough metallic films coated on silicon wafers [29]. They observed a rapid decrease in the pull-off force when the roughness rms increased from $0.3nm$ to $1nm$. Further increase in the roughness, however, did not change the pull-off force.

Despite the extensive research on adhesion using AFM with either sharp cantilevers or cantilevers with a colloidal probe, the measured surface topography of the cantilever tip and the substrate has never been considered to explain the roughness effect on the measured pull-off forces. It is noted that the rms roughness is not the only parameter describing the random nature of the roughness. In addition, multi-asperity models come along with several issues such as the lack of interaction between neighboring asperities and considering merely the summits and discarding the rest of the surface. The ideal case, thus, is to use the exact profile of the contacting surfaces as measured. This paper focuses on experimental

evaluation of a recently developed BEM (Boundary Element Method) model for the adhesive contact at a rough interface, where the measured topography of the contacting surfaces should be implemented as an input [30]. The contact between a cantilever with a colloidal probe and a substrate is made both in vacuum and in ambient conditions in order to investigate the respective contribution of van der Waals and capillary forces. The topography of both the colloidal probe and the substrates is measured with AFM using a sharp tip. The results of this study can help to predict the adhesive behavior at a rough interface and also improve the measurement of surface energy of the materials.

2 BEM model

This section summarizes a BEM model which will be used for comparison to the experimental results. This model deals with the adhesive elastic contact at the rough interface of two surfaces onto which thin water films are adsorbed due the humid environment.

In a vacuum environment, since there is no water film, the van der Waals forces between the contacting solids are responsible for the adhesion force, as shown in Figure 1. This figure shows the adhesive contact at the rough interface of two surfaces, where a normal force of F_0 is exerted on it. Here, a constant negative stress, $-\sigma_0$, pulls the surfaces toward one another right around the contacting and at the near-contacting areas as far as the local separation is smaller than a critical value, h_0, given by:

$$h_0 = \frac{\Delta\gamma}{\sigma_0} = 0.974 z_0 \tag{3}$$

where $\Delta\gamma$ and σ_0 are the work of adhesion and maximum tensile stress of the Lennard-Jones potential. In addition, z_0 is the equilibrium distance ranging from $0.2nm$ to $0.4nm$. For this situation, the contact problem to be solved is to find the pressure distribution, $P(x, y)$, and separation profile, $g(x, y)$, at the interface in such a way to meet the following conditions [31]:

$$P(x,y) > -\sigma_0 \quad at \quad g(x,y) = 0 \tag{4a}$$

$$P(x,y) = -\sigma_0 \quad at \quad 0 < g(x,y) < h_0 \tag{4b}$$

$$P(x,y) = 0 \quad at \quad g(x,y) > h_0 \tag{4c}$$

$$\int_\Omega P(x,y)dxdy = F_0 \tag{4d}$$

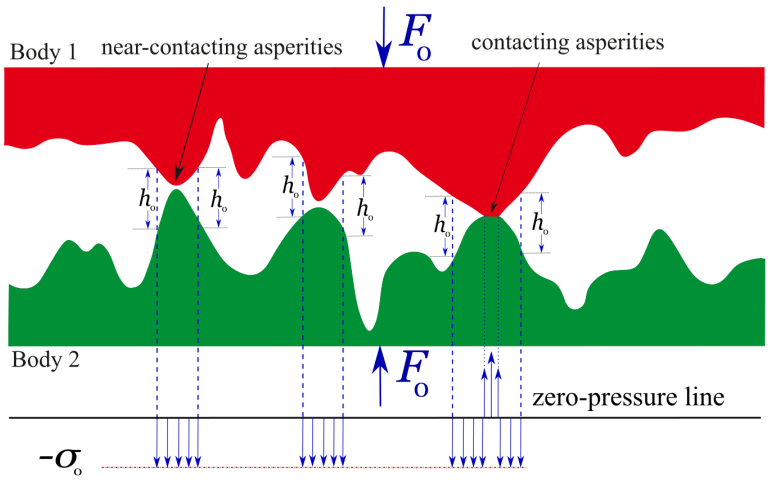

Figure 1: Schematic representation of the contact pressure profile in vacuum.

These conditions state that, first, at areas with no separation (where surfaces are touching, i.e. $g(x, y) = 0$), the pressure is greater than $-\sigma_0$. Second, the pressure takes a constant negative value, $-\sigma_0$ at separated areas with separation, yet, smaller than h_0 (i.e. $0 < g(x, y) < h_0$). Third, there is no pressure at separated areas with separation larger than h_0 (i.e. $g(x, y) > h_0$). In addition, the summation of the pressure distribution over the computation domain, Ω, needs to be equal to the external normal force. Bazrafshan et al. developed a BEM model as an extended version of Conjugate Gradient Method (CGM), originally developed by Polonsky and Keer [32], to solve this adhesive contact problem at a rough interface given by Eq. (4) [31].

In ambient, water vapor condenses from the humid environment to adsorb on the surfaces, fill in the gaps and holes, and form micro-menisci around the contacting and at the near-contacting asperities. Figure 2(a) illustrates the interface of two rough surfaces, where formation of such micro-menisci is mediated in presence of thin water films adsorbed from the humid environment. It is noted that the volume of adsorbed water onto a solid depends on the surface properties as well as the humidity of the environment. In order to locate these micro-menisci, the topographies of the contacting surfaces are combined. Moreover, the summation of the local water films thickness is put on a flat surface which touches the combine rough surface around the contacting areas and also non-contacting areas where the local separation is smaller than the

combined water films thickness (see Figure 2(b)). The extent to which a micro-meniscus extends, depends on the capillary rise given by:

$$S = 2r_k + e_1 + e_2 \tag{5}$$

where e_1 and e_2 are the water films thickness adsorbed on the surfaces before contact and r_k is the Kelvin radius, controlled by RH as:

$$r_k = \frac{\gamma V}{R_g T \log RH} \tag{6}$$

where V, R_g, γ, and T are the molar volume of water, the universal gas constant, water surface tension, and the absolute temperature, respectively. Three components contribute to the total adhesive force: capillary force, solid-solid, and water-solid van der Waals interactions. At areas wetted by a micro-meniscus, Ω_{wetted}, there is a constant capillary pressure pulling the surfaces toward each other (see Figure 2(b)):

$$\Delta P_{cap} = \frac{\gamma}{r_k} = \frac{R_g T \log RH}{V} \tag{7}$$

The solid-solid van der Waals interaction, the same as the one for vacuum conditions, is present right around the contacting and near-contacting areas, where the local separation is smaller than h_0. It must be noted that the solid-solid interaction and capillary pressure cannot be present together at a single spot as the critical separation of h_0 is smaller than a water molecule diameter and thus, no meniscus is present in such areas. Water-solid van der Waals interaction is also the third adhesive component which is actually a solid-solid interaction with water as the medium. This interaction is present at areas where a micro-meniscus has also formed, Ω_{ws}. However, this weak interaction decays very quickly with the local separation which makes its contribution very small, compared to the other two components:

$$P_{ws} = \frac{A_{1w2}}{6\pi e_w^3} \tag{8}$$

where A_{1w2} is the Hamaker constant for bodies 1 and 2 interacting through water, and e_w is the local separation which is filled with water.

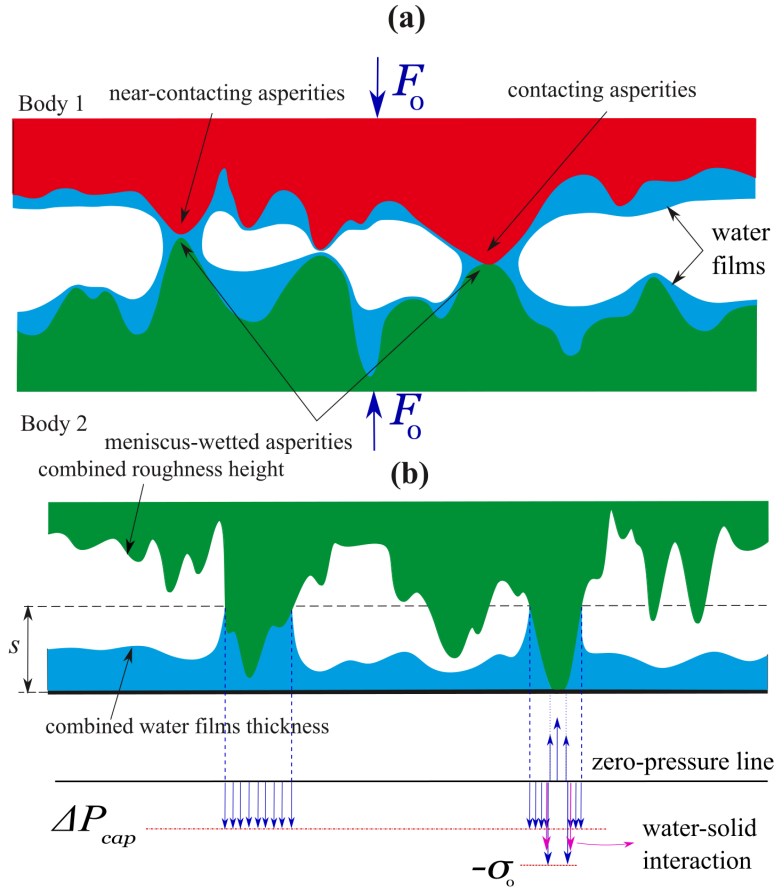

Figure 2: (a) Formation of micro-menisci at a rough interface in ambient and (b) schematic representation of the contact pressure profile.

In total, the contact problem, in ambient conditions, to be solved is to find the pressure distribution at the interface in such a way to meet the following conditions:

$$P(x,y) > -\sigma_0 \quad at \quad g(x,y) = 0 \tag{9a}$$
$$P(x,y) = -\sigma_0 \quad at \quad 0 < g(x,y) < h_0 \tag{9b}$$
$$P(x,y) = \Delta P_{cap} \quad at \quad \Omega_{wetted} \tag{9c}$$
$$P(x,y) = P_{ws} \quad at \quad \Omega_{ws} \tag{9d}$$
$$\int_\Omega P(x,y)dxdy = F_0 \tag{9e}$$

Bazrafshan et al. developed a BEM model to solve this adhesive contact problem in a humid environment in the presence of thin water films to meet the conditions given by Eq. 9. This model is more comprehensive than the one in [31] as it can also cover the vacuum conditions by simply neglecting the water films.

3 Experiments

The experiments are conducted using a vacuum AFM (Parksystems NX10) in a cleanroom. A pre-calibrated (with known spring constant) silicon cantilever with a $5\mu m$ SiO_2 colloidal probe is used to make contact with the substrate and measure the pull-off force. The substrate is either a bare silicon wafer (1 0 0) or a silicon wafer with a $300nm$ thick silicon dioxide layer on top. No cleaning is performed prior to the measurements as they have been protected in their original packages. The roughness of the colloidal probe is measured once before and another time after the measurements.

There are three states of measurements. State 1 refers to the initial pull-off force measurements in ambient conditions, where the temperature and relative humidity are 22°C and 35%, respectively. State 2 is a vacuum condition (HV) with 10^{-5}mbar of pressure which is left overnight, before performing the pull-off force measurements, to remove the organic contaminants from the substrate. Finally, state 3 starts 10 minutes after we vent the vacuum chamber and open it, where the samples are exposed to the ambient conditions again.

For each state and substrate, the pull-off force measurement is carried out on a 16×16 grid over a $10\mu m \times 10\mu m$ area (256 spots in total). The loading-unloading speed and the normal force setpoint are also set to $0.2\mu m/sec$ and $100nN$, respectively. The experiments are first conducted in state 1 for both substrates and then, the other two states are followed in a row for each substrate.

4 Simulations

In this section, the mentioned BEM model is implemented to predict the pull-off force at the interface of the colloidal probe and the substrate for given environmental conditions. Based on definition, the pull-off force is the largest negative force on the force-distance curve for an adhesive normal contact. Numerically, the negative normal force is increased gradually as

Table 2: Mechanical properties of the contacting surfaces

	Si	**SiO_2**
Elastic modulus (GPa)	130	64
Poission's ratio	0.28	0.17

long as the contact problem converges to a stable pressure profile. Therefore, the largest negative force for which the contact pressure still converges is known as the pull-off force.

The mechanical properties of the contacting surfaces are listed in Table 2. The van der Waals work of adhesion between two bodies of 1 and 2, with surface energies of γ_1 and γ_2, is defined as:

$$\Delta\gamma = \gamma_1 + \gamma_2 - \gamma_{12} \tag{10}$$

where γ_{12} is the interfacial energy and is neglected for the contact of identical materials [33]. The work of adhesion is here set to $\Delta\gamma = 2\gamma_{SiO_2} = 88mJ/m^2$ for both interfaces since there is always a native oxide layer on a silicon wafer [33].

An important input to the model is the surface topography of the contacting bodies. The AFM measurement of the roughness height of a $2\mu m \times 2\mu m$ area on the silicon wafer and silicon dioxide film is shown in Figure 3(a) and (b). Figure 3(c) compares the power spectral density (PSD) of these two surfaces. The higher power, C, of the SiO_2 surface roughness in lower wavevectors (q) suggests a rougher surface compared to Si. This is also indicated by the rms roughness of their surface profiles where $\text{rms}_{\text{Si}} = 0.46nm$ and $\text{rms}_{\text{SiO}_2} = 0.74nm$. The roughness height of the Si and SiO_2 samples has been measured at four more spots (not shown here) to be used for simulation and calculate the pull-off force at different spots. This helps to investigate the simulations sensitivity to different topographies while they have similar statistical properties.

Figure 4 illustrates the colloidal probe surface topography on a $2\mu m \times 2\mu m$ area before and after the measurements. A zoomed-in view reveals that, despite the low contact pressures (as we assume), the topography of the probe has changed during the experiments. As it will be discussed in the next section, this change of topography has a noticeable impact on the pull-off force.

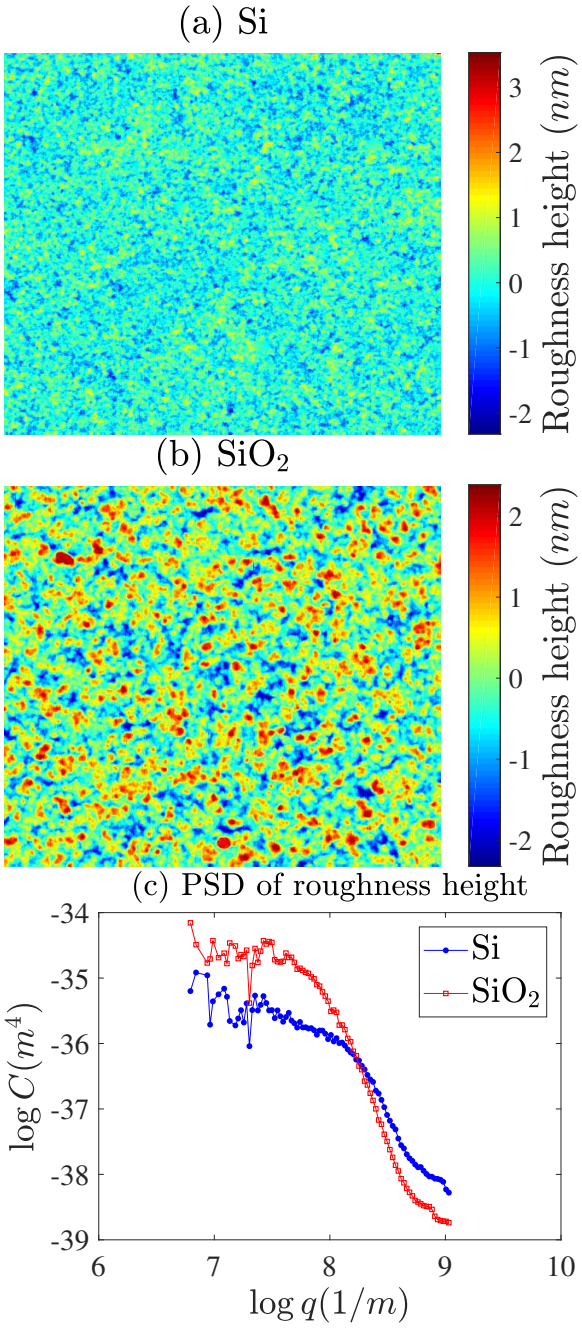

Figure 3: Roughness height of (a) Si and (b) SiO_2 substrates on a $2\mu m \times 2\mu m$ area (512×512 pixels) and (c) their PSD.

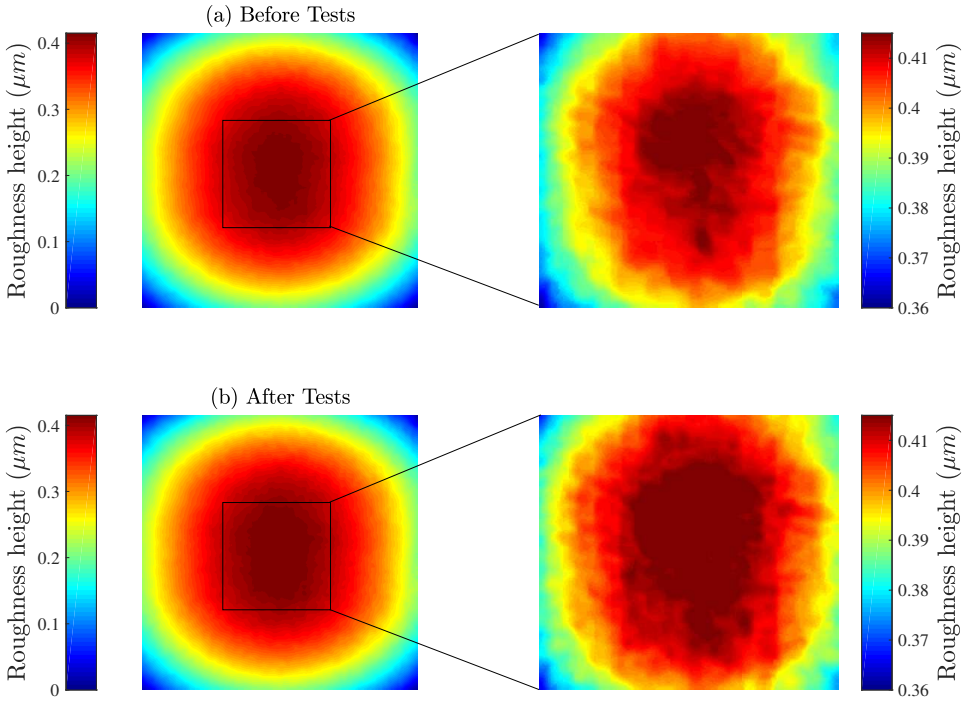

Figure 4: The zoomed-in view of the colloidal probe topography (a) before and (b) after the tests.

The relative humidity (RH) of the environment is another important input to the model as it determines how much water is adsorbed on the contacting surfaces. In other words, since the available adsorbed water film on the surfaces mediates the formation of micro-menisci at the contact interface and also contributes to the van der Waals interaction, the total adhesive force is, to a large extent, influenced by the RH of the environment. Asay and Kim [34] and Chen et al. [35] have measured the water vapor adsorption isotherms on SiO_2 and Si substrates at the room temperature, respectively. The RH in the ambient conditions, that we have conducted the measurements, is around 35%. At this RH, the water film thickness on SiO_2 and Si have reported to be approximately $0.9nm$ and $0.6nm$, respectively. Such thin films correspond to monolayers of water molecules and not its bulk form. Therefore, the formation of micro-menisci cannot be fully developed. Asay and Kim found out that, on the SiO_2 substrate, water starts to form its bulk at 30% of RH and completes at 60%. Thus, they suggested a linear relation between RH and the contribution coefficient of the capillary force in this range [34], which is

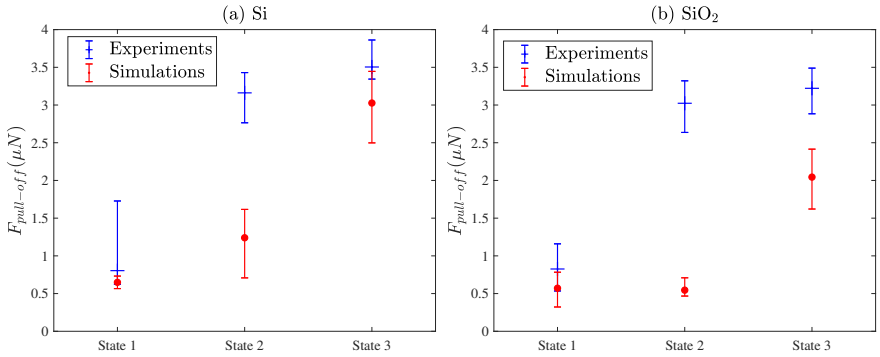

Figure 5: Comparison of measured (blue) and predicted (red) pull-off forces for (a) Si and (b) SiO_2 substrates.

equal to 0.17 for RH = 35%. Hence, in the simulation, only 17% of the total capillary pressure is considered. For the vacuum environment, it is also assumed that the RH is very low $(1-2\%)$ and also, there are no water molecules. Nevertheless, the water molecules are the last to disappear in vacuum and it might take days or even weeks. This means that water monolayers are always on the substrates during the measurements and they cannot be easily eliminated. However, for the simulation in the present study, we assume that there is no water in the vacuum environment influencing the pull-off force.

5 Results and discussion

The spread (the mean value with error bars) of measured and predicted pull-off forces at the mentioned three states are plotted in Figure 5(a) and (b) for the Si and SiO_2 substrates, respectively. As mentioned before, the measurements have been performed at 256 spots for each state to investigate the repeatability and effect of topography change on the experimental results. The simulations have also performed with the five topographies measured on each substrate.

For both cases, there is a steep rise in the measured pull-off force from the ambient conditions of state 1 to the vacuum conditions of state 2. This increase seems to be in contrast to the theory as, in vacuum, the interface experiences only van der Waals forces between the solids, while in ambient conditions, the presence of micro-menisci and van der Waals contribution of the water-solid interaction add up to the total adhesive force. Comparison

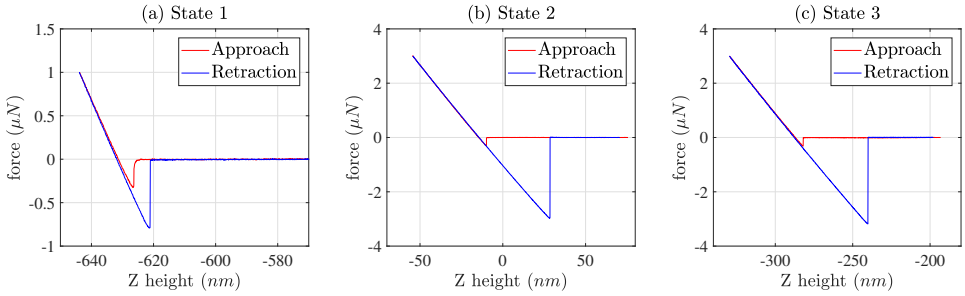

Figure 6: Typical measured force-distance curve for the SiO_2 substrate at three states.

of the measured force-distance curve for the three states can explain this discrepancy. Figure 6 shows a typical measured force-distance curve for the SiO_2 substrate. Although both states 1 and 3 are conducted in ambient conditions, they show a different behavior. The curvy snap-in shape in the approach part of state 1 suggests that the probe is first touching a soft material. Since this behavior is not observed in state 3, where there are water monolayers adsorbed on the substrate, it is suggested that this soft material is a hydrocarbon contamination film (or even a mix of water molecules and contamination) which is removed in vacuum. The same behavior for the Si substrate has been observed (not shown here). Such contamination film reduces the surface energy of the contacting materials, leading to a lower pull-off force than expectation.

Another possible reason for this steep increase in the measured pull-off force after vacuuming the AFM chamber, is the change in the topography of the probe during the measurements. As shown previously, the smoothened tip of the colloidal probe, due to a large number of measurements, has a larger potential contact area which leads to a larger adhesive force, too.

The measured surface topographies before the tests are implemented to predict the pull-off force in the ambient conditions of state 1. Although there seems to be good agreement between simulations and experiments for both Si and SiO_2 substrates, the agreement is merely a coincidence since the impact of the contamination layer on the measurements of this state is not considered in the simulations.

To predict the pull-off force for states 2 and 3, the probe roughness measured after the experiments is used. The predicted pull-off force for state 2 is lower than the measurements. As mentioned before, we assume that there is no water molecule in vacuum, however, it is pretty demanding and

time-consuming to remove water monolayers from the hydrophilic surfaces of Si and SiO_2 only by vacuuming the AFM chamber. In other words, the difference between predictions and experiments is highly probably due to the neglected effect of water monolayers in vacuum in simulations. This can be confirmed by the slight increase in the measured pull-off force from state 2 to 3, where a larger increase, as also suggested by the simulations, is expected.

The contact area along with the adhesive regions at the pull-off moment are shown in Figure 7 for both substrates and the three states, with topographies of Figures 3 and 4 as inputs. The predicted pull-off force for the Si substrate, as shown in Figure 5, is larger than that of the SiO_2. This is due to the smoother surface of Si than SiO_2 (as discussed in section 4) which leads to larger adhesive areas. Nonetheless, this difference is rather small at state 1 since the combined roughness of the interface is dominated by the probe roughness (compare Figures 7 (a) and (d)). This difference is more obvious at states 2 and 3 where the surface of the colloidal probe has become smoothened so that the probe roughness is no longer dominant and the substrate roughness contributes to the pull-off force, too (compare Figures 7 (c) and (f)). Therefore, both contact and adhesive areas are potentially larger.

The variation of the contact area vs. the normal load is also depicted in Figure 8. It is confirmed that the contact area for Si as substrate is larger than that of SiO_2 due to its smoother surface. Because of the same reason, the contact area is less sensitive to the normal load for Si compared to SiO_2 close to the pull-off point as increasing the pulling force (decreasing the normal load) does not change the contact area remarkably and only breaks the adhesive bonds. There is only a slight difference in the pull-off force due to the larger capillary area in the case of Si (see Figure 7 (a) and (d)).

6 Conclusions

In this paper, we conducted AFM pull-off force measurements at the interface of a micron-size silicon dioxide colloidal probe and two different substrates, namely a silicon wafer and a silicon dioxide layer on top of a silicon wafer, in ambient and vacuum conditions. The steep increase in the measured pull-off force from ambient to vacuum was attributed to the hydrocarbon contamination removal and change of the colloidal probe topography during the measurements. The numerical prediction of the pull-off force was in agreement with experiments for the ambient

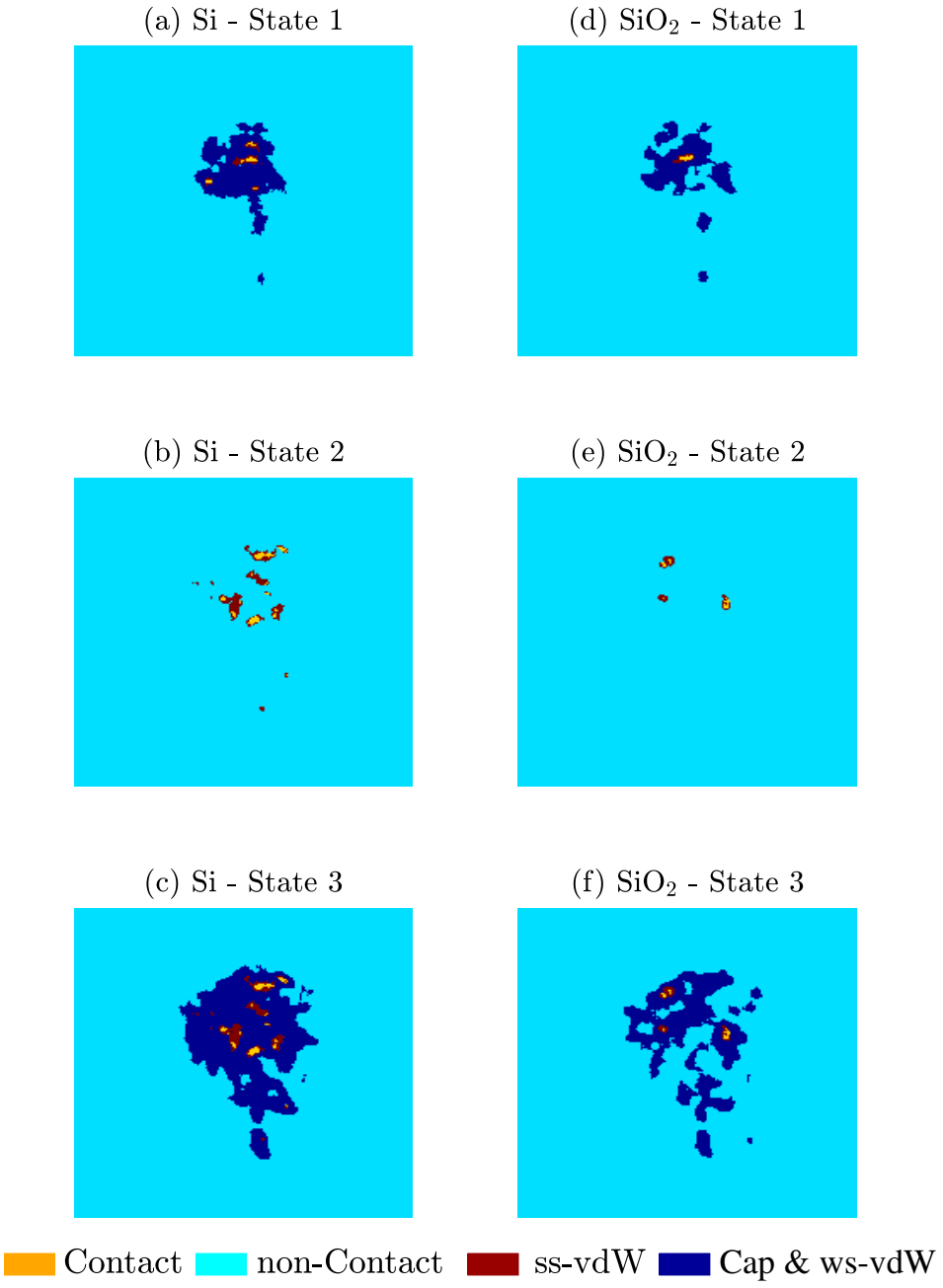

Figure 7: The (zoomed-in view of) contact area as well as the adhesive regions at the pull-off moment (ss-vdW: Solid-Solid van der Waals interaction, Water-Solid van der Waals interaction, and Cap: Capillary.)

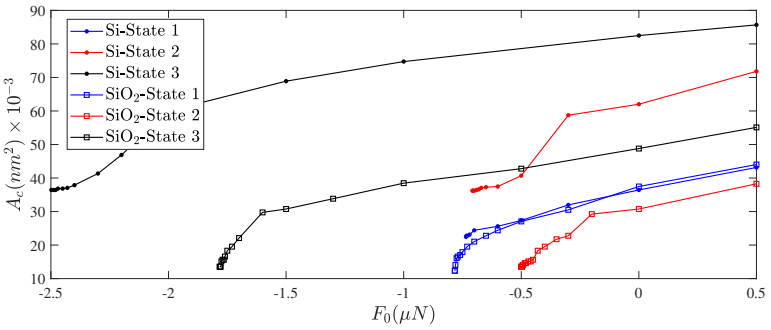

Figure 8: The variation of the contact area vs. normal load for all states and both substrates.

conditions after vacuum, while the lower predicted pull-off force was due to neglecting the present monolayers of water molecules on the contacting surfaces. The trend for both substrates in state 1 is quite similar as the interface topography is dominated by the probe roughness.

7 Acknowledgment

This research was carried out under project number S61.1.13492 in the framework of the Partnership Program of the Materials innovation institute M2i (www.m2i.nl) and the Technology Foundation TTW (www.stw.nl), which is part of the Netherlands Organization for Scientific Research (www.nwo.nl).

Bibliography

[1] M. Bazrafshan, M. de Rooij, and D. Schipper, "On the role of adhesion and roughness in stick-slip transition at the contact of two bodies: A numerical study," *Tribology International*, vol. 121, no. July 2017, pp. 381–388, 2018.

[2] M. Bazrafshan, M. de Rooij, and D. Schipper, "The Effect of Adhesion and Roughness on Friction Hysteresis Loops," *International Journal of Mechanical Sciences*, 2019.

[3] O. T. Sari, G. G. Adams, and S. Muftu, "Nano-Scale Effects in the Sliding and Rolling of a Cylinder on a Substrate," *Journal of Applied Mechanics*, vol. 72, no. 5, p. 633, 2005.

[4] G. G. Adams, "Stick, partial slip and sliding in the plane strain micro contact of two elastic bodies.," *Royal Society open science*, vol. 1, no. 3, p. 140363, 2014.

[5] M. A. Yaqoob, M. B. de Rooij, and D. J. Schipper, "On the transition from bulk to ordered form of water: A theoretical model to calculate adhesion force due to capillary and van der Waals interaction," *Tribology Letters*, vol. 49, no. 3, pp. 491–499, 2013.

[6] J. C. Mergel, R. Sahli, J. Scheibert, and R. A. Sauer, "Continuum contact models for coupled adhesion and friction," *Journal of Adhesion*, vol. 00, no. 00, pp. 1–33, 2018.

[7] A. Rota, E. Serpini, G. C. Gazzadi, and S. Valeri, "AFM-based tribological study of nanopatterned surfaces: The influence of contact area instabilities," *Journal of Physics Condensed Matter*, vol. 28, no. 13, 2016.

[8] J.-K. Kim and M. Varenberg, "Contact splitting in dry adhesion and friction: reducing the influence of roughness," *Beilstein Journal of Nanotechnology*, vol. 10, pp. 1–8, 2019.

[9] K. L. Johnson, K. Kendall, and A. D. Roberts, "Surface Energy and the Contact of Elastic Solids," *Proceedings of the Royal Society of London. Series A, Mathematical and Physical Sciences*, vol. 324, pp. 301–313, 1971.

[10] B. Derjaguin, V. Muller, and Y. Toporov, "Effect of contact deformations on the adhesion of particles," *Journal of Colloid and Interface Science*, vol. 53, no. 2, pp. 314–326, 1975.

[11] D. B. Asay and S. H. Kim, "Effects of adsorbed water layer structure on adhesion force of silicon oxide nanoasperity contact in humid ambient," *Journal of Chemical Physics*, vol. 124, no. 17, 2006.

[12] D. B. Asay, E. Hsiao, and S. H. Kim, "Effects of adsorbate coverage and capillary on nano-asperity friction in atmosphere containing organic vapor," *Journal of Applied Physics*, vol. 110, no. 6, 2011.

[13] M. He, A. Szuchmacher Blum, D. E. Aston, C. Buenviaje, R. M. Overney, and R. Luginbühl, "Critical phenomena of water bridges in nanoasperity contacts," *Journal of Chemical Physics*, vol. 114, no. 3, pp. 1355–1360, 2001.

[14] N. Zarate, A. Harrison, J. Litster, and S. Beaudoin, "Effect of relative humidity on onset of capillary forces for rough surfaces," *Journal of Colloid and Interface Science*, vol. 411, pp. 265–272, 2013.

[15] M. Kober, E. Sahagun, P. Garcia-Mochales, F. Briones, M. Luna, and J. J. Saenz, "Nanogeometry matters: Unexpected decrease of capillary adhesion forces with increasing relative humidity," *Small*, vol. 6, no. 23, pp. 2725–2730, 2010.

[16] M. Farshchi-Tabrizia, M. Kappl, and H. J. Butt, "Influence of humidity on adhesion: An atomic force microscope study," *Journal of Adhesion Science and Technology*, vol. 22, no. 2, pp. 181–203, 2008.

[17] C. Ziebert and K. H. Zum Gahr, "Microtribological properties of two-phase Al2O3ceramic studied by AFM and FFM in air of different relative humidity," *Tribology Letters*, vol. 17, no. 4, pp. 901–909, 2004.

[18] D. I. Kim, J. Grobelny, N. Pradeep, and R. F. Cook, "Origin of adhesion in humid air," *Langmuir*, vol. 24, no. 5, pp. 1873–1877, 2008.

[19] C. Birleanu, M. Pustan, F. Rusu, C. Dudescu, R. Muller, and A. Baracu, "Relative humidity effect on pull-off forces in MEMS flexible structures measured by AFM," *Symposium on Design, Test, Integration and Packaging of MEMS/MOEMS, DTIP 2017*, 2017.

[20] M. Bartosik, L. Kormos, L. Flajsman, R. Kalousek, J. Mach, Z. Liskova, D. Nezval, V. Svarc, T. Samoril, and T. Sikola, "Nanometer-sized water bridge and pull-off force in AFM at different relative humidities: Reproducibility measurement and model based on surface tension change," *Journal of Physical Chemistry B*, vol. 121, no. 3, pp. 610–619, 2017.

[21] X. Zhang, Y. He, M. L. Sushko, J. Liu, L. Luo, J. J. De Yoreo, S. X. Mao, C. Wang, and K. M. Rosso, "Direction-specific van der Waals attraction between rutile TiO2nanocrystals," *Science*, vol. 356, no. 6336, pp. 434–437, 2017.

[22] Ducker WA, Senden TJ, and Pashley PA, "Direct measurement of colloidal forces using an atomic force microscope," *Nature*, vol. 353, no. 353, p. 2239, 1991.

[23] A. Fukunishi and Y. Mori, "Adhesion force between particles and substrate in a humid atmosphere studied by atomic force microscopy," *Advanced Powder Technology*, vol. 17, no. 5, pp. 567–580, 2006.

[24] S. Biggs, R. G. Cain, R. R. Dagastine, and N. W. Page, "Direct measurements of the adhesion between a glass particle and a glass surface in a humid atmosphere," *Journal of Adhesion Science and Technology*, vol. 16, no. 7, pp. 869–885, 2002.

[25] A. Ata, Y. I. Rabinovich, and R. K. Singh, "Role of surface roughness in capillary adhesion," *Journal of Adhesion Science and Technology*, vol. 16, no. 4, pp. 337–346, 2002.

[26] R. Jones, H. M. Pollock, J. A. S. Cleaver, and C. S. Hodges, "Adhesion forces between glass and silicon surfaces in air studied by AFM: Effects of relative humidity, particle size, roughness, and surface treatment," *Langmuir*, vol. 18, no. 21, pp. 8045–8055, 2002.

[27] A. Colak, H. Wormeester, H. J. W. Zandvliet, and B. Poelsema, "Surface adhesion and its dependence on surface roughness and humidity measured with a flat tip," *Applied Surface Science*, vol. 258, no. 18, pp. 6938–6942, 2012.

[28] S. Yang, H. Zhang, and S. M. Hsu, "Correction of random surface roughness on colloidal probes in measuring adhesion," *Langmuir*, vol. 23, no. 3, pp. 1195–1202, 2007.

[29] S. Matope, Y. I. Rabinovich, and A. F. V. D. Merwe, "Colloids and Surfaces A : Physicochemical and Engineering Aspects Van der Waals interactions between silica spheres and metallic thin films created by e-beam evaporation," *Colloids and Surfaces A: Physicochemical and Engineering Aspects*, vol. 411, pp. 87–93, 2012.

[30] M. Bazrafshan, M. B. de Rooij, and D. J. Schipper, "Adhesive force model at a rough interface in the presence of thin water films: The role of relative humidity," *International Journal of Mechanical Sciences*, vol. 140, no. January, pp. 471–485, 2018.

[31] M. Bazrafshan, M. B. de Rooij, M. Valefi, and D. J. Schipper, "Numerical method for the adhesive normal contact analysis based on a Dugdale approximation," *Tribology International*, vol. 112, no. April, pp. 117–128, 2017.

[32] I. A. Polonsky and L. M. Keer, "A numerical method for solving rough contact problems based on the multi-level multi-summation and conjugate gradient techniques," *Wear*, vol. 231, no. 2, pp. 206–219, 1999.

[33] J.N. Israelachvili, *Intermolecular and surface forces*. Elsevier, 2013.

[34] D. B. Asay and S. H. Kim, "Evolution of the adsorbed water layer structure on silicon oxide at room temperature.," *Journal of Physical Chemistry. B*, vol. 109, no. 35, pp. 16760–16763, 2005.

[35] L. Chen, X. He, H. Liu, L. Qian, and S. H. Kim, "Water Adsorption on Hydrophilic and Hydrophobic Surfaces of Silicon," *Journal of Physical Chemistry C*, vol. 122, no. 21, pp. 11385–11391, 2018.

Paper D

On the role of adhesion and roughness in stick-slip transition at the contact of two bodies: a numerical study

M. Bazrafshan[1,2*], M.B. de Rooij[2], and D.J. Schipper[2]

[1] *Materials innovation institute (M2i), Elektronicaweg 25, 2628 XG , Delft, Netherlands*
[2] *Laboratory for Surface Technology and Tribology, Department of Engineering Technology, University of Twente, P.O. box 217, 7500AE, Enschede, Netherlands*

Abstract

This paper proposes a boundary element model for the stick-slip transition at the contact of two bodies of dissimilar materials in presence of adhesion due to van der Waals force. The adhesion is modeled using a Dugdale approximation of adhesive energy. The coupling between the normal pressure and shear stresses is included so that there is no full-stick condition, even in the absence of an external shear stress. Furthermore, the evolution of the slip area over the contact area is different from the well-known Cattaneo-Mindlin solution due to the difference in the mechanical properties of the contacting bodies. It is also shown that the adhesion increases the pre-sliding distance and the static friction. While roughness can only increase the former one. However, the combined effect of roughness and adhesion on the pre-sliding distance is not cumulative as these two parameters are found to be symbiotic.

1 Introduction

When two surfaces in contact are tangentially loaded by a force smaller than the force required to cause a gross sliding (here named the static friction force), surface strains are not uniformly distributed over the two surfaces. Consequently, the contact area is divided into two different regions of stick and slip. Each spot in the contact area corresponds to two adjacent points on the two surfaces. In the stick region, the two points move together while sticking to each other and there is no relative displacement. In slip region, whereas, they gradually separate from each other due to the difference in displacements. Increasing the tangential force makes the slip area develop over the contact area (and stick area shrink) and as soon as it covers the entire contact area, full slip or gross sliding occurs. This behavior is called stick-slip or micro-slip and can be frequently found in many engineering applications. In addition, the displacement at which full slip starts is called pre-sliding distance and serves as an important specification in precision engineering.

The analytical solution to this problem for cylindrical contacts of identical materials was derived by Cattaneo [1] and Mindlin [2], separately. Later on, Ciavarella solved the generalized Cattaneo partial slip plane contact problem [3, 4]. When the contacting materials are identical, as in the case of Cattaneo-Mindlin solution, the normal pressure and shear tractions are automatically decoupled. It means that the normal pressure

cannot impose any tangential displacement (and therefore any change in the shear tractions) and on the other hand, the shear tractions cannot cause any normal displacement (and any change in the normal pressure). The contact of dissimilar materials, nevertheless, does not obey this classical theory and the interaction between normal pressure and shear tractions cannot be neglected. This matter implies that even in the absence of an external shear stress, a normal load can cause relative tangential displacement in some areas of the contact and thus micro-slip. Deriving analytical solution for this problem is quite complicated. For such problems, the numerical analysis is a good alternative. Finite Element Method (FEM) has been widely used for simulation with complicated material behavior and shapes [5, 6]. Chen and Wang developed a BEM (Boundary Element Method) model to study the partial slip problem for the contact of dissimilar materials [7]. Wang et al proposed a BEM model to analyze the partial slip contact problem on 3D layered materials [8].

In addition to material properties, surface roughness is a key factor affecting the frictional behavior between two contacting surfaces. When two rough surfaces meet one another, the contact is restricted only to the high asperities and therefore, the real contact area is essentially less than the nominal one and this matter strongly influences the frictional behavior. It is, therefore, very important to take into account this factor as well while studying the stick-slip transition. The first studies on the role of roughness in contact and friction were conducted by Archard [9], Greenwood and Williamson [10], and Bowden and Tabor [11]. In particular, several authors have studied the stick-slip contact between rough surfaces. Paggi et al studied the transition from full-stick to full-slip condition at fractal surfaces with different values of the Hurst exponent by means of a BEM model [12]. Grzemba et al estimated the preliminary displacement of a frictional contact at the self-affine fractal surface to be dependent on only the normal force for low values of this parameter and also on the roughness rms for a higher normal force [13]. Medina et al provided analytical and numerical models for the tangential stiffness for elastic contact of rough surfaces, which is proportional to the normal load and independent from the Youngs modulus of elasticity [14]. A numerical model for the tangential contact of rough surfaces has been developed by Wang et al [15]. They considered the contribution of both elastically and plastically deformed asperities. Kennedy et al used scale-sensitive fractal parameters to characterize the surface roughness of glass and aluminum computer hard disks and correlate these parameters with the stick-slip behavior of textured hard disks [16]. They found out that the friction

coefficient is well correlated with the thickness of the adsorbed water layer at the interface, which is determined by the shape of asperity height distribution, especially the high asperities. Wei et al studied the roughness dependent stick-slip behavior occurring between a rigid indenter and a Si specimen numerically and experimentally [17]. Gavrila and Cretu proposed a numerical model to investigate the wear for smooth and rough contacts under partial slip conditions [18]. Chen and Wang presented a deterministic numerical model to predict the static friction coefficient for rough sphere-on-flat contacts [19]. Dini and Hills investigated the stick-slip behavior for a rough ball-on-flat contact of identical materials [20]. The roughness is distributed over the flat by means of a uniform array of spherical asperities. Kasarekar et al developed a numerical model to study the pressure and contact geometry evolution for rough surfaces subjected to fretting wear under partial slip conditions [21].

Although the roughness on the contacting surfaces makes the real contact area remarkably less than the nominal one, the presence of adhesive forces between the two surfaces can increase the real contact area through increasing the local pressure on the asperities and pulling the non-contacting areas toward each other. There has been extensive research into the effect of this parameter on the contact area of rough surfaces [22–27]. The effect of adhesion on the contact area in the plane strain version of the Cattaneo/Mindlin problem is considered in [28]. The contact area is determined by the adhesive forces using the Maugis theory independent from the tangential forces. The tangential forces are distributed between a central stick zone and the surrounding slip zones in which the shear stress is assumed to be constant. Adams studied the plane strain problem of a curved elastic body pressed against an elastic half-space [29]. The effect of adhesion is included through the use of surface energy in a manner similar to the well-known JKR theory for spherical contacts. The contact is characterized by complete stick up to a critical value of the tangential force when there is a transition either directly to complete sliding or to a partial slip state in which a central stick zone is surrounded by two slip zones.

This paper proposes a BEM model for the adhesive stick-slip contact between two bodies (smooth against rough) of dissimilar materials. The coupling effect between the normal pressure and shear stresses is included so that there is no full-stick condition, even in the absence of an external shear stress. In the slip area, the shear stress is proportional to the local normal pressure, based on the Amontons law of friction. Whereas, the shear stress in the adhesive zone is neglected. A tangential force is applied on the

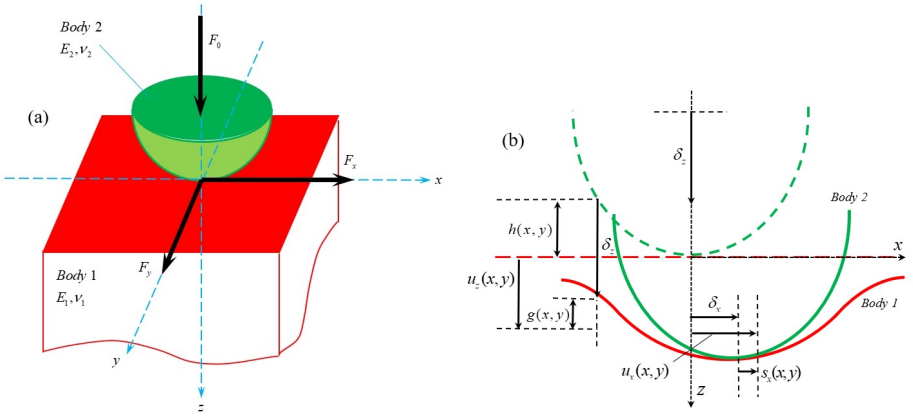

Figure 1: Contact variables in the $x-z$ plane, δ_z and δ_x are the rigid body displacements, u_z and u_x elastic displacement, and g is the gap between the two bodies

system, reducing the stick area, until the slip zone develops and covers the entire contact area. At this moment, full slip starts. The combined effect of roughness and adhesion is also studied.

2 Theory and problem definition

Figure 1 illustrates the contact geometry between bodies 1 (rigid) and 2 (elastic half-space). The x and y axes are on the surface and the z axis goes inward the half-space. The rigid body 1 is compressed into the half-space by a normal force F_0. Body 1 is tangentially loaded by forces F_x and F_y in x and y directions, respectively (Figure 1(a)). These contact loads result in normal pressure p and shear tractions q_x and q_y at the interface. The relative surface displacements at point x, y are expressed as:

$$\begin{aligned} u_x(x,y) &= c_{xx} * q_x + c_{xy} * q_{xy} + c_{xz} * p \\ u_y(x,y) &= c_{yx} * q_x + c_{yy} * q_{xy} + c_{yz} * p \\ u_z(x,y) &= c_{zx} * q_x + c_{zy} * q_{xy} + c_{zz} * p \end{aligned} \tag{1}$$

where symbol * means continuous convolution and $c_{mn}(m,n = x,y,z)$ are the Greens functions [7]:

$$
\begin{aligned}
c_{xx} &= \frac{1}{\pi r^3}\left(\frac{x^2}{E'}+\frac{y^2}{E^*}\right), \quad c_{xy} = \frac{xy}{\pi\mu^* r^3}, \quad c_{xz} = -\frac{x}{\pi\mu' r^2} \\
c_{yy} &= \frac{1}{\pi r^3}\left(\frac{x^2}{E^*}+\frac{y^2}{E'}\right), \quad c_{yx} = c_{xy}, \qquad c_{yz} = -\frac{y}{\pi\mu' r^2} \\
c_{zz} &= \frac{1}{\pi E^* r^3}, \qquad\qquad\quad c_{zx} = -c_{xz}, \quad c_{zy} = -c_{yz}
\end{aligned}
\tag{2}
$$

in which:

$$
r = \sqrt{x^2+y^2}, \qquad \frac{1}{E'} = \frac{1+\nu_1}{E_1}+\frac{1+\nu_2}{E_2}, \qquad \frac{1}{E^*} = \frac{1-\nu_1^2}{E_1}+\frac{1-\nu_2^2}{E_2},
$$
$$
\frac{1}{\mu'} = \frac{(1+\nu_1)(1-2\nu_1)}{2E_1} - \frac{(1+\nu_2)(1-2\nu_2)}{2E_2}, \quad \frac{1}{\mu^*} = \frac{\nu_1(1+\nu_1)}{E_1}+\frac{\nu_2(1+\nu_2)}{E_2}
\tag{3}
$$

In order to perform the numerical calculation, the contact area is divided into N^2 rectangular surface elements with grid sizes of Δx and Δy. Therefore, one can assume a piecewise constant function within each surface element for the contact pressure and shear tractions distribution. In the discrete format, the surface deformation at node (i,j), is given by:

$$
u_{ij}^m = \sum_{k=1}^{N}\sum_{l=1}^{N}\left(C_{mx}^{i-k,j-l}q_x^{kl} + C_{my}^{i-k,j-l}q_y^{kl} + C_{mz}^{i-k,j-l}p^{kl}\right), \qquad m = x,y,z, \;\; i,j = 1,2,...,N
\tag{4}
$$

where p^{kl}, q_x^{kl}, and q_y^{kl} are the uniform pressure and shear tractions acting upon the element centered at node (k,l) and the influence coefficients are expressed as (x_i and y_j are the spatial coordinates of the node (i,j)):

$$
C_{mn}^{ij} = \int_{-\Delta x/2}^{\Delta x/2}\int_{-\Delta y/2}^{\Delta y/2} c_{mn}(x_i-\xi, y_j-\eta)\, d\eta d\xi, \qquad m,n = x,y,z, \;\; i,j = 1,2,...,N
\tag{5}
$$

The analytical expressions for the influence coefficients are presented in Ref. [7]. In practice, the DC-FFT algorithm can be used to evaluate the linear convolution of Eq. (4), efficiently:

$$u_m = IFFT\left[\tilde{C}_{mx}q_x + \tilde{C}_{my}q_y + \tilde{C}_{mz}p\right], \quad m = x, y, z, \;\; i, j = 1, 2, ..., N \tag{6}$$

where IFFT stands for Inverse Fast Fourier Transform and $\tilde{X}$ is the FFT of X. This method was first introduced by Stanley and Kato [30], and later on used by many several authors [31–38].
The general contact model is expressed as [39]:

$$\begin{cases} s_x^{ij} = u_x^{ij} - \delta_x \\ s_y^{ij} = u_y^{ij} - \delta_y \\ g^{ij} = u_z^{ij} + h^{ij} - \delta_z, \quad i, j = 1, 2, ..., N \end{cases} \tag{7}$$

Here, δ_x, δ_y, and δ_z are the rigid body displacements of all elements due to the external forces along the three axes, respectively, s_x and s_y the relative slip distance parallel to the and axes, the gap between the two bodies after loading, and is the initial gap, as shown in Figure 1(b). Bazrafshan et al proposed a CGM (Conjugate Gradient Method) based BEM algorithm to solve the adhesive normal contact between two bodies, given by [40]:

$$p^{ij} > -\sigma_0 \qquad \text{at} \quad g^{ij} = 0 \tag{8a}$$

$$p^{ij} = -\sigma_0 \qquad \text{at} \quad 0 < g^{ij} < h_0 \tag{8b}$$

$$p^{ij} = 0 \qquad \text{at} \quad g^{ij} > h_0 \tag{8c}$$

$$\Delta x \Delta y \sum_{i=1}^{N} \sum_{j=1}^{N} p^{ij} = F_0 \tag{8d}$$

in which $-\sigma_0$, the maximum attractive pressure of the Lennard-Jones potential, is applied such that [41]:

$$\Delta\gamma = \sigma_0 h_0, \quad \sigma_0 = \frac{16\Delta\gamma}{9\sqrt{3}z_0} \tag{9}$$

This results in $h_0 = 9\sqrt{3}z_0 = 0.974z_0$, where $\Delta\gamma$ is the work of adhesion. The parameter h_0 is the maximum allowable gap for the presence of

adhesion (the constant negative stress $-\sigma_0$ as a Dugdale approximation of adhesion energy). In the equation above, z_0 is the equilibrium separation, ranging from 0.2 nm to 0.4 nm. Having the adhesive normal contact solved, each node $[i,j]$ is considered to be non-contacting ($[i,j] \in A_{nc}$) if the local pressure at this node is either zero or $-\sigma_0$ and the local gap is greater than zero:

$$A_{nc} = \left\{ [i,j] \mid p^{ij} = \{-\sigma_0 \; or \; 0\},\; g^{ij} > 0 \right\} \tag{10}$$

On the other hand, a contacting element ($[i,j] \in A_c$) can experience each of the following conditions:

$$\begin{cases} A_c^1 = \left\{ [i,j] \mid p^{ij} \geq 0,\;\; g^{ij} = 0 \right\} \\ A_c^2 = \left\{ [i,j] \mid \; -\sigma_0 < p^{ij} < 0,\;\; g^{ij} = 0 \right\} \\ A_c = A_c^1 \cup A_c^2 \end{cases} \tag{11}$$

Here, A_c^1 refers to the nodes with positive pressure and zero gap, while A_c^2 indicates the nodes with a negative stress (yet greater than $-\sigma_0$) and zero gap. A_c^2 specifies the nodes close to the contact boundaries to define the continuous transition from a positive pressure to the negative adhesive stress ($-\sigma_0$). In the end, the total contact area,A_c is the union of A_c^1 and A_c^2.

In the present study, the loading process is assumed to be slow. The general assumptions of a stick-slip contact model can be summarized as follows [39]:

- In the stick region (A_{st}), shear traction does not exceed a limiting value (namely static friction) determined by the Amontons law of friction with a constant coefficient of friction (μ_f), and the slip distance between the two contact surfaces is equal to zero.

- In the slip region (A_{sl}), shear traction is equal to the static friction, and the slip distance of two contact surfaces is relatively small compared with the contact dimension. The direction of the shear traction must be opposite to the direction of the slip.

This assumption regarding the shear traction is different from the constant shear traction in the slip zone implemented by Savkoor [42] and Hanke et al [43]. Here, the shear traction in the slip zone is controlled by the local pressure. The statements above can be mathematically expressed as:

$$\begin{cases} A_{st} = \left\{ [i,j] \in A_c^1 \mid \sqrt{{q_x^{ij}}^2 + {q_y^{ij}}^2} < \mu_f p^{ij},\ \sqrt{{s_x^{ij}}^2 + {s_y^{ij}}^2} = 0 \right\} \\ A_{sl} = \left\{ [i,j] \in A_c^1 \mid \sqrt{{q_x^{ij}}^2 + {q_y^{ij}}^2} = \mu_f p^{ij},\ \sqrt{{s_x^{ij}}^2 + {s_y^{ij}}^2} \neq 0 \right\} \end{cases} \tag{12}$$

It must be noted that the shear stress at nodes with a negative stress (whether in contact or not) is neglected. In addition, the union and intersection of sticking and slipping areas are:

$$A_{sl} \cup A_{st} = A_c^1, \quad A_{sl} \cap A_{st} = 0 \tag{13}$$

An outline of the solution to the stick-slip problem in the presence of adhesion is depicted in Figure 2. In step 1, material properties, initial surface geometry, contact forces, work of adhesion, and the static coefficient of friction are input to the algorithm. Step 2 solves the adhesive normal contact problem as described in [40]. In step 3, CGM is used to calculate the shear tractions as in [7]. In steps 4 and 5, the tangential forces are estimated and checked whether they are within an accepted tolerance from the real (external) tangential forces. If the convergence is not met, the rigid body displacements in tangential directions are updated in step 6, based on the estimated tangential forces and the shear tractions are again calculated. In step 7, the convergence in the normal contact pressure is checked and if it is not met, the surface geometry, in step 8, is updated through including the effect of shear stresses on the deformation in direction [7].

3 Results and discussion

The current algorithm is used to analyze the adhesive stick-slip transition of a rigid ball of radius $R = 10\mu m$ compressed into an elastic half-space by a normal force $F_0 = 10\mu N$. The deformations, everywhere in this study, are assumed to be elastic. The mechanical properties for the elastic half-space are set to $E_2 = 130GPa,\ \nu_2 = 0.3$. The friction coefficient is also considered to be $\mu_f = 0.2$. The Tabor parameter is then defined to calculate the work of adhesion:

$$\mu_T = \left(\frac{R\Delta\gamma^2}{E^{*2} z_0^3} \right)^{1/3} \tag{14}$$

The chosen values for this parameter are $\mu_T = 0.5, 1, 2$ and for each value, the adhesive contact problem is solved analytically to calculate the adhesive radius, c_0 [41]. Then, the target domain is considered to be $-c_0 < x, y < c_0$.

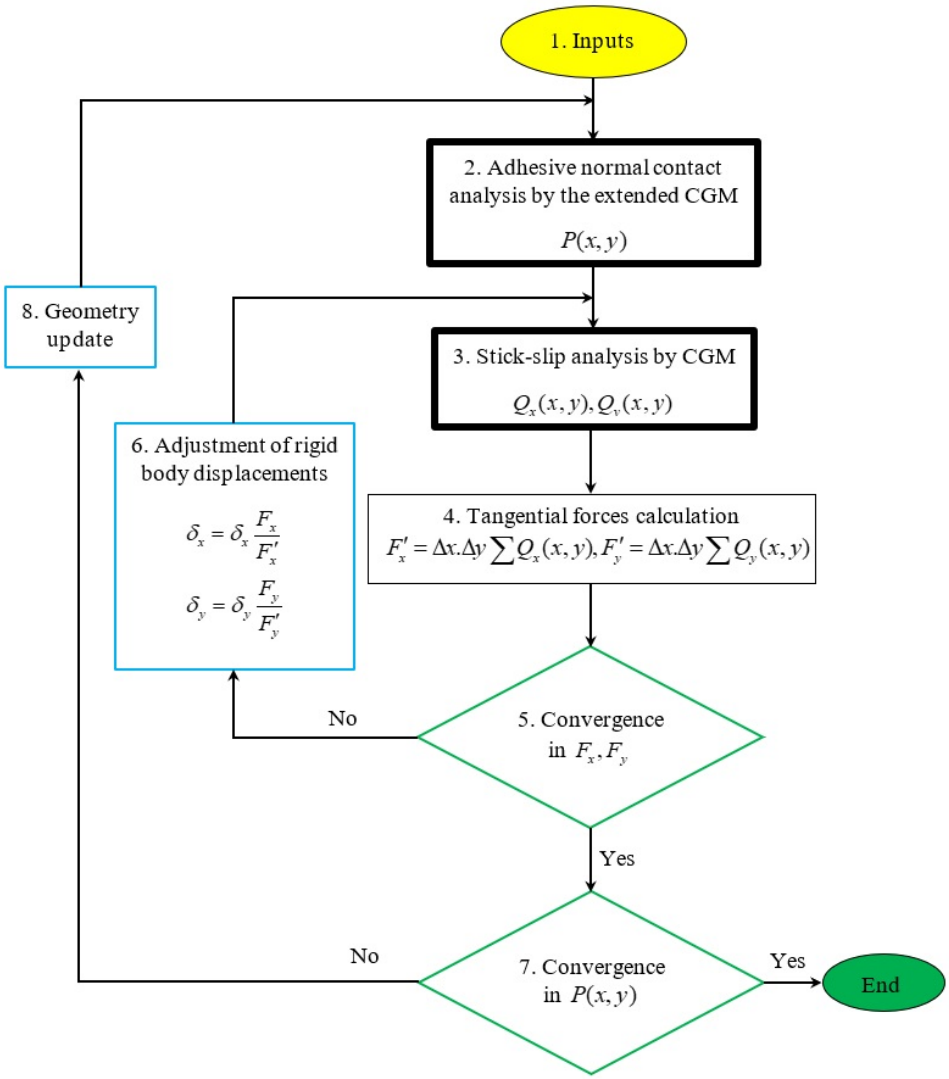

Figure 2: Solution algorithm (steps with thicker borders summarize multi-steps)

It must be noted that, in order to minimize the periodicity error due to the DC-FFT, the target domain needs to be expanded by zero-padding the applied pressure outside this domain [38]. The whole computation domain is then discretized into 1024×1024 square elements, which results in $\Delta x = \Delta y = 8 - 13nm$ for the grid size.

3.1 Smooth ball-on-flat contact

In this section, the contact of a rigid ball over a smooth elastic half-space is studied. First, the normal force, in the absence of an external shear stress, is applied on the system. An annulus of slip is created around the sticking area in the center. This is due to the difference in the mechanical properties of the contacting bodies which leads to different strains and deformations at the contact interface [7]. By applying and then increasing a tangential force (in x direction for instance), the stick zone is dragged to the left side (when body 1 is stiffer than body 2) until it touches the contact border. Further increase in the tangential force makes the stick zone shrink dramatically at the rear part of contact area until it vanishes entirely. This evolution is depicted in Figure 3. The normalized tangential force is defined as:

$$F_{nr} = \frac{F_x}{\mu_f F_0} \tag{15}$$

For the non-adhesive contact of the identical materials, the full slip takes place at $F_{nr} = 1$ since only q_x (shear stress in only one direction) exists. For the case of dissimilar materials, however, it is indicated that the stick zone reduces to zero at a normalized tangential force slightly smaller than unity due to the presence of the shear traction in the y direction as well [7]. When the contact is adhesive, depending on the magnitude of the work of adhesion, the contact area and contact pressure distribution are different even under the same external normal force. Thus, a different transition from stick to slip is expected. For instance, Figure 3 shows that the full slip starts at $F_{nr} = 1.56$, in the presence of adhesion, rather than $F_{nr} \simeq 1$ for a non-adhesive contact. To explain this, one should note that the external normal force is the summation of the contact positive force (F_0^+) and the adhesive force (F_0^-):

$$F_0 = F_0^+ + F_0^- \tag{16a}$$

$$F_0^+ = \Delta x \Delta y \sum_{p^{ij}>0} p^{ij} \tag{16b}$$

$$F_0^- = \Delta x \Delta y \sum_{p^{ij}<0} p^{ij} \tag{16c}$$

As mentioned before, the shear stress in adhesive areas is neglected and only inside the area with positive pressure is considered. The required tangential force to start full slip, i.e. the static friction force, is $\mu_f F_0^+$ rather than (nearly) $\mu_f F_0$, and since $F_0^+ > F_0$, it can be verified that a tangential force higher than $\mu_f F_0$ is needed for the start of the full slip.

To demonstrate the effect of adhesion on stick-slip transition, the same problem is solved for three different values of the Tabor parameter. The ratio of the sticking area to contacting area, $A_{stick}/A_{contact}$, is considered to be the criterion to check how far the contact is from the full slip. When the tangential force is zero, this ratio is smaller than one, implying that a part of the contact is already slipping (for the contact of identical materials, it starts from 1, based on the Cattaneo-Mindlin solution). With increasing the tangential force, this ratio decreases gradually and in the end, as soon as it becomes zero (the stick zone vanishes), full slip starts. Figure 4(a) illustrates the variation of $A_{stick}/A_{contact}$ versus the normalized tangential force. The normalized tangential force versus rigid body displacement is also shown in Figure 4(b). The rigid body displacement at the start of full slip is called pre-sliding distance and serves as an important specification in precise engineering. It is conspicuous that as the Tabor parameter increases, the static friction force and also the corresponding pre-sliding distance increase, too. This behavior can be interpreted by looking at the corresponding adhesive force, F_0^- presented in Table 1, which increases with the Tabor parameter and accordingly increases the positive force, F_0^+, based on Eq. (16). It is worth noting that if the tangential force, F_x, is normalized by $\mu_f F_0^+$, as shown in Table 1, the corresponding value is still slightly smaller than unity. One may, therefore, conclude that in order to have an estimation of the static friction force in an adhesive contact, $\mu_f F_0^+$ might serve as an acceptable approximation rather than $\mu_f F_0$. Another point that one might note is that the initial value of $A_{stick}/A_{contact}$ decreases with an increase in the Tabor parameter which is due to the increase in contact area for higher values of this adhesive parameter.

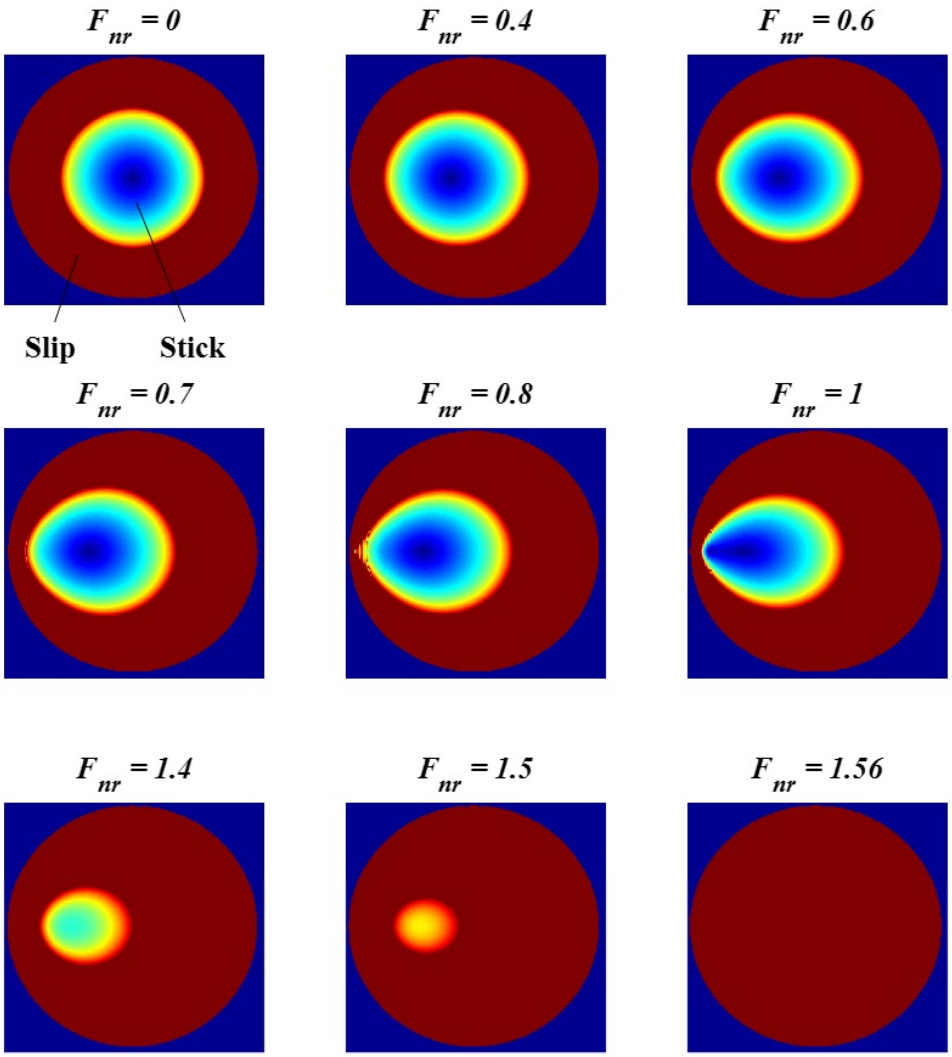

Figure 3: Evolution of the stick zone with increasing the tangential force for $\mu_T = 0.5$

Table 1: Comparison between different Tabor parameters in terms of the corresponding positive and adhesive forces and normalized tangential forces

μ_T	$F_0^-(\mu N)$	$F_0^+(\mu N)$	$F_{nr} = F_x/\mu_f F_0$	$F_x/\mu_f F_0^+$
0	0	10.000	0.97	0.9700
0.5	-6.088	16.088	1.56	0.9697
1	-16.018	26.018	2.52	0.9685
2	-42.114	52.114	5.04	0.9690

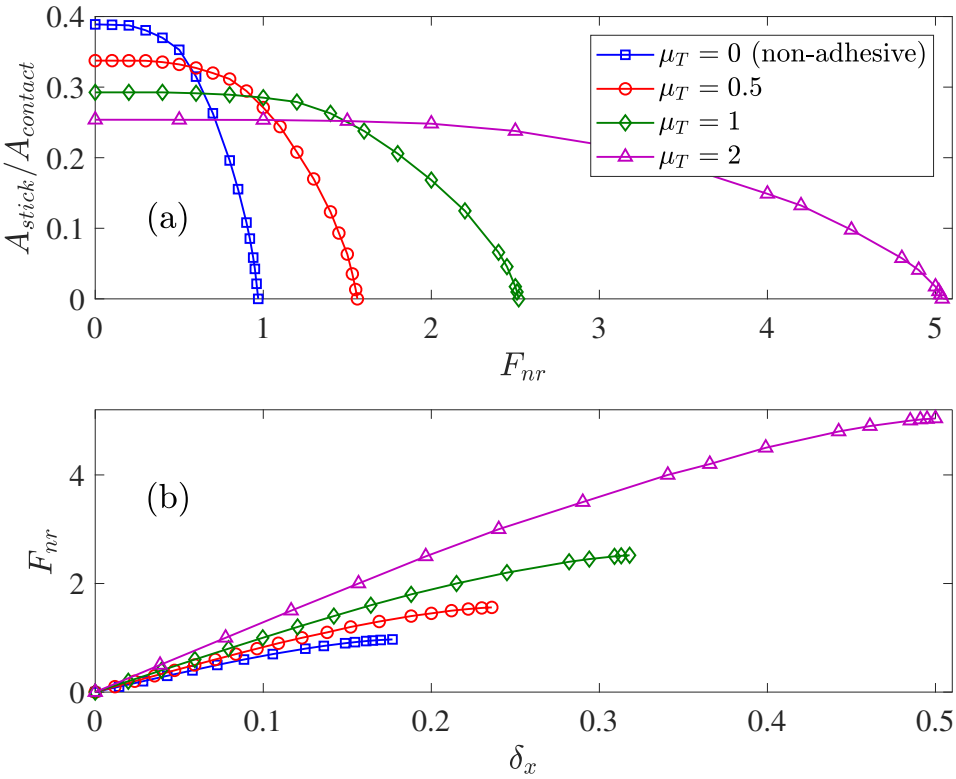

Figure 4: (a) Variation of the stick area to contact area as a function of the normalized tangential force (b) Normalized tangential force vs. rigid body displacement in x direction

3.2 A rigid smooth ball on a rough elastic half-space

In the previous section, it was shown that the determining factor in transition from stick to full slip for a smooth contact is $\mu_f F_0^+$ rather than $\mu_f F_0$ and adhesion imposes its influence through changing this positive force. This section aims at studying the combined effect of roughness rms and adhesion on this transition. So far, no comprehensive understanding of the effect of roughness rms on the static friction coefficient has been achieved. In the present study, the level of roughness and therefore the local slopes are kept low ($rms < 100z_0 = 20nm$) and also, one of the contacting bodies is smooth. Hence, we neglect the variation of this coefficient with roughness rms. The adhesive contact between a smooth ball of radius $R = 100\mu m$ and a rough half-space is considered. The mechanical properties and loading conditions are the same as those in previous section. The method proposed by Hu and Tonder has been implemented to numerically generate a Gaussian rough surface [44]. The $10\mu m \times 10\mu m$ generated profile with roughness rms of $20z_0 = 5nm$, slope rms of 0.113 is illustrated in Figure 5(a). The power spectral density of this profile is also shown in Figure 5(b). The rough profile is first subtracted by its arithmetic average value and then scaled in the vertical direction to create rough surfaces with different values of rms and keep the spatial distribution of peaks and valleys the same [45]. The mentioned subtraction is necessary in order to keep higher order statistical parameters such as skewness and kurtosis unaffected. This technique enables one to isolate the effect of varying roughness rms and maintain the same distribution of asperities, since different distributions of asperities (even with the same rms) lead to different adhesive behaviors.

The problem is first solved for a non-adhesive case to investigate the individual effect of roughness rms on pre-sliding behavior. Figure 5(a) displays the variation of non-adhesive $A_{stick}/A_{contact}$ as a function of the normalized tangential force, F_{nr}, for different rms values. Imposing a rough profile on a smooth surface decreases the contact area. However, it was shown by Chen and Wang that the decrease in the stick area is larger which, in total, results in a smaller value for $A_{stick}/A_{contact}$ for rough contacts compared to smooth ones [19]. It is also worth mentioning that all curves, although starting from different point, end up in the same point on the horizontal axis which means that, for a rough contact, the static friction force is independent from the roughness rms. Using a multi asperity model, Winogrodzka showed that increasing the roughness rms at the contact of two rough surfaces increases the pre-sliding distance [46].

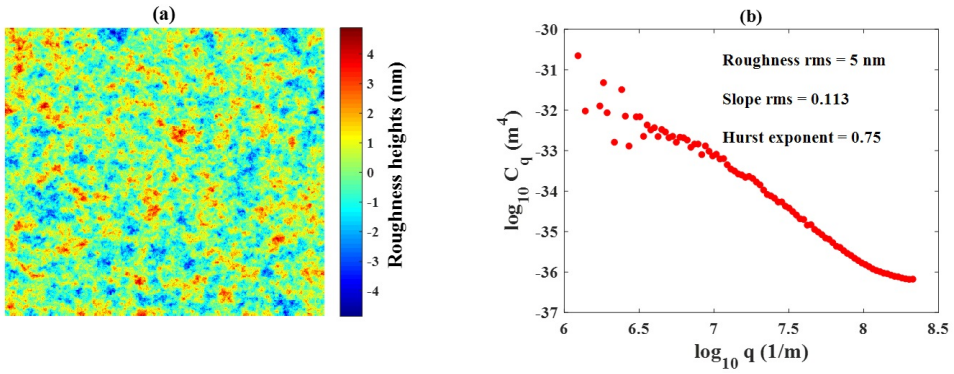

Figure 5: (a) The generated Gaussian profile and (b) its power spectral density (q is the wave-vector)

The same behavior is observed in Figure 6 which illustrates the tangential displacement, δ_x, versus the normalized tangential force.

At this stage, the problem is solved in presence of adhesion characterized by three different values of Tabor parameter. Figure 5(b, c, d) depicts the variation of $A_{stick}/A_{contact}$ versus normalized tangential force for these values of the Tabor parameter. It is apparent that increasing the roughness rms can move the static friction force either forward or backward on the horizontal axis compared to a smooth contact. As mentioned in previous section, the start of a full-slip in an adhesive contact is directly controlled by the contact positive force, F_0^+. Small amount of roughness rms can cause a large zone within the macro contact to experience a small separation (smaller than h_0), where the adhesive stress is maximum. As we further increase the roughness rms, the majority of the contact zone is separated by greater distances (greater than h_0), and experiences no adhesive forces. Only local areas surrounding the asperities with a positive pressure are in the zone for a high adhesive force. Therefore, increasing roughness rms first increases and then decreases the adhesive force and consequently the contact positive force. This transition is highly dependent on the work of adhesion (or namely the Tabor parameter).

(a) $\mu_T = 0$ $(non - adhesive)$

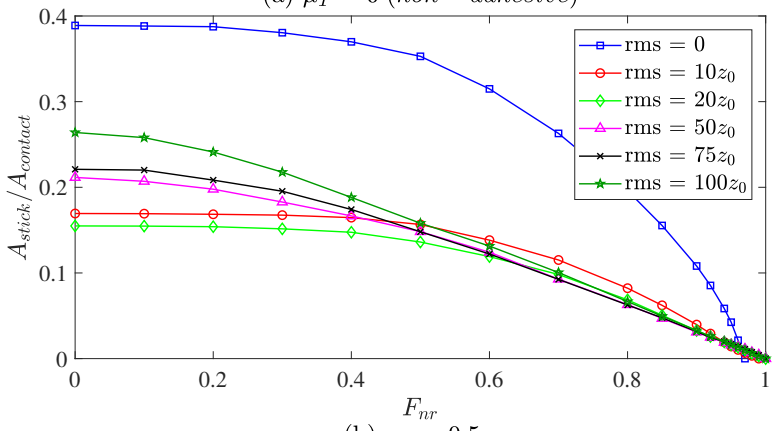

(b) $\mu_T = 0.5$

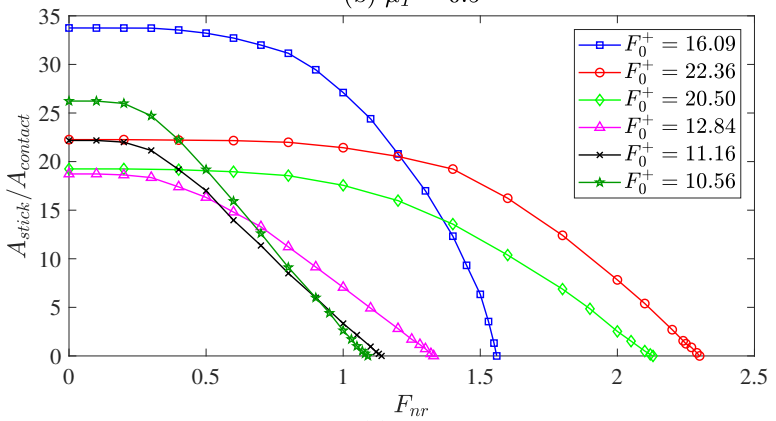

(c) $\mu_T = 1$

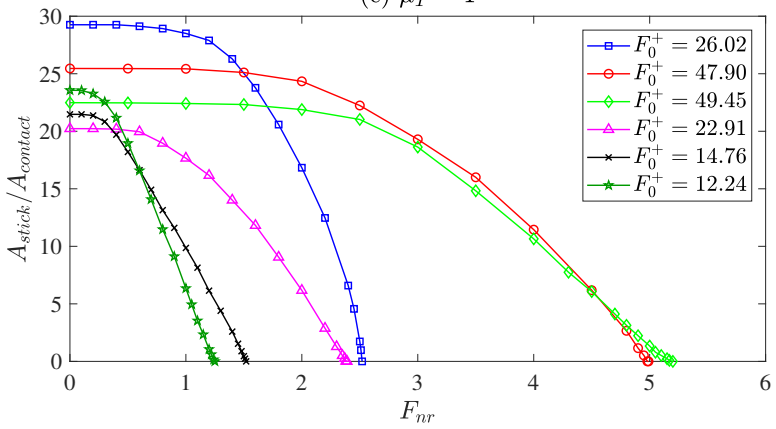

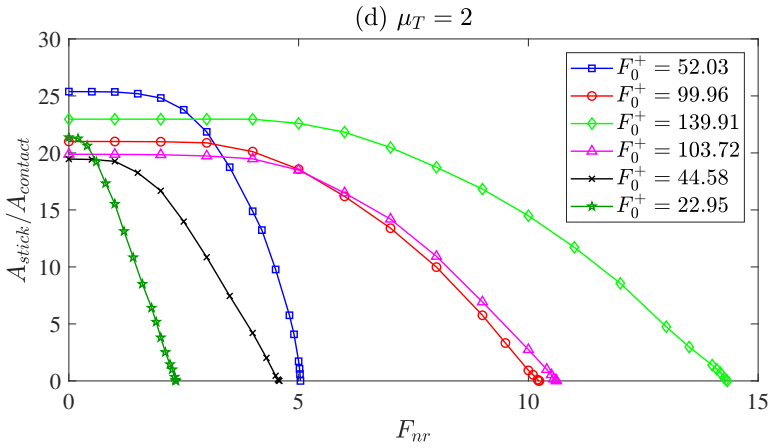

Figure 6: The variation of $A_{stick}/A_{contact}$ versus normalized tangential force, F_{nr}, for a non-adhesive case and three different values of the Tabor parameter, μ_T, and different rms values; subplots (b), (c), and (d) have the same legends as subplot (a) for rms values

Figure 7 shows the variation of the positive force as a function of roughness rms for different values of the Tabor parameter for $F_0 = 10\mu N$ to illustrate at which rms value, this positive force is maximum and so is the static friction force. It also shows that this maximum shifts to higher rms values for higher values of the Tabor parameter.

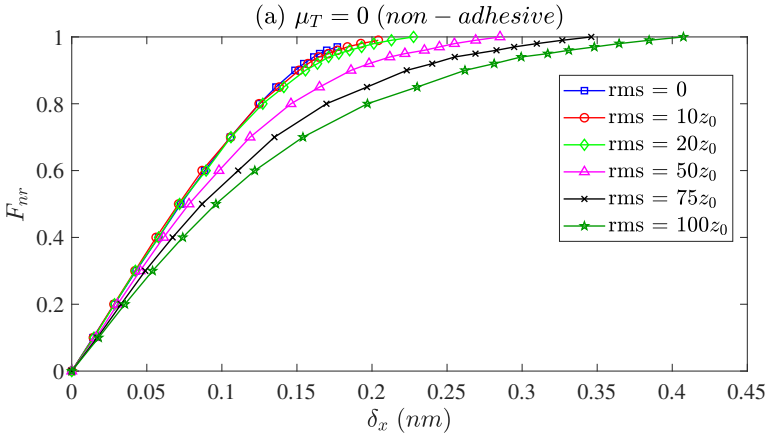

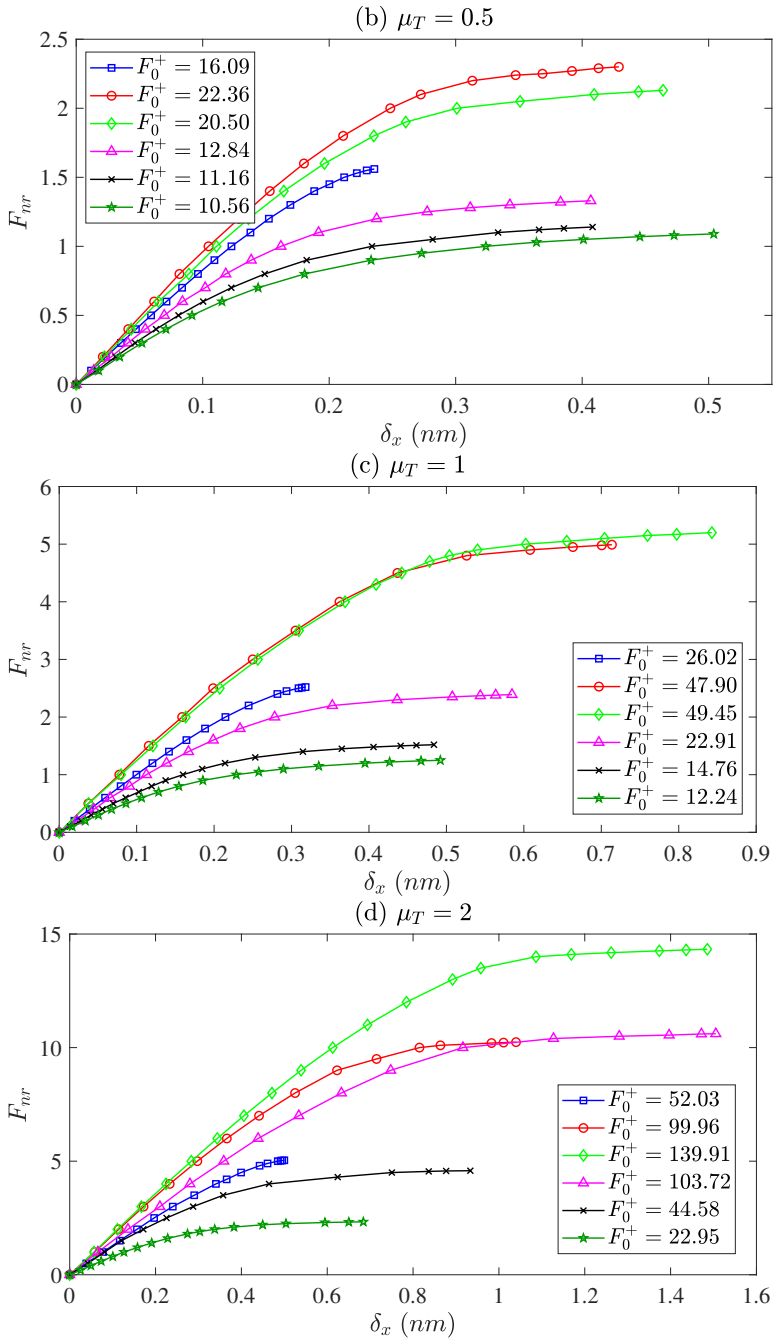

Figure 7: The variation of δ_x versus normalized tangential force, F_{nr}, for a non-adhesive case and three different values of the Tabor parameter, μ_T, and different rms values; subplots (b), (c), and (d) have the same legends as subplot (a) for rms values

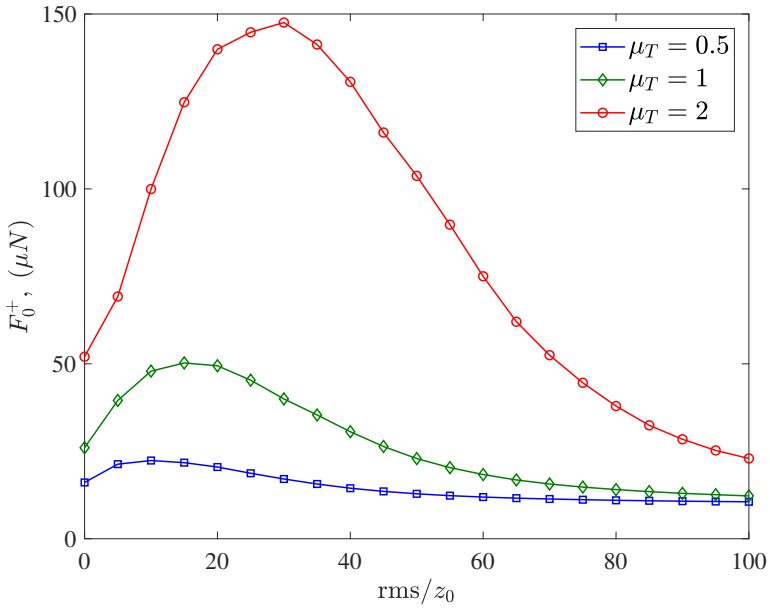

Figure 8: The variation of δ_x versus normalized tangential force, F_{nr}, for a non-adhesive case and three different values of the Tabor parameter, μ_T, and different rms values; subplots (b), (c), and (d) have the same legends as subplot (a) for rms values

The variation of the normalized tangential force versus rigid body displacement for different values of roughness rms and Tabor parameter is shown in Figure 6. This variation, in contrast to $A_{stick}/A_{contact}$, is not merely controlled by the contact positive force, but by a combined effect of adhesion and roughness (which are symbiotic). Figure 8 illustrates the pre-sliding distance for different combinations of roughness rms and Tabor parameter. As mentioned before, the higher roughness rms, the higher pre-sliding distance for non-adhesive contact. In addition, Figure 8 shows that adhesion can exclusively increase the pre-sliding distance. Nonetheless, the combined effect of these two parameters is not cumulative which means that increasing both parameters simultaneously does not increase the pre-sliding distance. The reason behind this behavior is that adhesion and roughness are interdependent and changing roughness affects the adhesive force.

Although the results presented in this study were due to a single value for the external normal force, the same trends and behaviors are expected for other normal forces as well. It only needs to be considered that the static

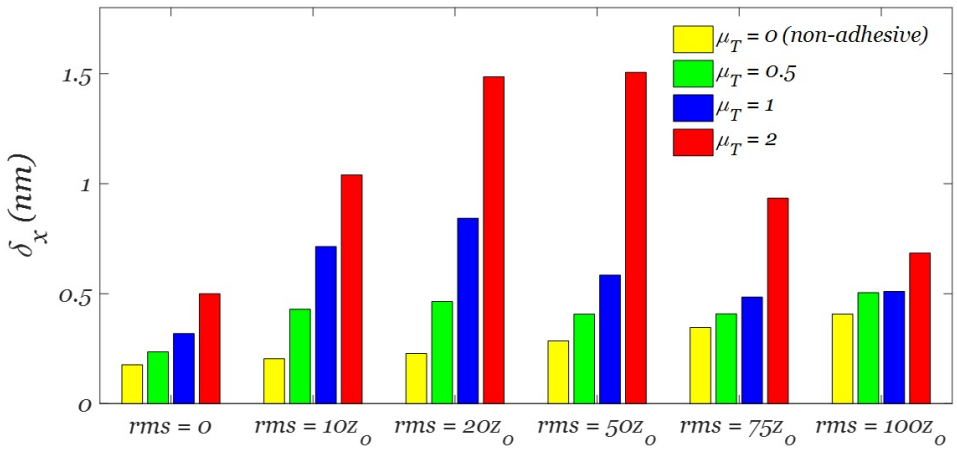

Figure 9: Pre-sliding distance for different combinations of the roughness rms and Tabor parameter

friction coefficient might differ as a function of normal load (as long as its dependence on roughness rms and material properties is not considered).

4 Conclusions

In this paper, a BEM model was presented for the stick-slip transition for the adhesive contact of two bodies of dissimilar materials. The adhesion was modeled using a Dugdale approximation of adhesive energy. The coupling between the normal pressure and shear stresses was taken into account. Via this coupling, normal pressure and shear tractions imposed displacement in other directions. Consequently, there was no full stick condition, even in the absence of an external shear stress. It was shown that the adhesion increases both pre-sliding distance and static friction force. While, roughness can only increase the former one. However, the combined effect of roughness and adhesion is not cumulative as these two parameters are found to be interdependent and any change in the roughness significantly changes the adhesive behavior and thus, normal pressure distribution.

5 Acknowledgment

The authors would like to express their gratitude to ASML Company, Veldhoven, the Netherlands (www.asml.com) for the financial support of

this research project. This research was carried out under project number S61.7.13492 in the framework of the Partnership Program of the Materials innovation institute M2i (www.m2i.nl) and the Netherlands Organization for Scientific Research NWO (www.nwo.nl).

Bibliography

[1] Cattaneo C., "Sul Contatto Di Due Corpi Elastici: Distribuzione Locale Degli Sforzi," *Atti Accad Naz Lincei*, vol. 27, pp. 342–348, 1938.

[2] R. Mindlin, "Compliance of elastic bodies in contact," *Journal of Applied Mechanics*, vol. 16, no. 1945, pp. 259–268, 1949.

[3] M. Ciavarella, "The Generalized Cattaneo Partial Slip Plane Contact Problem. I-Theory," *International Journal of Solids and Structures*, vol. 35, no. 18, pp. 2349–2362, 1998.

[4] M. Ciavarella, "The generalized Cattaneo partial slip plane contact problem. II - Examples," *International Journal of Solids and Structures*, vol. 35, no. 18, pp. 2363–2378, 1998.

[5] S. Spinu and D. Gradinaru, "A Numerical Study of the Partial Slip Elliptical Contact under Fretting Conditions," *Applied Mechanics and Materials*, vol. 371, pp. 576–580, 2013.

[6] L. Kogut and I. Etsion, "A Semi-Analytical Solution for the Sliding Inception of a Spherical Contact," *Journal of Tribology*, vol. 125, no. 3, pp. 499–506, 2003.

[7] W. W. Chen and Q. J. Wang, "A numerical model for the point contact of dissimilar materials considering tangential tractions," *Mechanics of Materials*, vol. 40, no. 11, pp. 936–948, 2008.

[8] Z. J. Wang, W. Z. Wang, H. Wang, D. Zhu, and Y. Z. Hu, "Partial Slip Contact Analysis on Three-Dimensional Elastic Layered Half Space," *Journal of Tribology*, vol. 132, no. 2, p. 021403, 2010.

[9] J. Archard, "Elastic deformation and the laws of friction," *Proceedings of the Royal Society of London. Series A. Mathematical and Physical Sciences*, vol. 243, pp. 190 LP – 205, dec 1957.

[10] J. Greenwood and J. Williamson, "Contact of Nominally Flat Surfaces," *Proceedings of the Royal Society of London . Series A , Mathematical and Physical Published*, vol. 295, no. 1442, pp. 300–319, 1966.

[11] F. P. Bowden and D. Tabor, *The Friction And Lubrication Of Solids*. Oxford: Clarendon Press, 1986.

[12] M. Paggi, R. Pohrt, and V. L. Popov, "Partial-slip frictional response of rough surfaces.," *Scientific reports*, vol. 4, p. 5178, 2014.

[13] B. Grzemba, R. Pohrt, E. Teidelt, and V. L. Popov, "Maximum micro-slip in tangential contact of randomly rough self-affine surfaces," *Wear*, vol. 309, no. 1-2, pp. 256–258, 2014.

[14] S. Medina and D. Dini, "Aspects of modelling adhesion with surface topography," pp. 1–4, 2013.

[15] D. Wang, C. Xu, and Q. Wan, "Modeling Tangential Contact of Rough Surfaces With Elastic- and Plastic-Deformed Asperities," *Journal of Tribology*, vol. 139, no. 5, p. 051401, 2017.

[16] F. E. Kennedy, "Fractal Analysis of Hard Disk Surface Roughness and Correlation With Static and Low-Speed Friction," vol. 121, pp. 968–974, 1999.

[17] P. J. Wei, P. W. Tsai, and J. F. Lin, "Analysis based on microcontact mechanism for the roughness dependent stick-slip motion," *Wear*, vol. 266, no. 1-2, pp. 310–315, 2009.

[18] G. Gavrila and S. Cretu, "Influence of Roughness and Friction Coefficient on the Contact Wear in Partial Slip Conditions," in *MECAHITECH12 International Conference*, (Bucharest), pp. 55–63, 2012.

[19] S. C. Chen, P. J. Wei, and J. F. Lin, "A model developed for the adhesion forces formed between an atomic force microscopy tip and a rough surface under different humidity levels," *Japanese Journal of Applied Physics*, vol. 48, no. 5, pp. 0550011–0550015, 2009.

[20] D. Dini and D. A. Hills, "Frictional Energy Dissipation in a Rough Hertzian Contact," *Journal of Tribology*, vol. 131, no. 2, pp. 21401–1, 2009.

[21] A. T. Kasarekar, N. W. Bolander, F. Sadeghi, and S. Tseregounis, "Modeling of fretting wear evolution in rough circular contacts in partial

slip," *International Journal of Mechanical Sciences*, vol. 49, no. 6, pp. 690–703, 2007.

[22] G. Carbone and E. Pierro, "The Influence of the Fractal Dimension of Rough Surfaces on the Adhesion of Elastic Materials," *Journal of Adhesion Science and Technology*, vol. 26, no. 22, pp. 2555–2570, 2012.

[23] H. Eid, G. G. Adams, N. E. McGruer, a. Fortini, S. Buldyrev, and D. Srolovitz, "A Combined Molecular Dynamics and Finite Element Analysis of Contact and Adhesion of a Rough Sphere and a Flat Surface," *Tribology Transactions*, vol. 54, no. 6, pp. 920–928, 2011.

[24] F. W. Delrio, M. P. de Boer, J. a. Knapp, E. David Reedy, P. J. Clews, and M. L. Dunn, "The role of van der Waals forces in adhesion of micromachined surfaces.," *Nature materials*, vol. 4, no. 8, pp. 629–634, 2005.

[25] N. Mulakaluri and B. N. J. Persson, "Adhesion between elastic solids with randomly rough surfaces: Comparison of analytical theory with molecular-dynamics simulations," *EPL (Europhysics Letters)*, vol. 96, no. 6, p. 66003, 2011.

[26] B. N. J. Persson and M. Scaraggi, "Theory of adhesion: Role of surface roughness," *Journal of Chemical Physics*, vol. 141, no. 12, pp. 1–18, 2014.

[27] L. Pastewka and M. O. Robbins, "Contact between rough surfaces and a criterion for macroscopic adhesion.," *Proceedings of the National Academy of Sciences of the United States of America*, vol. 111, no. 9, pp. 3298–303, 2014.

[28] O. T. Sari, G. G. Adams, and S. Muftu, "Nano-Scale Effects in the Sliding and Rolling of a Cylinder on a Substrate," *Journal of Applied Mechanics*, vol. 72, no. 5, p. 633, 2005.

[29] G. G. Adams, "Stick, partial slip and sliding in the plane strain micro contact of two elastic bodies.," *Royal Society open science*, vol. 1, no. 3, p. 140363, 2014.

[30] H. M. Stanley and T. Kato, "An FFT-Based Method for Rough Surface Contact," *Journal of Tribology*, vol. 119, no. 3, pp. 481–485, 1997.

[31] W. W. Chen, S. Liu, and Q. J. Wang, "Fast Fourier Transform Based Numerical Methods for Elasto-Plastic Contacts of Nominally Flat Surfaces," *Journal of Applied Mechanics*, vol. 75, no. 1, p. 011022, 2008.

[32] Y. A. Karpenko and A. Akay, "Mechanical engineering, a numerical model of friction between rough surfaces.," *Tribology International*, vol. 34, pp. 531–545., 2001.

[33] L. Chang and Y. Gao, "A simple numerical method for contact analysis of rough surfaces," *Journal of tribology*, vol. 121, no. July, pp. 425–432, 1999.

[34] A. Akchurin, R. Bosman, P. M. Lugt, and M. Van Drogen, "On a model for the prediction of the friction coefficient in mixed lubrication based on a load-sharing concept with measured surface roughness," *Tribology Letters*, vol. 59, no. 1, pp. 1–11, 2015.

[35] a. Jourani, "A New Three-Dimensional Numerical Model of Rough Contact: Influence of Mode of Surface Deformation on Real Area of Contact and Pressure Distribution," *Journal of Tribology*, vol. 137, no. 1, p. 011401, 2014.

[36] S. Cai and B. Bhushan, "A numerical three-dimensional contact model for rough, multilayered elastic/plastic solid surfaces," *Wear*, vol. 259, no. 7-12, pp. 1408–1423, 2005.

[37] J. Zhao, E. A. Vollebregt, and C. W. Oosterlee, "A fast nonlinear conjugate gradient based method for 3D concentrated frictional contact problems," *Journal of Computational Physics*, vol. 288, pp. 86–100, 2015.

[38] S. Liu, Q. Wang, and G. Liu, "A versatile method of discrete convolution and FFT (DC-FFT) for contact analyses," *Wear*, vol. 243, no. 1-2, pp. 101–111, 2000.

[39] K. L. Johnson, *Contact Mechanics*. Cambridge: Cambridge University Press, 1985.

[40] M. Bazrafshan, M. B. de Rooij, M. Valefi, and D. J. Schipper, "Numerical method for the adhesive normal contact analysis based on a Dugdale approximation," *Tribology International*, vol. 112, no. April, pp. 117–128, 2017.

[41] D. Maugis, "Adhesion of spheres: The JKR-DMT transition using a dugdale model," *Journal of Colloid And Interface Science*, vol. 150, no. 1, pp. 243–269, 1992.

[42] A. R. Savkoor, *Dry adhesive friction of elastomers: a study of the fundamental mechanical aspects*. Phd thesis, Delft University of Technology, 1987.

[43] S. Hanke, J. Petri, and D. Johannsmann, "Partial slip in mesoscale contacts: Dependence on contact size," *Physical Review E - Statistical, Nonlinear, and Soft Matter Physics*, vol. 88, no. 3, pp. 1–14, 2013.

[44] Y. Hu and K. Tonder, "Simulation of 3-D random rough surface by 2-D digital filter and Fourier analysis," *International Journal of Machine Tools and Manufacture*, vol. 32, no. 1-2, pp. 83–90, 1992.

[45] S. Medina and D. Dini, "A numerical model for the deterministic analysis of adhesive rough contacts down to the nano-scale," *International Journal of Solids and Structures*, vol. 51, no. 14, pp. 2620–2632, 2014.

[46] A. Winogrodzka, *Pre-sliding behavior of multi asperity ceramic contacts*. PhD thesis, University of Twente, 2015.

Paper E

The Effect of Adhesion and Roughness on Friction Hysteresis Loops

M. Bazrafshan[1,2*], M.B. de Rooij[2], and D.J. Schipper[2]

[1]*Materials innovation institute (M2i), Van der Burghweg 1, 2628 CS Delft, Netherlands*
[2]*Laboratory for Surface Technology and Tribology, Department of Engineering Technology, University of Twente, P.O. box 217, 7500AE, Enschede, Netherlands*

Abstract

Friction hysteresis results from an oscillating friction force at a contact interface. At nano-scale, this phenomenon is affected by the roughness of the contact interface and adhesion. In nanotribology, therefore, it is highly desirable to understand and predict this behavior to estimate the energy loss and possible wear. This paper presents a boundary element model (BEM) for the adhesive friction hysteresis contact at the interface of two bodies of arbitrary geometry. In the model, adhesion is represented by means of a Dugdale approximation of the total work of adhesion at local areas with a very small gap between the two surfaces. The amplitude of the oscillating tangential displacement is very small compared to the contact area which means that the interface does not experience gross-sliding between the two surfaces (the contact remains in the pre-sliding state). Hence, the frictional contact is divided into sticking and slipping regions, defined based on the local values for shear stress and normal pressure, and the rate of relative displacement. The model is first verified by comparing the numerical and analytical (Mindlin theory) solutions for the contact of a smooth ball and a flat of identical materials under a fixed normal force and an oscillating friction force. Then, the problem is solved at the smooth interface between a rigid ball and an elastic flat for various values of the work of adhesion. It is shown that as the work of adhesion increases, both static friction force and pre-sliding displacement increase due to the increase in the contact repulsive force. In addition, the rough interface between a glass ball against a silicon wafer and a DLC (Diamond-Like Carbon) coating is considered. Since adhesion depends on the interface roughness, the corresponding contact repulsive force is different for these interfaces. For the smoother interface, a larger contact repulsive force and consequently, a larger static friction force and pre-sliding displacement are obtained.

Keywords: Boundary Element Method, Friction, Hysteresis, Adhesion, Roughness, Pre-sliding

1 Introduction

It is nowadays very well-known that tribological phenomena such as friction, adhesion, and wear start at asperity level where the roughness details of the mating surfaces, along with their physical properties, dominate the real contact area. In nanotribology, specifically, both roughness and adhesion symbiotically influence the contact area. One of the phenomena, on which the functionality and lifetime of mechanical components depend, is the frictional hysteresis, where mechanical contacts are subject to small (compared to the contact area) oscillating tangential displacements. If the oscillating friction force is small enough to avoid gross-sliding at the interface, pre-sliding friction (also known as partial slip) takes place. This can cause fretting wear of the surfaces and fretting fatigue. In line with the elegant studies of Cattaneo [1] and Mindlin [2, 3] on the partial slip problem for the contact of bodies of identical materials, other researchers followed numerical approaches. Kogut and Etsion conducted a FEM simulation on the contact of a rigid flat pressed against an elastic perfectly plastic ball [4]. They used an approximate analytical solution to evaluate the static friction force. Rather than using the Amontons law of friction, they treated the sliding friction as a failure mechanism based on the plastic yield. Wang et al proposed a FEM model to study the partial slip fretting contact of a ball against a flat, where the friction coefficient in the slip region is not fixed [5]. Yue and Abdel Wahab studied the effect of variable coefficient of friction on the gross-sliding and partial slip conditions of fretting wear [6]. They found out that considering a variable coefficient of friction is more crucial for the partial slip conditions and the FEM results are close to the experimental ones. Chen and Wang developed a 3D numerical model for the partial slip contact of elastically dissimilar materials [7]. They used a CGM-based (Conjugate Gradient Method) algorithm to determine the contact area and stick region. Wang et al followed the same strategy to study the partial slip on a 3D elastic layered half-space, which is suitable to study the role of a coating in a contact problem [8]. An extension to this model, to simulate the friction hysteresis behavior in the partial slip contact mode, is provided in [9]. Rodriguez-Tembleque et al proposed a BEM formulation to model wear under gross-sliding and partial slip conditions [10]. Gallego et al also proposed a CGM-based model and implemented DC-FFT (Discrete Convolution-Fast Fourier Transform) to calculate the convolution integrals to simulate the fretting modes I, II, and III [11]. They found a discrepancy between their numerical results and those of the Mindlin solution for the

contact of dissimilar materials. In contrast to the Mindlin solution, the development of the slipping area is no longer symmetric. Furthermore, due to the dissimilarity of the elastic properties of the contacting bodies, normal pressure causes relative displacement at the interface and therefore, a slipping area exists even in the absence of a shear stress.

Although all these models deal with ideally smooth contact interfaces, they can serve as a basis for multi-asperity models for the frictional contact of rough surfaces. The initial studies were conducted by combining the Mindlin solution and Greenwood-Williamson statistical model to investigate the proportionality of the friction force and normal load at a rough interface [12]. Further similar research, known as multi-asperity contact models, were conducted to study the partial slip and gross-sliding friction [13–16]. As one of the main limitations of multi-asperity models is that the interaction between asperities is not taken into account, other numerical approaches were employed by researchers [17–22].

It is well-known that the surfaces are, even at nano-scale, rough, meaning that the contact loads are carried only by the high asperities of the profile. In other words, as the contact is restricted to such local areas, the real area of contact, as an important parameter in friction studies, is essentially much less than the nominal contact area. In the presence of adhesion at the interface, the separated areas are pulled toward the counter surface, leading to higher contact pressures and making new contact patches at near-contacting regions and right outside the boundaries of already contacting areas. There is rich literature on the effect of adhesion on the contact area and pressure at a rough interface [23–37]. Sari et al studied the plane-strain version of the Cattaneo-Mindlin problem in the presence of adhesion where the contact area is determined using the Maugis theory independent of the tangential forces [38]. The contact area is composed of a central stick zone surrounded by an annulus of slip in which the shear stress is assumed constant. Adams studied the adhesive pre-sliding contact of a smooth curved elastic body and a flat half-space [39]. He assumed the surface energy to be in a manner similar to the JKR (Johnson, Kendall, Roberts) theory for spherical contact (with infinitely large adhesive stress at the edges of contact [40]). In the plane strain condition, the contact is in full stick regime until the tangential force reaches a critical value. This critical force causes a direct transition to either full slip or to a partial slip condition where two slip regions surround the central stick zone. Bazrafshan et al proposed a numerical model for the adhesive contact of rough surfaces in partial slip regime [41]. They numerically showed that, for an adhesive contact, it is the contact repulsive force, rather than the external normal force, that controls

the start of gross-sliding. In their model, the tangential force is applied in one single step. In other words, they did not include the history-dependence of the friction force which is needed to simulate friction hysteresis.

This paper presents a BEM model for the adhesive frictional contact at a rough interface of two bodies with dissimilar materials. The history-dependence of friction is considered to determine the stick and slip regions in the partial slip regime and simulate the hysteresis behavior of friction. The coupling between the normal pressure and shear stress components leads to asymmetry of the stick-slip transition. The shear stress is locally proportional to the normal pressure in the slip region, while it is neglected in the adhesive area. The stick zone as well as the corresponding shear stress are unknown and must be calculated numerically so that they fulfill the conditions imposed by the stick-slip definition. An oscillating tangential force is applied step-by-step between the two entities of loading where the gross-sliding is about to start.

2 Theory and problem definition

The contact configuration at the interface of bodies 1 (elastic) and 2 (rigid) is shown in Figure 1. Body 2 is pressed against body 1 under a normal force of F_0. The tangential forces F_x and F_y are applied on body 1 in x and y directions, respectively. In addition, h and g are the separation before and after the deformation, respectively, and $\delta_m(m = x, y, z)$ is the rigid body displacement. The deformation in each direction, $u_m(m = x, y, z)$, resulted from the normal pressure, p, and shear stress components, q_x and q_y, at point (x, y) and time t, is given by:

$$\begin{aligned} u_x(x,y,t) &= c_{xx} * q_x(x,y,t) + c_{xy} * q_{xy}(x,y,t) + c_{xz} * p(x,y,t) \\ u_y(x,y,t) &= c_{yx} * q_x(x,y,t) + c_{yy} * q_{xy}(x,y,t) + c_{yz} * p(x,y,t) \\ u_z(x,y,t) &= c_{zx} * q_x(x,y,t) + c_{zy} * q_{xy}(x,y,t) + c_{zz} * p(x,y,t) \end{aligned} \tag{1}$$

Here, symbol * means continuous convolution and $c_{mn}(m, n = x, y, z)$ are the time-independent Greens functions [7]. After deformation points 1 and 2 on bodies 1 and 2 move to points 1' and 2'. Therefore, in the normal direction, the separation, g, can be related to the deformation, rigid body displacement, and initial separtion as:

$$g(x,y) = u_z(x,y) + h(x,y) - \delta_z \tag{2}$$

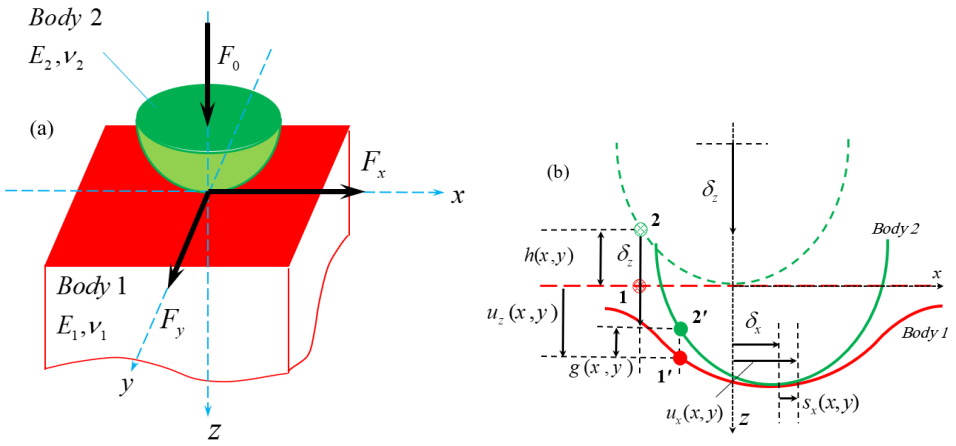

Figure 1: Contact variables (adapted from [41])

When tangential forces are small enough to avoid gross-sliding, the non-uniform deformations at the interface are locally different from the global rigid body displacement. Consequently, the relative displacement, s_m, could be locally non-zero and thus, partial slip takes place.

$$s_m(x,y,t) = u_m(x,y,t) - \delta_m(t), \quad m = x,y \tag{3}$$

Therefore, the entire contact area is divided to two regimes of stick and slip, distinguished by two criteria. In the stick region, the shear traction, $\sqrt{x^2+y^2}$, must not exceed the limiting value of $\mu_f p$, while these two must be the same in the slip zone. This condition is in analogy with the Amontons law of friction. The nonlinearity of friction due to the stick-slip transition results in a hysteresis behavior once an oscillating tangential force is applied on the contact interface. This leads to the dependence of a contact state to the previous ones. As a result, the contact stress components and deformations in Eq. (1) are functions of time, t, too. Hence, the secondary condition needed to be fulfilled, to determine stick and slip regions, is the rate of relative displacement which must be zero and non-zero in stick and slip zones, respectively. Here, this rate is defined by the change of the relative displacement at each moment compared to the previous one:

$$\Delta s_m(x,y,t) = s_m(x,y,t) - s_m(x,y,t-\Delta t), \quad m = x,y \tag{4}$$

where Δt is the time increment which is replaced by loading steps for the quasi-static application of the tangential force in the current study. The mentioned criteria, at time t, can be mathematically expressed as:

$$\begin{aligned} A_{st} = (x,y) \in A_c \mid & \sqrt{q_x(x,y)^2 + q_y(x,y)^2} < \mu_f p(x,y), \\ & \sqrt{\Delta s_x(x,y)^2 + \Delta s_y(x,y)^2} = 0 \\ A_{sl} = (x,y) \in A_c \mid & \sqrt{q_x(x,y)^2 + q_y(x,y)^2} = \mu_f p(x,y), \\ & \sqrt{\Delta s_x(x,y)^2 + \Delta s_y(x,y)^2} \neq 0 \end{aligned} \tag{5}$$

here, A_c refers to the contact area, or in other words, the nodes with positive pressure and zero gap. The presence of adhesion results in a larger contact area compared to a non-adhesive contact. In this study, the total work of adhesion, $\Delta\gamma$, is expressed by means of a Dugdale approximation, meaning that the constant negative stress, $-\sigma_0$ (maximum negative stress of the Lennard-Jones potential), is present at areas with a smaller separation than h_0, given by [42]:

$$h_0 = \frac{\Delta\gamma}{\sigma_0}, \quad \sigma_0 = \frac{16\Delta\gamma}{9\sqrt{3}z_0} \tag{6}$$

where z_0 is the equilibrium distance ranging from 0.2 to $0.4nm$ [43]. In that sense, the normal pressure, over the computation domain Ω, in the presence of adhesion, described in Eq. (6), is also dealt with [42].

$$p(x,y,t) > -\sigma_0 \quad at \quad g(x,y,t) = 0 \tag{7a}$$
$$p(x,y,t) = -\sigma_0 \quad at \quad 0 < g(x,y,t) < h_0 \tag{7b}$$
$$p(x,y,t) = 0 \quad at \quad g(x,y,t) > h_0 \tag{7c}$$
$$\int_\Omega p(x,y,t)dxdy = F_0 \tag{7d}$$

An outline of the algorithm for the hysteresis behavior of the adhesive friction problem is illustrated in Figure 2. Material properties, initial

separation, loading conditions, work of adhesion, and the static friction coefficient are input to the algorithm, in the first step. In step 2, the adhesive stick-slip problem in the absence of an external shear force, as described in [41], is solved. In step 3, the tangential forces are increased by a specified increment. Step 4 solves the adhesive normal contact as explained in [42]. Then, step 5 solves the stick-slip problem for the shear stress components based on a CGM algorithm [41]. In steps 6, the tangential forces increments are calculated and checked in step 7 to see whether they are within an accepted tolerance from the ones set in step 3. If the convergence is not fulfilled, the increment of the rigid body displacements in tangential directions are updated in step 8. Step 9 checks the convergence in the normal contact pressure and if it is not met, the surface geometry, in step 10, is updated by taking into account the deformation in z direction caused by the current shear stress components [7]. Step 11 checks whether the loading steps in tangential directions has ended. If not, the increments of the tangential forces are adjusted in step 3. In the proposed algorithm, all the calculations are carried out on a discretized interface and history of tangential loading, as described in [41].

3 Numerical examples and discussion

The proposed algorithm is implemented to study the adhesive pre-sliding contact of a ball of radius $R = 50\mu m$ pressed against an elastic half-space by the normal force of F_0. The interface deformations, everywhere in this study, are considered elastic. The mechanical properties of the elastic half-space are set to $E_1 = 70GPa,\ \nu_1 = 0.3$. The friction coefficient is also set to $\mu_f = 0.2$. Bazrafshan et al showed that, for adhesive contacts, it is the contact repulsive force, F_0^+, that controls the start of gross-sliding and not the external normal force [41]. The contact repulsive force, defined as the contact force resulting from the contact positive pressure, is given as:

$$F_0^+ = \int_{\Omega^+} p(x,y)dxdy \tag{8}$$

in which, Ω^+ is the domain at which the pressure is positive. Based on the definition, this force is always greater than the external normal force for an adhesive contact, i.e. $F_0^+ > F_0$. Therefore, the tangential force is considered to vary between $-\mu_f F_0^+$ and $\mu_f F_0^+$. One must note that the amplitude of the oscillating friction force can be smaller than $\mu_f F_0^+$. This

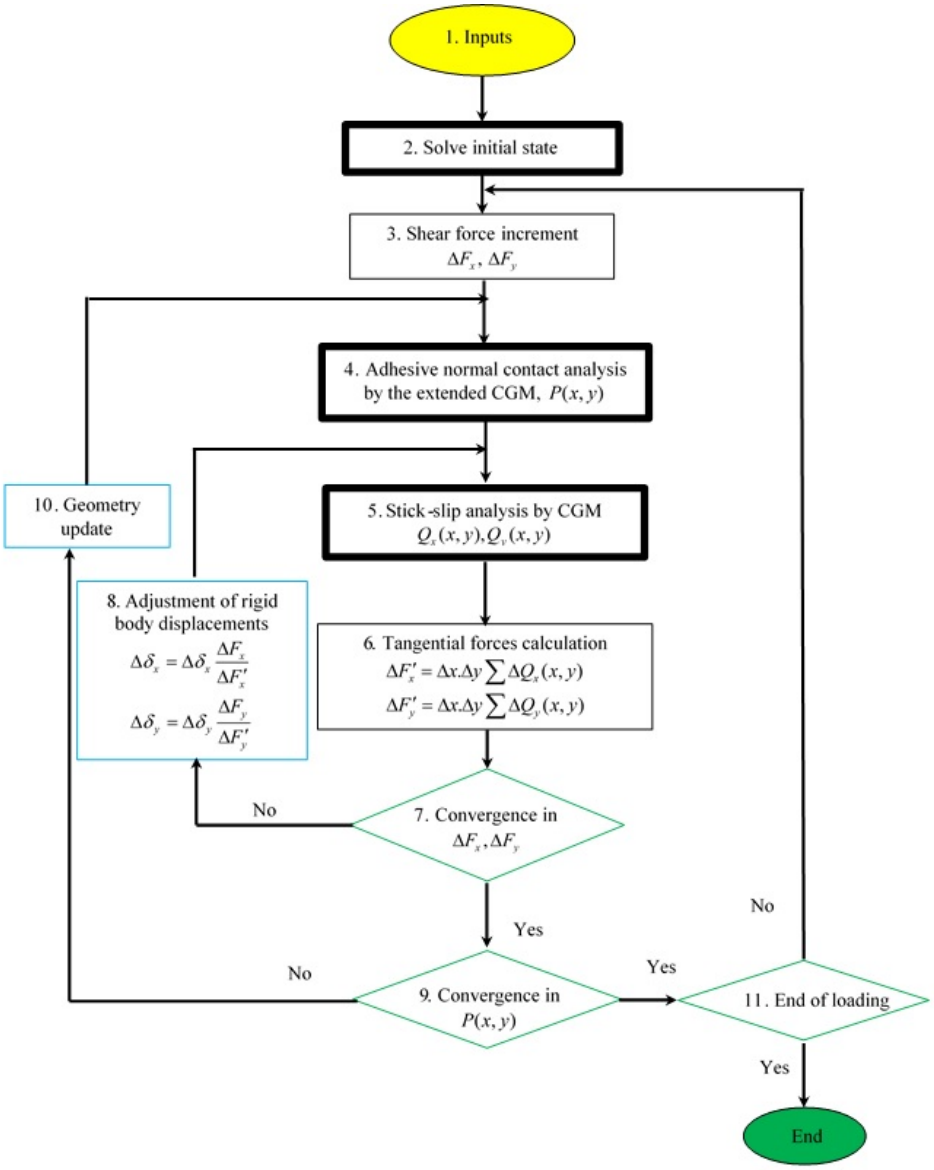

Figure 2: Algorithm flowchart

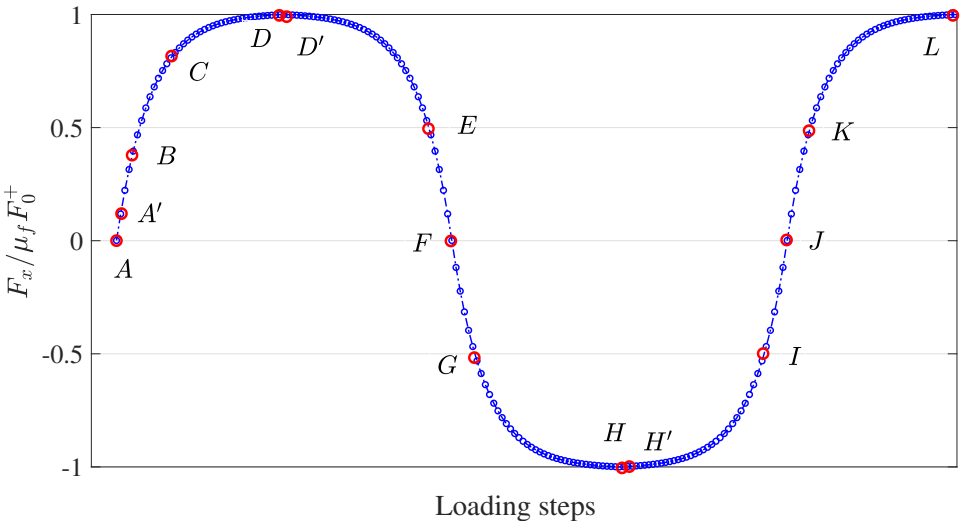

Figure 3: Tangential loading path

choice, here, is made to investigate the effect of roughness and adhesion on the static friction force and pre-sliding displacement, which correspond to the moment right before the start of gross-sliding.

The tangential loading path is demonstrated in Figure 3, where the normal force is fixed. The load increment is chosen to be exponential in order to have more points close to the turning points (points D, H, L, and so on) to achieve a more accurate behavior since even a tiny change in the tangential force near these points causes a noticeable tangential displacement. Points A', D', and H' are placed right after the points A, D, and H, respectively. For contact of dissimilar materials, the loading is repeated for two more loops to reach a constant friction hysteresis loop.

3.1 Friction hysteresis at the contact of identical materials (Mindlin solution)

To verify the accuracy of the proposed algorithm, it is first used to simulate the non-adhesive elastic contact of a smooth ball against a flat, both of identical materials, for which the analytical solution of Mindlin applies [3]. For the numerical simulation, the normal force is $F_0 = 10\mu N$ and the Hertzian contact radius, a, is first calculated and the computation domain is then chosen to be $-2a < x, y < 2a$ (the factor 2 extension is to minimize the periodicity error due to the DC-FFT). Moreover, the entire

computation domain is divided into 256×256 square elements. Figure 4 depicts the transition from the full stick to the full slip condition. For this simulation, only one tangential loading loop is studied, due to the symmetricity of the results. In the absence of an external shear force, the entire contact area is in stick regime. As soon as a small tangential force is applied, an annulus of slip forms around the central stick zone and develops toward the center of contact upon the further increase of the tangential force. When the tangential force reaches $\mu_f F_0$ (the static friction force for this case), the entire contact area is in slip condition (Point D). At this moment, the tangential force is reversed and (almost) the whole contact area goes to the stick condition (point D'), and the same behavior is repeated for the rest of loading path. Figure 5(a) compares the normalized friction force vs. tangential displacement curves resulted from the proposed numerical algorithm and the analytical solution of Mindlin which are, as can be seen, in good agreement. The variation of the ratio of stick to contact area, A_{st}/A_c, is also compared in Figure 5(b) and shows good agreement between numerical and analytical results.

3.2 Friction hysteresis at the contact of dissimilar materials

In this section, the adhesive hysteresis contact of a rigid ball on a smooth elastic half-space is investigated. The elastic properties of the half-space are the same as those of the previous section. For the total work of adhesion, three values of 0 (corresponding to the non-adhesive contact), $50mJ/m^2$ and $100mJ/m^2$ are considered. Then, the contact radius, a, is analytically calculated for each case and the computation domain is considered to be $-2a < x, y < 2a$. Then, the entire computation domain is discretized to 256×256 square elements. Since the contact radius varies with the normal force and the work of adhesion, the resulting grid size for the case studies in this paper varies from $2nm$ to $6nm$.

First consider the non-adhesive contact at this interface under a normal load of $F_0 = 10\mu N$. Figure 6 displays the transition from stick to slip at such an interface (points A to L in Figure 3 correspond to Figure 6 A to L), while the normal force is fixed and a uni-directional oscillating friction force, F_x, is applied to the interface. When a pure normal force is applied on such a configuration (point A), an annulus of slip surrounds a circular sticking region. This results from the difference between the mechanical properties of the contacting materials which leads to different displacements at the contact interface and therefore, relative displacement between the two bodies and initial slip, even in the absence of an external shear force. As soon as an

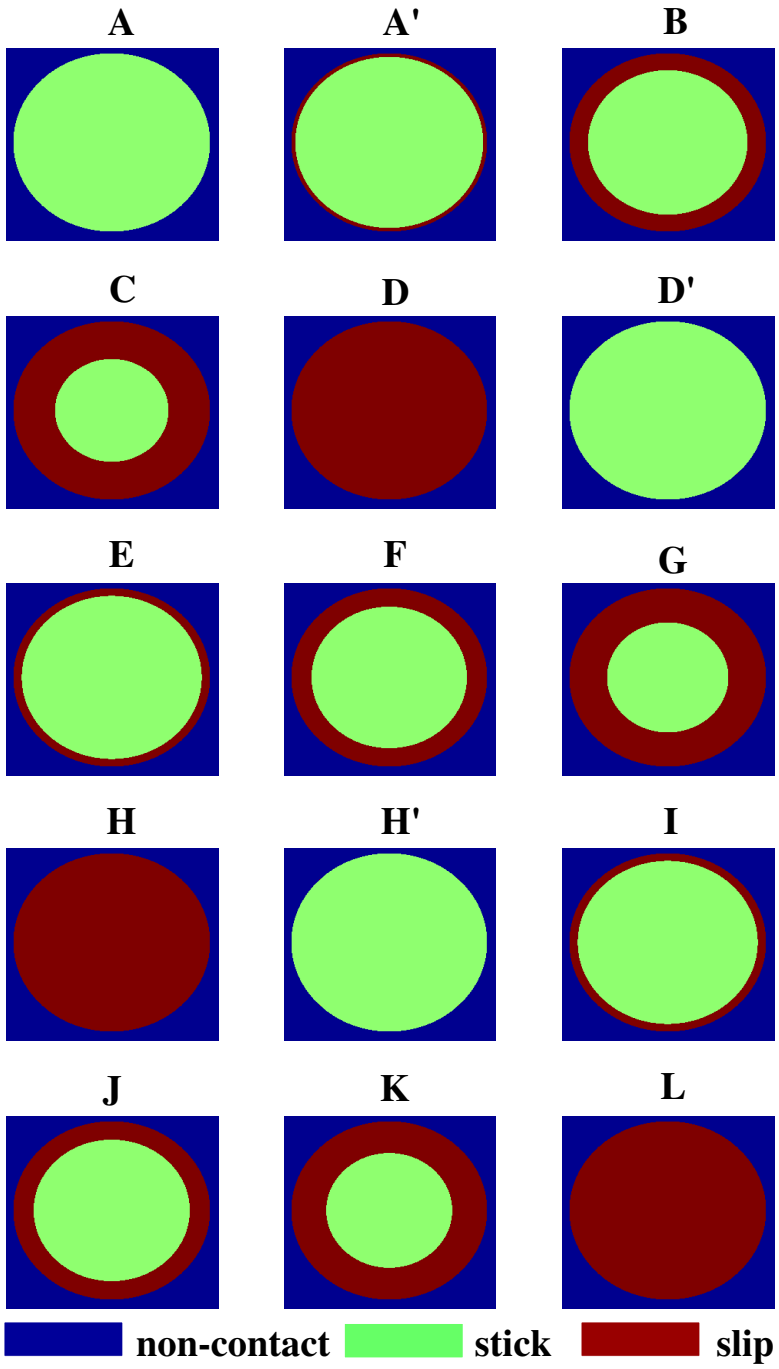

Figure 4: Transition from stick to slip for the contact of identical materials, Mindlin solution

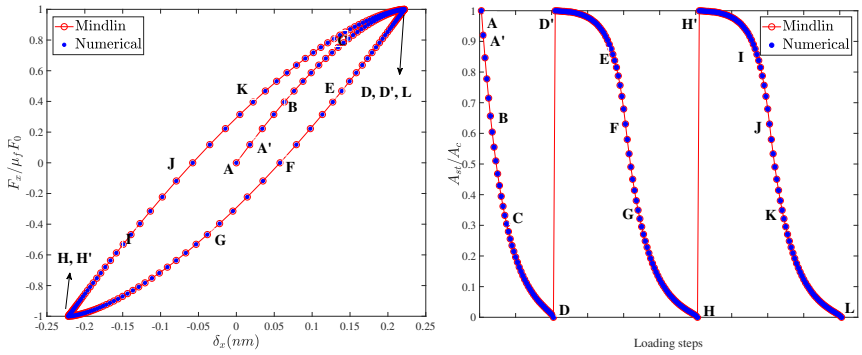

(a) (b)

Figure 5: Comparison of the proposed numerical algorithm with the analytical solution of Mindlin for the non-adhesive contact of a ball against a flat, both of identical materials, (a) normalized friction force vs. tangential displacement and (b) variation of the A_{st}/A_c ratio

infinitesimal friction force is applied (corresponds to point A'), the shape of the stick zone changes (Figure 6A'). At this moment, a part of slipping region, experiencing small relative displacement in the direction opposite to that of the applied friction force, enters the stick region (point A'), leading to a larger sticking area compared to the initial circular region at the center of the contact. This behavior can be also noticed through the abrupt initial increase in the A_{st}/A_c ratio, as shown in Figure 7(a) (which shows only one loop of loading). Further application of the shear force makes the sticking area shrink and disappear at the turning point D, which corresponds to a full slip state. At this point, the friction force direction is reversed and the whole contact area experiences a full-stick state, point D', which shrinks toward the center (similar to the Mindlin solution, however non-symmetrically) as shown for points D' to H. At the turning point H, the friction force direction is again reversed, and the same behavior is repeated up to the next turning point. It is noted that after the first cycle of loading, the development of the slipping area becomes symmetric; yet, it differs from the Mindlin solution as the trend in A_{st}/A_c ratio is not the same and the numerical algorithm suggests that upon reversing the friction force, the slipping area develops faster than the one predicted by Mindlin. This is suggested by the quick drop in the A_{st}/A_c ratio after each turning point (see Figure 7(a)). Another difference is the asymmetry of the friction force vs. tangential displacement curve in the numerical simulations which results from the initial loading

cycle which shifts the equilibrium point to the sides on the horizontal axis of this curve (see Figure 7(a)).

Figure 8 illustrates the friction hysteresis loops at the mentioned contact interface for three values of the normal force. It is clear that the pre-sliding displacement is directly controlled by the external normal force (which is, for a non-adhesive contact, the same as the contact repulsive force), whereas the normalized static friction force is entirely independent from the normal force.

To study the effect of adhesion on the friction hysteresis loops, the same simulation is conducted at the normal force of $F_0 = 10\mu N$ for three values of the work of adhesion, as mentioned before. Figure 9 depicts these loops for these cases. Although the normal force is fixed, the contact repulsive force increases with the work of adhesion resulting in a larger pre-sliding displacement. Moreover, comparing the maximum normalized shear force with the ratio of the repulsive to external normal force, F_0^+/F_0, proves that the static friction force is controlled by the contact repulsive force and not the external normal force.

Figure 10 shows the adhesive friction hysteresis loops at three different values of the normal force for a fixed value of the work of adhesion. As it can be noticed, a larger normal force, resulting in a larger contact repulsive force, leads to a larger pre-sliding displacement but a lower normalized static friction force. On must, however, note that the absolute value of the static friction force increases with the external normal force as denoted in Figure 10 (see the F_0^+ values).

3.3 Friction hysteresis at a rough interface

The adhesive friction hysteresis at the contact of a rigid smooth ball against a rough elastic flat is studied in this section. The elastic and geometrical properties are the same as those of the previous section. Two different rough profiles, measured by an Atomic Force Microscopy (AFM), for the elastic flat is considered. One is the surface topography of a DLC coating on a $2\mu m \times 2\mu m$ area including 512×512 pixels as shown in Figure 11 (a). The second profile is the roughness of a silicon wafer on a $2\mu m \times 2\mu m$ area including 512×512 pixels (Figure 11 (b)). The DLC surface has a rougher profile compared to the Si surface as suggested by their roughness rms values.

Figure 12(a) compares the friction hysteresis loops at the non-adhesive contact of the ball against a smooth half-space and each of the two rough profiles. It is observed that the higher the roughness rms, the higher the

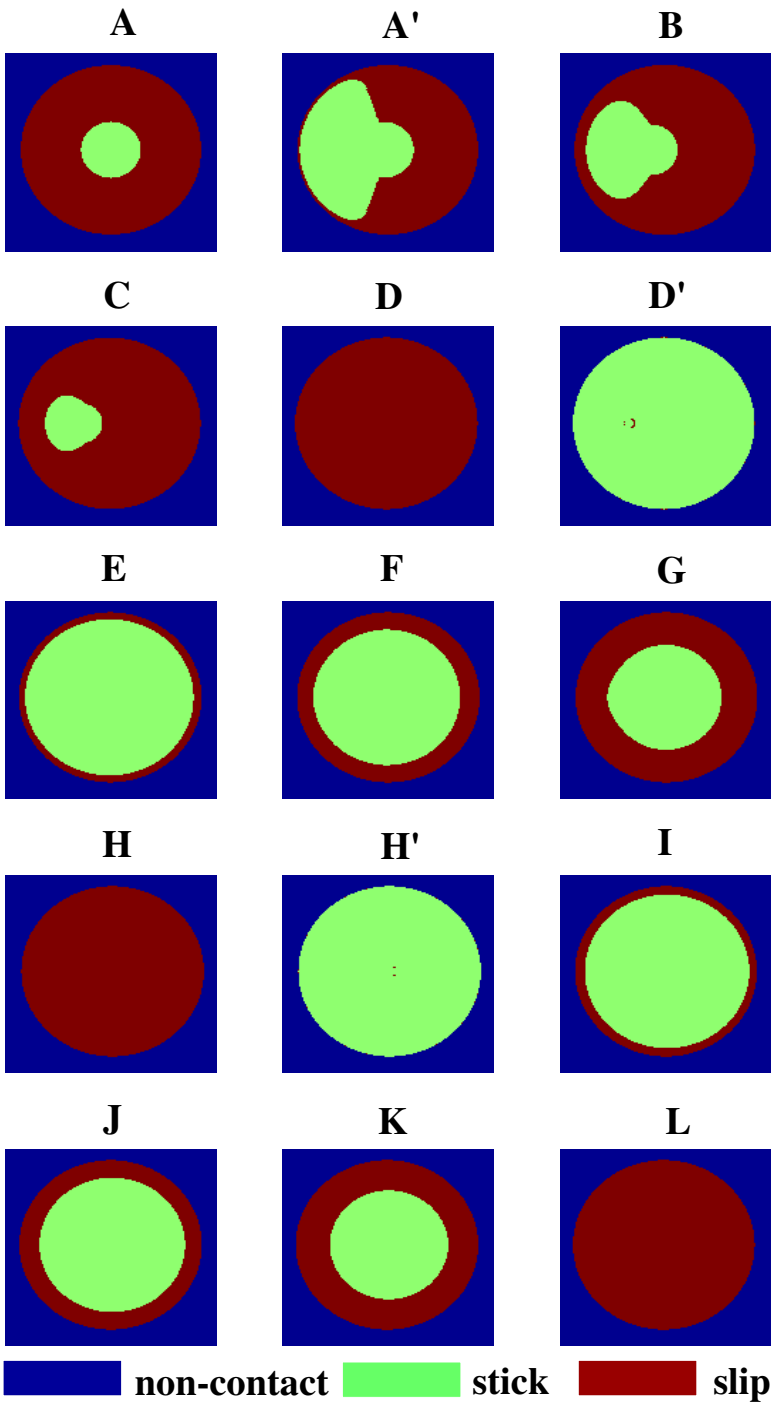

Figure 6: Transition from stick to slip for the contact of dissimilar materials, numerical solution

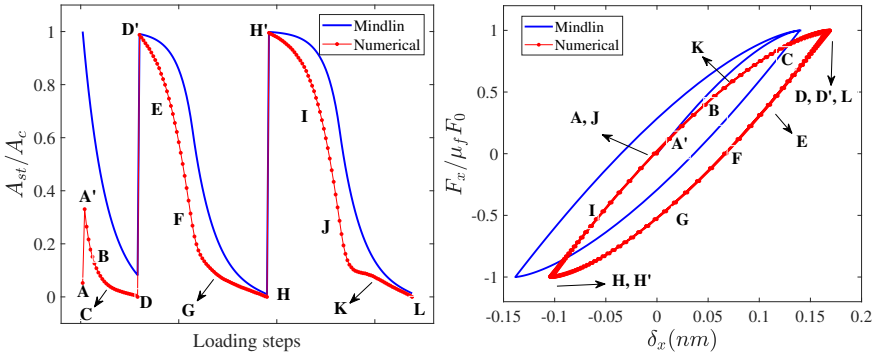

(a) (b)

Figure 7: Contact of dissimilar materials, (a) normalized friction force vs. tangential displacement, comparison to the Mindlin solution (b) variation of the A_{st}/A_c ratio, comparison to the Mindlin solution

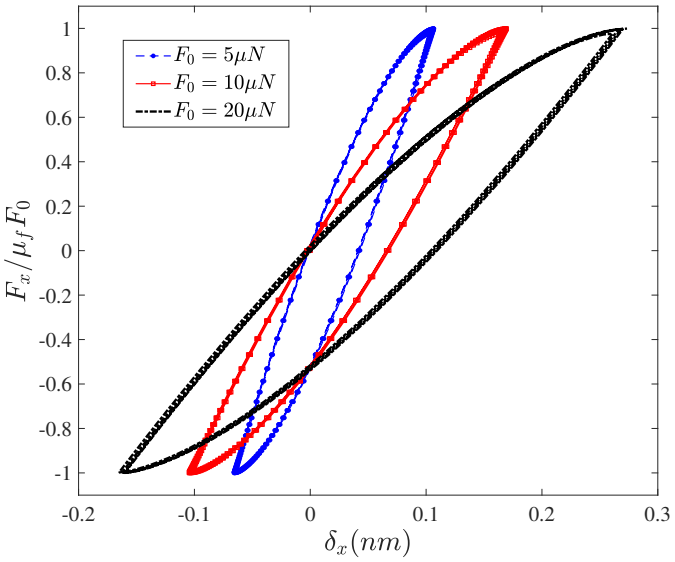

Figure 8: Non-adhesive friction hysteresis loops at a ball on flat contact with different normal forces

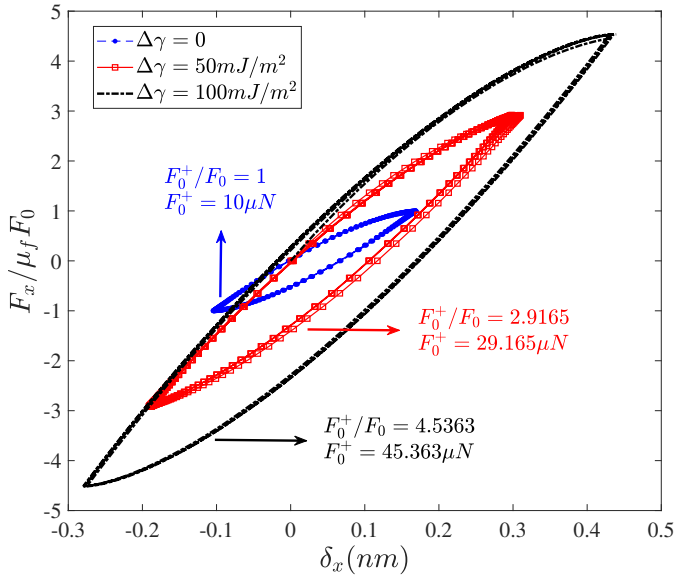

Figure 9: Adhesive friction hysteresis loops for different values of the work of adhesion, $F_0 = 10\mu N$

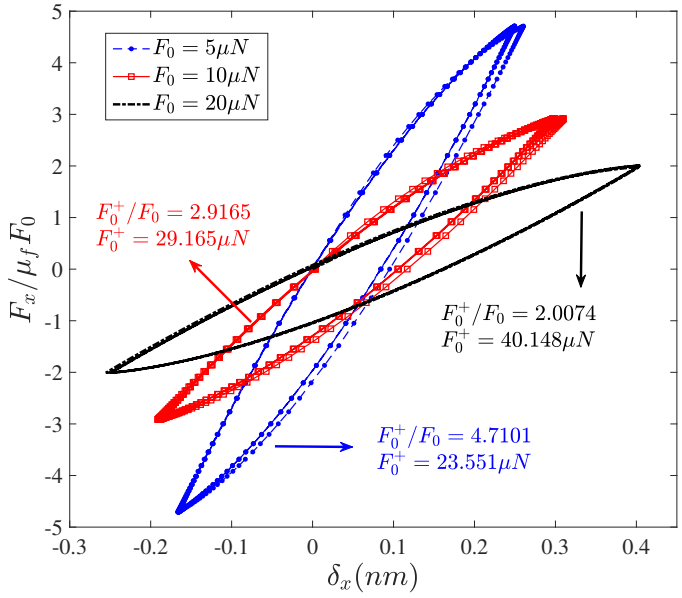

Figure 10: Adhesive friction hysteresis loops for different values of the normal force, $\Delta\gamma = 50mJ/m^2$

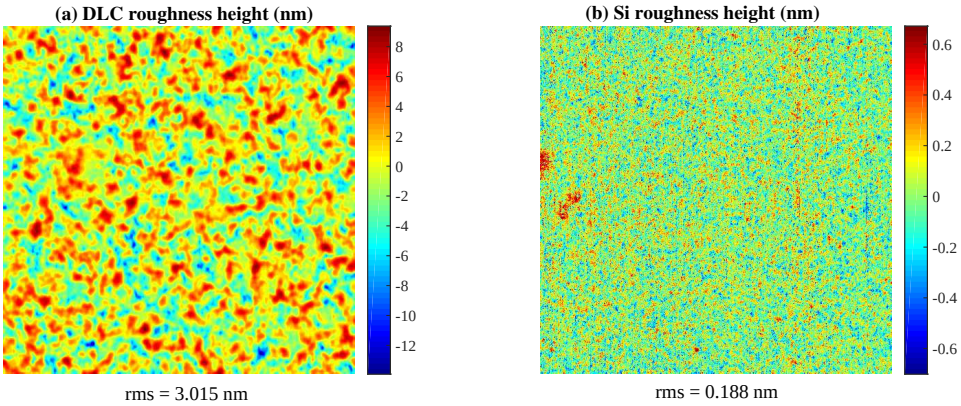

Figure 11: The AFM measurement of the surface roughness of (a) a DLC coating and (b) a silicon wafer; the area of each measured profile is $2 \times 2\mu m^2(512 \times 512\text{pixels})$

pre-sliding displacement, while the static friction force is the same and equal to $\mu_f F_0$. This confirms that for a non-adhesive contact, the roughness can only change the pre-sliding displacement. In the presence of adhesion, the extent to which adhesion can change static friction force and pre-sliding displacement depends on the roughness properties of the interface. Figure 12(b) suggests that adhesion only slightly increases the pre-sliding displacement and static friction for the DLC contact. On the other hand, Figure 12(c) illustrates that a lower level of roughness rms, provided all other conditions are the same, can remarkably increase both these two parameters. This comparison can be also verified through checking the contact repulsive force which is almost three times larger for the latter case compared to the former one. Figure 12(c) also indicates that for a fixed contact, adhesion can increase not only the pre-sliding displacement but also the static friction. One has to, of course, note that the combined effect of roughness and adhesion is not cumulative, as shown in Figure 12(d), where the pre-sliding displacement is larger for the rougher surface although the static friction force is lower. It is well-known that the roughness can reduce the adhesive force. However, it has been shown that introducing a small level of roughness, like that of the Si profile, can increase adhesion compared to a smooth interface [42, 44]. Here, going from a smooth interface to the slightly rough profile of Si increases the contact repulsive force from 29.165 to $30.672\mu N$ which results in a slight increase in both the static friction and pre-sliding displacement.

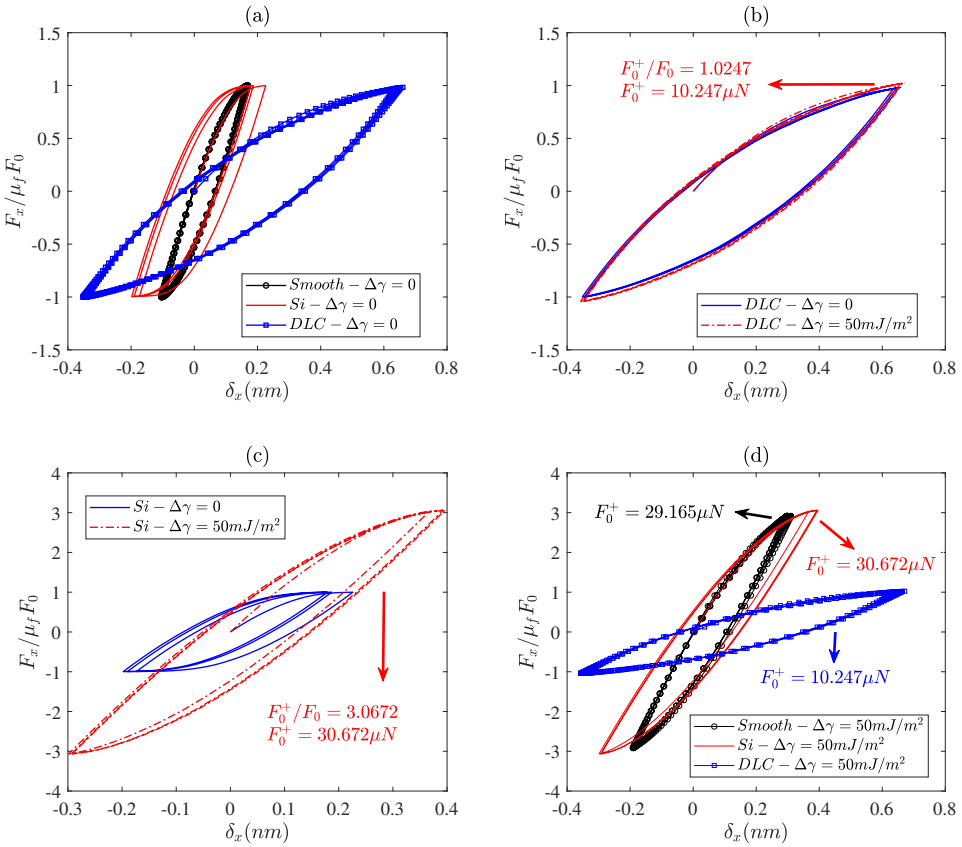

Figure 12: Friction hysteresis behavior for different combinations of roughness and work of adhesion, $F_0 = 10m\mu N$

Furthermore, the rougher profile, DLC, experiences, in one hand, a smaller contact repulsive force and thus, a lower static friction force, and on the other hand, a larger pre-sliding displacement.

4 Conclusions

We extended a previously developed BEM model for the hysteresis behavior of adhesive partial slip friction at the interface of two rough surfaces to take into account the history dependence of friction and simulate its hysteresis behavior. Adhesion was modeled by means of a Dugdale approximation of the total work of adhesion. The contact area was divided into stick and slip regions that were distinguished by the local values of shear stress

components and normal pressure, and the rate of relative displacement at the interface. The results showed that, for an adhesive contact, it is the contact repulsive force that controls the start of gross-sliding state and not the external normal force. In addition, adhesion can exclusively increase static friction force and pre-sliding displacement at a smooth interface. On the other hand, roughness can only increase the pre-sliding displacement for a non-adhesive contact. For an adhesive contact at a rough interface, however, the effect of combined adhesion and roughness is not cumulative.

5 Acknowledgment

This research was carried out under project number S61.1.13492 in the framework of the Partnership Program of the Materials innovation institute M2i (www.m2i.nl) and the Netherlands Organization for Scientific Research NWO (www.nwo.nl).

Bibliography

[1] Cattaneo C., "Sul Contatto Di Due Corpi Elastici: Distribuzione Locale Degli Sforzi," *Atti Accad Naz Lincei*, vol. 27, pp. 342–348, 1938.

[2] R. Mindlin, "Compliance of elastic bodies in contact," *Journal of Applied Mechanics*, vol. 16, no. 1945, pp. 259–268, 1949.

[3] R. Mindlin and H. Deresiewicz, "Elastic Spheres in Contact Under Varying Oblique Force," *Journal of Applied Mechanics*, vol. 20, pp. 327–344, 1953.

[4] L. Kogut and I. Etsion, "A Semi-Analytical Solution for the Sliding Inception of a Spherical Contact," *Journal of Tribology*, vol. 125, no. 3, pp. 499–506, 2003.

[5] R. H. Wang, V. K. Jain, and S. Mall, "A non-uniform friction distribution model for partial slip fretting contact," *Wear*, vol. 262, no. 5-6, pp. 607–616, 2007.

[6] T. Yue and M. Abdel Wahab, "Finite element analysis of fretting wear under variable coefficient of friction and different contact regimes," *Tribology International*, vol. 107, no. December 2016, pp. 274–282, 2017.

[7] W. W. Chen and Q. J. Wang, "A numerical model for the point contact of dissimilar materials considering tangential tractions," *Mechanics of Materials*, vol. 40, no. 11, pp. 936–948, 2008.

[8] Z. J. Wang, W. Z. Wang, H. Wang, D. Zhu, and Y. Z. Hu, "Partial Slip Contact Analysis on Three-Dimensional Elastic Layered Half Space," *Journal of Tribology*, vol. 132, no. 2, p. 021403, 2010.

[9] Z.-j. Wang, W.-z. Wang, F.-m. Meng, and J.-x. Wang, "Fretting Contact Analysis on Three-Dimensional Elastic Layered Half Space," *Journal of Tribology*, vol. 133, no. 3, p. 031401, 2011.

[10] L. Rodríguez-Tembleque, R. Abascal, and M. H. Aliabadi, "A boundary elements formulation for 3D fretting-wear problems," *Engineering Analysis with Boundary Elements*, vol. 35, no. 7, pp. 935–943, 2011.

[11] L. Gallego, D. Nélias, and S. Deyber, "A fast and efficient contact algorithm for fretting problems applied to fretting modes I, II and III," *Wear*, vol. 268, no. 1, pp. 208–222, 2010.

[12] J. Archard, "Elastic deformation and the laws of friction," *Proceedings of the Royal Society of London. Series A. Mathematical and Physical Sciences*, vol. 243, pp. 190 LP – 205, dec 1957.

[13] Bowden FP and Tabor D, *The Friction and Lubrication of Solids*. Oxford University Press, 1986.

[14] M. Eriten, A. A. Polycarpou, and L. A. Bergman, "Physics-based modeling for fretting behavior of nominally flat rough surfaces," *International Journal of Solids and Structures*, vol. 48, no. 10, pp. 1436–1450, 2011.

[15] M. Eriten, A. A. Polycarpou, and L. A. Bergman, "Physics-based modeling for partial slip behavior of spherical contacts," *International Journal of Solids and Structures*, vol. 47, no. 18-19, pp. 2554–2567, 2010.

[16] K. Farhang, D. Segalman, and M. Starr, "Prediction of dissipation in joints subject to oscillating force," *2007 Proceedings of the ASME/STLE International Joint Tribology Conference, IJTC 2007*, vol. PART A, pp. 5–7, 2008.

[17] M. Paggi, R. Pohrt, and V. L. Popov, "Partial-slip frictional response of rough surfaces.," *Scientific reports*, vol. 4, p. 5178, 2014.

[18] R. Pohrt and Q. Li, "Complete Boundary Element Formulation for Normal and Tangential Contact Problems," *Physical Mesomechanics*, vol. 17, no. 4, pp. 334–340, 2014.

[19] S. Medina, D. Nowell, and D. Dini, "Analytical and numerical models for tangential stiffness of rough elastic contacts," *Tribology Letters*, vol. 49, no. 1, pp. 103–115, 2013.

[20] Z. Wang, W. Wang, Y. Hu, and H. Wang, "A Numerical ElasticPlastic Contact Model for Rough Surfaces," *Tribology Transactions*, vol. 53, no. 2, pp. 224–238, 2010.

[21] A. T. Kasarekar, N. W. Bolander, F. Sadeghi, and S. Tseregounis, "Modeling of fretting wear evolution in rough circular contacts in partial slip," *International Journal of Mechanical Sciences*, vol. 49, no. 6, pp. 690–703, 2007.

[22] W. W. Chen and Q. J. Wang, "A Numerical Static Friction Model for Spherical Contacts of Rough Surfaces, Influence of Load, Material, and Roughness," *Journal of Tribology*, vol. 131, no. 2, p. 021402, 2009.

[23] Z. Song and K. Komvopoulos, "Adhesive contact of an elastic semi-infinite solid with a rigid rough surface: Strength of adhesion and contact instabilities," *International Journal of Solids and Structures*, vol. 51, no. 6, pp. 1197–1207, 2014.

[24] N. W. Moore and J. E. Houston, "The Pull-Off Force and the Work of Adhesion: New Challenges at the Nanoscale," *Journal of Adhesion Science and Technology*, vol. 24, no. 15-16, pp. 2531–2544, 2010.

[25] C. Yang, B. N. J. Persson, J. N. Israelachvili, and K. Rosenberg, "Contact mechanics with adhesion: Interfacial separation and contact area," *Europhysics Letters (EPL)*, vol. 84, no. 4, p. 5, 2008.

[26] N. Mulakaluri and B. N. J. Persson, "Adhesion between elastic solids with randomly rough surfaces: Comparison of analytical theory with molecular-dynamics simulations," *EPL (Europhysics Letters)*, vol. 96, no. 6, p. 66003, 2011.

[27] M. Ciavarella, A. Papangelo, and L. Afferrante, "Adhesion between self-affine rough surfaces: Possible large effects in small deviations from the nominally Gaussian case," *Tribology International*, vol. 109, no. December 2016, pp. 435–440, 2017.

[28] M. Ciavarella, "A Comment on Meeting the Contact-Mechanics Challenge by Muser et al. [1]," *Tribology Letters*, vol. 66, no. 1, pp. 18–20, 2018.

[29] L. Pastewka and M. O. Robbins, "Contact between rough surfaces and a criterion for macroscopic adhesion.," *Proceedings of the National Academy of Sciences of the United States of America*, vol. 111, no. 9, pp. 3298–303, 2014.

[30] M. Ciavarella, "A note on the possibility of roughness enhancement of adhesion in Persson's theory," *International Journal of Mechanical Sciences*, vol. 121, no. February 2016, pp. 119–122, 2017.

[31] S. Perni and P. Prokopovich, "Multi-asperity elliptical JKR model for adhesion of a surface with non-axially symmetric asperities," *Tribology International*, vol. 88, pp. 107–114, 2015.

[32] B. N. J. Persson and M. Scaraggi, "Theory of adhesion: Role of surface roughness," *Journal of Chemical Physics*, vol. 141, no. 12, pp. 1–18, 2014.

[33] B. N. J. Persson and E. Tosatti, "The effect of surface roughness on the adhesion of elastic solids," *Proceedings of the Royal Society A*, vol. 5597, no. 2001, 2001.

[34] R. A. Sauer, "A Survey of Computational Models for Adhesion," *The Journal of Adhesion*, vol. 92, no. 2, pp. 81–120, 2015.

[35] M. H. Muser, "A dimensionless measure for adhesion and effects of the range of adhesion in contacts of nominally flat surfaces," *Tribology International*, vol. 100, pp. 41–47, 2016.

[36] M. H. Muser, W. B. Dapp, R. Bugnicourt, P. Sainsot, N. Lesaffre, T. A. Lubrecht, B. N. Persson, K. Harris, A. Bennett, K. Schulze, S. Rohde, P. Ifju, W. G. Sawyer, T. Angelini, H. Ashtari Esfahani, M. Kadkhodaei, S. Akbarzadeh, J. J. Wu, G. Vorlaufer, A. Vernes, S. Solhjoo, A. I. Vakis, R. L. Jackson, Y. Xu, J. Streator, A. Rostami, D. Dini, S. Medina, G. Carbone, F. Bottiglione, L. Afferrante, J. Monti, L. Pastewka, M. O. Robbins, and J. A. Greenwood, "Meeting the Contact-Mechanics Challenge," *Tribology Letters*, vol. 65, no. 4, 2017.

[37] N. H. Zini, M. B. de Rooij, M. Bazr Afshan Fadafan, N. Ismail, and D. J. Schipper, "Extending the Double-Hertz Model to Allow Modeling of an Adhesive Elliptical Contact," *Tribology Letters*, vol. 66, no. 1, pp. 1–13, 2018.

[38] O. T. Sari, G. G. Adams, and S. Muftu, "Nano-Scale Effects in the Sliding and Rolling of a Cylinder on a Substrate," *Journal of Applied Mechanics*, vol. 72, no. 5, p. 633, 2005.

[39] G. G. Adams, "Stick, partial slip and sliding in the plane strain micro contact of two elastic bodies.," *Royal Society open science*, vol. 1, no. 3, p. 140363, 2014.

[40] K. L. Johnson, K. Kendall, and A. D. Roberts, "Surface Energy and the Contact of Elastic Solids," *Proceedings of the Royal Society of London.*

Series A, Mathematical and Physical Sciences, vol. 324, pp. 301–313, 1971.

[41] M. Bazrafshan, M. de Rooij, and D. Schipper, "On the role of adhesion and roughness in stick-slip transition at the contact of two bodies: A numerical study," *Tribology International*, vol. 121, no. July 2017, pp. 381–388, 2018.

[42] M. Bazrafshan, M. B. de Rooij, M. Valefi, and D. J. Schipper, "Numerical method for the adhesive normal contact analysis based on a Dugdale approximation," *Tribology International*, vol. 112, no. April, pp. 117–128, 2017.

[43] J.N. Israelachvili, *Intermolecular and surface forces*. Elsevier, 2013.

[44] S. Medina and D. Dini, "A numerical model for the deterministic analysis of adhesive rough contacts down to the nano-scale," *International Journal of Solids and Structures*, vol. 51, no. 14, pp. 2620–2632, 2014.

Paper F

Evaluation of Pre-Sliding Behavior at a Rough Interface: Modeling and Experiment

M. Bazrafshan[1,2*], M.B. de Rooij[2], E.G. de Vries[2], and D.J. Schipper[2]

[1] *Materials innovation institute (M2i), van der Burghweg 1, 2628 CS Delft, Netherlands*
[2] *Laboratory for Surface Technology and Tribology, Department of Engineering Technology, University of Twente, P.O. box 217, 7500AE, Enschede, Netherlands*

Abstract

One of the main issues in precision engineering is the lack of deep understanding of the pre-sliding behavior at the interface of mating surfaces of positioning mechanisms. In addition to the mechanical properties of the contacting bodies, their surface topography plays a key role in the pre-sliding regime and has a great impact on the frictional stiffness. This paper experimentally evaluates a BEM (Boundary Element Method) model for the pre-sliding behavior at the interface of a smooth silicon wafer and a rough polymeric ball. The polymeric ball is either HDPE (High-Density Polyethylene) or POM (Polyoxymethylene). The experiments are conducted at three different normal loads and at five different spots on the wafer. The sliding stroke and coefficient of friction are extracted from experiments to be implemented as inputs to the numerical model. The roughness of the balls is also another input. The numerical and experimental friction hysteresis loops are compared. Although there is a small difference in the predicted pre-sliding distance from the experiments, the calculated lateral stiffness, compared at three different points on the pre-sliding regime of friction hysteresis loops, is in good agreement with the experimental ones for both contact interfaces and normal loads.

Keywords: Pre-sliding, Lateral stiffness, Roughness, Boundary Element Method, Experiment, Simulation

Nomenclature

A_c	contact area
A_{sl}	slip area
A_{st}	stick area
a	Hertzian contact radius
c_1, c_2, n	curve-fitting parameters
d_s	lateral displacement stroke
E	elastic modulus
F_0	external normal force
F_x	lateral force
$g(x, y)$	separation profile

$h(x, y)$	initial separation
K_c	spring constant of the spring-slider element
K_L	contact lateral stiffness
$K_L^{Mindlin}$	contact lateral stiffness from the analytical solution of Mindlin
K_s	setup lateral stiffness
$p(x, y)$	pressure profile
$q_{x,y}(x, y)$	shear stress components in x and y directions
R	radius of the polymeric ball
$s_{x,y}(x, y)$	relative displacement in x and y directions
$u_{x,y,z}(x, y)$	deformation in x, y and z directions
x_{cs}	displacement measured by the capacitive sensor
x_{ps}	XY stage displacement in x direction
μ_f	coefficient of friction
$\delta_{x,y,z}$	rigid body displacement in x, y and z directions
ν	Poisson's ratio

1 Introduction

Achieving high-precision positioning is one of the main goals in precision engineering. Nevertheless, the friction between the mating surfaces of the sliding components of the mechatronic devices gives rise to a positioning inaccuracy. Friction is commonly divided into two regimes of partial slip and full slip. As the former one is treated as a more crucial phenomenon due to the complexity of stick to slip transition, its understanding and prediction is vital for more accurate positioning.

Initial studies on the partial slip contact have been conducted independently by Cattaneo [1], and Mindlin [2] for the elastic contact at the smooth interface of a ball and a flat, where, within the circular contact area, a central sticking zone is surrounded by an annulus of slip which develops toward the center of contact upon an increase in the tangential force and finally covers the entire contact area and starts the full slip state as soon as the tangential force reaches the static friction force. Later on, Mindlin and Deresiewicz extended this solution to deal with an oscillating tangential force, which leads to friction hysteresis behavior [3].

In the original Mindlin solution, it was assumed that the contacting materials are identical. This assumption simplifies the solution since the normal pressure and shear stress components become decoupled and

cannot affect each other as they cannot induce any deformations in the other directions. The contact of dissimilar materials, nevertheless, does not follow this condition and the normal pressure and shear stress components are coupled. Since there is no analytical solution for this complex problem, researchers have resorted to numerical solutions such as Finite Element Method (FEM) [4–6] and Boundary Element Method (BEM) [7–11].

All these analytical and numerical approaches deal with the contact at a smooth interface. In reality, however, engineering surfaces have a certain level roughness, meaning that the microgeometry details of the mating surfaces at the asperity level determine how the surfaces interact. The mentioned approaches form the basis for multi-asperity methods where the single-asperity solutions are combined with a statistical distribution of asperities, such as Gaussian, to study the partial slip and full slip friction [12–17]. Experiments have also been conducted to evaluate the roughness effect on the pre-sliding behavior and possibly compare the results with such models. Al-Bender and Moerlooze combine the Maxwell-Slip model with the Greenwood-Williamson theory for the contact of rough surfaces to evaluate the experimental relation between the normal load and the friction force in the pre-sliding regime [18, 19]. Eriten et al. investigated the impact of roughness on the frictional energy dissipation in the fretting contact between two nominally flat rough surfaces by considering the probability distribution of asperities [20]. They quantitatively showed that rougher surfaces dissipate more energy. Song and Yan conducted experiments to relate the friction and normal forces with the real contact area, measured optically at the interface of two transparent PMMA (Polymethyl Methacrylate) blocks [21]. Raeymaekers and Talke studied the effect of laser polishing on the fretting wear behavior at the interface of a rough hemisphere and a flat plate [22]. They did not observe any noticeable difference in the wear production between a laser polished and a regular stainless steel hemisphere.

Researchers have also pursued other numerical methods due to the well-known limitations of multi-asperity methods such as the lack of interaction between asperities. Pohrt and Li [23], and Paggi et al. [24], proposed a CGM-based BEM model for the partial slip contact at a rough interface. They assumed a uni-directional shear stress proportional to the normal pressure in the slip zone. Yet, they did not take the coupling between the normal pressure and shear stress into account. Grzemba et al. proposed a characteristic length parameter defining the crossover from sticking to slipping for the contact of self-affine fractal surfaces [25]. Kasarekar et al. developed a numerical approach to study the fretting wear

under partial slip conditions [26]. They found the roughness details at small length-scales a major factor in wear simulations. Chen and Wang extended their previously developed BEM model for the point contact of dissimilar materials to evaluate the static friction force and coefficient of friction at a rough interface of a ball and a flat [27]. Rather using the Amontons law of friction, they set a constant shear strength all over the contact area as a local criterion for transition from stick to slip.

Although there seems to be rich literature on the pre-sliding behavior at a rough interface of two contacting surfaces, to the best of the authors knowledge, there is no experimentally validated numerical model to deal with this problem while using a measured topography of the contacting surfaces and taking the coupling between the normal pressure and the contact shear stress components into account. Therefore, the aim of this paper is to experimentally evaluate the recently developed BEM model for the stick-slip transition at a rough interface [28]. First, a summary of the proposed BEM model for the hysteresis behavior of the friction at a rough interface will be provided. In section 3, the test setup will be explained. Section 4 deals with the simulation using the input data to be compared with experimental results in section 5. Finally, conclusion is provided in section 6.

2 BEM model

This section summarizes a recently proposed BEM model for the hysteresis behavior of the adhesive friction at the rough interfaces of two contacting bodies [28]. As the adhesion can be neglected due to the relatively rough (high local slope) interface of the polymeric ball, the same numerical methodology, excluding the adhesion part, is implemented in this study. Figure 1 illustrates the contact of two bodies in the xz-plane, where it is loaded by the constant normal force of F_0 and the tangential force of F_x. The resulted contact pressure and shear stress components in x and y directions are represented by $p(x, y)$, $q_x(x, y)$ and $q_y(x, y)$, respectively. The deformation, rigid body displacement, and relative displacement in the x-direction (y-direction) are also denoted by u_x, δ_x and s_x (u_y, δ_y, s_y), respectively. Depending on the friction force, the contact can experience either of the two states of partial slip or full slip. As long as the friction force is smaller than the static friction force (the force required for the start of full slip), the contact area is sticking in some regions and slipping in the rest, though there is no macroscopic relative displacement between

the two contacting surfaces. As soon as, the friction force reaches the static friction force, the entire contact area experiences the slip state and therefore, the full slip or gross sliding starts. In this state, the two surfaces move macroscopically with respect to one another. For a quasi-static tangential loading, where the friction force is history-dependent, there are two criteria to distinguish between stick and slip regions within the contact area. In the stick regime, the shear stress is smaller than friction coefficient times the local pressure and rate of relative displacement is zero. In the slip region, however, the shear stress is equal to the friction coefficient times local pressure and the relative displacement is no longer zero. These criteria are mathematically given by:

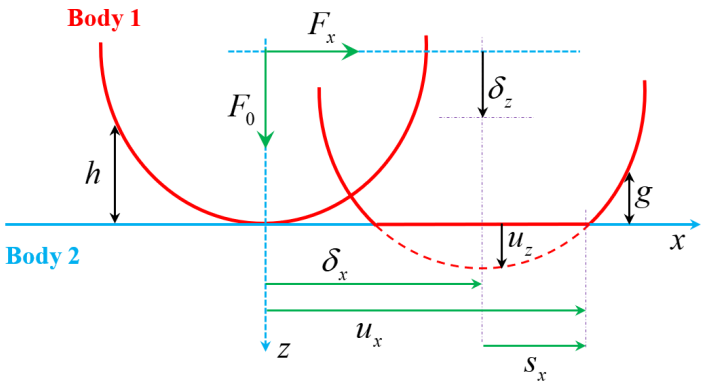

Figure 1: Contact variables.

$$
\begin{aligned}
A_{st} = (x,y) \in A_c \mid & \sqrt{q_x(x,y)^2 + q_y(x,y)^2} < \mu_f p(x,y), \\
& \sqrt{\Delta s_x(x,y)^2 + \Delta s_y(x,y)^2} = 0 \\
A_{sl} = (x,y) \in A_c \mid & \sqrt{q_x(x,y)^2 + q_y(x,y)^2} = \mu_f p(x,y), \\
& \sqrt{\Delta s_x(x,y)^2 + \Delta s_y(x,y)^2} \neq 0
\end{aligned}
\tag{1}
$$

Here, Δ refers to the change of a parameter between two consecutive loading steps.

Given the contact geometry and elastic properties of the materials, normal force, friction coefficient, and tangential loading path, the BEM

model first solves the normal contact problem to find the contact pressure and separation, g, while meeting the complementarity conditions given as:

$$p(x,y) = 0, \quad \text{at} \quad g(x,y) > 0 \tag{2a}$$
$$p(x,y) > 0, \quad \text{at} \quad g(x,y) = 0 \tag{2b}$$
$$\int_{\Omega} p(x,y)dx\ dy = F_0 \tag{2c}$$

which states that the pressure is zero at separated areas (where $g > 0$), while it is positive at contact areas (where $g = 0$). Moreover, the summation of the pressure over the contact problem domain, Ω, must be the same as the external normal force.
The next step is to find the shear stress components at each loading step meeting the criteria given in Eq. (1). It is very important to note that the effect of shear stress components on the contact pressure is also included in an iterative manner. More details on the numerical procedure to solve this problem can be found in [28–30].

3 Experiments

The experimental setup, as shown in Figure 2, consists of three positioning stages and three capacitive sensors. The Z and XY positioning stages have a stroke of 18, 26 and $18mm$ and resolutions of $20nm$, $0.2nm$ and $100nm$, respectively. The elastic hinge behind the indenter acts as the force measuring mechanism of the setup with two degrees of freedom to measure normal and tangential forces as independently as possible (the reader is referred to [31] for more details about this mechanism).

The setup has a ball-on-flat configuration, where the polymeric ball, with $10mm$ of diameter, is fixed inside the ball holder. The ball holder is mounted on the indenter, which is centrally fixed at the elastic hinge, which in turn mounted, along with a back plate, on the Z stage which is placed behind the back plate (not visible in Figure 2). This stage is used to bring the ball into contact with the flat surface, placed on the XY stage, and apply the normal load up to $100mN$ with an accuracy of $8\mu N$. To apply the tangential load thereafter, the X stage moves reciprocally in the X direction. The Y stage is used to conduct parallel measurements on the flat surface. In addition, a permanent magnet, as an eddy current damper, is placed close to the indenter to reduce the vibration induced by the Z positioning stage.

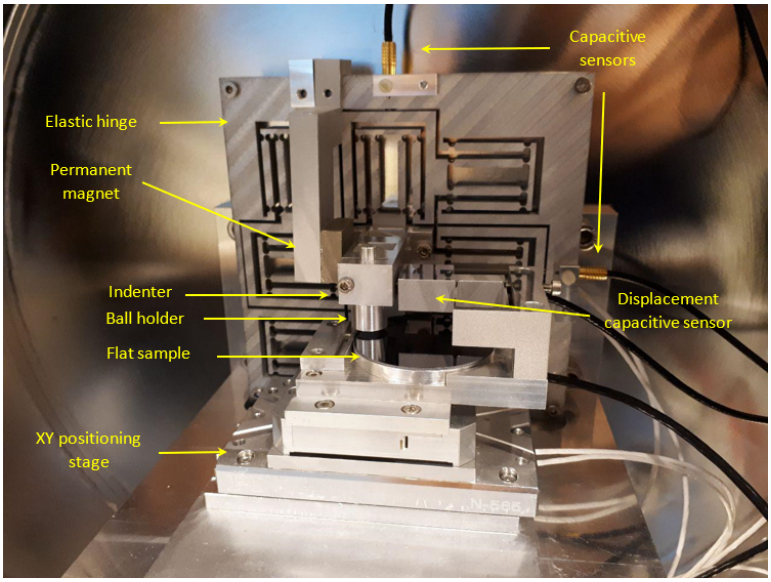

Figure 2: Experimental test rig.

Two of the capacitive sensors, with the resolution of $< 0.15nm$ and measuring range up to $50\mu m$, are mounted on the elastic hinge. Having the elastic hinge calibrated for its stiffness in Z and X directions, the recorded deflections by theses two sensors are used to measure the normal and friction forces. The third similar capacitive sensor, with the ultrahigh resolution of better than $0.2nm$ and measuring range up to $50\mu m$, is mounted on the XY stage to measure the true contact displacement and exclude the deformations of the elastic hinge and the indenter. It must be noted that since this sensor does not see the displacement due to the bending of the ball holder and neither due to the torsion of the elastic hinge and the indenter, an FEM simulation has been carried out to ensure that this displacement is negligible in comparison to the measured tangential displacements.

Before the measurements, the samples are rinsed with Isopropanol alcohol and then dried with nitrogen to remove any possible dirt particles from the samples. The entire setup is also placed in a chamber which is kept closed during the measurements.

Both normal and tangential loadings are conducted at a quasi-static manner. First, the Z positioning stage moves downward at the speed of $1\mu m/sec$ to reach the desired normal force after the contact is made. Then, having the normal load fixed, the XY stage moves reciprocally, for a given number of cycles and sliding stroke, in X direction at the speed of $0.1\mu m/sec$.

For either of the HDPE or POM balls in contact with the silicon wafer, the friction tests are conducted at five different spots and three normal loads for each spot.

Figure 3(a) depicts a typical friction force measurement with the setup, shown in Figure 2, for a normal load of $75mN$ and sliding stroke of $9\mu m$ applied by the X stage, where the horizontal axis is the displacement recorded by the displacement capacitive sensor. The asymmetry of the hysteresis loop with respect to the vertical axis is due to two reasons. One is the asymmetry of the displacement path itself, which varies between zero and the given sliding stroke. The other reason can be explained by Figure 3(b), which provides a schematic representation of the friction force measurement. Here, the ball is in contact with the silicon wafer, clamped on the XY stage, through a spring-slider contact element. The spring constant of this element, K_c, denotes the contact stiffness and the slider, similar to the Coulomb friction model, has a certain threshold of force (static friction force) and has no relative displacement with respect to the wafer as long as the friction force is below this threshold. The contact element is in series with another spring, K_s, denoting the setup stiffness. The frame O is attached to the ground and x_{ps} denotes the displacement of the XY stage. Moreover, the frame O' is attached to the XY stage and x_{cs}, as measured by the displacement capacitive sensor, representing the absolute displacement of the ball with respect to the wafer (it excludes the setup deformation from the stage displacement). Therefore, x_{ps}, as an input to the experiments, must be always larger than x_{cs} and the measured friction loop is asymmetric with respect to the vertical axis.

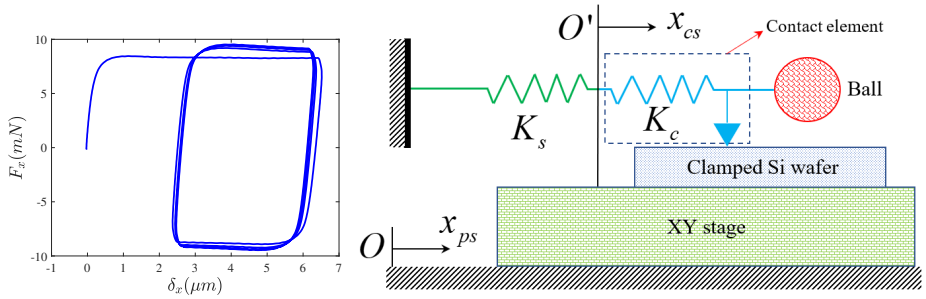

(a) (b)

Figure 3: (a) Typical friction force measurement with $75mN$ of normal force and $9\mu m$ as the sliding distance of the XY positioning stage and (b) Schematic representation of the friction force measurement.

The point to note here is that the curved corner of the hysteresis loop at the end of each stroke is due to the visco-elasticity of the polymeric ball which tends to move even after the sliding direction has reversed. This phenomenon can be avoided by decreasing the sliding speed as much as possible. In fact, in the current experiments which are carried out at the lowest possible speed of the XY stage ($0.1\mu m/sec$), this effect is already minimized.

4 Simulation

The first step to numerically predict the friction hysteresis loops, to be compared with experimental ones, is to measure the roughness of the contacting surfaces. The roughness of the polymeric balls after the final friction measurements, is measured by a Sensofar confocal microscope (50X magnification). The $1.1mm \times 1.1mm$ measured images of the HDPE and POM balls, with 1024 pixels in each direction, are shown in Figure 4 with a zoomed-in view to see the highest asperities where the contact patches form.

In the current study, the contact pressures are low enough to neglect any possible plastic deformation of the ball during the friction measurements. Even if there were any, they can be easily neglected for the final measurements (that are presented here) as they have happened during the initial measurements. The silicon wafer is also so smooth that its roughness can be neglected in comparison to that of the polymeric balls. Therefore, the flat surface is assumed to be ideally smooth. Two of the inputs to the numerical model are extracted from the experimental results. First is the stroke and second the coefficient of friction.

The stroke, d_s, is the range of tangential displacement measured by the third capacitive sensor. For this, only the last loop of the friction hysteresis, which is the converged (most stable) one, for each measurement is selected and then, the stroke is considered to be the range between the minimum and maximum displacement on this loop. As the measurements are carried out on five different spots, the average of the stroke for each point (at each normal load), as given in Table 1, is used as one of the mentioned experimental inputs to the simulation. Therefore, rather than a loading path, a displacement path (of four cycles), as shown in Figure 5, is considered to be the input to the simulation, similar to the experiments. As friction takes a few loops to converge, due to the dissimilarity of the contacting surfaces (and also perhaps the running-in effect), only the last

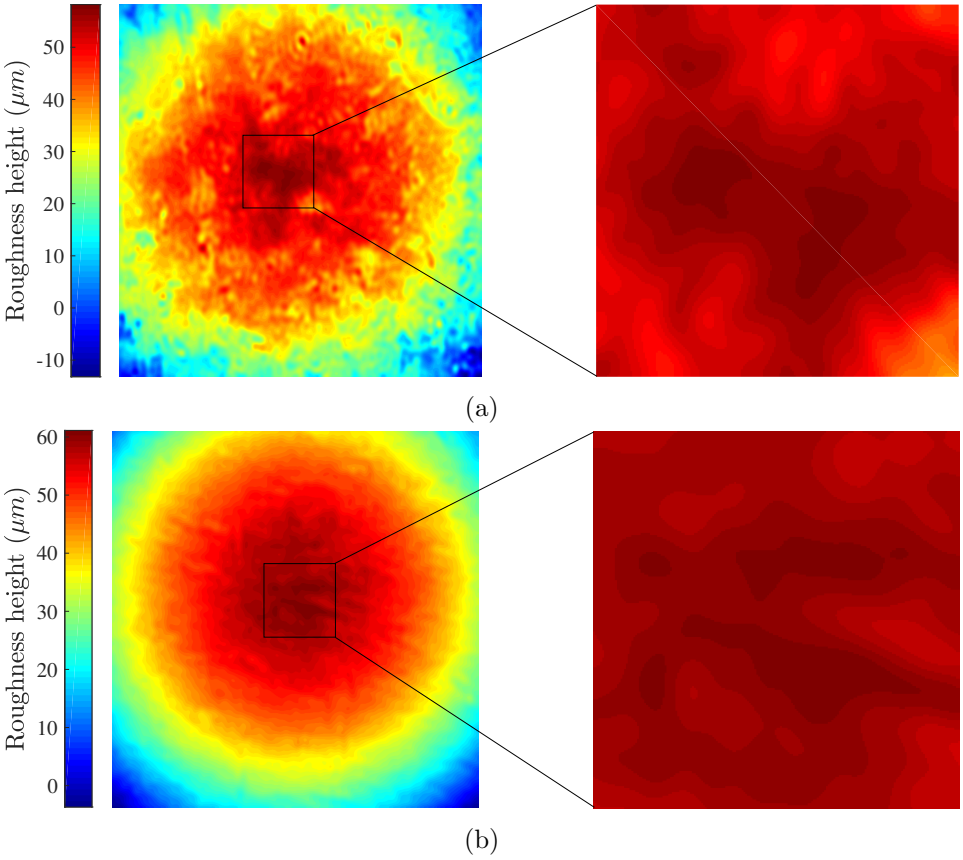

Figure 4: Roughness height of the balls on a $1.1mm \times 1.1mm$ area (left) and a zoomed-in view ($0.2mm \times 0.2mm$) of the center: (a) HDPE and (b) POM.

Table 1: Average values of stroke and friction coefficient, extracted from experimental results, used as inputs to the numerical simulation.

$F_0(mN)$	$d_s(\mu m)$		μ_f	
	HDPE	**POM**	**HDPE**	**POM**
25	2.805	2.700	0.153	0.108
50	2.943	3.370	0.146	0.104
75	3.697	4.264	0.129	0.099

loop of the simulation (the converged one) is considered to be compared with experiments.

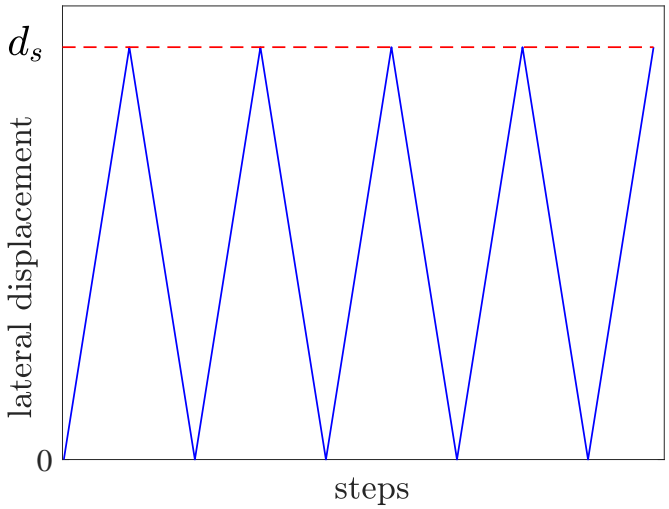

Figure 5: Displacement path.

The coefficient of friction is also calculated as the ratio of the sliding friction force and the normal force. For each set of normal load, the stroke and friction coefficient are extracted separately. The average value of this parameter is also listed in Table 1.

The elastic moduli of HDPE and POM have been measured using an Anton Paar nanoindentation tester (NHT^2). For each ball, the measurements are conducted on 25 spots. Figure 6 shows one of the load-indentation curves for the HDPE ball. The apparatus fits the analytical model of Oliver and Pharr on this curve to obtain the slope of the curve at the starting point of unloading, S, and relates it to the elastic modulus of the material [32]. However, due to the viscoelasticity of the

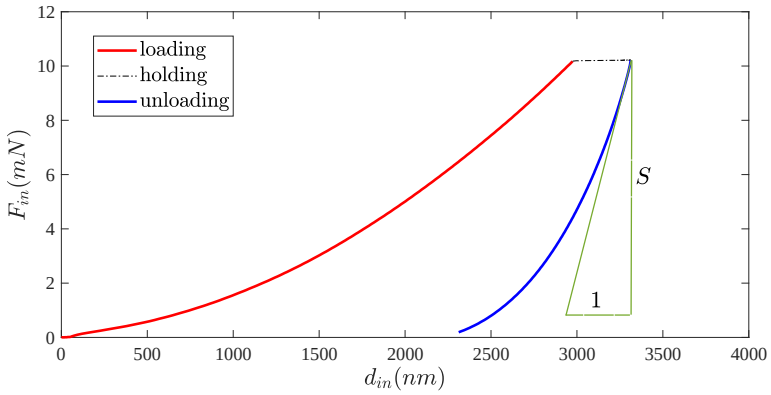

Figure 6: Load-Indentation curve for one spot on the HDPE ball, measured by the nanoindentation tester.

Table 2: Mechanical properties of the contacting surfaces

	Silicon wafer	**HDPE**	**POM**
Elastic modulus (GPa)	130	0.98	1.38
Poission's ratio	0.28	0.50	0.50
roughness rms (μm)	$\simeq 0$	3.17	0.67

balls, both loading and displacement rates right before unloading need to be used to correct the values given by the tester [33]. In the end, the average values as well as the elastic properties of the silicon wafer are listed in Table 2. These values are in good agreement with those provided by the supplier of the balls.

5 Results and discussion

Given the surface topography and mechanical properties of the contacting surfaces along with the loading conditions, the simulation has been conducted to predict the frictional behavior at the contact of either of the balls against a silicon wafer. Figures 7 and 8 show the contact pressure at the interface of HDPE and POM balls against the wafer, respectively, at three different normal loads. As it can be seen, only a small central part of the balls with rather higher heights (see Figure 4) touch the counter surface. It should be also noted that the calculated contact pressures are small enough to neglect any plastic deformation of the balls.

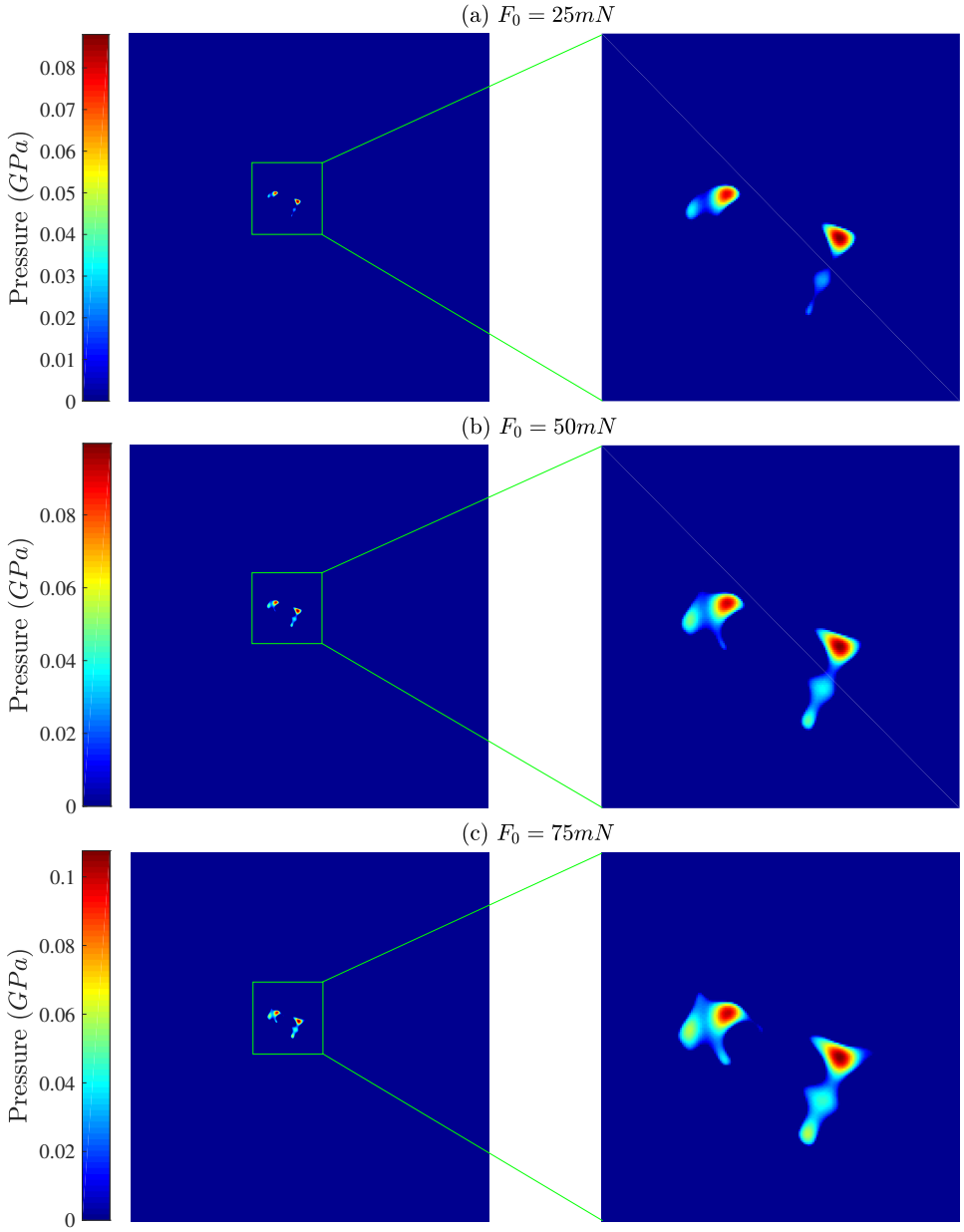

Figure 7: Contact pressure at the HDPE ball-silicon wafer interface.

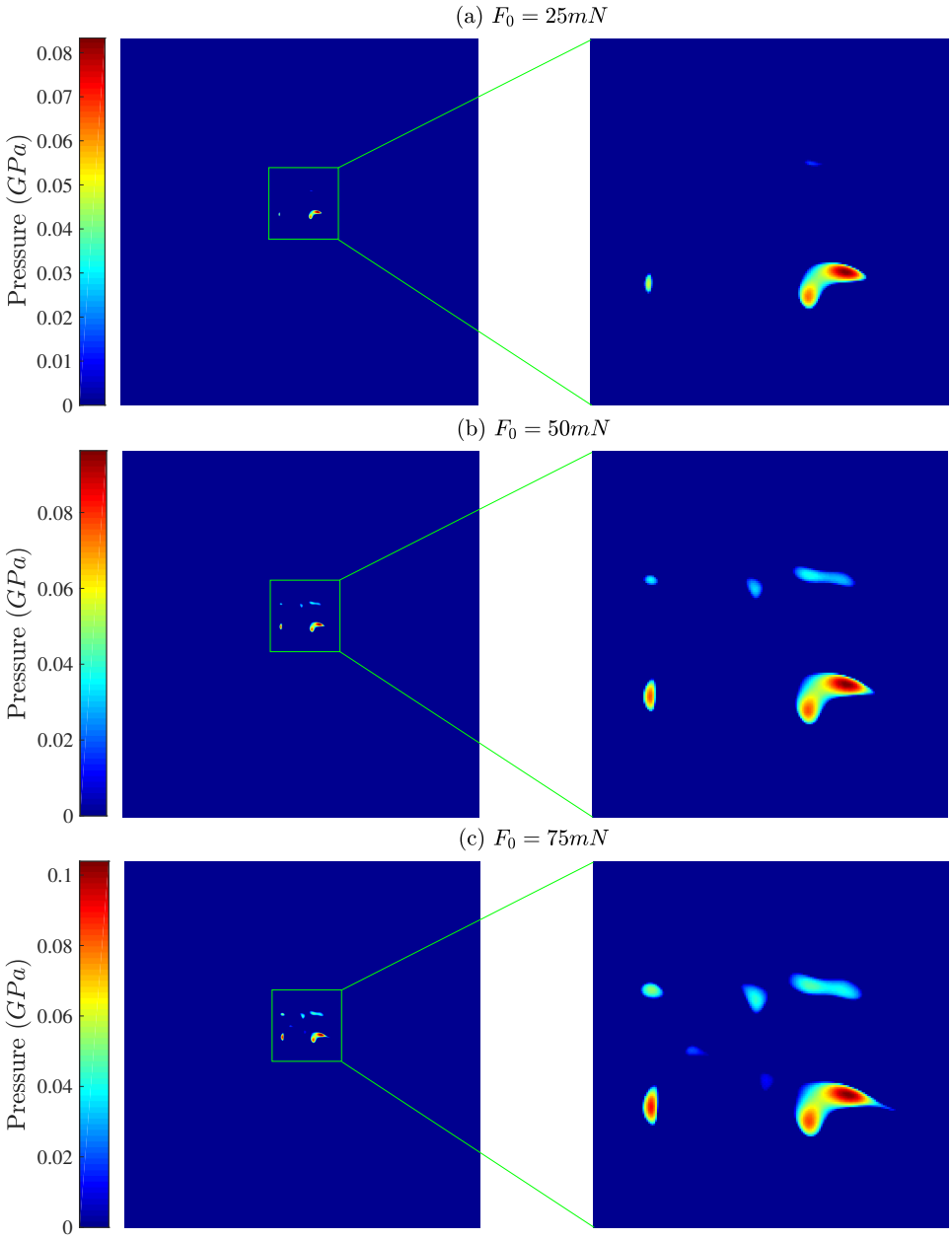

Figure 8: Contact pressure at the POM ball-silicon wafer interface.

In the pre-sliding regime of the frictional contact, three points of A, B, and C, as shown in Figure 9, are chosen to evaluate the partial slip

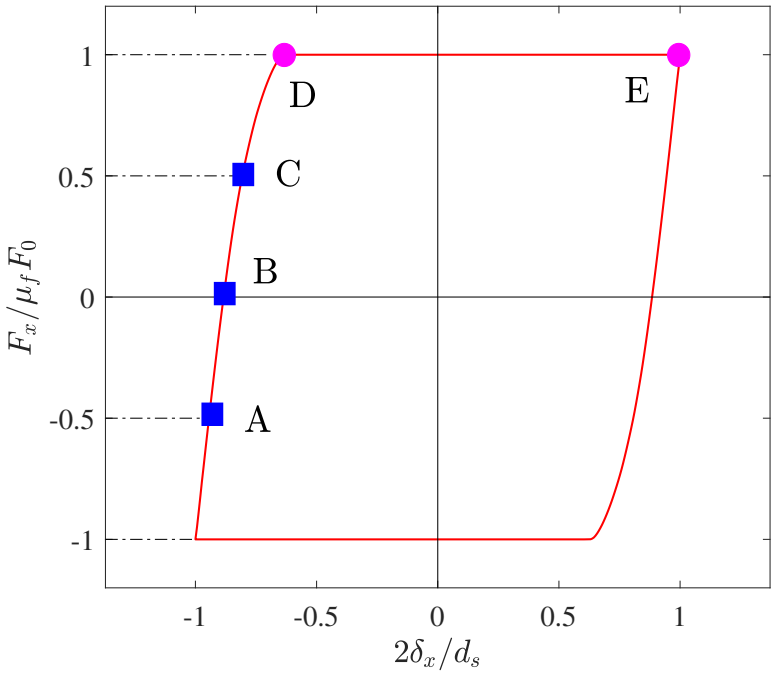

Figure 9: Position of selected spots on friction hysteresis loop.

behavior. The normalized shear stress, $\sqrt{q_x^2+q_y^2}/\mu_f p$, is used to demonstrate the development of the slip zone (and the shrinking of stick zone) on the contact area. Based on the definition of Eq. 1, this parameter is smaller than and equal to one in the stick and slip regions, respectively. The development of the slip region on the contact area for both studied contact interfaces at the mentioned three normal loads is shown in Figures 10 and 11. It is noted that the contact area is the combination of stick and slip regions. Going from point A to C, the imposed tangential displacement increases both local relative displacements and shear stress so that some previously sticking regions enter the slipping regime. This behavior will continue until the slip region covers the entire contact area and the sticking region completely disappears (point D). At this moment, the gross sliding or full slip regime starts and continue until the direction of imposed displacement is reversed (point E).

Figures 12 and 13 compare the experimental and numerically predicted friction hysteresis loops for both HDPE and POM contacts against a silicon wafer at five different spots, while using the stroke and friction coefficients extracted from the these experiments (given in Table 1). There is good

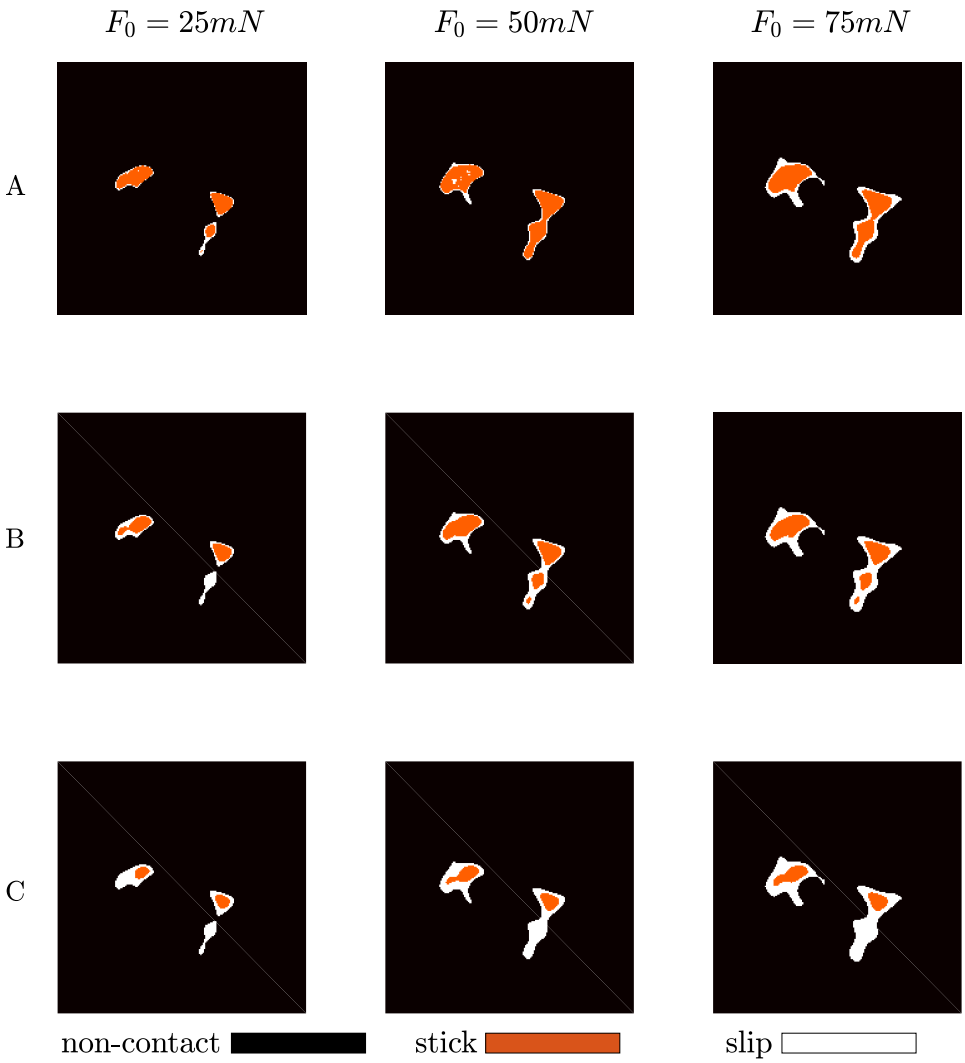

Figure 10: Stick-slip transition from point A to C (see Figure 7) for three different normal loads: HDPE ball-silicon wafer contact (on the $0.2mm \times 0.2mm$ zoomed-in view).

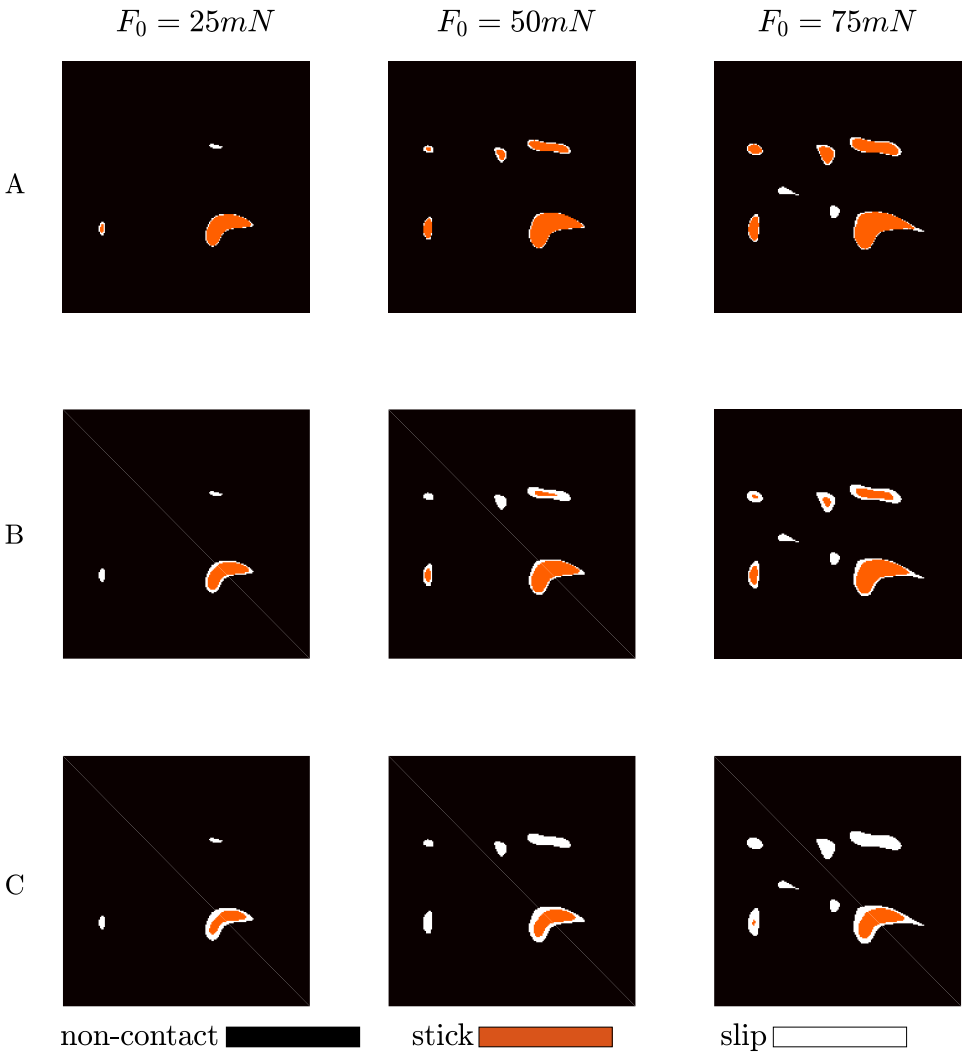

Figure 11: Stick-slip transition from point A to C (see Figure 8) for three different normal loads: POM ball-silicon wafer contact (on the $0.2mm \times 0.2mm$ zoomed-in view).

agreement between the experimental and simulation results.

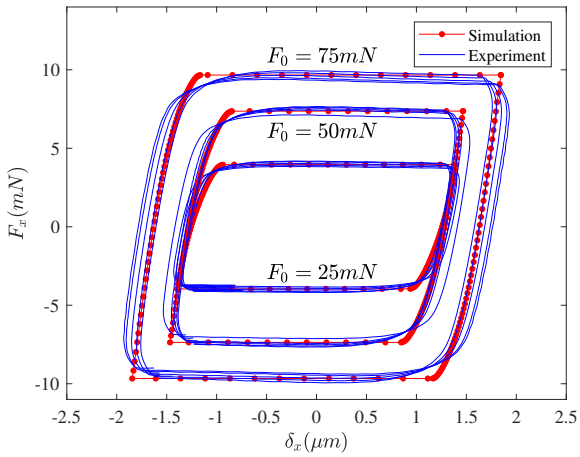

Figure 12: Comparison of simulation and experimental friction hysteresis loops for HDPE ball - silicon wafer contact.

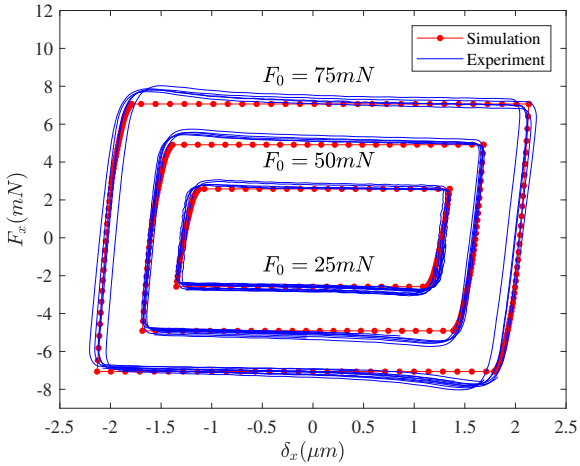

Figure 13: Comparison of simulation and experimental friction hysteresis loops for POM ball - silicon wafer contact.

To have a quantitative comparison between experiments and simulations, the lateral stiffness of the contact, K_L, defined as the slope of the friction hysteresis loop in the pre-sliding regime, is evaluated at points A, B, and C both numerically and experimentally. To calculate the slope more accurately, rather than a finite difference approach, a curve with the

form of $F_x = c_1\left(1-(1-c_2\delta_x)^n\right)$ (by analogy to the Mindlin solution) is fitted on the pre-sliding region of the friction hysteresis loop in order to calculate the lateral stiffness analytically as:

$$K_L(\delta_x) = \frac{dF_x}{d\delta_x} = c_1 c_2 n\left(1-c_2\delta_x\right)^{n-1} \tag{3}$$

Here, $c_1, c_2,$ and n are the fitting parameters which are calculated for each fit separately. Figure 14(a,b) compares the lateral stiffness values at points A, B, and C for the three normal loads at the interface of HDPE and POM balls against the silicon wafer, respectively, between experimental and numerical results. The experiments are quite stable in terms of the lateral stiffness as the spread in this parameter for each case is rather narrow. Except for the case of the POM ball contact at point A for normal loads of $25mN$ and $75mN$, the rest of numerically predicted values for the lateral stiffness are in good agreement with those of the experiments. It is confirmed that from point A to point C, the lateral stiffness decreases since a larger part of the contact area is slipping and experiencing a greater relative displacement and thus, the contact becomes laterally more compliant.

Comparing Figure 14(a) with Figure 14(b) reveals that, for a fixed normal load, the lateral stiffness at the POM-silicon wafer contact interface is higher than that of the HDPE-silicon wafer contact. Three parameters can be considered for this comparison: elastic modulus, friction coefficient, and surface roughness. Based on the Mindlin solution for a frictional smooth ball on flat contact, the relation between friction force and tangential lateral displacement is expressed by:

$$F_x = \mu_f F_0\left(1-(1-\frac{\delta_x}{\delta_0})^{3/2}\right), \quad \delta_0 = \frac{3\mu_f F_0(2-\nu)(1+\nu)}{8aE} \tag{4}$$

where E and ν are the elastic modulus and Poisson' ratio of the contacting materials (here the polymeric ball, as that of the silicon wafer is far larger and can be neglected). The Hertzian contact radius, a, is also given by:

$$a^3 = \frac{3F_0R(1-\nu^2)}{4E} \tag{5}$$

where R is the ball radius. Eq. 4 gives rise to the lateral stiffness as:

$$K_L^{Mindlin} = \frac{3\mu_f F_0}{2\delta_0}\left(1-\frac{\delta_x}{\delta_0}\right)^{1/2} \tag{6}$$

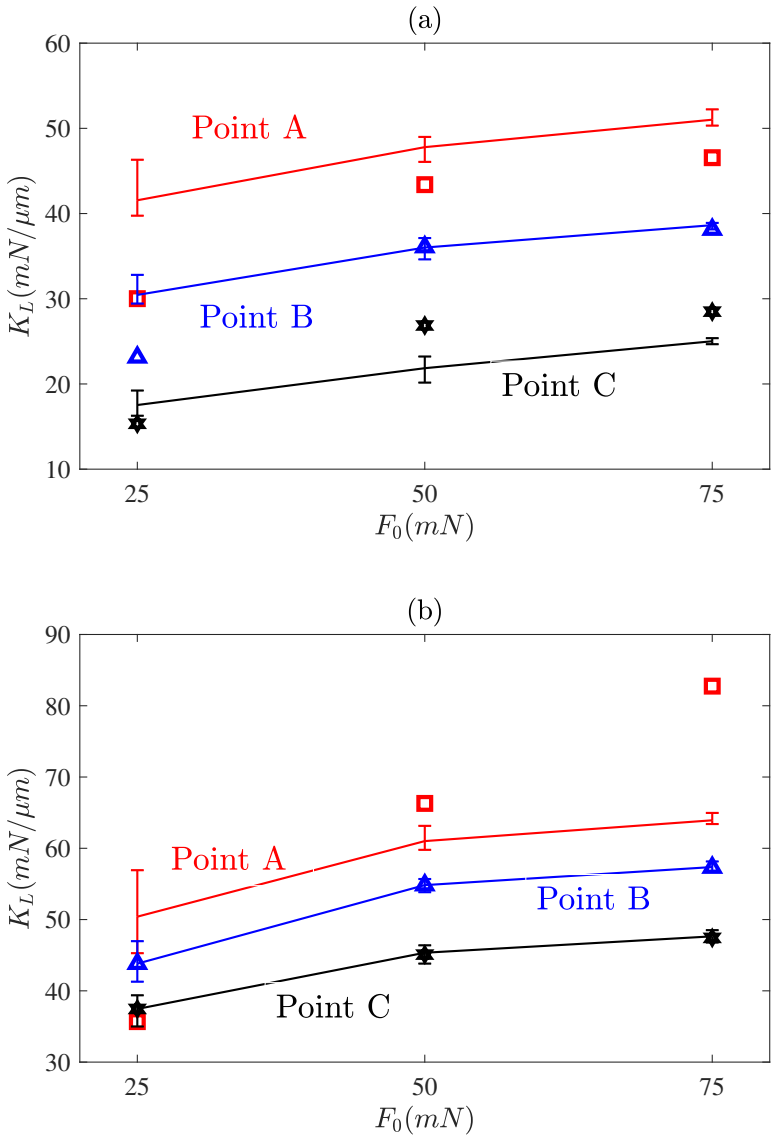

Figure 14: Comparison of the experimental (solid lines) and numerical (markers) lateral stiffness at points A, B, and C for (a) HDPE and (b) POM contact on the silicon wafer.

It should be noted that the Mindlin solution holds only for the contact of identical materials. However, its analytical solution is here used to qualitatively compare the effect of different involved parameters. Based on Eq. 6, it appears that the lateral stiffness depends on both the friction coefficient and elastic modulus. Therefore, in order to see the effect of these two parameters more clearly, the variation of $K_L^{Mindlin}$ as a function of E and μ_f is studied numerically here. For this, the normal force is fixed at $50mN$. E is set to vary from $0.9GPa$ to $1.5GPa$ and four values of $0.10, 0.12, 0.14$, and 0.16 are considered for the friction coefficient. The other parameters are also set as $R = 5mm$ and $\nu = 0.5$. Since δ_0 depends on both E and μ_f, the parameter δ_0^m is defined as the smallest value of δ_0 in order to avoid imaginary values for the lateral stiffness. Figure 15 shows the variation of the lateral stiffness vs. elastic modulus at four different values for the friction coefficient and at three values of the lateral displacement. It can be seen that the initial lateral stiffness (at $\delta_x = 0$) does not depend on the friction coefficient but increases with elastic modulus. At other points, the friction coefficient increases the lateral stiffness. However, that the lateral stiffness increases with elastic modulus depends on the point at which it is calculated and the friction coefficient as well (see Figure 15(c)). Therefore, the higher lateral stiffness in case POM might be attributed to its higher elastic modulus.

The last parameter to discuss is the surface roughness. Figure 16 shows the flattened view of the confocal images of Figure 4. As suggested by the rms value of the surface roughness, the HDPE ball has a rougher surface. For a similar situation, it has been shown that an increase in the interface roughness decreases the contact lateral stiffness [34]. Thus, the rougher surface of the ball is the other parameter that attributes to a lower lateral stiffness in case of HDPE.

6 Conclusions

In this paper, the pre-sliding behavior at the interface of a polymeric ball, either HDPE or POM, and a silicon wafer was studied. Friction experiments were conducted at these two interfaces for different normal loads and at several spots. Extracting the friction coefficient and stroke from the experiments and using them as two inputs to a BEM model, the same friction hysteresis loops were generated to be compared with experiments. The roughness of the polymeric ball, as in important factor in pre-sliding behavior, was also measured and put into the model. The

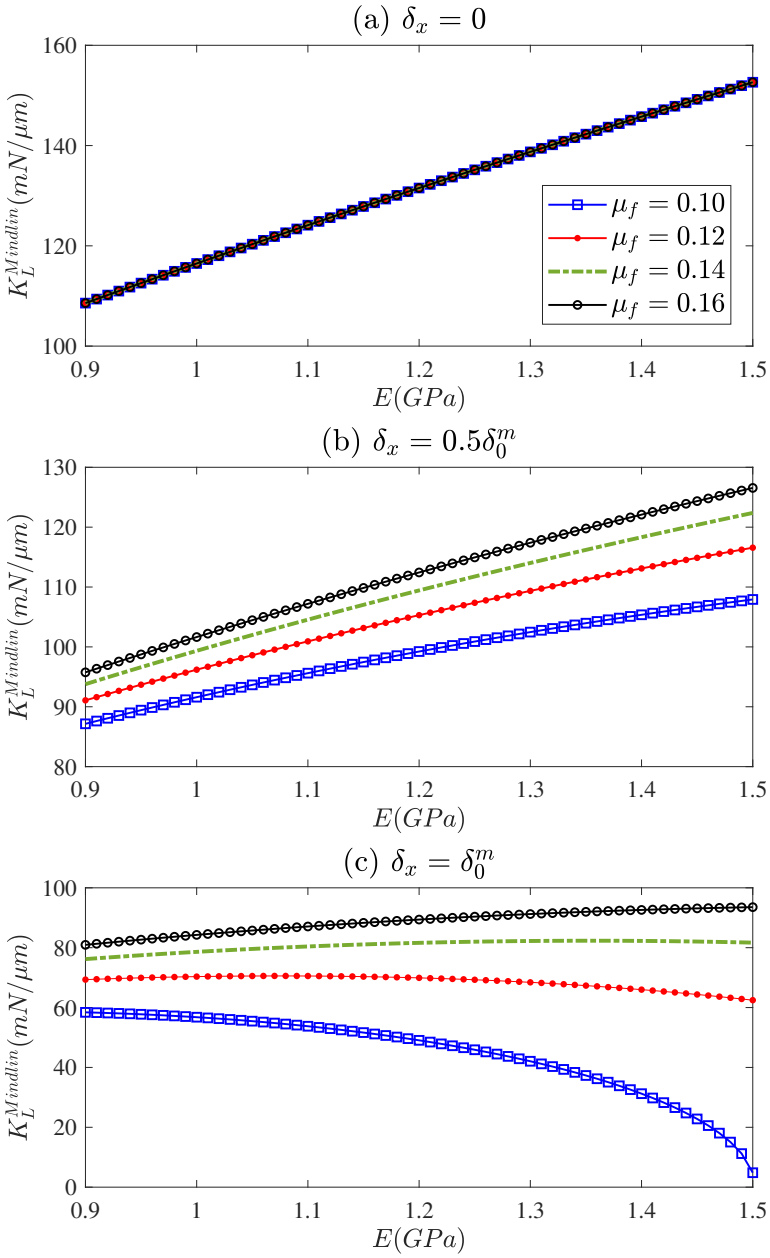

Figure 15: Variation of the lateral stiffness vs. elastic modulus for different values of the friction coefficient at three points on the friction hysteresis loop (subfigures have identical legends).

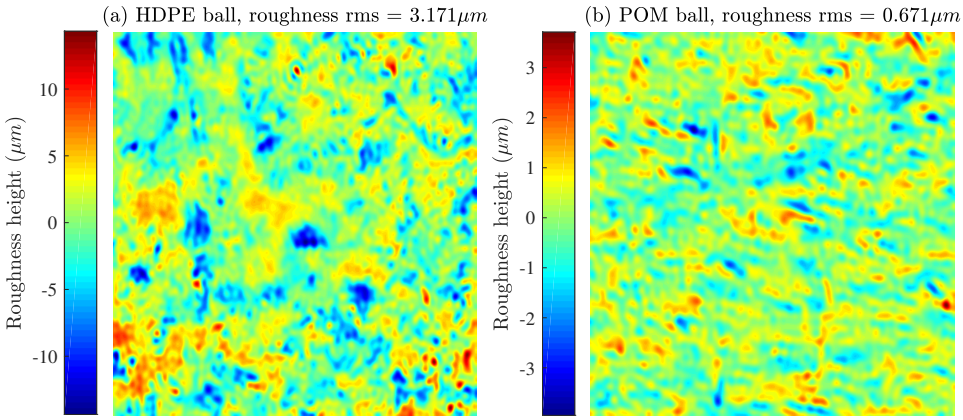

Figure 16: Flattened roughness height of the (a) HDPE and (b) POM balls (on a $1.1mm \times 1.1mm$ area)

predicted friction hysteresis loops are in good agreement with experiments. The lateral stiffness of the contact was also calculated at three different points on the friction loop both experimentally and numerically to quantitatively compare the results. In most cases, there was good agreement between the numerical and experimental values for the lateral stiffness. The difference in the lateral stiffness between the HDPE and POM was attributed to the difference in the elastic modulus, friction coefficient, and their surface roughness.

7 Acknowledgment

This research was carried out under project number S61.1.13492 in the framework of the Partnership Program of the Materials innovation institute M2i (www.m2i.nl) and the Technology Foundation TTW (www.stw.nl), which is part of the Netherlands Organization for Scientific Research (www.nwo.nl).

Bibliography

[1] Cattaneo C., "Sul Contatto Di Due Corpi Elastici: Distribuzione Locale Degli Sforzi," *Atti Accad Naz Lincei*, vol. 27, pp. 342–348, 1938.

[2] R. Mindlin, "Compliance of elastic bodies in contact," *Journal of Applied Mechanics*, vol. 16, no. 1945, pp. 259–268, 1949.

[3] R. Mindlin and H. Deresiewicz, "Elastic Spheres in Contact Under Varying Oblique Force," *Journal of Applied Mechanics*, vol. 20, pp. 327–344, 1953.

[4] L. Kogut and I. Etsion, "A Semi-Analytical Solution for the Sliding Inception of a Spherical Contact," *Journal of Tribology*, vol. 125, no. 3, pp. 499–506, 2003.

[5] R. H. Wang, V. K. Jain, and S. Mall, "A non-uniform friction distribution model for partial slip fretting contact," *Wear*, vol. 262, no. 5-6, pp. 607–616, 2007.

[6] T. Yue and M. Abdel Wahab, "Finite element analysis of fretting wear under variable coefficient of friction and different contact regimes," *Tribology International*, vol. 107, no. December 2016, pp. 274–282, 2017.

[7] W. W. Chen, S. Liu, and Q. J. Wang, "Fast Fourier Transform Based Numerical Methods for Elasto-Plastic Contacts of Nominally Flat Surfaces," *Journal of Applied Mechanics*, vol. 75, no. 1, p. 011022, 2008.

[8] Z. J. Wang, W. Z. Wang, H. Wang, D. Zhu, and Y. Z. Hu, "Partial Slip Contact Analysis on Three-Dimensional Elastic Layered Half Space," *Journal of Tribology*, vol. 132, no. 2, p. 021403, 2010.

[9] Z.-j. Wang, W.-z. Wang, F.-m. Meng, and J.-x. Wang, "Fretting Contact Analysis on Three-Dimensional Elastic Layered Half Space," *Journal of Tribology*, vol. 133, no. 3, p. 031401, 2011.

[10] L. Rodríguez-Tembleque, R. Abascal, and M. H. Aliabadi, "A boundary elements formulation for 3D fretting-wear problems," *Engineering Analysis with Boundary Elements*, vol. 35, no. 7, pp. 935–943, 2011.

[11] L. Gallego, D. Nélias, and S. Deyber, "A fast and efficient contact algorithm for fretting problems applied to fretting modes I, II and III," *Wear*, vol. 268, no. 1, pp. 208–222, 2010.

[12] J. Archard, "Elastic deformation and the laws of friction," *Proceedings of the Royal Society of London. Series A. Mathematical and Physical Sciences*, vol. 243, pp. 190 LP – 205, dec 1957.

[13] J. Greenwood and J. Williamson, "Contact of Nominally Flat Surfaces," *Proceedings of the Royal Society of London. Series A. Mathematical and Physical Sciences*, vol. 295, no. 1442, pp. 300–319, 1966.

[14] F. P. Bowden and D. Tabor, *The Friction And Lubrication Of Solids*. Oxford: Clarendon Press, 1986.

[15] M. Eriten, A. A. Polycarpou, and L. A. Bergman, "Physics-based modeling for partial slip behavior of spherical contacts," *International Journal of Solids and Structures*, vol. 47, no. 18-19, pp. 2554–2567, 2010.

[16] M. Eriten, A. A. Polycarpou, and L. A. Bergman, "Physics-based modeling for fretting behavior of nominally flat rough surfaces," *International Journal of Solids and Structures*, vol. 48, no. 10, pp. 1436–1450, 2011.

[17] K. Farhang, D. Segalman, and M. Starr, "Prediction of dissipation in joints subject to oscillating force," *2007 Proceedings of the ASME/STLE International Joint Tribology Conference, IJTC 2007*, vol. PART A, pp. 5–7, 2008.

[18] F. Al-Bender and K. De Moerlooze, "On the relationship between normal load and friction force in pre-sliding frictional contacts. Part 1: Theoretical analysis," *Wear*, vol. 269, no. 3-4, pp. 174–182, 2010.

[19] K. De Moerlooze and F. Al-Bender, "On the relationship between normal load and friction force in pre-sliding frictional contacts. Part 2: Experimental investigation," *Wear*, vol. 269, no. 3-4, pp. 183–189, 2010.

[20] M. Eriten, A. A. Polycarpou, and L. A. Bergman, "Surface Roughness Effects on Energy Dissipation in Fretting Contact of Nominally Flat Surfaces," *Journal of Applied Mechanics*, vol. 78, no. 2, p. 021011, 2011.

[21] B. Song and S. Yan, "Relationship between the real contact area and contact force in pre-sliding regime," *Chinese Physics B*, vol. 26, no. 7, 2017.

[22] B. Raeymaekers and F. E. Talke, "The effect of laser polishing on fretting wear between a hemisphere and a flat plate," *Wear*, vol. 269, no. 5-6, pp. 416–423, 2010.

[23] R. Pohrt and Q. Li, "Complete Boundary Element Formulation for Normal and Tangential Contact Problems," *Physical Mesomechanics*, vol. 17, no. 4, pp. 334–340, 2014.

[24] M. Paggi, R. Pohrt, and V. L. Popov, "Partial-slip frictional response of rough surfaces.," *Scientific reports*, vol. 4, p. 5178, 2014.

[25] B. Grzemba, R. Pohrt, E. Teidelt, and V. L. Popov, "Maximum micro-slip in tangential contact of randomly rough self-affine surfaces," *Wear*, vol. 309, no. 1-2, pp. 256–258, 2014.

[26] A. T. Kasarekar, N. W. Bolander, F. Sadeghi, and S. Tseregounis, "Modeling of fretting wear evolution in rough circular contacts in partial slip," *International Journal of Mechanical Sciences*, vol. 49, no. 6, pp. 690–703, 2007.

[27] S. C. Chen, P. J. Wei, and J. F. Lin, "A model developed for the adhesion forces formed between an atomic force microscopy tip and a rough surface under different humidity levels," *Japanese Journal of Applied Physics*, vol. 48, no. 5, pp. 0550011–0550015, 2009.

[28] M. Bazrafshan, M. de Rooij, and D. Schipper, "The Effect of Adhesion and Roughness on Friction Hysteresis Loops," *International Journal of Mechanical Sciences*, 2019.

[29] M. Bazrafshan, M. B. de Rooij, M. Valefi, and D. J. Schipper, "Numerical method for the adhesive normal contact analysis based on a Dugdale approximation," *Tribology International*, vol. 112, no. April, pp. 117–128, 2017.

[30] M. Bazrafshan, M. B. de Rooij, and D. J. Schipper, "Adhesive force model at a rough interface in the presence of thin water films: The role of relative humidity," *International Journal of Mechanical Sciences*, vol. 140, no. January, pp. 471–485, 2018.

[31] M. A. Yaqoob, M. B. de Rooij, and D. J. Schipper, "Design of a vacuum based test rig for measuring micro adhesion and friction force," *High Performance Structure and Materials*, vol. 124, no. VI, pp. 261–274, 2012.

[32] W. C. Oliver and G. M. Pharr, "An improved technique for determining hardness and elastic modulus using load and displacement sensing indentation experiments," *Journal of Materials Research*, vol. 7, no. 6, pp. 1564–1583, 1992.

[33] B. Tang and A. H. Ngan, "Accurate measurement of tip - Sample contact size during nanoindentation of viscoelastic materials," *Journal of Materials Research*, vol. 18, no. 5, pp. 1141–1148, 2003.

[34] M. Bazrafshan, M. de Rooij, and D. Schipper, "On the role of adhesion and roughness in stick-slip transition at the contact of two bodies: A numerical study," *Tribology International*, vol. 121, no. July 2017, pp. 381–388, 2018.